THE EFFECT OF HEAT TREATMENT/IRRADIATION ON THE MICROSTRUCTURE AND PROPERTIES OF IRON-BASED REACTOR ALLOYS

Guma Yeli

Linacre College

A thesis submitted for the degree of Doctor of Philosophy

Michaelmas Term 2017

Abstract

The Effects of Heat Treatment/Irradiation on The Microstructure and Properties Of Iron-based Reactor Alloys

Guma Yeli
Linacre College
A thesis submitted for the degree of Doctor of Philosophy
Michaelmas Term 2017

Nuclear power is considered to be a reliable way to satisfy the fast growing energy demand while reducing greenhouse gas emissions. However, many material challenges need to be addressed to safely extend the operational lifetime of current reactors and to develop advanced new reactors with maximised performance efficiency. This is due to the extreme reactor environment, of high temperatures and irradiation, that many components must withstand in-service. Iron-based alloys, especially Fe-Cr based steels are widely used as structural materials in current reactors and are proposed as core materials in the design of the next generation of reactor systems. To this end, using atom probe tomography (APT), this study investigates the atomic-scale microstructural changes within two Fe-Cr based steels, 17-4PH steel and T91 steel, subject to heat treatment and irradiation.

17-4PH steel is heat treated at two different temperatures, 480 °C and 590 °C for times up to 1000 hours and 24 hours respectively. The sequence of microstructural changes at the atomic scale in a 17-4PH steel is characterized by APT. At the lower temperature, the segregation of NbN/CrN ionic species, Cu-rich precipitates (CRPs), Nb-rich precipitates, Cr-rich precipitates and ultimately a Mn, Ni, and Si-rich (MNS) phase was observed to form, the latter two of which were not observed at the higher temperature. The evolution in number density and fraction of CRPs and Cr-rich α'phase, has been quantified and a simple model has been developed to estimate their respective contributions to the overall precipitation hardening of the material.

As part of a US-UK Integrated Research Project (IRP) project, another aim of this study is to demonstrate the capability to predict the in-reactor evolution of T91 microstructure at high doses, using ion irradiation as a surrogate for neutrons. APT has characterized the microstructural changes in T91 steel for different irradiation conditions, single beam (Fe^{++}) irradiation, dual beam irradiation (Fe^{++} and He^{++}) and BOR-60 reactor irradiation. Irradiation-induced precipitation, grain boundary segregation and modification of pre-existing precipitates has been directly compared between dual ion beam irradiation and reactor irradiation. APT characterisation together with complementary chemiSTEM shows that dual beam irradiation can be calibrated such that the atomic scale microstructural changes are in relatively good agreement with those caused by the corresponding reactor irradiation conditions.

Acknowledgements

I would like to express my gratitude to my supervisor, Prof. Michael Moody. I have been extremely lucky to have a supervisor who cared about my work and career development so much, and who responded to my questions so promptly throughout my time as his student. His motivation and guidance have helped me grow as a young scientist. I also want to thank my co-supervisor Dr. Paul Bagot for his tremendous support on my research project and my thesis. I am also very grateful to Dr. Maria Auger for her supervision on sample preparation, data analysis and thesis writing. Without their supervision the completion of this thesis would not be possible.

Special thanks go to Prof Steve Roberts. I have learnt a lot from MFFP group meetings. I am also very grateful to Prof George Smith for his inspirational advice on my project. I also would like to thank Rolls Royce for supplying the 17-4PH materials for this study.

I would like to thank my collaborators with mention of Dr Zhijie Jiao and Prof Gary Was from University of Michigan.

I would like to thank all the members of Atom Probe Group for the support and help. Special gratitude goes to Dr Daniel Haley and Dr Andrew London for their advice on atom probe data analysis. I also want to mention Dr Tomas Martin, Dr. Jennifer Zelenty, Dr James Douglas for being awesome officemates and organizing lots of fun group events. I want to thank Dr Michal Dagan, for spending time with me at Begbroke. I also want to thank Qifeng Yang for lots of helpful discussion. I would like to express my gratitude to all the members of APT group. I feel very lucky to work in such an inspiring and friendly group.

Oxford is a place to meet many interesting people. However, it is not easy to make lifelong friends. I am really indebted to my dearest friends, with special mention to Andrea De Franco, Yakun Gao, Yilun Gong, Zuliang Hong, Christiane Kowatsch, Kimiko Kuga, Sherry Lu, Qingji Shen, Xiaochen Wang, Weiyue Xu, Liye Yan**,** Shangyi Zhao and Jasper Zhong. I had an extremely good time in Oxford with their support.

I would like to thank the China Scholarship Council for providing the funding which allowed me to undertake this research at Oxford.

Finally, but by no means least, thanks go to mum and dad for almost unbelievable support in every aspect. They are the most important people in my world and I dedicate this thesis to them.

Preface

This doctoral thesis is an account of the work carried out by the author in the Department of Materials, University of Oxford between October 2013 and November 2017 under the supervision of Professor Michael Moody, Dr. Paul Bagot and Dr. Maria Auger. All the work is original, and where the work of others is included it is clearly referenced and acknowledged in the text. Not part of this thesis has been submitted for accepted for any other degree at this university of elsewhere.

Part of this work have been published in the following peer reviewed journals and conferences:

GumaYeli, Maria A. Auger, Keith Wilford, George D. W. Smith, Paul A. J. Bagot, Michael P. Moody, *Sequential nucleation of phases in a 17-4PH steel: Microstructural characterisation and mechanical properties*, Acta Materialia, Volume 125, 15 February 2017: 38-49

GumaYeli, Maria A. Auger, Paul A. J. Bagot, Michael P. Moody, *The effect of thermal ageing on the microstructure and properties of 17-4PH steel*, Atom Probe Tomography & Microscopy 2014 (APT&M 2014), oral presentation, Stuttgart, Germany

GumaYeli, Maria A. Auger, Paul A. J. Bagot, Michael P. Moody, *Atom probe tomography (APT) characterization of the sequence of phase nucleation in a 17-4PH Steel, International Conference on Solid-Solid Phase Transformations in Inorganic Materials (PTM 2015),* oral presentation, Whistler BC. Canada

GumaYeli, Maria A. Auger, Paul A. J. Bagot, Michael P. Moody, *APT characterization of microstructural changes in T91 steel after ion/reactor irradiation*, Atom Probe Tomography & Microscopy 2016 (APT&M 2016), Gyeongju, South Korea

Table of Contents

1 INTRODUCTION 1

2 LITERATURE REVIEW 4

2.1 Structural materials for nuclear power plant 4

2.2 Fe-Cr based steels 6

2.2.1 Precipitation hardened stainless steel 6
2.2.2 Ferritic/martensitic (F/M) steel 11
2.2.3 Effects of alloying elements 14

2.3 Microstructure evolution of 17-4PH under heat treatment 18

2.3.1 Matrix microstructure change 19
2.3.2 Cu-rich precipitates (CRPs) 20
2.3.3 Cr redistribution 24
2.3.4 Other precipitates 27

2.4 Effects of neutron/ion irradiation on microstructure of T91 steel 30

2.4.1 Introduction of irradiation damage and its consequence 30
2.4.2 Radiation induced segregation (RIS) of F/M steel 32
2.4.3 Phase stability of T91 steel under irradiation 36
2.4.4 Ion irradiation as a surrogate 39

3 MATERIALS AND EXPERIMENTAL METHODS 44

3.1 Materials 44

3.1.1 17-4PH steel 44
3.1.2 Heat treatment of 17-4PH steel 44
3.1.3 As-received T91 steel 45
3.1.4 Heat treated T91 steel 46
3.1.5 Ion/reactor irradiation of T91 steel 46

3.2 Vickers Hardness Measurements 49

3.3 XRD measurements 49

3.4 Electron backscatter diffraction (EBSD) 50

3.5 Atom probe tomography (APT) analysis 50

3.5.1 Fundamentals 50
3.5.2 Sample preparation 52
3.5.3 3-D reconstruction 56
3.5.4 Calibrating reconstruction 58
3.5.5 Mass-spectrum ranging 62
3.5.6 Data quality assessment 65
3.5.7 APT experiment parameters 69

4 APT DATA ANALYSIS TECHNIQUES 71

4.1 Data visualization 71
4.2 Compositional measurements 71
4.3 Analysis of phase boundaries/grain boundaries 72
4.4 Techniques for characterising precipitates 76
4.4.1 Nearest neighbour distribution 76
4.4.2 Cluster identification algorithms 77
4.4.3 Selection of cluster analysis parameters for maximum separation method 80
4.4.4 Selection of Iso-concentration value for concentration threshold method 85
4.4.5 Statistics of the precipitates 86
5 EFFECT OF HEAT TREATMENT ON 17-4PH STEEL 88
5.1 Introduction 88
5.2 Microstructure of 17-4PH steel after solution treatment 88
5.2.1 XRD 88
5.2.2 APT atom maps 89
5.3 Hardness variation of 17-4PH after heat treatment 90
5.4 Microstructural changes after heat treatment at 480 ºC 91
5.4.1 XRD 91
5.4.2 Atom maps 92
5.4.3 CRPs 94
5.4.4 Nb-rich precipitates 97
5.4.5 Spatial correlation between CRPs and Nb-rich precipitates 98
5.4.6 Cr-rich precipitates 101
5.4.7 MNS-rich phase 104
5.5 Microstructural changes after heat treatment at 590 ºC 110
5.5.1 XRD 110
5.5.2 EBSD results 111
5.5.3 Atom maps 112
5.6 Number density and volume fraction of CRPs and Cr-rich precipitates 114
5.6.1 CRPs 115
5.6.2 Cr-rich precipitates 115
5.7 Precipitation hardening effects 116
5.8 Summary 120
6 EFFECTS OF SINGLE ION BEAM IRRADIATION ON T91 STEELS 122
6.1 Introduction 122
6.2 SEM characterisation of T91 after heat treatment and irradiation 122
6.3 Microstructure of non-irradiated T91 123
6.3.1 As received T91 123
6.3.2 T91 steel heat treated at 470 ºC 127
6.4 Microstructure of single ion irradiated T91 132

6.4.1 1 dpa at 470 ºC 132
6.4.2 10 dpa at 470 ºC 137
6.4.3 20 dpa irradiation at 420 ºC 144
6.5 Discussion: microstructural changes after irradiation 146
6.5.1 Irradiation induced precipitation 146
6.5.2 Stability of pre-existing precipitates 148
6.5.3 Grain boundary segregation 149
6.6 Summary: 151
7 BOR60 AND DUAL ION BEAM IRRADIATION OF T91 152
7.1 Introduction 152
7.2 Microstructure of T91 after BOR60 irradiation 153
7.2.1 Elemental distribution of T91 after BOR60 irradiation at 412 ºC 153
7.2.2 MNS-rich cluster composition after BOR60 irradiation at 412 ºC 155
7.2.3 Segregation to dislocation loops 156
7.2.4 Elemental distribution of T91 after BOR60 irradiation at 386 ºC 158
7.2.5 MNS-rich cluster composition after BOR60 irradiation at 386 ºC 159
7.2.6 Size effect of MNS-rich cluster composition 160
7.2.7 Carbide composition after BOR60 irradiation 162
7.2.8 Comparison to TEM results 164
7.3 Microstructure of T91 after dual ion beam irradiation 165
7.3.1 SEM images 165
7.3.2 Atom maps after DI beam irradiation at 432 ºC 166
7.3.3 MNS-rich cluster composition after Dual ion beam irradiation at 432 ºC 169
7.3.4 Solute segregation to dislocations after dual ion irradiation at 432 ºC 170
7.3.5 Carbide/matrix interface after dual ion beam irradiation at 432 ºC 172
7.3.6 Grain boundary segregation after Dual ion beam irradiation 173
7.3.7 V-rich nitride composition after DI irradiation at 432ºC 175
7.3.8 Atom maps after DI irradiation at 406 ºC 176
7.3.9 Solutes segregation at defects in DI irradiated T91 at 406 ºC 178
7.4 Discussion: BOR60 vs DI irradiation 180
7.4.1 Nearest neighbour distribution of Ni-Ni 180
7.4.2 Cr segregation to dislocation loops 184
7.4.3 Carbide/matrix interface 185
8 CONCLUSIONS 186
8.1 Characterizing Fe-Cr based steels using APT 186
8.2 Microstructural changes of 17-4PH after heat treatment 186
8.3 Effects of ion/reactor irradiation on T91 steel 187
8.4 Implications of the findings 188
8.5 Future work 189
9 REFERENCES 192

1 Introduction

Due to the increasing demand for low-carbon energy sources, there is renewed interest in developing nuclear energy [1–3]. One of the key factors for safe operation of current reactors and implementation of advanced nuclear energy systems has been the development of suitable structural materials to withstand the high neutron flux, high temperature and high corrosive environment in a nuclear reactor [4,5]. Developing an understanding of how the microstructure of these materials evolves under these harsh conditions, correlating this to mechanical properties and ultimately predicting safe operating lifetime of key components is critical to improve the performance of materials used in nuclear reactors.

Fe-Cr based steels are the most widely used materials within the nuclear industry due to their combination of high strength, good ductility, corrosion resistance, irradiation resistance and weldability [6]. For example, in the current Pressurized Water Reactors (PWRs), the main core structural materials and cladding materials are dominated by austenitic stainless steels (i.e. Types 304, 316) [7]. Duplex steels and precipitation hardened steels are used for components such as blades, pumps and pipes [8]. Ferritic/martensitic steels have also been proposed as the main structural materials for the new generation of fission reactors and concept fusion reactors [9–13]. However, there are still material performance issues to be resolved, such as the phase stability of materials, radiation induced segregation and precipitation under heat and irradiation. These can result in changes to mechanical properties, which can be hazardous to the lifetime of reactors.

This work focuses on the atomic scale characterization of microstructural changes after irradiation/heat treatment in two Fe-Cr steels relevant to the design and construction of nuclear reactors, namely 17-4PH and T91, primarily using atom probe tomography (APT).

The literature review in **Chapter 2** introduces the types and development of Fe-Cr containing steels and the challenges when used as structural materials in nuclear reactors. It also summarises the current understanding of the microstructure of 17-4PH and T91 steel subjected to different heat treatments/irradiation. The chapter then goes on to discuss the challenges of using ion irradiation as an alternative of neutron irradiation as a means to investigate the damage sustained by materials in the reactor environment.

As described in **Chapter 3**, Atom Probe Tomography (APT) has the potential to provide unique atomic-scale chemical information in 3D. However, careful interpretation of the results is required. A section of work has been dedicated to optimal analysis conditions for APT experiments and better interpretation of the obtained APT data. This chapter includes a description of the APT image reconstruction calibration methods applied in this work using algorithms developed by Dr Daniel Haley. Cluster analysis within APT data is one of the key aspects necessary to understand the evolving complex microstructure in these materials. Methods to select appropriate cluster analysis parameters and interpret the results are presented in **Chapter 4**.

The microstructural changes of 17-4PH steel after heat treatment as a function of time at different temperatures are investigated in **Chapter 5**. The formation mechanism of various phases, including Cu-rich precipitates (CRP), Nb-rich precipitates, Cr-rich precipitates and Mn, Ni, Si (MNS)-rich phase have been characterized using APT. This chapter also attempts to understand the correlation between the microstructure and the hardness changes observed in the material. Precipitation hardening models have been applied to CRPs and Cr-rich precipitates to estimate their contribution to hardness increases.

Another main aim of this study is to understand the irradiation effects on T91 steel and investigate to what extent ion irradiation can mimic reactor irradiation. The as-received T91 steel and the microstructural changes after single ion irradiation have been investigated and are presented in **Chapter 6**.

The microstructure changes after dual ion beam irradiation and irradiation in the BOR60 reactor, in terms of solute clustering, grain boundary segregation and solute segregation to the carbide/matrix interface have been discussed in **Chapter 7**. In this chapter, not only have the irradiation effects been investigated, but the microstructure between neutron irradiation and ion-irradiation has been directly compared, which enables tuning of the latter to better match the effects of neutron irradiation.

2 Literature review

2.1 Structural materials for nuclear power plant

Nuclear power has been considered as a reliable way to satisfy the fast growing demand for energy while reducing greenhouse gas emissions [14]. By the end of 2016, there were 447 nuclear power plants (NPPs) in operation across the world and 60 more under construction [1]. Safety is always a prime concern for the development of nuclear reactors. Incidents such as the Fukushima-Daiichi accident highlight the critical importance of safety and since this time new efforts to further improve safety are being made throughout the world [15,16].

Safety of structural materials is a great concern for long-term operation of NPPs. The failure of structural materials can cause severe damage to the reactors with catastrophic consequences including radioactive leakage. The operating environment for these materials is exceptionally harsh: a combination of high temperature and stress, intense neutron flux and a chemically corrosive coolant [11,17,18]. Furthermore, the activities to extend the lifetime of current reactors, the design of advanced fission reactors and the emergence of fusion energy increase the potential burden on these materials even further. The operating temperature and displacement dose of some advanced reactors are shown in Figure 2-1. It is notable that a common feature for advanced reactor design is the use of even higher temperatures and irradiation doses compared to current fission reactors. The assessment of materials that meet these requirements has become the key issue for the development of advanced reactors [11,19,20].

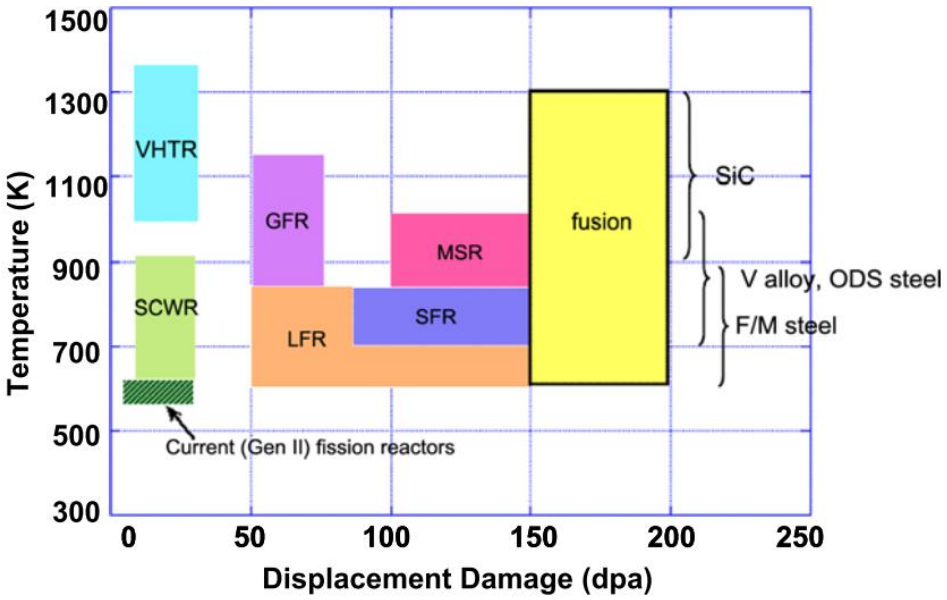

Figure 2-1 Operating temperature and displacement dose for different reactor systems [11]. VHTR: very-high-temperature reactor, SCWR: supercritical water reactor, GFR: gas-cooled fast reactor, LFR: Lead-cooled fast reactor, MSR: molten salt reactor, SFR: sodium-cooled fast reactor

S. J. Zinkle and G. S. Was [6] reviewed various materials degradation phenomena in current fission reactors and identified into six key effects: (1) radiation hardening and embrittlement; (2) radiation-induced or -enhanced solute segregation and phase stability; (3) creep; (4) void swelling; (5) He embrittlement; (6) corrosion and stress corrosion cracking.

Fe-Cr steels are often used as structural materials due to their desired properties under extreme conditions. However, there are still material degradation issues to be resolved. Thus, it is of great importance to have a thorough understanding of the long-term in-service behaviour of Fe-Cr based steels so as to safely extend the lifetime of current reactors, and to design and construct new ones. Considering that different components are exposed to different levels of irradiation, corrosion and temperature, the main limiting issues for each material must be addressed independently.

2.2 Fe-Cr based steels

There are several types of widely used Fe-Cr steels with varying chemical composition and microstructure, including austenitic, ferritic/martensitic, duplex and precipitation hardened stainless steel [17,21–23]. The most extensively utilised materials in current reactors are austenitic stainless steels. These steels normally contain 18 - 30 wt. % Cr and 8 - 40 wt. % Ni, which provides high corrosion resistance at high temperature [21,22]. However, the mechanical strength of the standard solution-treated austenitic steel is relatively low. Precipitation hardened stainless steel can exhibit higher strength [23]. Furthermore, the face centred cubic (FCC) structure of austenite is highly susceptible to void swelling under high dose compared to ferritic/martensitic steels [24–26]. The main focus of this chapter is the microstructural behaviour subject to in-service conditions (high temperature and irradiation) of precipitation hardened martensitic steels and ferritic/martensitic steels.

2.2.1 Precipitation hardened stainless steel

Precipitation hardened steels, with a combination of high strength, corrosion resistance and wear resistance, are suitable for applications where higher load is required [27]. Martensitic precipitation hardened steels normally contain 14 - 17 wt. % Cr, 4 - 7 wt. % Ni and other precipitation forming elements, such as Cu, Al, Ti, Nb, and Mo to further increase tensile strength by heat treatment [28,29].

- Mechanism of precipitate formation

Precipitation hardening is achieved by producing second phase precipitates, acting as obstacles to dislocation movement. Precipitation hardening always originates from a supersaturated solid solution. The return to equilibrium requires that the dissolved solute

atoms group together in the form of precipitate particles. The supersaturated solute atoms first diffuse together to form a so called “A Guinier–Preston (G. P.) Zones” [29], which are regions of higher solute concentration. As the process continues, these zones become coherent precipitates. In this stage, the alignments of atoms and the lattice planes still remain continuous with those of the matrix. Certain solute atoms replace the matrix atoms and others occupy interstitial positions. However, the atomic arrangement of the original matrix is disturbed. The final stage is the formation of precipitates which are in equilibrium with the matrix with a clearly defined chemical composition [29].

- Mechanism of precipitation hardening

Precipitation hardening mechanism has been subject of research since age hardening was first discovered. The introduction of the role of dislocations [30] and the equation derived later by Orowan stands as landmark achievement in the development of understanding of the fundamentals of precipitation hardening mechanism [31]. Since then a number of attempts have been made to quantify precipitation hardening. The progress in understanding precipitation mechanisms has been thoroughly discussed in [32], [33] and [34].

The basic model illustrating dislocation-point obstacle interaction is shown in Figure 2-2. When a glide dislocation encounters an array of obstacles, it can be bent to some angle, the bowing angel ϕ, before it can move on. The strength of the precipitates, F, as an obstacle can be expressed by:

$$F = 2T\cos\frac{\phi}{2} \qquad 2\text{-}1$$

where T is the line tension of the dislocation. When the breaking angle $\phi = 0$, the particle behaves as an impenetrable obstacle, while for values of $\phi > 0$, the particle can be sheared by the glide dislocation, with the required shearing force equal to F.

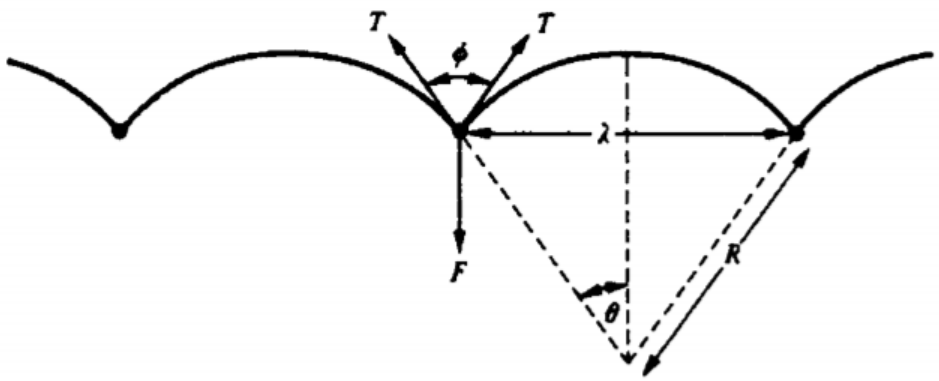

Figure 2-2 Dislocation held up at an array of point obstacles. The bowing angle ϕ is defined as shown [32]

- Particle shearing

In the case of particles that can be sheared by the glide dislocation, as shown in Figure 2-3, the critical resolved shear stress can be expressed by [32]:

$$\tau_c = \frac{2}{bLT^{1/2}}\left(\frac{F}{2}\right)^{3/2} = \frac{4T(\cos\frac{\phi}{2})^{3/2}\pi r^2}{3bf} \qquad 2\text{-}2$$

where b is the magnitude of the Burgers vector, L is the spacing of the particles, r is the size of the particle and f is the volume fraction of the particle.

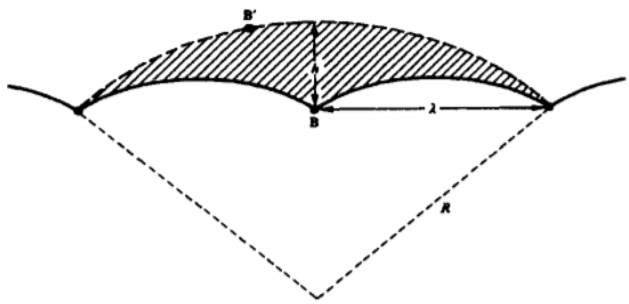

Figure 2-3 The Friedel process for dislocations interacting with point obstacles [32]

In such cases, precipitate particles can impede the motion of dislocations through a variety of interaction mechanisms. Those mechanisms for which theories for the value of F (or ϕ) have been developed include:

1. chemical strengthening, which arises from the increased matrix-particle surface energy when the particle is sheared by the dislocation;
2. stacking-fault strengthening, which occurs when there is a stacking difference between the particle and the matrix;
3. modulus hardening, which arises from differences between the elastic modulus of the particle and matrix;
4. coherency strengthening, which arises from the elastic strains surrounding a particle that does not perfectly fit the matrix lattice;
5. order strengthening, which is related to the additional work required to create an antiphase boundary in the case of dislocations passing through precipitates which have an ordered lattice.

The detailed derivation and effect of each mechanism can be found in [32] and [34]. The hardening interactions vary in different systems and in some cases more than one strengthening mechanisms can work simultaneously.

- Impenetrable particles

As a precipitate grows, it becomes increasingly difficult for it to be sheared by the passage of a dislocation, because of the increase in F with r (equation 2-2). However, as F increases, the breaking angle ϕ decreases, and eventually becomes zero. For larger values of F the dislocation by-passes the particle rather than shearing it, so the force exerted by the particle is balanced by the line tension of the two arms of the dislocation on each side of the particle. The by-passing stress is thus obtained by substituting $F = 2T$

$$\tau_c = \left(\frac{3}{2\pi}\right)^{1/2} \frac{\mu b}{r} f^{1/2} \qquad 2\text{-}3$$

- 17-4PH stainless steel

17-4PH steel is one of the most commonly used precipitation hardened stainless steels. 17-4PH was first developed by Armco Steel Co [35]. It is used in valves, turbine blades, pumps and lead screws in current PWRs. The extension of current water reactors requires a thorough understanding of long-term in-service behaviour of this material. 17-4PH contains a much higher amount of Cu (3 - 4 wt. %) than the solubility limit in Fe. Cu is deliberately supersaturated so as to harden 17-4PH during heat treatment. The martensitic microstructure in combination with precipitation hardening of copper gives a high strength and good wear resistance while maintaining a degree of ductility and toughness for damage tolerance. Also, the relatively high Cr content (16 - 18 wt. %) provides reasonable corrosion resistance.

2.2.2 Ferritic/martensitic (F/M) steel

Another type of widely used Fe-Cr based materials in reactors are F/M steels. F/M steels normally contain 7 - 12 wt. % Cr, which is lower than Cr content in 17-4PH. The Cu levels are also significantly reduced (normally lower than 0.1 wt. %) in F/M steels.

- Development of F/M steel

Until the 1970s, the primary materials for fast reactor core structures were austenitic steels. F/M steels (9 - 12 wt. % Cr) became of interest because of their better swelling behaviour compared to conventional austenitic stainless steels under irradiation. Figure 2-4 shows a comparison between void swelling rates of austenitic steels and ferritic/martensitic (F/M) steels (shown in green). The F/M steels exhibit a much better swelling resistance. In addition, they also have a better irradiation embrittlement resistance and corrosion behaviour than austenitic steels in more aggressive coolant such as Pb-alloys. They are now considered as promising candidates for sodium or lead cooled reactors, pressure vessel of gas-cooled reactors as well as for the core structures of fusion reactors [9,12].

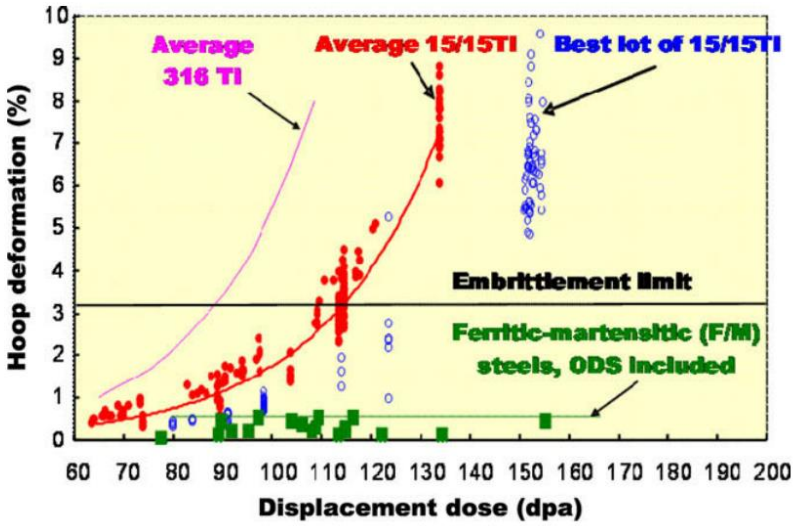

Figure 2-4 Comparison of void swelling behaviour of conventional austenitic steels and ferritic/martensitic steels [12]

The development of ferritic/martensitic steels is shown in Table 2-1. Historically, one of the main properties to improve was the maximum temperature of application and in particular their creep strength behaviour. The first primary ferritic/martensitic steel developed was HT9 (chemical composition in Table 2-2). In HT9, Nb and V were added to conventional 9Cr1Mo steel to form fine Nb and V containing precipitates to increase creep strength. It was considered as the first generation of ferritic/martensitic steel. Later, steels with lower Cr and C content were favoured due to the better irradiation embrittlement behaviour [9,10,36]. At that stage, Nb and V composition was optimized and N was added to form a fine MX (M refers to Nb and V, X refers to C and N) precipitates in modified 9Cr1Mo steel (T91) to further increase creep strength [37]. In the third generation of ferritic/martensitic steels, the high activation solutes such as Mo and Nb are now replaced by more stable W and V. In the future, the development of ferritic/martensitic steels will also need to consider the requirement of high temperature behaviour, low irradiation-reactivity and high neutron irradiation resistance.

Table 2-1 Evolution of ferritic/martensitic steels for power-generation industry [10]

1	1960-1970	Addition of Mo, Nb and V to simple Cr-Mo steels	HT9
2	1985-1995	Optimization of C, Nb, V and N	T91
3	1985-1995	Partial substitution of W for Mo and adding Cu, B	NF616
4	Future	Increasing W and adding Co	NF12

Table 2-2 Nominal composition of HT9

Elements	C	Si	Mn	Cr	Ni	Mo	W	V
wt. %	0.2	0.4	0.6	12.0	0.5	1.0	0.5	0.25

- Composition and microstructure of T91

T91 martensitic steel is a typical F/M steel that has been studied extensively. The chemical composition is listed in Table 2-3. T91 exhibits a lower swelling rate compared to austenitic steel, and remarkable creep strength compared to HT9. Additionally, T91 was also found to have satisfactory corrosion resistance in both flowing Pb and Lead-Bismuth Eutectic (LBE, one of primary coolant candidates for advanced reactors) up to 500 ^{o}C [38].

Table 2-3 Nominal composition of T91 (wt. %)

Elements	C	Si	Mn	Cr	Ni	Mo	V	Nb	N
wt. %	0.1	0.4	0.4	9.0	0.1	1.0	0.2	0.08	0.05

Figure 2-5 shows optical microscopy of T91, the microstructure of the material is basically martensite with fine prior austenitic grain boundaries, similar to that of 17-4PH. However, it is difficult to reveal the fine-scale structure of martensite using optical microscopy. Therefore, attention has moved to Transmission Electron Microscopy (TEM) and Atom Probe Tomography (APT), with even higher spatial resolution, to allow study of the microstructural changes.

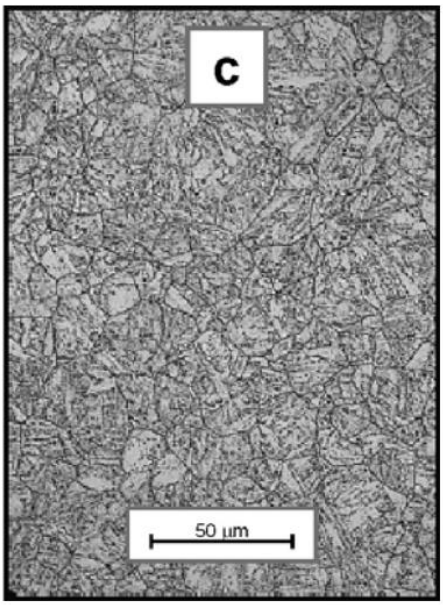

Figure 2-5 Microstructure of T91 by light optical microscope [39]

2.2.3 Effects of alloying elements

As discussed above, in both precipitation hardened steel 17-4PH and F/M steel T91, a number of solute elements have been added to achieve better mechanical properties. However, under heat or irradiation, they can also produce new phases, precipitation and segregation, which cause changes in the mechanical properties.

- Cr composition

The Cr composition in Fe-Cr based materials is one of the key parameters to be optimized in order to obtain the best combination of properties. Cr is added mainly to increase corrosion resistance. Higher Cr content increases the corrosion resistance, but it also affects the phase stability. The binary Fe-Cr phase diagram is presented in Figure 2-6. Notably, for the temperatures of interest (290 ^{o}C - 500 ^{o}C according to the service temperature of various types of reactors) and for a wide range of compositions, it indicates a phase separation reaction occurs where Fe-rich α phase and Cr-rich α’ phase form. This phase separation

causes hardening embrittlement known as “475 ºC embrittlement”. The α-α’ miscibility gap is critical to many applications, however the exact position on the phase diagram is still under research. The phase diagram calculated by CALPHAD (black line in Figure 2-6) predicts an extremely low Cr solubility at low temperature. Bonny et al. [40] reviewed experimental data on α’ phase formation and the result showed a mismatch between the experimental data and the CALPHAD prediction. They made a modification to the original phase diagram (shown in red line). However, it should be noted that Bonny et al. included results from irradiation experiments and made an assumption that irradiation does not influence the thermal equilibrium. Xiong et al. used ab-initio calculation (details can be found in [41]) and indicated a possible region within the phase diagram where this miscibility line can occur, as shown in green area in Figure 2-7.

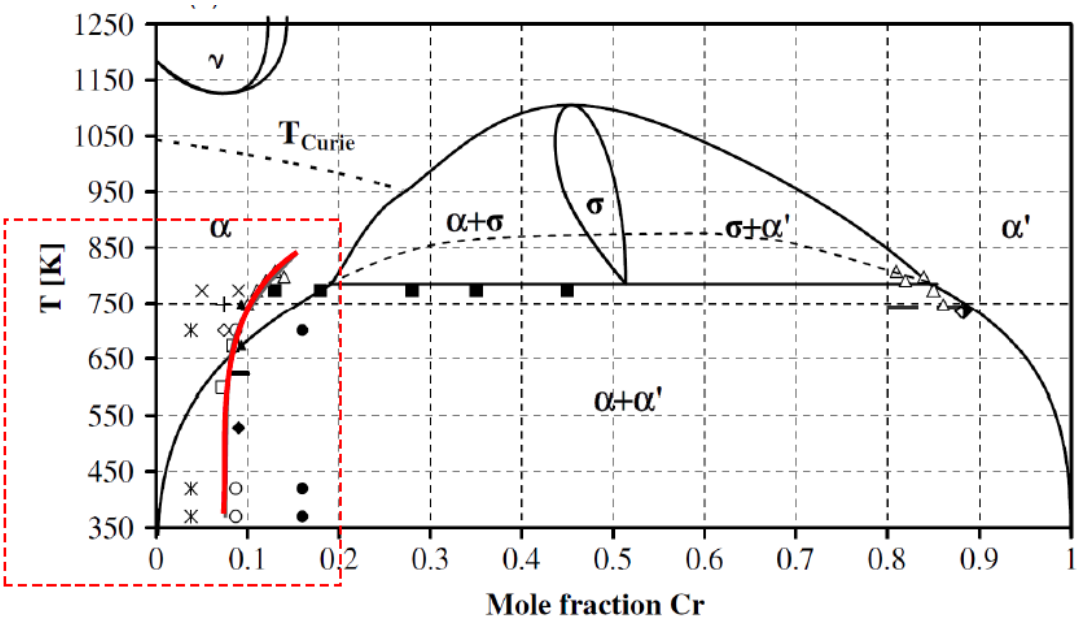

Figure 2-6 low temperature part of Fe-Cr phase diagram according to CALPHAD calculations (from [42]); Some experimental data (symbols) are presented as well as the new position of α domain limit (red line) proposed by Bonny et al. [40]

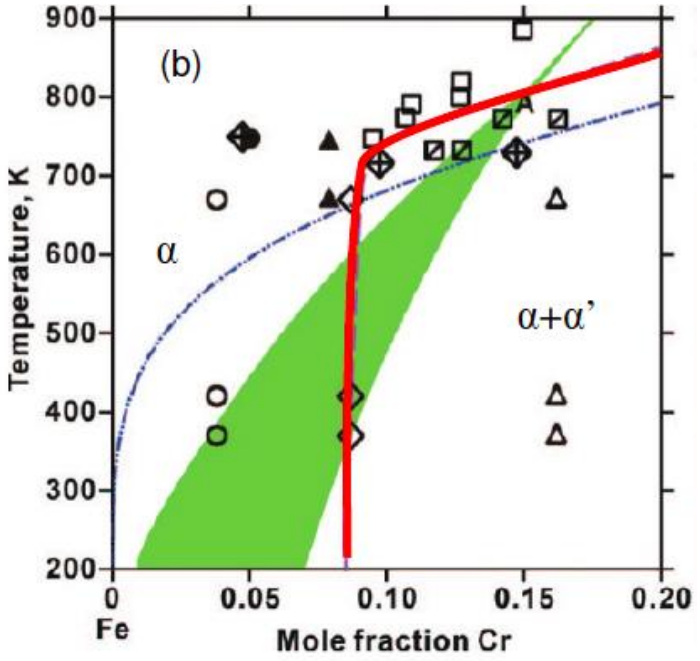

Figure 2-7 Low Cr part of the α-α' miscibility gap; the position of the α domain limit, proposed by Bonny et al. is shown in red [40]; the possible location for Fe-rich region determined by Xiong et al. [41] is represented by the green area

The difficulty of conducting experiments to define the α-α' miscibility gap is due to reduced diffusion efficiency of Cr at lower temperature as well as difficulty of detecting the α' formation at its early stage as Cr has a similar lattice parameter with the BCC matrix. Utilizing atom probe tomography, the formation of Cr-rich phase is unambiguously detected. In a recent work by Bachhav et al. [43], a series of alloys with different Cr contents were irradiated to 1.82 dpa at 290 ^{o}C. The atom probe results are shown in Figure 2-8. From the result, α'-phase formed when the Cr content is greater than 9 wt. % and did not form in sample with Cr content of 6 wt. %. Thus, they argued the miscibility line falls between 6 - 9 wt. %, which is in good agreement with the recent modification of the phase diagram.

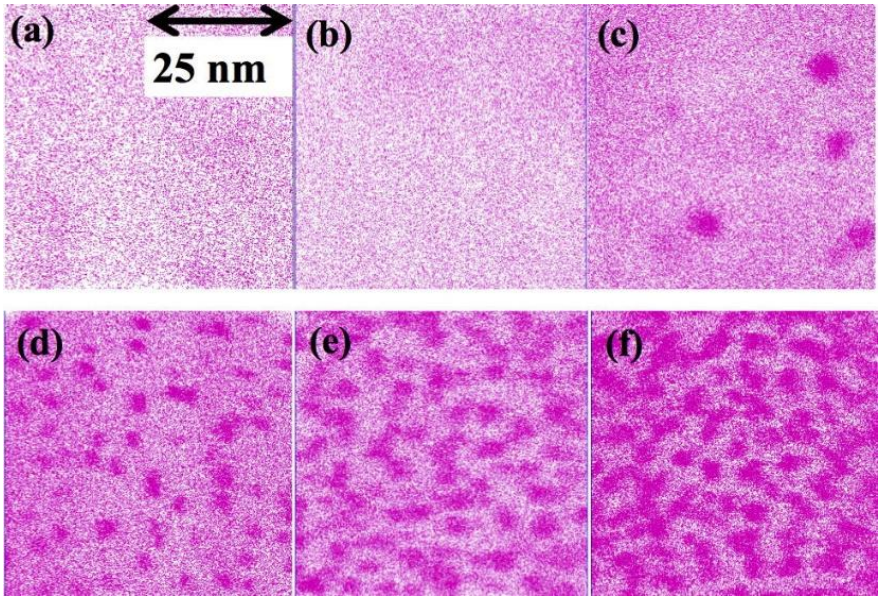

Figure 2-8 20 nm thick slices of APT reconstruction showing the distribution of Cr atoms for each of the analysed alloys: (a) Fe-3Cr, (b) Fe-6Cr, (c) Fe-9Cr, (d) Fe-12Cr, (e) Fe-15Cr, (f) Fe-18Cr [43]

- Effects of other elements

In order to achieve a desired property, a variety of other alloying elements are added to the Fe-Cr system.

Phase stabilizers Elements that have the same BCC crystal structure as ferrite, restrict the formation of γ austenite and stabilize the ferritic/martensitic phase. The following elements have a ferrite stabilizing effect: Cr, W, Mo, V, Al, Si. In contrast, elements like Ni, Mn and Co widen the γ austenite formation temperature and stabilize the austenite.

Carbide and nitride formation Some strong carbide- and nitride-forming elements (i.e. Cr, Mo, V, Nb, Ti and Ta) are typically introduced to the steels to increase hardness and strength. Carbides and nitrides generally precipitate during the tempering process after quenching. Large (60 - 200 nm in size) carbides $M_{23}C_6$ (M is primarily Cr, Fe, Mo)

precipitate and smaller (20 - 80 nm in size) MX (M is primarily V, Nb, Ti, Ta, and X is C and N) are often observed in precipitation hardened steels and F/M steels.

Modifying mechanical properties Some alloying elements do not form carbides or nitrides. Instead, they only change the properties of the bulk material. Cu increases the hardness and strength but the precipitation of Cu can cause embrittlement. Ni increases strength, toughness, hardenability and impact strength of steels. Mn improves ductility and wear resistance as well as eliminating formation of harmful iron sulfides, increasing high temperature strength. Si is one of the principal deoxidizers used in steelmaking. Si contributes to the increase of as-rolled strength and hardness. P increases strength and hardness but decreases ductility and toughness because of segregation at grain boundaries (therefore, P is normally controlled to low levels). S decreases ductility, toughness and weldability.

In this section, the effects of alloying elements in precipitation hardened steels and F/M steels have been introduced.17-4PH steel is mostly used in outer core components for nuclear fission reactors. Thus, the microstructure stability under elevated temperature is the primary concern. T91 steel, on the other hand, is proposed as a structural material for the core of modern reactors, where the irradiation effects are much more significant. In the following Sections 2.3 and 2.4, a detailed description of microstructure changes of 17-4PH under heat treatment and T91 under irradiation will be presented.

2.3 Microstructure evolution of 17-4PH under heat treatment

Many applications of precipitation-hardened steels require stable mechanical properties at relatively high temperature, for example in current water reactor some components are held

at 290 ºC for decades of time. However, studies have revealed that microstructure induced material property can change upon long-term ageing at elevated temperatures [44–46]. Therefore, it is essential to understand the microstructure changes with respect to different heat treatment conditions. 17-4PH is commonly supplied in the solution treated condition (solution treatment at 1038 ºC followed by quenching). It is then heat treated to different conditions to obtain a wide range of properties. Two commonly used heat treatment conditions are: 482 ºC for 1h (condition H900) and 593 ºC for 4h (condition H1150). Precipitates produced by different heat treatments also differ in density, size and structure. This initial microstructure also influences the subsequent in-service behaviour. The microstructure changes include matrix microstructure and secondary phase nucleation. For most heat treatment conditions, the matrix microstructure of 17-4PH remains martensitic. The diffusion of alloying elements can alter local chemical composition and phase stability, leading to the changes in mechanical property.

2.3.1 Matrix microstructure change

- Solution treated microstructure of 17-4PH

Hsiao et al [47] showed that the martensite transformation of 17-4PH starts (Ms) at 105 ºC from a dilatometric curve. Thus, the martensite structure can be easily obtained by solution treatment at 1038 ºC and quenching. A typical microstructure for the solution treated condition is shown in Figure 2-9. The microstructure is basically martensitic, with a low percentage (around 2 - 5 % in volume fraction) of δ-ferrite. The presence of δ-ferrite has also often been observed in a number of previous studies. Later Hsiao et al. argued that twinned structure is also frequently observed at solution treated stage [47]. Carbides, such as $M_{23}C_6$ and NbC, are also observed at solution treated stage.

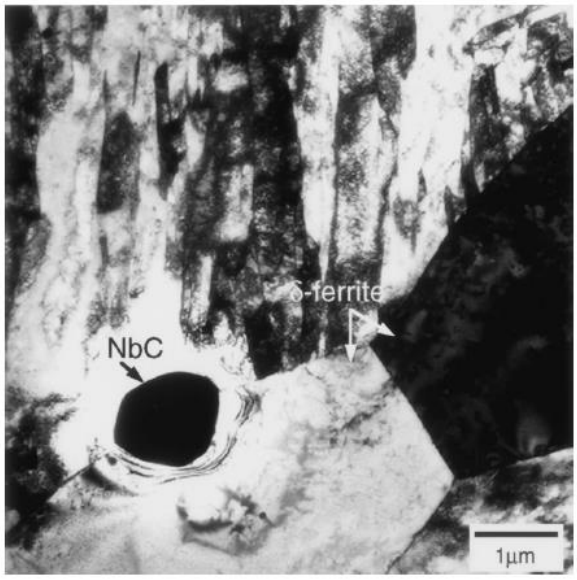

Figure 2-9 microstructure of 17-4PH by TEM [48]

- Matrix microstructure changes under heat treatment

At most heat treatment conditions, the main microstructure of 17-4PH remains martensitic. However, while heat treated at relatively high temperature, above 580 ^{o}C, reversed austenite has been found to form at the lath boundaries and within martensite lath [46]. At even higher temperature of 620 ^{o}C, significant amounts of reversed austenite have been observed after 4 h [47]. Even at much lower temperature of 350 ^{o}C, the presence of reverse austenite is found after ageing for 10000 h [49]. It indicates when tempered above 350 ^{o}C and given sufficient time, reversed austenite can form after long-term ageing.

2.3.2 Cu-rich precipitates (CRPs)

Due to its low solubility in iron, Cu atoms tend to precipitate out from the matrix when the Cu concentration in steel exceeds a certain level (about 1 wt. %). Cu-rich precipitates have been extensively studied in various Cu bearing steels, and especially in reactor pressure vessel (RPV) steels [50–53]. It is known that, in a solid solution, metastable body centred

cubic (BCC) precipitates form at first. These precipitates are coherent with the matrix and thus require less energy to form. Once the precipitates reach a critical size, they transform from coherent precipitates to a 9R structure, which is characterized by a high density of twins. As the precipitates grow even larger, they transform into an equilibrium face centred cubic (FCC) structure. Ni and Mn has found to segregate at the edge of the Cu precipitates to reduce the surface energy between CRPs and matrix [54]. These CRPs hinder dislocation movement and cause hardening embrittlement. Thus, in RPV steels, Cu levels have been greatly reduced.

However, in 17-4PH, Cu is deliberately added to form fine-scale precipitates during heat treatment to strengthen the material. According to the Fe-Cu binary phase diagram, at 1038 ^{o}C the solubility of Cu exceeds 7 at. %. Thus, in the solution treated condition, the Cu atoms are supersaturated in the martensitic lath. Murayama et al. reported fine CRPs in δ-ferrite after solution treatment [48]. They proposed that CRPs in δ-ferrite formed during cooling from solution treatment, caused by the higher diffusivity of Cu in δ-ferrite than austenite. A similar feature was also observed by Rack and Kalish [44] but identified as NbC. Both works concluded that these fine features in δ-ferrite were not affected by heat treatment. As mentioned above, the δ-ferrite is a minor feature in 17-4PH, thus the researches have focused on the CRPs that form within the martensite during heat treatment.

Previous studies have shown the formation of CRPs subject to treatments for various times and temperatures. The early works focused on using TEM, however it was difficult to detect coherent precipitates. The utilization of atom probe field ion microscopy (APFIM), a forerunner of atom probe tomography, made it possible to detect the early stage of CRPs formation [55]. The structures of CPRs observed in heat treatment of 17-4PH and a very similar material 15-5PH are summarized in Figure 2-10. There is a variation between

different experiments. A trend can still be identified: At lower temperature and shorter time (at 480 ºC for 0.5 h) the precipitates were still coherent such that TEM could not detect them but from APFIM, the Cu-rich region is detected. At longer ageing time at 480 ºC, the 9R structure begins to appear. At higher temperature or longer time, FCC structured CRPs are often observed [47]. Some TEM studies failed to see these FCC structure at higher temperature and longer ageing time. This could be due to the instrument limitations or a real effect due to specific sample conditions. The orientation between CRPs with a FCC structure and the matrix is reported to be consistent with a Kurdjumov-Sachs (K-S) relation [47,56]. From APFIM, the composition of the CRPs was determined to be about 97 % Cu, with a small amount of Ni and Mn. These CRPs were found to coarsen in size, become cylindrical in shape and segregate along grain boundaries or dislocations after prolonged ageing.

Examples of coherent precipitate observed by APFIM, typical 9R structure obtained from HRTEM and a dark field image of incoherent CRPs are shown in Figure 2-11 as a sequence of CRPs development.

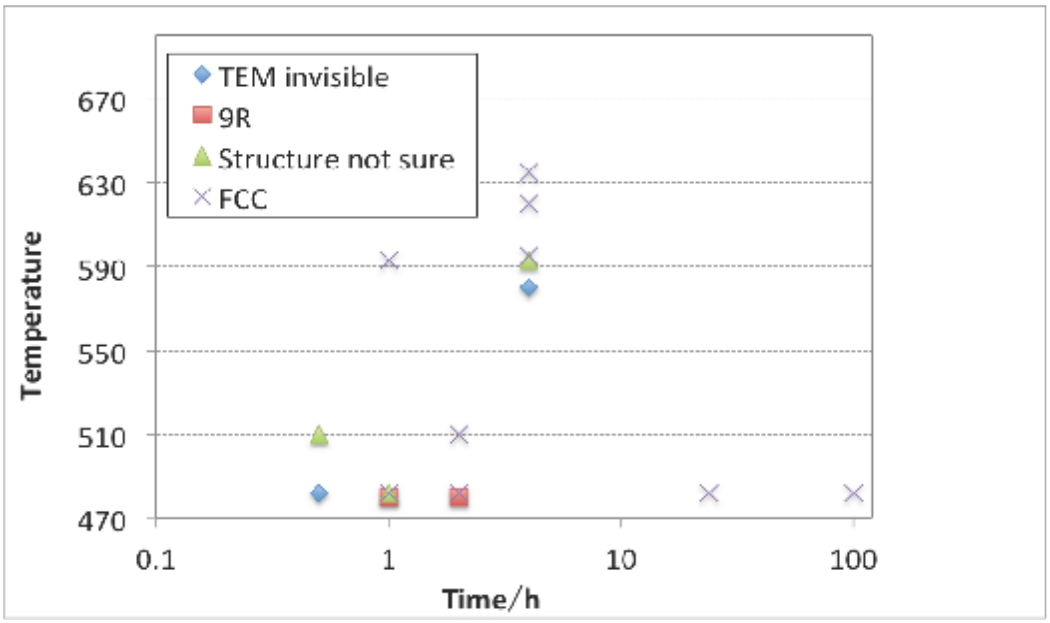

Figure 2-10 Structures of CRPs observed in previous studies on 17-4PH [35,46–48,55,57]. The symbols are: blue-TEM invisible clusters detected by APFIM; green-TEM visible but too fine to get a diffraction pattern; red-9R structure; purple cross-CRPs with diffraction pattern of FCC structure

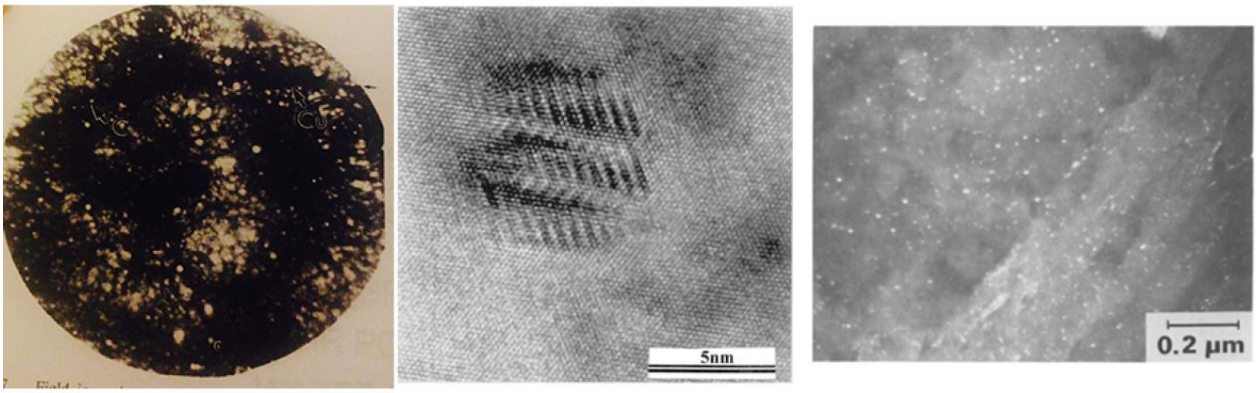

(a) (b) (c)

Figure 2-11 (a) APFIM image of coherent Cu precipitates [55]; (b) High resolution electron micrograph of a Cu precipitate in 15-5 PH stainless steel, showing a 9R structure [56]. Hsiao [47] also observed this twinned 9R structure at the same condition for 17-4PH but could not get a clear diffraction pattern; (c) A dark field micrograph taken using a (022) FCC reflection, revealing homogeneous copper precipitation in the martensite matrix, in the alloy aged for 2 h at 510 ^{o}C [46]

2.3.3 Cr redistribution

According to the Fe-Cr phase diagram shown in Figure 2-6, 17-4PH steel is within the miscibility gap. The Fe-Cr system has been known to be susceptible to embrittlement when aged at intermediate temperatures, i.e. in the range of 300 - 500 ^{o}C [58,59]. This embrittlement, known as 475 ^{o}C embrittlement, is related to the microstructure evolution caused by redistribution of Cr.

- Cr decomposition in Fe-Cr system

Within the Fe-Cr miscibility gap, there are two domains, representing the two possible paths to reach the equilibrium state, namely nucleation and growth (NG) and spinodal decomposition (SD). The classical distinction between these two mechanisms is that in the NG case, α' nuclei form with their equilibrium composition since the early stage of phase separation, whereas for spinodal decomposition, composition fluctuations become greater throughout the system, and increasingly develop both in size and amplitude towards an equilibrium distribution. Both domains of the equilibrium phase diagram are separated by the spinodal line, classically described in the linear Cahn-Hilliard (CH) theory as the locus of the points where the second derivative of the free enthalpy vs. composition is zero. Later, a more refined non-linear Langer-Bar-on-Miller (LBM) theory has been proposed [60].

Early studies on Fe-Cr decomposition focused on using Mossbauer Spectroscopy (MS) and Small-Angle Neutron Scattering (SANS) [6]. MS can detect α' domains at the early stages because they induce a modification of the hyperfine field. However, with this method, no information of characteristic distance, which can define the nature of the spinodal decomposition could be obtained. SANS can give such information. Utilizing High Resolution TEM (HR-TEM), a contrast could be obtained between α and α' [61]. However,

it was difficult to confirm unambiguously due to the similar lattice parameter between the matrix and precipitates region. The first analyses of Fe-Cr system by field ion microscopy (FIM) was conducted by Brenner et al. [62]. Their research was on Fe-32 % Cr alloy aged at 470 ^{o}C. The most significant contribution from this work was to plot the concentration profiles of specimen as a function of ageing time (shown in Figure 2-12). The results provided an experimental evidence of spinodal decomposition: the development of both the amplitude and wavelength of Cr concentration fluctuations is consistent with the continuous transformation mechanism, the classical description of the spinodal mechanism. Later, some other works were also conducted on Fe-Cr alloy, Hyde and Miller et al. used atom probe field ion microscopy to characterise spinodal decomposition in binary Fe-Cr alloys containing 24 – 45 at. % Cr and the results show a good agreement between experimental observations and atomistic Monte Carlo modelling and numerical solution to the Cahn-Hilliard-Cook equation [63,64].

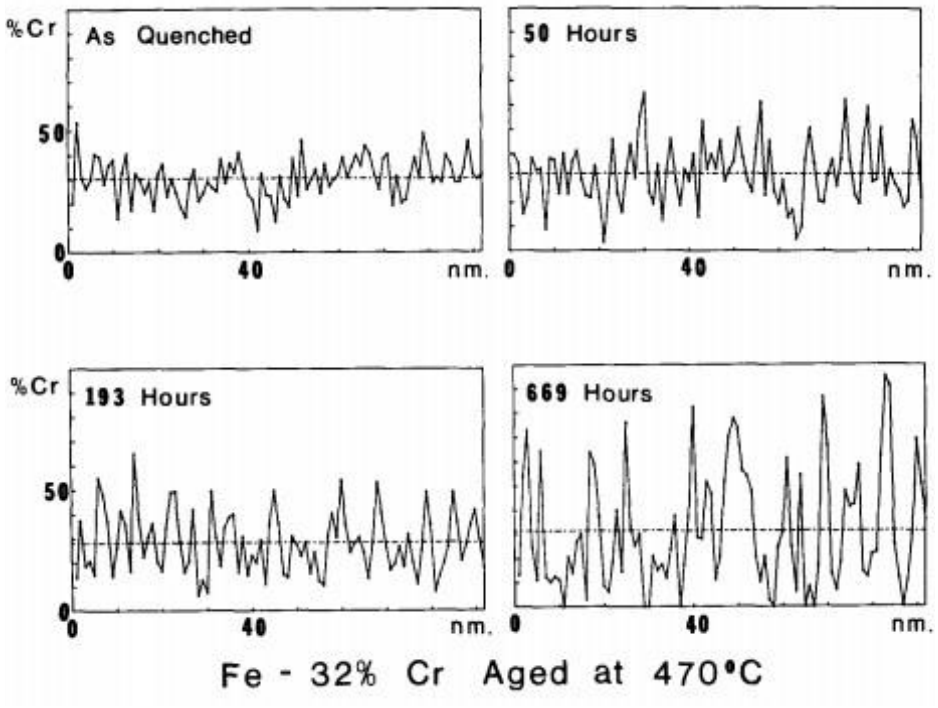

Figure 2-12 Concentration profiles of Fe-32 at. %Cr in the as-quenched condition, and after ageing at 470 ^{o}C using FIM analysis [62]

- Cr precipitation/decomposition in 17-4PH

Early works of Antony [35] mentioned the relation between changes in mechanical properties and the presence of α' phase, but no direct evidence of α' phase was shown. Later, Yrieix and Guttmann [45] reported that 17-4PH exhibits high susceptibility to hardening embrittlement at 400 ^{o}C, and they concluded it was due to the α' phase formation. In 1993, utilizing Atom probe field ion microscope (APFIM), Miller and Burke made a direct observation of α' phase in 17-4PH aged at 480 ^{o}C for 100 h [65]. They reported the Cr content at the centre of α' precipitate exceeds 70 at. %. The same work stated no α' was present in the sample aged at higher temperature (635 ^{o}C for 4 h).

As the ageing temperature is lowered, the decomposition path tends to be spinodal type. Murayama et al. [48] studied 17-4PH aged at 400 ^{o}C by APT, the result shows a spinodal feature after ageing for 100 h. The Cr concentration of α' at this stage was about 20 at. %. After ageing for 5000 h, the concentration of Cr rich phase increased to 70 at. %. The Cr atom map after 5000 h is shown in Figure 2-13. The Cr enriched regions appeared to be interconnected and the periodicity of the fluctuation was in the order of 3 nm. Wang et al. studied 17-4PH at an even lower temperature of 350 ^{o}C [66]. They reported a spinodal decomposition ageing for 6500 h by TEM. The decomposition structure by TEM is shown in Figure 2-14. They proposed that the black and white stripe feature in this image is due to the atom migration by spinodal decomposition and resulting in α phase (dark image domains) and α' (white image domains) phase. The spinodal wavelength was estimated to be about 6 nm. However, the compositional information of α' is difficult to obtain using TEM.

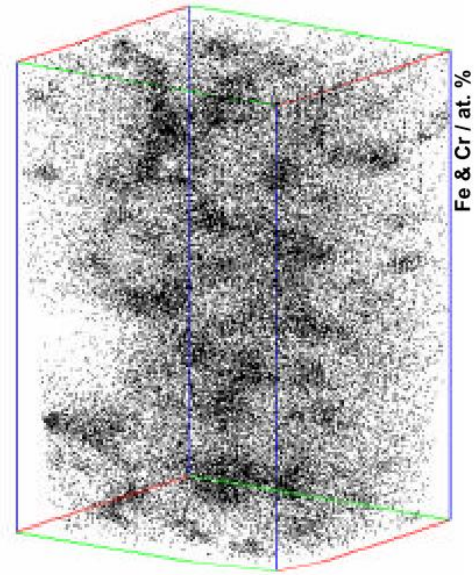

Figure 2-13 Cr atom map after ageing at 400 ºC for 5000 h by APT [48]. The regions of higher concentration represent the Cr-rich α' phase

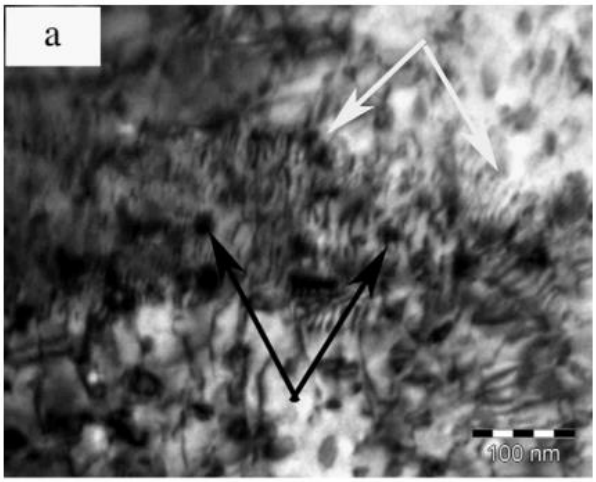

Figure 2-14 TEM image of 17-4PH aged for 11000 h at 350 ºC [66]

2.3.4 Other precipitates

Other types of precipitates have also been observed in17-4PH. The formation of these precipitates affects not only mechanical properties, but also the composition in the matrix. Thus it is also important to understand their behaviour.

Carbides $M_{23}C_6$ was reported to be present at both solution treated and prolonged ageing conditions [44,49]. Coarse NbC was observed at the grain boundary for the solution treated stage [48]. The carbide precipitates are relatively large, and the shape and size remain stable during ageing. Some fine secondary carbides are considered to affect the mechanical properties of the steel. Even though the large carbides at the grain boundary are thought to not alter the mechanical properties, their presence alters the chemical composition in bulk.

G-phase G-phase is an inter-metallic phase enriched in Ni and Si that often forms in ferrite after ageing at intermediate temperature, and has a FCC structure (space group Fm3m, lattice parameter 1.09 nm). After long-term ageing (5000 - 10000 h) G-phase was found in 17-4PH aged at 350 - 400 ^{o}C [48,57]. Murayama used TEM and APFIM to prove the presence of G-phase [48]. The concentration profiles resulting from the APFIM experiment are shown in Figure 2-15. The G-phase was found to form next to Cu precipitates. This might be because Cu precipitates provide a preferential nucleation site for G-phase.

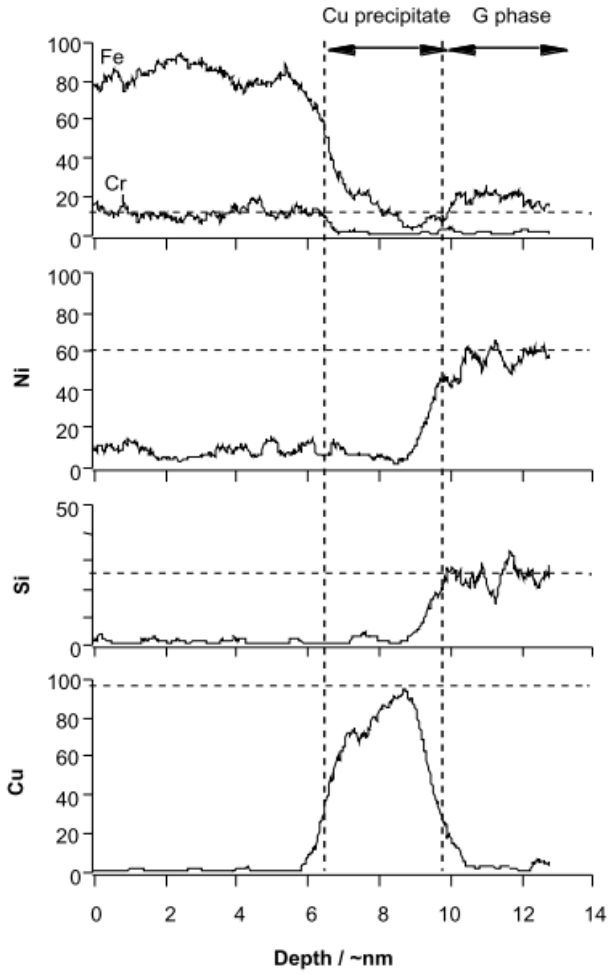

Figure 2-15 Concentration depth profile across the Cu precipitate and the Ni-Si enriched particle obtained from a selected region near the Cu precipitate by APFIM [48]

In this section, the microstructure evolution of 17-4PH under heat treatment has been presented. For relatively short heat treatment (i.e. condition H900 and H1100), CRPs and nitride phase can form. This can strengthen the steel and give rise to hardness. The details of hardening mechanism of CRPs can be found in [67–70]. However, during long term ageing at lower temperatures (350 - 400 ^{o}C), the formation of α' can cause hardening embrittlement [8,57]. Still more microstructure investigation work is needed to understand the formation mechanisms of the precipitates and their relations to mechanical properties.

2.4 Effects of neutron/ion irradiation on microstructure of T91 steel

Unlike 17-4PH which is mostly used in outer core components, T91 steel is one of the candidates for the core structure of advanced reactors. In such applications, it is critical to study the effects of irradiation on the material's microstructure correlated to any changes in bulk properties.

2.4.1 Introduction of irradiation damage and its consequence

The complex effects of irradiation on materials are rooted in an initial event when an energetic neutron (MeV level in reactor condition) strikes lattice atoms, which are called primary knock-on atoms (PKAs). This initial process results in a single vacancy-interstitial pair (Frenkel pair). When the energy of the PKA is high enough, it can also strike other atoms out of their lattice sites. As a consequence, a displacement cascade of defects pairs will form. Therefore, irradiation produces a high concentration of vacancy defects and self-interstitial atoms [71]. The basic defects (vacancies and interstitials) form the foundation for all observed effects of irradiation on the physical and mechanical properties of materials. After their formation, the reaction of the defects can be summarised as: 1. Loss of defects at sinks such as dislocations and grain boundaries. 2. Growth or shrinkage of defect clusters by the capturing point defects. 3. Mutual annihilation of a vacancy and interstitial [72,73].

The migration and reaction of the irradiation-induced defects leads to the key irradiation effects on microstructure: Radiation induced segregation (RIS), dislocation loops, voids and bubbles, phase stability. These detrimental microstructural changes can lead to bulk property degradation in a variety of forms, including radiation hardening and embrittlement;

irradiation creep; void swelling; and high-temperature helium embrittlement. [74]. The history of point defects after creation is shown in Figure 2-16.

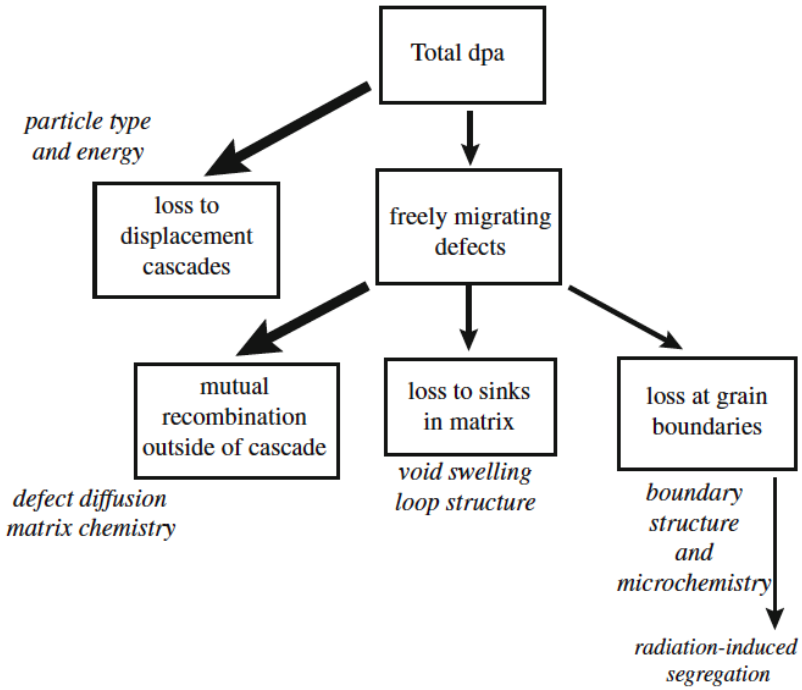

Figure 2-16 History of point defects after creation in the displacement cascade [75]

The flux of defects can couple with solutes leading to the redistribution of the chemical species. This may change the phase stability or induce the formation of thermodynamically non-equilibrium phases. In this case, the driving force is kinetic. This process is called radiation induced segregation (RIS)/precipitation. Because of the competition between kinetic and thermodynamic driving force, it is suggested that the materials under irradiation can only reach steady state instead of equilibrium [76].

Radiation induced segregation and precipitation alters both the intra- and inter-granular chemical composition, which can lead to changes in properties. For example, the segregation of Cr can cause a decrease in corrosion resistance in depleted regions. Furthermore, the formation of secondary precipitates like Ni-Mn-Si precipitates can result

in hardening embrittlement. In the following sections RIS and phase stability in irradiated F/M steel will be discussed in detail.

2.4.2 Radiation induced segregation (RIS) of F/M steel

F/M steels have been shown to be susceptible to radiation-induced segregation at extended defects like grain boundaries and dislocations. The segregation of Cr to grain boundaries could alter bulk composition and steel performance during service depending on the magnitude of segregation. Therefore, a need exists to understand the underlying mechanisms for RIS in F/M materials. The grain boundary segregation is classified into equilibrium segregation and non-equilibrium segregation [77]. Equilibrium segregation (Gibbsian segregation) is a thermodynamic process. It is caused by impurity atoms moving toward the interfaces (such as grain boundaries and surfaces) to reduce their free energy.

The schematic of non-equilibrium segregation is shown in Figure 2-17. It can be explained by the following mechanisms [78]

Inverse-Kirkendall mechanism When there is no strong binding energy between vacancy and atoms, the flux of vacancies to free surfaces induces fluxes of atoms in the opposite direction. In such a case, if A atoms diffuse faster than B atoms ($D_A > D_B$), the flux of vacancies towards the point defect sinks induces a depletion of A atoms at the defects sinks. In the opposite situation, if A atoms diffuse slower than B atoms ($D_A < D_B$), depletion of B is expected. This situation is referred as inverse-Kirkendall (IK) effect [79].

Solute drag mechanism When A atoms are strongly bound to vacancies, solute-vacancy complex exist, and the flux of the vacancies and the flux of A atoms are in the same

direction. A atoms are thus deposited at the sink. Such situation is referred as solute drag effects. The solute drag effect can also take place for interstitials.

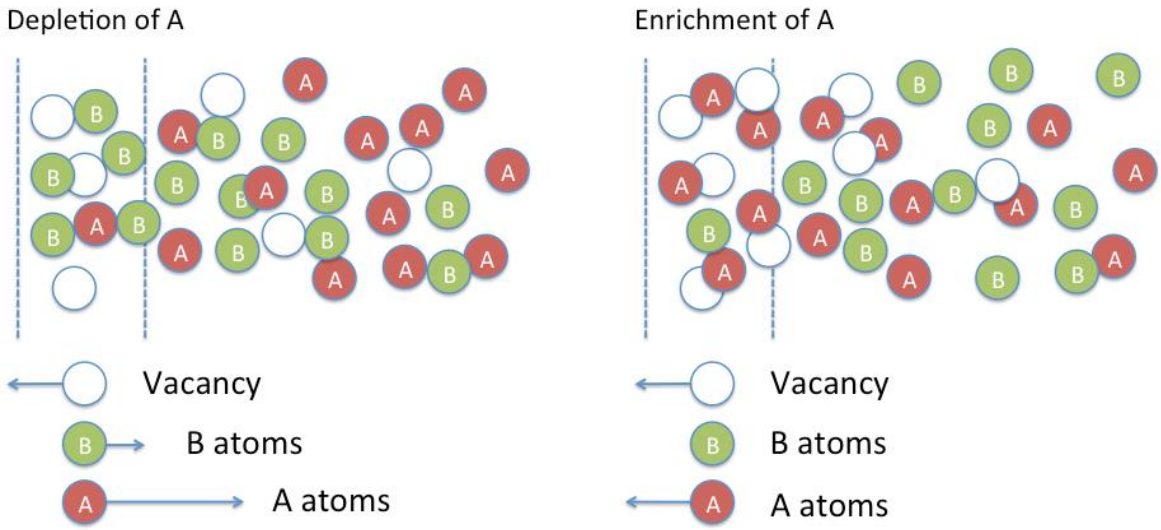

Figure 2-17 Schemetic of non-equilibrium segregation at grain boundaries of A-B system: (a) Inverse-Kirkendall mechanism (b) solute drag mechanism. The arrows represent the direction of diffusion

In general, undersized solutes as P, Si and C bind strongly to interstitials leading to enrichment at the sink. In contrast, oversized solutes like Nb and W exhibit weak binding to vacancies, leading to a depletion at sink and enrichment in the matrix [80]. These mechanisms successfully predict Ni enrichment and Cr depletion at grain boundaries for austenitic steel [79].

In the case of irradiated F/M steels, especially for investigation of Cr segregation, various studies revealed different results. Only a few studies have been specifically conducted on the T91material. Thus, here F/M materials with similar microstructure and composition to T91 has been also reviewed. Lu et al. [81] surveyed the literature on the RIS behaviour of F/M alloys and identified only about 10 studies that have been dedicated to RIS in a variety

of model and commercial F/M steels by 2006. Five subsequent works published after 2006 are also considered in the present study. The materials discussed here are a variety of F/M alloys with a composition of 5 - 13 % Cr. They are subject to irradiation over a range of temperatures (250 - 800 ^{o}C), doses (0.3 -118 dpa) and with a variety of irradiating particles. Table 2-4 is a summary of these works. Different materials types and irradiation conditions are listed. Cr enrichment or depletion after irradiation is labelled as : "+" (segregation) and "-" (depletion). "Before" and "after" stands for results before and after irradiation, respectively.

Table 2-4 A summary of Cr RIS behaviour of F/M steel irradiated by different particles

Materials	Radiation type	Temperature (^{o}C)	Dose (dpa)	Analysis method	Before	After
E911 [82]	Ion (Ni^{+})	300	0.305	FEGTEM EDX	+	-
13Cr2MoVNbB [83]	Ion (Cr^{3+})	575	48	TEM-EDX		-
13Cr2Mo+ODS [83]	Ion (Cr^{3+})			TEM-EDX		-
5 Cr [84]	Electron	400	3	TEM-EDX		-
13 Cr-1Ti [85]	Ion (C^{+})	525	118	TEM-EDX		-
13 Cr [83]	Ion (Cr^{3+})			TEM-EDX		-
13 Cr [84]	Electron	400	3	TEM-EDX		-
13 Cr [85]	Ion (C^{+})	525	118	TEM-EDX		+
13 CrSi [85]	Ion (C^{+})	525	118	TEM-EDX		+
10CrxMn3Al [86]	Electron	450	10		+	+
HT9 [87]	Neutron	410	13	AES	+	+
12CrMoVNb	Neutron	465	46	FEGTEM-EDX		+
HCM12A [88]	Ion (Ni^{+})	500	5	FEGSTEM	+	+
T91 [89]	Proton	456 10	10	FEGSTEM		+

Before irradiation (see column "before"), there is an enrichment trend of Cr at grain boundaries. While for Cr in various F/M steel after irradiation (see column "after"), the Cr behaviour falls into two groups: E911 [81], Fe-13Cr, 3Cr2MoVNbB, and 13Cr2Mo+ODS

[83], Fe-5Cr [90], Fe-13Cr-1Ti [85] exhibit a depletion at grain boundaries. In comparison, Fe-13Cr [85], Fe-13Cr-1Si [85], Fe-10Cr-xMn-3Al [86], HT-9 [87], 12CrMoVNb, HCM12A [88], T91 [91], Fe-9Cr [92] showed a Cr enrichment after irradiation. There are also works that reported both enrichment and depletion at the same condition for different grain boundaries [93,94]. There is no underlying trend in composition, which distinguishes between RIS and radiation induced depletion (RID) behaviour. Lu et al. suggested the most important reason for these controversial results is due to other precipitates on the grain boundary. There were a variety of precipitates found in grain boundaries in these studies. The coarsening or dissolution of existing phases and the nucleation of new phases on grain boundaries will have an effect on the grain boundary microchemistry, however, no conclusive trends were found for the RIS/RID behaviour in the ferritic steel data set. A most recent study from Wharry and Was [95] incorporated a modified Inverse-Kirkendall mechanism and the computational results suggest the presence of a "crossover" temperature for various bulk Cr compositions. The cross over temperature of as a function of bulk Cr content is shown is Figure 2-18. Effectively, this study proposed that above a certain irradiation temperature and greater Cr content, the Cr tends to deplete. In contrast, below a certain temperature and Cr content, Cr tends to segregate. As shown in Figure 2-18, it is consistent with some experimental results. However, they could not explain the others, especially when both segregation and depletion is found at the same condition. They claimed that some ion irradiation condition and RIS measurements make it difficult to assess the true direction of Cr RIS.

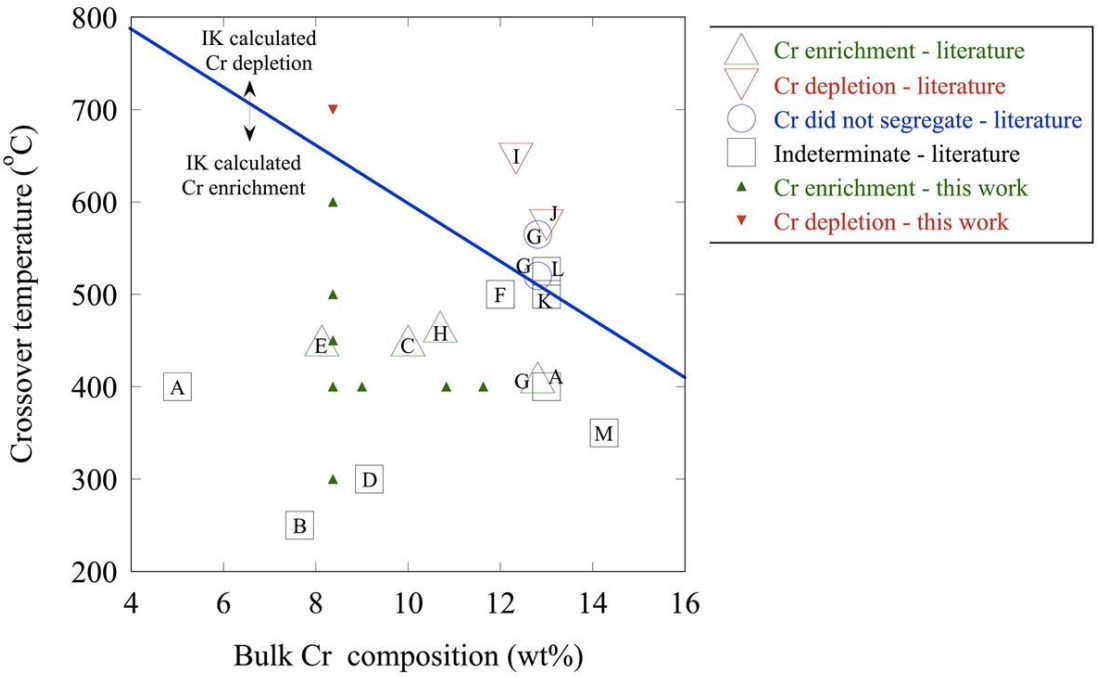

Figure 2-18 The crossover temperature calculated in [95] and experimental measurements of Cr RIS from [96] (closed marks) and other literature (open marks)

To date, there is still no full explanation of RIS of Cr. From Table 2-4 it is noticeable that a variety of materials, irradiation condition and temperatures have been used, which makes it difficult to compare between experiments. More systematic work is needed, especially on the effect of different irradiation particles. Heavy ion irradiation produces a damage layer very close to the surface, which makes it only possible to make RIS samples from a certain region.

2.4.3 Phase stability of T91 steel under irradiation

At their tempered state, the main precipitates in F/M steels are carbides or nitrides (for instance, $M_{23}C_6$ and MX precipitates where M refers to substantial component and X refers to C or N). These precipitates can strengthen the materials and are expected to be stable under service conditions. However, research has shown that pre-existing precipitates

become unstable and modification of structure, density, size and composition could happen under irradiation [97,98]. In addition to the modification of pre-existing precipitates, the local solute concentration in the vicinity of a point defect sink can reach the solubility limit leading to radiation-induced precipitation (heterogeneous nucleation on surfaces, grain boundaries, dislocations or homogeneous nucleation on fluctuations of composition). These changes in precipitates could alter mechanical properties. The phases usually observed in irradiated F/M steels are: $M_{23}C_6$-a carbide with a diamond-cubic structure enriched by Si, Cr and Ni [89,99]; M_2X-hexagonal Cr and V enriched phase that takes the shape of fine needles [100], G phase-Mn, Ni and Si enriched phase [100,101], χ (Chi) phase-a bcc inter-metallic phase enriched in Fe, Si, Ni and contains a significant amount of Mo and P [89,99], σ (sigma) phase and Laves phase have also been reported. The α' phase can form during thermal ageing under 480 ^{o}C or irradiation in ferritic steels with Cr contents higher than 10 at. % according to the Fe-Cr phase diagram (Figure 2-6 and Figure 2-7).

In T91, the pre-existing precipitates are mainly $M_{23}C_6$ and MX type. $M_{23}C_6$ is coarser (100 - 300 nm) and found along prior austenite grain boundaries (PAGB) and lath boundaries. Nb and V rich finer (20 - 50 nm) particles are also observed at the same site. Under irradiation, both in size and grain boundary coverage ratio has been found to increase [102]. This is related to the irradiation-enhanced diffusion. Jia and Dai [97] reported amorphization of $M_{23}C_6$ after proton irradiation at temperatures lower than 205 ^{o}C.

G-phase has been observed in T91 irradiated to 39 dpa at 300 - 600 ^{o}C in High Flux Isotope Reactor (HFIR) and to 47 dpa at 400 ^{o}C in Fast Flux Test Facility (FFTF) [103]. After proton irradiation to 7 dpa at 400 - 500 ^{o}C, Ni, Si, Mn-rich precipitates and CRPs have been found using atom probe tomography. The atom map from this study is shown in Figure 2-19. The average size of the precipitates was at 2 - 4 nm. Some of the CRPs and Ni, Si,

Mn-rich phase are found to form adjacent to each other. The absence of Ni, Si, Mn-rich phase under lower dose suggest that the formation is enhanced by irradiation. Van den Bosch et al [104] also reported formation of G-phase under FFTF irradiation up to 184 dpa at 400 ^{o}C.

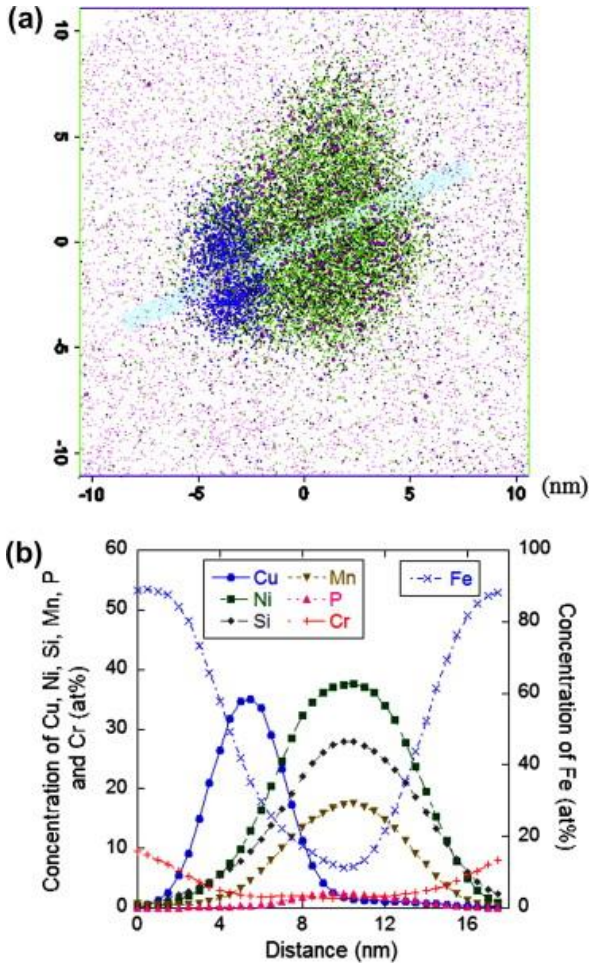

Figure 2-19 (a) APT atom map showing the morphologies of Cu-rich (blue) and Ni/Si/Mn-rich (green) precipitates in T91 following irradiation to 7 dpa at 500 °C; (b) Composition line profile across the precipitates. The profile is along the light blue rectangle in (a) [102]

In most results, α' phase was not observed in irradiated T91, but recently Mathon et al. [105] reported a modification of SANS measurement after neutron irradiation to 0.7 dpa under 325 °C and attributed it to formation of α'. As mentioned above, the onset of α' phase is

difficult to observe in TEM, thus more work on atom probe analysis is still needed on T91 at lower temperature irradiation.

2.4.4 Ion irradiation as a surrogate

Conventionally, research to understand irradiation induced changes is conducted via radiation experiments in test reactors, followed by a post-irradiation characterization plan. As referenced above, many studies have been successfully carried out on neutron irradiation in thermal test reactors or fast reactors. However, the time and effort cost of the research can be enormous. Neutron irradiated samples are difficult to handle. In addition, it is not amenable to study a wide range of radiation conditions by neutron irradiation. In any reactor type the damage rate is generally too slow to "get ahead" of problems which might happen during operation. There are also not enough test reactors in the world to conduct sufficient experiments.

Since the 1970s, heavy ion irradiation has been used for simulating the neutron damage that occur in fast breeder reactor [72,76,106]. In contrast to the neutron irradiation, heavy ion irradiation enjoys considerable advantages: Dose rates (typically 10^{-3} to 10^{-4} dpa/s) are much higher compared to neutron irradiation (~10^{-6} dpa/s), which means 200 dpa (damage level of fast reactor) can be reached in days or weeks rather than decades. Furthermore, ion irradiation samples are not radioactive, which saves enormous time and effort in terms of sample handling. Another advantage is the ease of controlling the experiment. It is possible to study the effects of different irradiation conditions (temperatures, dose and dose rate). Ion irradiation studies have provided considerable advancement of understanding fundamental effects of irradiation on materials.

As the significant incentive to utilize ion irradiation to study neutron damage increases, the importance to discuss its validity as a surrogate also increases. One of the key questions is, *to what extend the ion irradiation can produce microstructure and property that is equivalent to neutron irradiation and what are the irradiation conditions required?* The final state of the material is important in the determination of equivalence. In the meantime, understanding the mechanisms of different irradiation types are vital to evaluate ion irradiation as a replacement of neutron to predict the microstructure and properties of materials.

– Energy spectrum

A primary difference between ion and neutron irradiation that need to be taken into consideration is the particle energy spectrum. Neutron energy spectrum extends much broader than ion energy spectrum from mono-energetic beam, thus presenting a more complicated source for radiation damage [107,108].

– Penetration depth

The second major difference in the nature of ion and neutron is their depth of penetration caused by different interactions with atoms. Ions lose energy quickly when passing through electrons, while in comparison neutrons can travel a long distance by virtue of their electrical neutrality, producing flat damage profile.

– Dose rate

For a given total dose, the effects of irradiation on the microstructure and properties will be influenced by the characteristic dose rate of the radiation source. Various types of interaction of the defects produced by irradiation have been discussed in Section 2.4.1. The

relative proportions of these reaction types are directly dependent on the density and mobility of the defects, and hence dependent on dose rate and temperature [72]. The reaction path influences the irradiation-induced features and phenomena such as dislocation loops, voids, RIS, swelling and creep. As a result, the irradiated microstructure is dependent on irradiation conditions such as dose rate and temperature. Experimental evidence of dose rate effect for model Fe-Cr alloys was studied by Hardie et al. [73]. The results show that ion implantation with a relatively low dose rate caused significantly higher irradiation hardening compared to the same alloys irradiated with a higher dose rate.

The difference in damage rate can be resolved using the invariance theory derived by Mansur [109]. According to this theory, a change in the value of an irradiation variable (i.e. dose rate) from reactor conditions is accommodated by a shift in other variables (i.e. temperature) with the goal of preserving the behaviour of defects during irradiation. Such shifts were constructed for specific microstructure processes such as RIS or void growth. In both cases, the higher dose rate in an accelerator relative to a reactor requires a corresponding increase in temperature to achieve the same result. Unfortunately, this quantitative "temperature shift" is predicted to vary for different microstructural features (e.g., voids, interstitial dislocation loops, precipitates), since they depend on rate-controlling processes such as vacancy or solute migration with different thermal activation energies [110]. In order to maintain the number of defects absorbed at sinks at different dose rate (in the case of radiation induced segregation), the temperature shift can be estimated by Equation 2-4 [109]:

$$T_2 - T_1 = \frac{\frac{kT_1^2}{E_m^v}\ln(\frac{G_2}{G_1})}{1-\frac{kT_1}{E_m^v}\ln(\frac{G_2}{G_1})}, \quad 2\text{-}4$$

where k is the Boltzmann's constant; G is the damage (dose) rate and E_m^v is the vacancy migration energy. Another type of temperature shift can be derived if the net flux of vacancies over interstitials to a particular type of sink (in the case of dislocation loop or voids). This net flux is relevant to swelling rate. In this case, the temperature shift can be estimated by [109]:

$$T_2 - T_1 = \frac{\frac{kT_1^2}{E_m^v + 2E_m^f}\ln(\frac{G_2}{G_1})}{1-\frac{kT_1}{E_m^v + 2E_m^f}\ln(\frac{G_2}{G_1})}, \quad 2\text{-}5$$

where E_f^v is the vacancy formation energy. Jiao et al [111] has used Mansur's theory to estimate the temperature shift for self-ion irradiation (5MeV Ni^{++}/Ni^{++}, 10^{-3} dpa/s) to emulate BOR60 irradiation (5×10^{-7} dpa/s) of 304L stainless steel (SS) and 316 SS. Their results show that temperature shift to match the RIS behaviour is 280 ^oC based on Equation 2-4 and match the dislocation loop growth is estimated as 60 ^oC based on that to Equation 2-5.

Very few experimental studies have directly compared the microstructure after ion and neutron irradiation at "equivalent" conditions. Was et al. [112] studied F/M steels subjected to self-ion and reactor irradiation. Their results show that by controlling the experimental

conditions that account for the differences between reactor- and accelerator-based irradiations can create the same radiation-produced defect clusters with comparable sizes and number densities as those created in reactor.

– Transmutation products

Helium is well known to assist void nucleation and thereby accelerate the onset of void swelling during irradiation [74,113]. Helium is produced in irradiated metals and alloys by (n, α) transmutation reactions in the reactor. To emulate transmutation in reactor, helium can be implanted prior to or simultaneously with the ion irradiation [112,114,115].

In general, in term of "simulation" or "emulation" of neutron irradiation using heavy ion, significant progress is being made to minimize the drawbacks of ion irradiation. Systematic work on the same materials under different particle irradiation is still needed.

3 Materials and Experimental Methods

3.1 Materials

3.1.1 17-4PH steel

The as-received material was an 8 mm diameter as-rolled rod of 17-4PH. The bulk chemical composition of the bulk material supplied by Rolls Royce and the measured composition by APT analysis on solution treated samples is shown in Table 3-1. The mass peak identification will be further discussed in § 3.5.5.

Table 3-1 Concentrations of the main elements of solution treated 17-4PH and measured concentrations by APT (at. %). Errors are obtained from averaging results from 4 different samples

Element	Fe	Cr	Ni	Cu	Mn	Si	Nb	Mo	Co	V	N	C
Bulk	74.20	16.42	4.41	2.90	0.75	0.67	0.15	0.08	0.06	0.05	0.12	0.06
APT	74.15	16.90	4.45	2.51	0.73	0.69	0.09	0.06	0.07	0.06	0.16	0.09
Error (±)	1.01	0.41	0.39	0.23	0.01	0.02	0.01	0.02	0.01	0.01	0.11	0.05

3.1.2 Heat treatment of 17-4PH steel

- Solution treatment

The 8 mm diameter as-received rod was sectioned into 15 cm in lengths and solution treated at 1040 ^{o}C for 1 hour and then quenched in oil.

- Precipitation hardening treatment

In order to produce precipitation hardening, solution treated 17-4PH samples were then heat treated at:

- 480 ^{o}C for 10 minutes, 30 minutes, 1 hours, 2 hours, 24 hours, 120 hours, 260 hours, 360 hours and 1000 hours, and
- 590 ^{o}C for 10 minutes, 20 minutes, 30 minutes, 2 hours and 24 hours.

There is an associated error of ± 4 ^{o}C in the actual temperature depending on the specimen position in the furnace.

3.1.3 As-received T91 steel

Unirradiated T91 steel for APT analyses were prepared from TEM disks after diamond lapping to 0.25 um at the University of Michigan. Some of the APT analysis enclosed grain boundaries or carbide/nitride precipitates. These features can significantly bias compositional measurements due to the small analysed volume. Thus, the compositions of T91 excluding all precipitates and grain boundaries obtained from APT measurements are shown in Table 3-2. The mass peak identification of APT analysis and composition measurements will be introduced in § 3.5.5, § 4.2 and further discussed in § 6.3.2. The differences between different APT experiments are negligibly small. Compared to the bulk chemistry, the Cr, Mo and V contents are slightly smaller in APT measurements. The loss of Cr, Mo and V is about 1.17 at. %, 0.25 at. % and 0.11 at. % respectively. Also, the majority of the expected C and N atoms were not detected in the APT analysed regions. The loss of these elements in the composition measurement is possibly due to the formation of nitrides and carbides outside the analysed region as well as grain boundary segregation.

Table 3-2 Bulk compositions of T91 from APT

T91	Chemistry Source	Alloy Chemistry (at. %)									
		Fe	Cr	Ni	C	N	Mn	Mo	Nb	Si	V
Bulk	PNNL	89.52	8.60	0.09	0.08	0.05	0.37	0.89	0.07	0.11	0.21
Tip1	APT	91.15	7.48	0.11	0.00	0.02	0.40	0.64	0.00	0.09	0.10
Tip2	APT	91.10	7.48	0.11	0.00	0.02	0.40	0.69	0.00	0.09	0.10
Tip3	APT	91.30	7.33	0.08	0.00	0.01	0.42	0.58	0.00	0.16	0.11
Differ-ence		+1.66	-1.17	+0.01	-0.08	-0.04	+0.04	-0.25	-0.07	0.00	-0.11

3.1.4 Heat treated T91 steel

The single ion beam irradiation was carried out at an elevated temperature of 470 °C. In order to understand the effect of heat treatment, samples from the non-irradiated region of T91, but subjected to the same heat treatment level as the irradiated region were analysed.

3.1.5 Ion/reactor irradiation of T91 steel

The irradiation conditions of T91 are listed in Table 3-3. Ion irradiations were conducted in the Michigan Ion Beam Laboratory (MIBL) at the University of Michigan. The reactor irradiation was conducted in the BOR60 test reactor in Russia.

Table 3-3 Irradiation conditions of T9 steel

	Dose (dpa)	Dose rate (dpa/s)	T (°C)	He (appm)
Single Ion (SI) Fe++	1	~5×10^{-4}	470	0
	10	~5×10^{-4}	470	0
	20	3.4 - 4.3 × 10^{-4}	420	0
Dual Ion (DI) Fe++ and He++	16.6	~5×10^{-4}	406	3.66
	16.6	~5×10^{-4}	432	3.66
BOR-60 (neutrons)	16.6	6-9 × 10^{-7}	386	
	16.6	6-9 × 10^{-7}	412	

Single ion irradiations were performed using 5 MeV Fe++. The irradiation dose were 470 °C : 1 dpa (temperature : dose), 470 °C : 10 dpa and 420 °C : 20 dpa at 600 nm. The dose

rate were kept at 5 × 10^{-4} dpa/s at 470 °C. At 420 °C, defocused ion beam has beam used and the dose rate achieved was 3.4 - 4.3 × 10^{-4} dpa/s. The samples were 1.5 mm × 1.0 mm × 7 mm bars. The damage profiles were calculated with SRIM simulation [116]. Displacement energies of metal alloying elements (i.e. Fe, Cr, Mo, Mn, V) were each set to 40 eV [117] and non-metal elements (i.e. C and N) to 28 eV [118]. Figure 3-1 shows the SRIM output using quick K-P calculation for 5 MeV Fe ion irradiation on T91 alloy. The reported irradiation doses of 1, 10 and 20 dpa correspond to the depth of 600 nm whereas the damage peak is around 1.4 μm depth, according to the SRIM output.

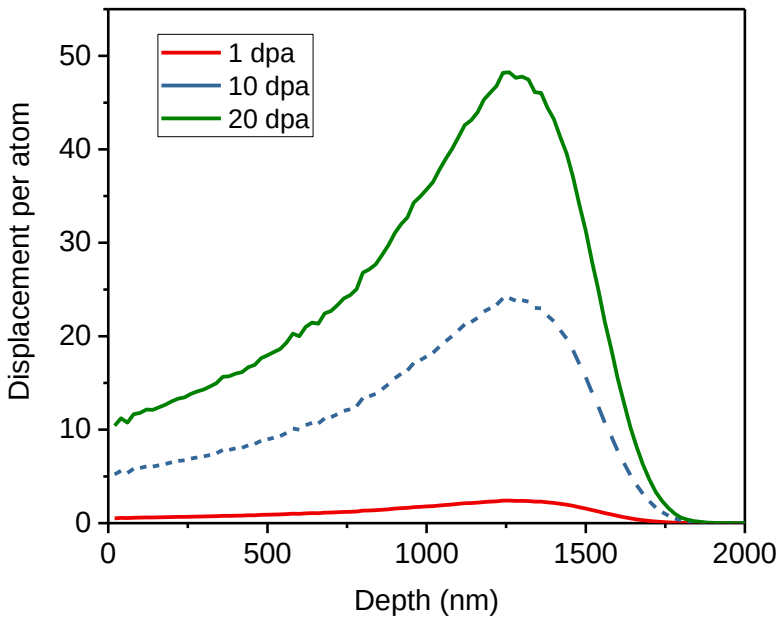

Figure 3-1 Damage profiles simulated by SRIM for 5 MeV Fe++ irradiated T91. The dose was set to 1, 10 and 20 dpa at the depth of 600 nm

The dual ion beam irradiations were performed using 5 MeV Fe++ and He++ to 3.66 appm at 600 nm. The injected He level is comparable to the He produced in BOR-60 reactor irradiation. The temperature is 20 °C higher than the corresponding BOR-60 reactor

irradiation condition to account for the dose rate effect since the recent experiments show that in a similar steel (HT9), shifting the temperature by 17 ºC results in comparable microstructures when using self-ion irradiation (5MeV Fe++) to emulate reactor irradiation [112]. The temperature shift values estimated from Equation 2-4 and Equation 2-5 are listed in Table 3-4. G_1 and G_2 are taken from the dose rate values in Table 3-3. k is 8.62×10^{-5} eV/K, T_1 is the BOR60 irradiation temperatures. The vacancy migration energy and formation energy is set to be 0.63eV and 1.6eV, same as in [95]. One can find that the estimates from the theory is higher than 20 ^{o}C.

Table 3-4 Temperature shift (ΔT) calculated from Equation 2-4 and 2-5

T_1 (^{o}C)	ΔT from Equation 2-4 (^{o}C)	ΔT from Equation 2-5 (^{o}C)
386	335	32
412	405	37

The predicted damage profile for dual ion beam irradiation provided by University of Michigan is shown in Figure 3-2. The He injected region is at 500 nm - 1000 nm from irradiated surface.w

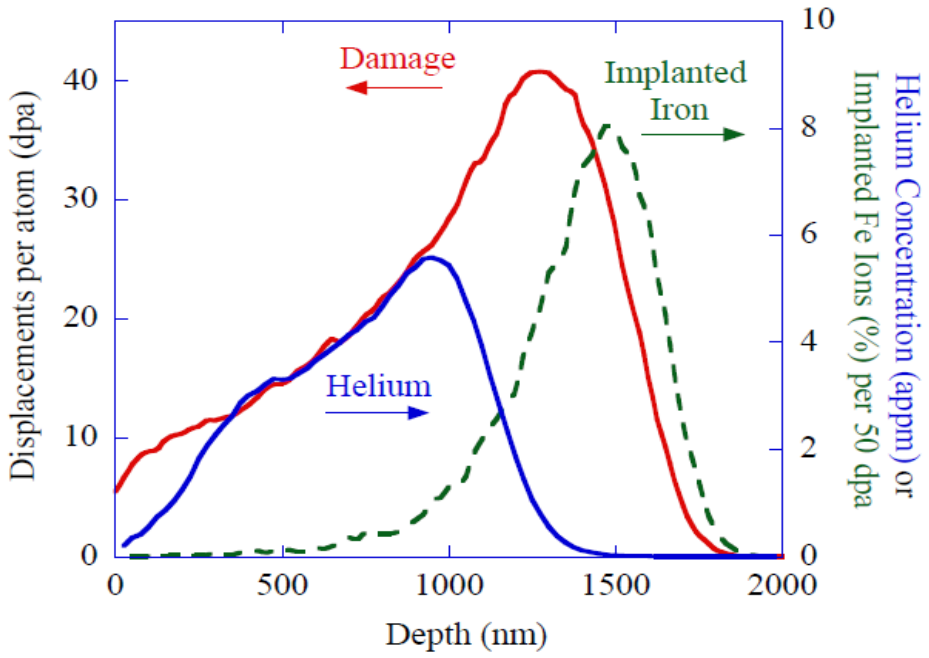

Figure 3-2 Damage profile of T91 after dual ion beam irradiation

Reactor irradiated samples are in the form of TEM disks. The materials were irradiated in BOR60 to 16.6 dpa at 386 ^{o}C and 416 ^{o}C respectively.

3.2 Vickers Hardness Measurements

1mm thick disc samples for hardness testing were cut from the 17-4PH heat treated materials and then polished to colloidal silica finish. The Vickers hardness was obtained by averaging 10 randomly selected regions under a load of 30 kg.

3.3 XRD measurements

The same 1 mm thick disc samples for X-ray diffraction (XRD) measurements were ground and polished to a colloidal silica finish after Vickers hardness measurements. Standard θ-2θ X-ray diffraction patterns were obtained in a Philips PW1710 diffractometer using Cu Kα radiation. The generator settings were 35 kV and 50 mA and the diffractograms were

collected over a 2θ range of 35-120° with a step width of 0.02° and a counting time of 1 s/step.

3.4 Electron backscatter diffraction (EBSD)

The same 1mm thick disc samples for XRD analysis was grinded and polished to colloidal silica finish. Then EBSD testing was performed by Dr. Zuliang Hong on a JEOL JSM-6500F at an acceleration voltage of 20 kV. A step size of 100 nm was used and an area of 50 μm × 80 μm was scanned to identify the reversed austenite dispersion.

3.5 Atom probe tomography (APT) analysis

In this study, the microstructures of the steels are examined primarily using APT. A comprehensive account of the development of the instrument can be found in [119]. Here, the basic theory, sample preparation, data acquisition and analysis techniques directly relevant to this work are introduced.

3.5.1 Fundamentals

Atom probe tomography is a high resolution 3D analytical technique that is built on the concept of field evaporation. A schematic of APT analysis is shown in Figure 3-3. The radius of a needle-shaped specimen required for atom probe tomography is typically 20 - 100 nm. When subjected to a very high voltage *V*, the electric field at the surface of the tip is estimated as

$$F = \frac{V}{k_f R}, \qquad 3\text{-}1$$

where F is the electric field induced at the apex of the tip with a radius of R and k_f is a field factor also related to the geometry of the tip. It should be noted that the electric field penetration is very small in metals. When a voltage pulse or laser pulse is applied in addition to the field induced by a DC voltage, surface atoms are ionized and field evaporated layer-by-layer in a sequence. These field evaporated ions are accelerated towards a position sensitive detector where their time of fight and hit position is recorded. Time-of-fight, t_{flight}, the time between the application of the HV/laser pulse and the moment of detection, is used to determine the mass-to-charge-state ratio and hence the chemical identity of each ion.

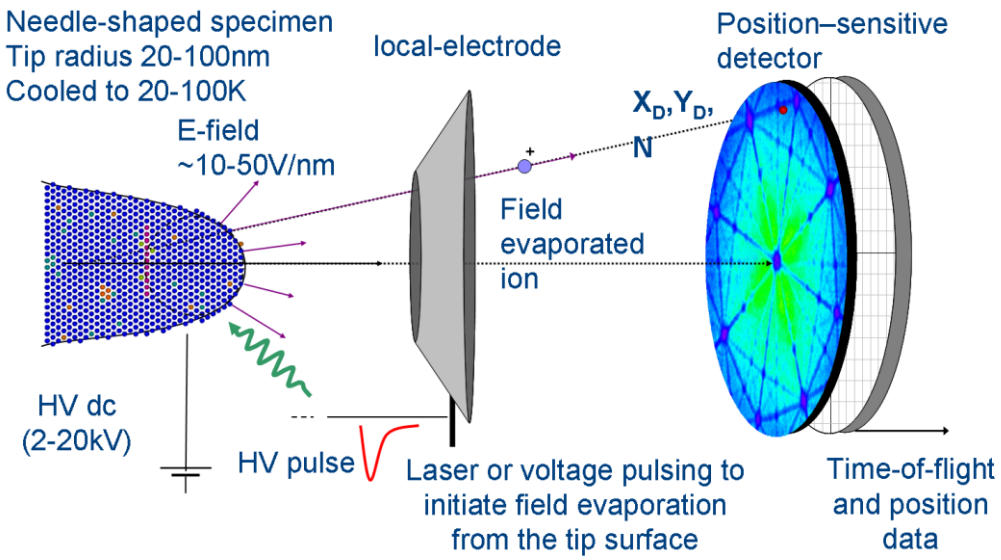

Figure 3-3 Schematic of atom probe tomography [119]

An ion in an electric field has a potential energy $E_p = neV$, where V is the voltage and ne is the charge-state of the ion. The kinetic energy is $E_c = \frac{1}{2}mv^2$ assuming the ion leaves the surface with no initial velocity. Its final velocity is given by $v = \frac{L}{t_{flight}}$, where L is the flight

path of the ion (from the tip surface to the detector). By equating the E_p and E_c, the mass-to-charge-state ratio can be obtained as:

$$\frac{m}{n} = M \approx 2eV\left(\frac{t_{flight}}{L}\right)^2 \qquad 3\text{-}2$$

where $\frac{m}{n} = M$ is the mass-to-charge-state ratio of the ion. Assuming the specimen geometry takes the form of a hemispherical cap on a shank, the x- and y-detector-hit positions can be reverse projected to estimate the relative original lateral position of the ion within the specimen. The sequence of evaporation is used to determine the z coordinates of the ion. Together with the chemical identity obtained by time of flight, a 3D reconstruction of the original specimen is obtained.

APT enables a unique 3D near-atomic resolution and continuous progress is being made in instrumental, sample preparation and data processing techniques [54,120–124]. APT enables atomic-scale studies of the microstructure, particularly the study of early stage precipitates formation, phase separation and grain boundary segregation.

3.5.2 Sample preparation

- Electropolishing

The 17-4PH steel bars were first cut into 1 × 1 × 15 mm3 ‘matchsticks’. Then the needle-shaped specimens required for APT were prepared by a standard two-stage electro-polishing method. The first step of the process is shown schematically in Figure 3-4. A thin layer of electrolyte (25 vol. % perchloric / 75 vol. % acetic acid solution) floats on an inert liquid (GaldenTM Perfluorinated fluid). The matchstick is connected to a positive DC voltage between 12 - 16 V. The electropolishing action is manually controlled up and down

as shown in the dashed arrow. The sample thins down and eventually separates into two pieces of rough needle. The needles were then polished to suitable sharpness using 2 vol. % perchloric acid in 2-butoxyethanol solution at 4 - 6 V. The schematic of the second stage is shown in Figure 3-5.

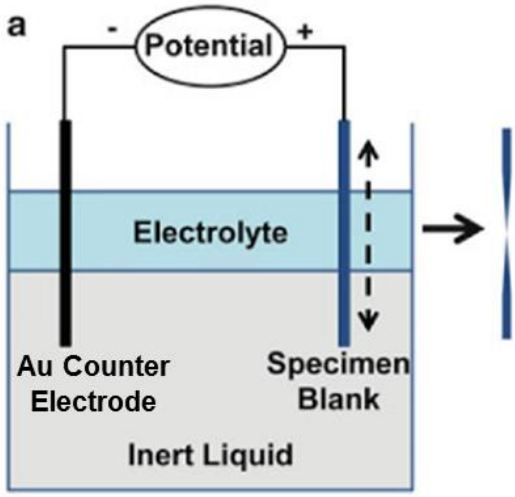

Figure 3-4 Schematic of first-stage electropolishing [125]

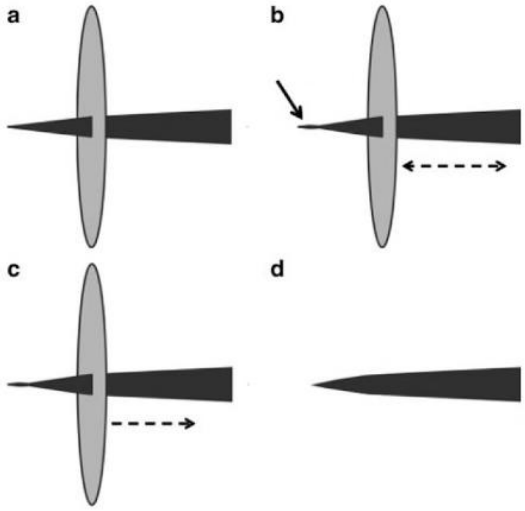

Figure 3-5 Schematic illustrating electropolishing procedure: (a) Placing a rough-polished sample (b) Motion of the loop (dashed arrow) producing necking (c) Continued motion of the loop (dashed arrow) causing further necking near the end of the tip (d) Final tip shape [125]

- Focused ion beam (FIB) sample preparation

For ion irradiated samples, the region of interest is confined to the surface region (up to ~1.5 um for this study) of the sample. It is not possible to use conventional electropolishing methods in this case. A lift-out process [126], as shown in Figure 3-6 was conducted directly from the sample surface using a dual beam microscope FEI Helios NanoLab 600i at Culham Center for Fusion Energy (CCFE) and/or Zeiss Auriga at Oxford. First, a protective Pt layer was deposited on the region-of-interest (ROI). The typical size of the Pt layer is approximately $3 \times 30 \times 1$ μm^3. Then the material around the ROI was removed by the Ga beam to produce a cantilever, as shown in Figure 3-6 (a). The wedge was then attached to an in-situ micromanipulator (Figure 3-6 (b)) and transferred onto a micro tip coupon (Figure 3-6 (c) and (d)). A SEM image of a microtip coupon is shown in Figure 3-7.

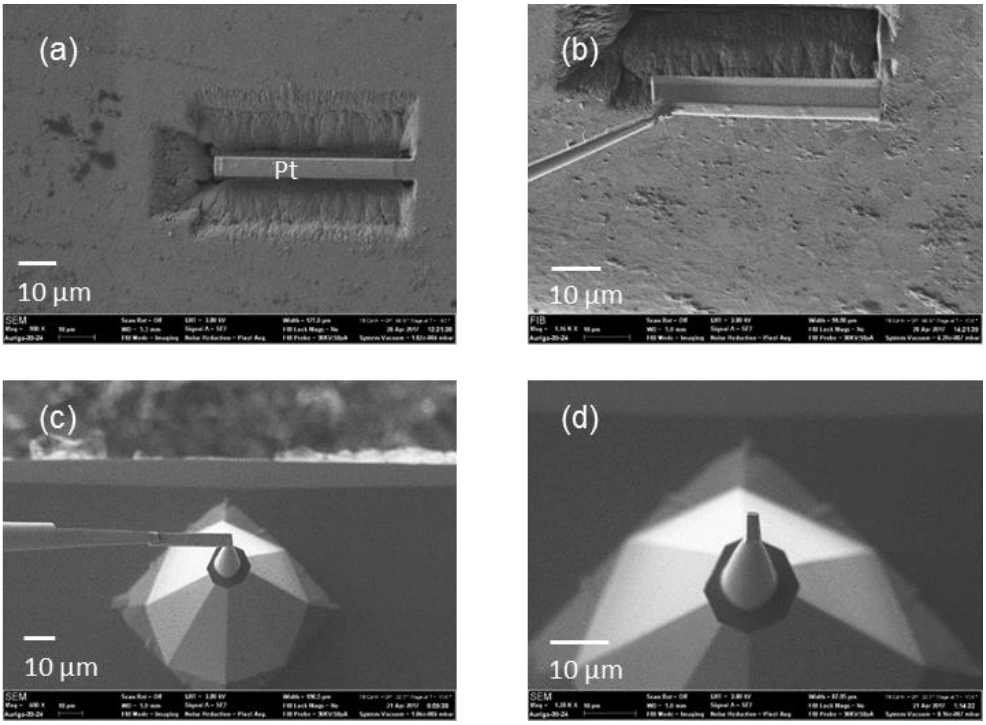

Figure 3-6 Lift out process using a dual beam FIB-SEM

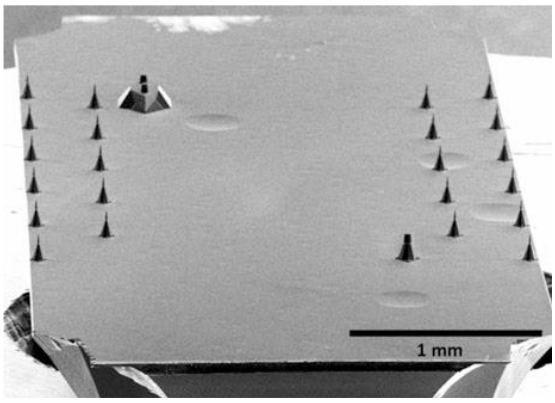

Figure 3-7 SEM image of a microtip array (coupon). The coupons are 3 mm × 7 mm with eleven carrier microtips positioned along two of the edges (22 carrier tips total) [125]

After attaching the samples to a coupon, a series of annular milling steps were applied to shape the tip into a sub-200 nm diameter sharp needle. In all ion irradiated samples, it is important to accurately know the depth from the surface in order to estimate the irradiation dose in the analysed volume.

Using the Pt layer as an indicator, as shown in Figure 3-8, the depth from the surface can be controlled so that the APT analysis region is within the irradiated region.

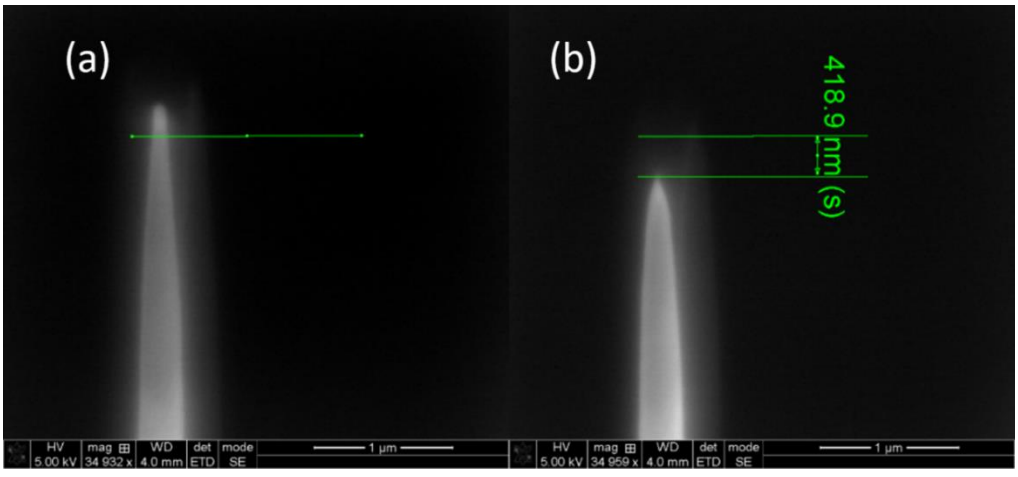

Figure 3-8 (a) Tip with Pt, green line indicates the position of surface (b) Final tip after milling, green lines indicate distance from the surface

3.5.3 3-D reconstruction

CAMECA IVAS software has been used to convert the detected information into 3D positions and chemical identity of each ion. The reconstruction process includes: selecting region of interest from the detector event, time of flight (TOF) correction, mass calibration, mass-to-charge peak ranging and tip shape calibration. Detailed principles and description of these steps can be found in [119] and [125]. Several protocols have been proposed to build the tomographic reconstruction [121,127,128].

As depicted in Figure 3-9, in all the protocols, the ion trajectories in APT are assumed to originate from a single projection point (point P) along the specimen axis. The distance between the projection point and the specimen apex (distance between P and A) can be expressed as $\xi R = (m+1)R$. The term ξ is the image compression factor (ICF), accounting for the compression of the launch angle θ towards the axis of the tip, resulting in the observed angle θ'. R is the radius of the tip, which can be calculated from Equation 3-1.

Assuming that the radius of the curvature is known for each ion, the cylindrical coordinates for an ion on the surface can be written as (z, ϕ).

In order to determine the depth coordinate z. Ions are it is assumed that ions are removed layer-by-layer. The specimen surface becomes further from the detector by a small increment dz, where

$$z^{i+1} = z^i + dz \qquad 3\text{-}3$$

where z is the position of the tip surface. dz is corresponding to the atomic volume on the analysis surface:

$$dz = \frac{\Omega}{\eta(dv/dz)} \qquad 3\text{-}4$$

Where Ω is the entire analysed volume, v is the analysed volume, η is the detection efficiency, and dv/dz is the function that describes the increase of the analysed volume as the surface is moved down.

The main difference of the different protocols are the estimation of dv/dz. Gault et al [121] used direct relationship introduced between the launch angle θ and the observed angle θ' to obtain the dv/dz:

$$\theta = \theta' + \arcsin(m \sin\theta') \qquad 3\text{-}5$$

Assuming that the polar angle remains constant through the ion flight, it is possible to reposition the ion directly onto the specimen surface based on its cylindrical coordinates (R, θ, ϕ).

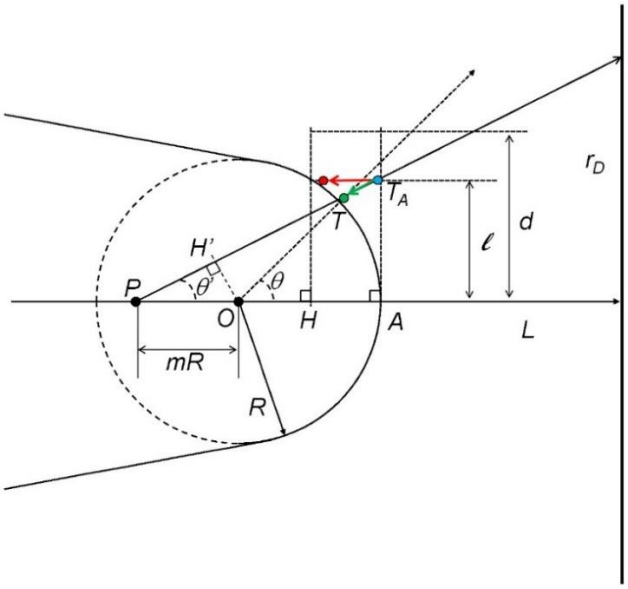

Figure 3-9 Schematic view of the ion projection in atom probe tomography [121]

One can find that the key input reconstruction parameters are ξ, R, and η. The detection efficiency is an intrinsic property to a specific instrument. The corresponding detection efficiency values for LEAP3000X HR and LEAP5000XR have been taken as 37 % and 52 %, respectively.

3.5.4 Calibrating reconstruction

Crystallographic information can be used to calibrate the reconstruction [129,130] by calculating the image compression factor and the initial radius of the tip. The atom probe specimens are generally assumed to take the form of a hemispherical cap on a shank. However, the actual surface is not continuously smooth due to the surface crystal structure. This results in non-uniform field distribution at the tip apex and leads to non-uniform projection of the ions towards the detector. Since the local surface structure of a sample directly depends on the crystal direction, the 2-D histogram of detected ions on the detector can reflect the crystal orientation.

- Determination of image compression factor ξ

The symmetry of the pattern on the detector histogram map corresponds to the specific crystal orientation. However, identifying the crystal orientation is not always straightforward, especially in high solute containing materials like T91 and 17-4PH. In the current study, an approach proposed by Yao in [131] is used to filter the detection histogram. This approach is based on the idea that the number of pulses (Np) applied to trigger evaporation of successive atoms is a function of the crystal orientation. The atoms on lower indexed planes are subjected to higher applied field and have a lower evaporation field [132], thus the number of attempts (i.e. applied pulses) required to evaporate the atoms is less than those not on a lower indexed planes. Hence, the number of pulses

between successive evaporated atoms can be used to filter the filed desorption map and highlight the atoms originating from lower index planes.

An example is shown to illustrate this method. Figure 3-10 (a) is the original field desorption map of a T91 sample. A four-fold symmetry ([200] direction) is obvious. In order to obtain the best contrast, a threshold for events at $N_p < 5$ are selected to filter the histogram using code written by Dr. Daniel Haley based on Yao's method [131]. The result is shown in Figure 3-10 (b). After filtering, a much clearer pole structure and zone lines are observed. From the symmetry of the zone lines, one can obtain the identity of several poles. The image compression factor can be estimated from any of two poles using equation:

$$\theta_{crys} = \theta_{obs} + \arcsin(m \sin \theta_{obs})$$
$$m = \xi - 1 \qquad 3\text{-}6$$

Where θ_{crys} is the angle between the two poles and θ_{obs} is the angle calculated from the position on the detector:

$$\theta_{obs} = \arctan(D / L) \qquad 3\text{-}7$$

Where D is the distance between the two poles and L is the flight path. For the LEAP 5000XR, a flight path value of 42 mm is used. The image compression factor ξ is then obtained as 1.58 by averaging the values obtained from distance between [200] - [103] and [200] - [103]. A further step is taken to confirm the pole identity. Daniel Haley also developed a protocol to simulate the projection of an APT tip from a BCC metal onto a detector with adjustable ξ value. We used the same value at 1.58 to generate the simulated detector map shown in Figure 3-10 (c). The pole identity is indexed, and a good agreement

is achieved between simulated and actual results, so the 1.58 ICF value is accurate in this case.

In most T91 datasets, only two poles were observable after filtering. ξ is then obtained from the distance between the two poles. ξ varied between 1.58-1.64 for different datasets. In some cases, only one pole was observable. In such a case, a value of 1.60 was chosen for the reconstruction.

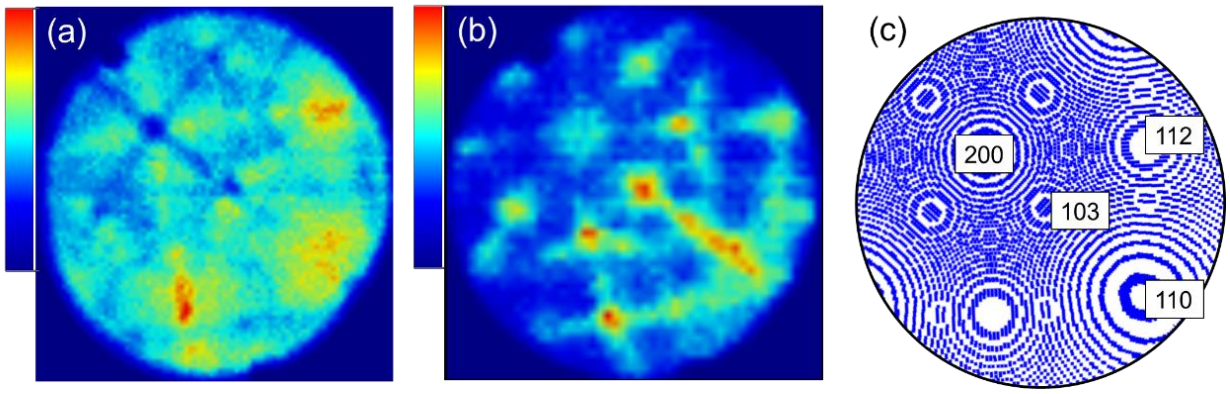

Figure 3-10 (a) Field desorption map of a T91 sample (b) Filtered desorption map using $N_p < 5$ (c) The simulated detector map and corresponding crystal orientations

- Determination of initial radius

Another input parameter critical to the reconstruction is the initial tip radius. The initial tip radius value is adjusted so that the reconstructed interspacing of atomic planes matches the theoretical value. It is known that in APT, the spatial resolution is highly anisotropic. The resolution in the direction of the analysis is often high enough to resolve atomic planes in the depth of material [133,134]. In order to obtain the atomic plane spacing, spatial distribution maps (SDM) have been generated in the *z*-direction. An SDM is a histogram of all interatomic position vectors in a dataset for a particular plane set [135]. One can directly obtain atomic plane spacing from the SDM by measuring the distance between the peaks in

the SDM. Figure 3-11 is an example of SDM analysis. From Figure 3-11, the plane spacing of {200} pole is 0.147 nm after adjusting the initial tip radius, which matches the theoretical value 0.144 nm. The same analysis was also performed along {103} pole to confirm, and all the plane spacing was within the ± 3 % of theoretical values.

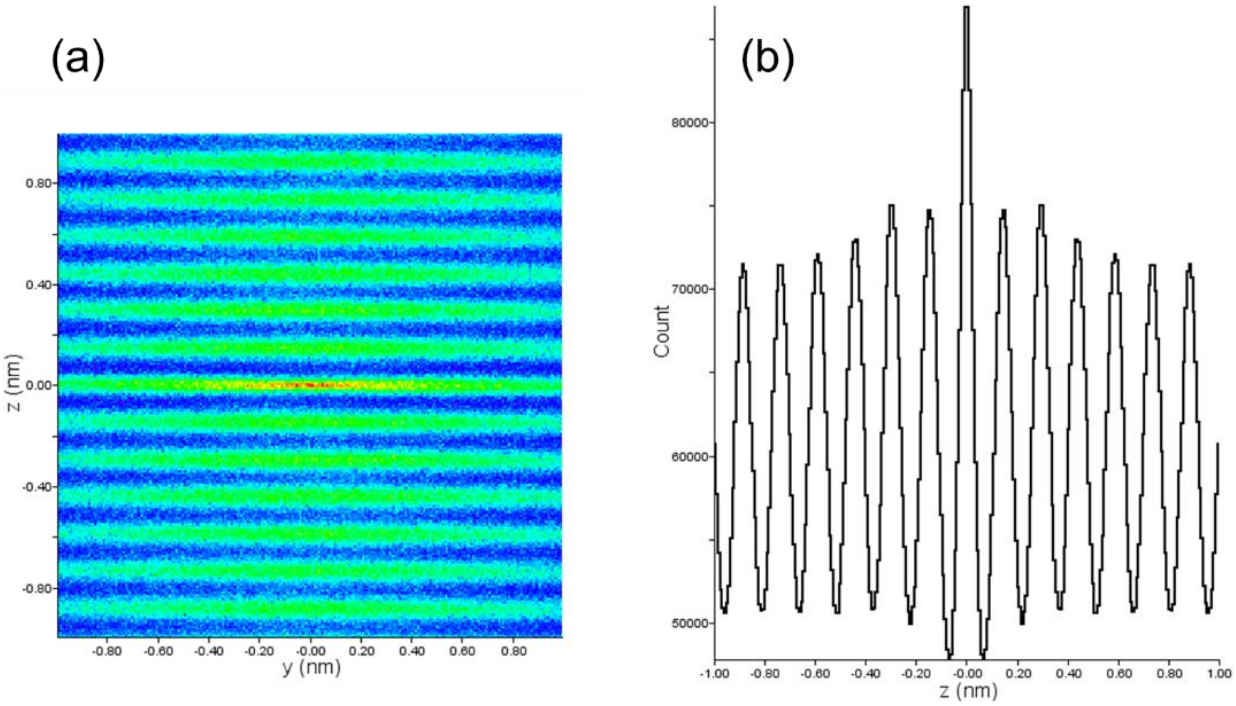

Figure 3-11 (a) View down the y axis of the SDM histogram taken from the dataset in Figure 3-10. The SDM is plotted near {200} pole (b) SDM in *z* along the {200} planes. The distance between peaks represents the inter-planer spacing. The plane spacing of {200} planes is 0.147 nm after adjusting the initial tip radius.

In this study, the reconstruction of all the T91 steel is calibrated using the above method. In 17-4PH steel, due to large amount of additive alloys and a high number density of fine precipitates the pole structure is not clear even after filtering. In such cases a basic voltage reconstruction described in [125] was used. The reconstructed tip shape is determined by shank angle and initial tip radius. In all the heat treated 17-4PH datasets, a high number density (in the order of $10^{23}/m^3$) of Cu-rich precipitates were observed. TEM observations

from previous studies have shown that these precipitates are mostly spherical [48]. Thus the input parameters for initial tips radius and shank angle were chosen to ensure the shape of the Cu-rich precipitates are spherical.

3.5.5 Mass-spectrum ranging

The mass spectra obtained from APT of 17-4PH and T91 are relatively straightforward to interpret due to the absence of oxides and other complex ions. Nevertheless, correct identification of peaks and consistent labelling of peak widths are essential to the following reconstruction and data analysis. Labelled mass spectra of 17-4PH and T91 steel are shown in Figure 3-12 and Figure 3-13 respectively. Most elements have multiple isotopes. The relative abundance of the isotopes can give information for labelling corresponding peaks. Dr. Daniel Haley's *rangecheck* program was used to check the peak identification. In some cases the mass-charge-states of two types of elements overlap. This can affect the composition measurements. An important example is shown in Figure 3-14. In T91 steel both Fe^{2+} and Ni^{2+} can contribute to mass peak at 29 amu. In order to obtain more accurate compositional information, relative contributions to the peaks are decomposed using IVAS software. The deconvolution of peak contribution is based on the relative natural abundance of the adjacent non-overlapping isotopes. From the counts of Fe^{2+} at 28 and 28.5 amu, the theoretical number of counts at 29 amu can be estimated. The same calculation can also be conducted on Ni^{2+}. As a result, 64 % of the peak is identified as Fe^{2+} and the rest is Ni^{2+} for the specific case in Figure 3-14.

Another important fact that needs to be taken into consideration is to define the peak widths consistently. In this study, peak extents are defined approximately at the full width at 9/10 maximum height. The labelling has been kept consistent across different samples.

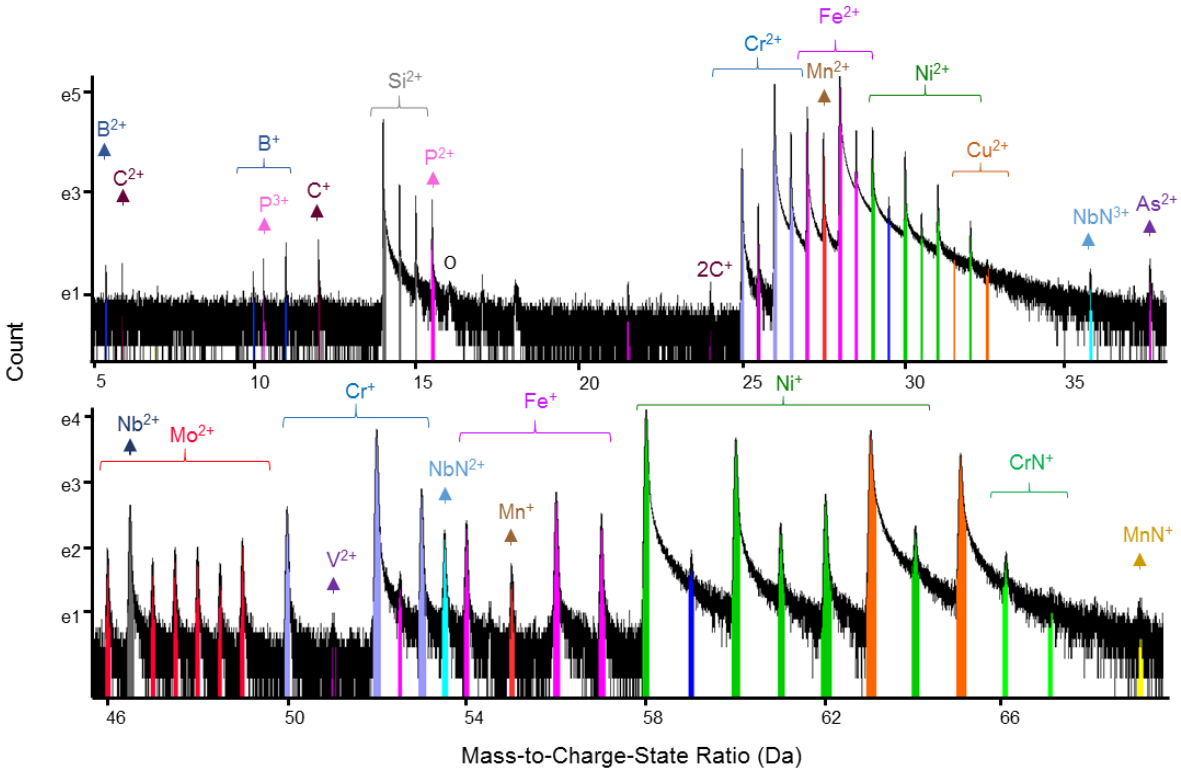

Figure 3-12 Labelled mass spectrum for solution treated 17-4PH steel obtained using laser pulsing on LEAP 3000. This mass spectrum was obtained at 50 K, laser energy 0.4 nJ, and contains approximately 32M ions

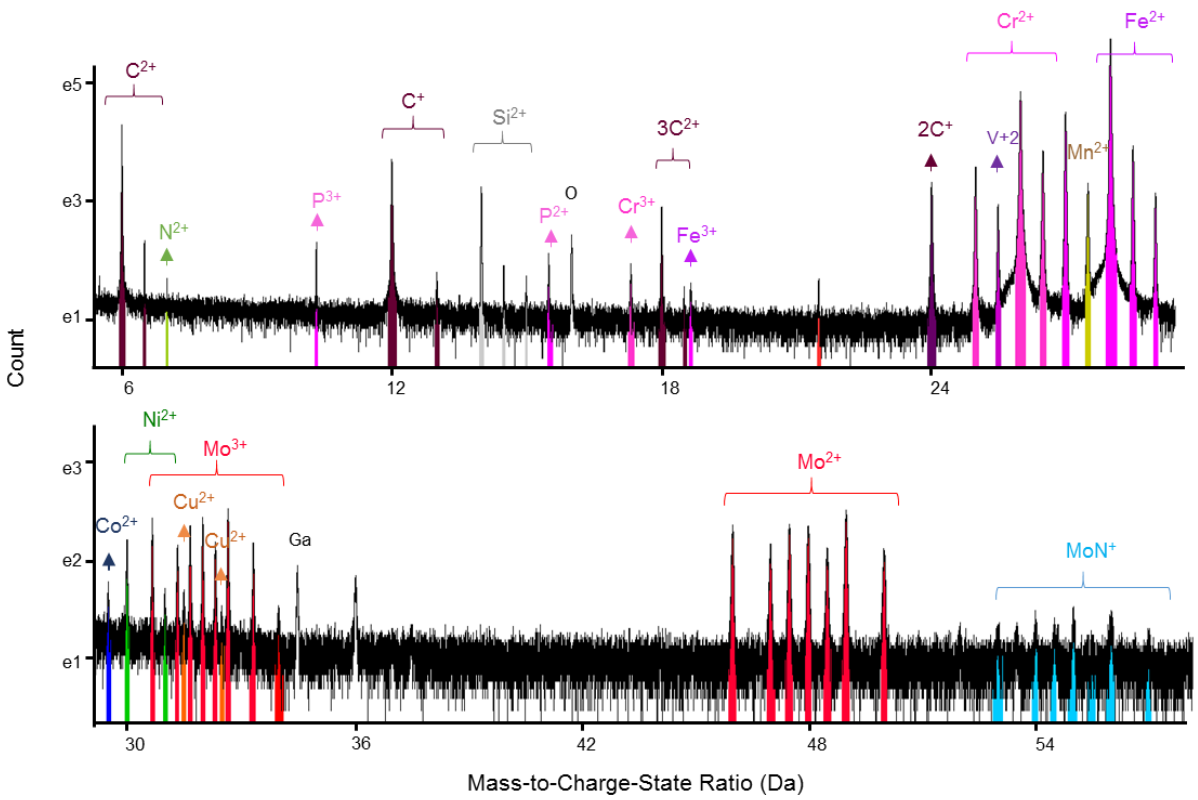

Figure 3-13 Labelled mass spectrum for T91 steel obtained using voltage pulsing on LEAP 5000. This mass spectrum was obtained at 50 K, voltage pulse fraction 20%, and contains approximately 12M ions

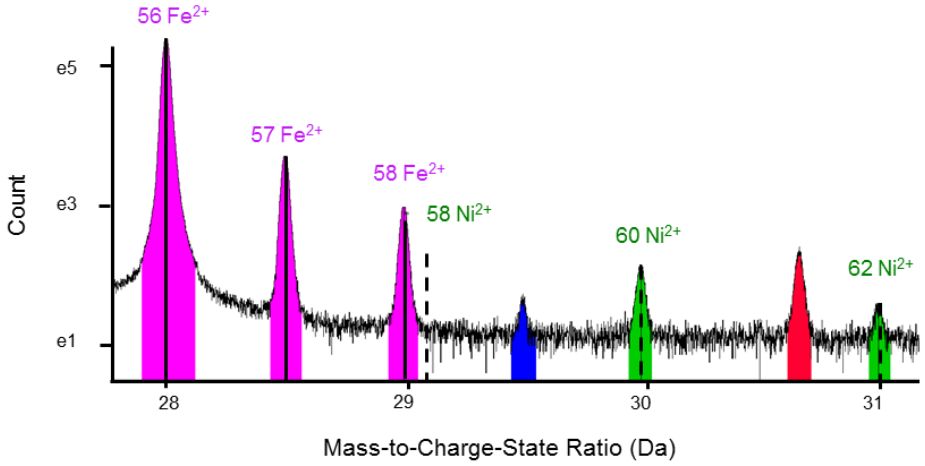

Figure 3-14 Close-up of mass spectrum of T91 steel in Figure 3-12 showing Fe^{2+} and Ni^{2+} peak overlap. The solid black line indicates the natural abundance of Fe^{2+} and the dashed line indicates the natural abundance of Ni^{2+}

3.5.6 Data quality assessment

Gault et al. proposed the criteria for data quality of APT experiments as the quality of the detector hit map, mass spectrum, measured composition and the multiplicity of the events [119]. These are influenced by a number of factors, including tip shape of the specimen, atom probe instrument and experimental conditions. In order to obtain good quality data, all specimens have been carefully prepared using a consistent procedure. Different instruments with different laser wavelengths and detection efficiencies also have an impact on the data quality. During an atom probe analysis, the experimental running parameters have a strong influence on data quality. For laser-pulsed experiments, the laser energy is the most important input parameter.

Taking solution treated 17-4PH steel as an example, the sample was prepared by electropolishing and the same sample was used to test the effect of laser energy on obtained data quality. The analysis temperature was set at 50K. Laser energies of 0.2 nJ, 0.4 nJ, 0.6 nJ and 0.8 nJ, respectively were used and for each energy around 6M ions have been collected. A constant evaporation rate of 0.4 % ion/pulse was kept throughout the experiment. No significant difference in the detector hit map was apparent for different laser energies. Due to the high concentration of solutes in the sample, crystallographic information is not available from all the desorption maps. Quality of mass spectra, measured composition and event multiplicity has been examined.

- Mass spectra

The quality of mass spectra is one of the key aspects to determine the optimal analysis condition. The quality of a mass spectrum is generally assessed by mass resolution, which is defined by $M/\Delta M$, where M is the mass-to-charge-state ratio of an ion and ΔM is the

peak width at selected height [119,136,137]. The M/ΔM of $^{56}Fe^{2+}$ at full-width half-maximum (FWHM) for different laser energy is listed in Table 3-5. The mass resolution improves dramatically from 651 to 1167 when laser energy increases from 0.2 nJ to 0.4 nJ. There is very small difference in mass resolution when changing laser energy from 0.4 nJ - 0.8nJ.

Table 3-5 Mass resolution as a function of laser energy

Laser energy (nJ)	M/ΔM
0.2	651
0.4	1167
0.6	1217
0.8	1167

Another difference in mass spectrum is the distribution of ion charge-states. In the mass spectrum of 17-4PH, as shown in Figure 3-12, the major ions Fe, Cr, Ni, Mn appear in both + and ++ charge state. Double or multiple charge states can be ascribed to post-ionization processes of single charged ions [138]. The influence of the laser pulse energy on the charge state ratios of the main alloying elements was studied. The intensity maxima of the most pronounced peaks of ions with + charge and ++ charge stage in the mass spectrum were examined, where isotopes having no overlap with other elements were chosen. The charge state ratios of the main alloying elements are displayed in Figure 3-15. The ratio of +/++ for all the elements increase dramatically when increasing the laser energy from 0.2 nJ to 0.8 nJ. This is consistent with other experimental results [139,140]. Fewer doubly charged ions indicates a lower electric field, which is indeed the case at higher laser energy.

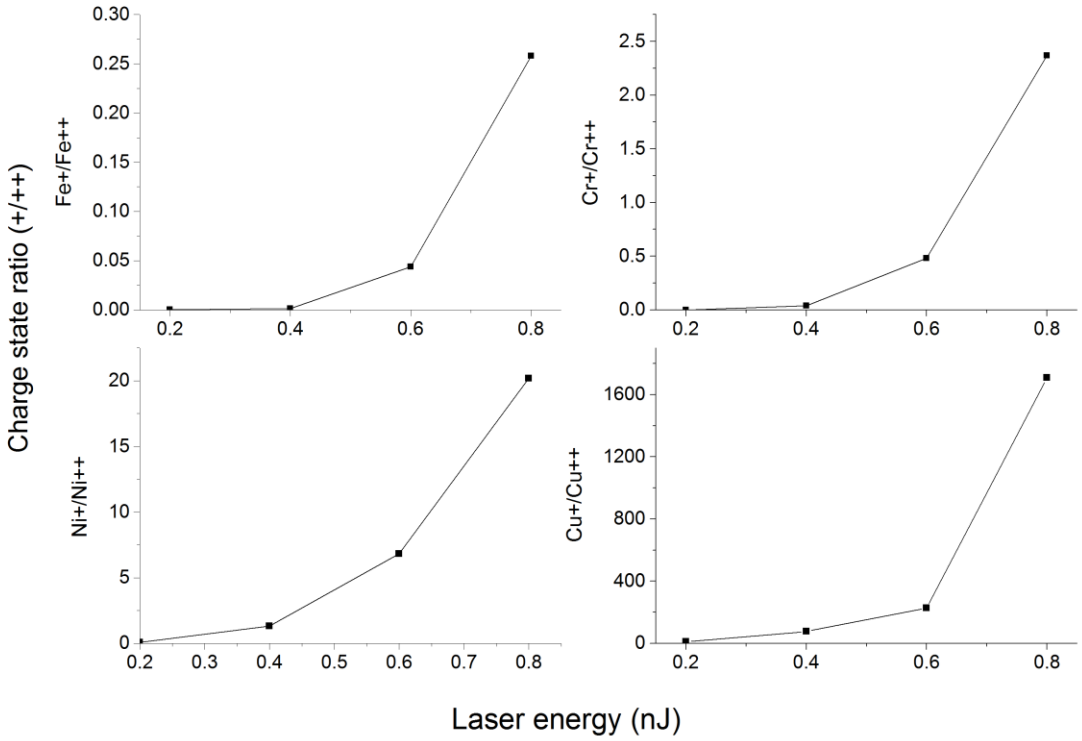

Figure 3-15 Charge-state frequency ratio of Fe, Cr, Ni and Cu as a function of laser energy

- Measured composition

Compositional accuracy is another most commonly used metric to examine the data quality. Due to preferential evaporation caused by laser pulsing, laser energy may have an impact on the measured composition [141,142]. The composition of the main elements in the 17-4PH steel as a function of laser energy is shown in Figure 3-16. There is no clear trend of concentration with respect to laser energy in this case. The variation may be due to small sampling volume of APT. Thus, selection of a preferable laser energy from compositional variations is not clear. It should be noted that the largest difference in concentration compared to bulk concentration is around 1 %, 4 %, 10 % and 5 % for Cr, Ni, Cu, Mn respectively. Considering possible Cu-rich precipitates present outside the analysis region, all the conditions tested here were deemed to be satisfactory.

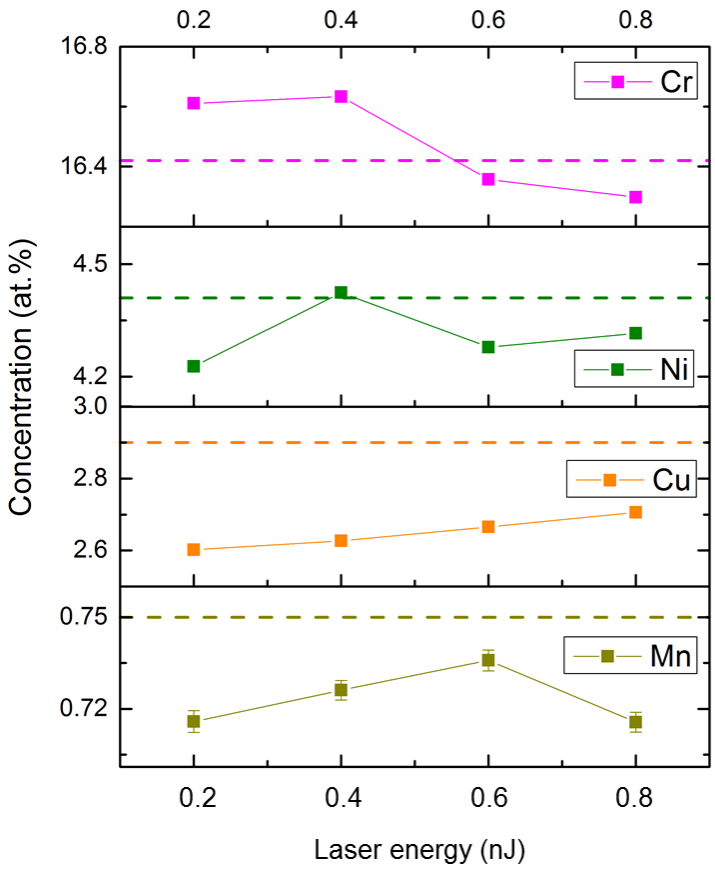

Figure 3-16 Concentrations of alloying elements in the 17-4PH steel as a function of laser energy. Dashed lines are bulk concentration for each element

- Multiple-hit detector events

Multiple-hit detector events are another important aspect of data quality assessment. Ions evaporated by the same laser/voltage pulse detected as multiples can arrive at the detector close in both space and time [143]. Under such circumstances, the detection system can fail to detect those ions arriving after the first and it can lead to a systematic loss of certain ions. The multiple event portion at different laser energies is listed in Table 3-6. The multiple event percentage is quite low at all the conditions tested and the number decreases as the laser energy increases. As the laser energy increases, the electric field required for evaporation decreases. Thus a decrease in multiple event portion is expected.

Table 3-6 Portion of multiple events with different laser energy

Laser energy (nJ)	Multiple event (%)
0.2	5.1
0.4	3.2
0.6	2.4
0.8	2.0

3.5.7 APT experiment parameters

In this study, all of the 17-4PH steel experiments were carried out on a Cameca LEAP 3000X HR and the unirradiated and single ion beam irradiated T91 steel experiments were also carried out on the Cameca LEAP 3000X HR. All the dual ion beam and BOR60 irradiated T91 steel analysis were carried out on a Cameca LEAP 5000XR. The dataset compared with each other are from the same analysis condition unless otherwise stated.

In order to select appropriate analysis parameters for APT experiments, all the requirements for good data quality in § 3.5.6 need to be taken into consideration. In addition, one must consider the success rate of the APT experiment. For example, the yield of 17-4PH steel under voltage pulsing mode is low due to the presence of carbides/nitrides, which can serve as points of specimen failure when exposed at the surface under intense electrostatic stress. Thus laser pulsing has been used, which results in use of lower applied electric fields. From section 3.5.6, at laser energy above 0.4 nJ, very good mass resolution and low multiple-hit percentage have been achieved. One concern is that higher laser energy may result in surface migration [144] and has an influence on cluster shape/composition. Thus, a consistent laser energy of 0.4 nJ is used for all 17-4PH steel analysis.

Gault et al. [135] studied the effect of analysis temperature for Al and proposed that increasing the analysis temperature from 20 K up to 80 K, there is little change in the in-depth resolution. Considering higher temperature is beneficial to the yield, the analysis

temperature is set at 50 K throughout this study. From the previous analysis, the obtained mass spectra and composition are satisfactory at this temperature.

Similar analysis has been conducted on T91 steel. For unirradiated and single ion irradiated T91 steel, Laser pulsing with an energy of 0.4 nJ was used as many of the samples contains carbides/nitrides, which are more prone to fracture under voltage mode.

However, for dual ion/BOR60 irradiated T91 steel, the laser pulsing did not increase the yield of successful experiments. The possible reason is that they are analysed using LEAP 5000XR with a much smaller laser spot size. Slight vibration of the tip/laser has a strong influence on the tip temperature and causes the sample fracture. Thus, for dual ion beam irradiated and BOR60 irradiated samples, voltage pulsing with 20 % pulse fraction was chosen.

4 APT data analysis techniques

4.1 Data visualization

The most basic and straightforward APT analysis is showing the atom maps of a sample. Figure 4-1 is an example of atom maps. Each dot in this figure represents one ion. Atom maps give direct information about the spatial distribution of each ionic species. Features like precipitates and segregation can be directly observed from atom maps.

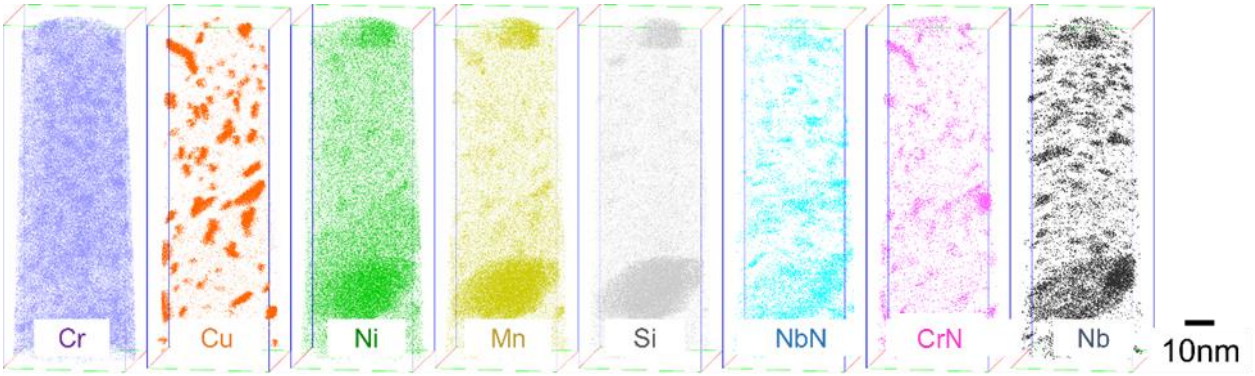

Figure 4-1 Atom maps of 17-4PH steel sample from the mass spectrum in Figure 3-12

4.2 Compositional measurements

The concentration of a given element, A, can be defined as

$$c_A = n_A / n_{tot}, \qquad 4\text{-}1$$

where n_A is the number of A atoms in the volume and n_{tot} is the number of all the atoms in the analysed volume. The error in this value is usually calculated as the standard deviation using the following equation:

$$\Delta c_A = \sqrt{c_A(1-c_A)/n_{tot}}, \qquad 4\text{-}2$$

This error calculation is purely counting error and does not consider the experimental errors, i.e. sampling errors and error induced by non-optimised parameter selection. In this study, the bulk composition error is accounted for by analysing multiple samples and calculating the standard error. The compositional measurements shown in Table 3-1 are calculated by averaging composition obtained from different dataset.

4.3 Analysis of phase boundaries/grain boundaries

- 1D concentration profile

The most straightforward method to examine the composition across an interface is the 1D concentration file. First, an analysis cylinder ROI is placed perpendicular to the interface in the data. Then the composition in slices with a defined width is calculated through the cylinder.

- Gibbsian interface excess

To do a further quantitative analysis across an interface, a calculation of the Gibbsian interface excess, as described below, can be carried out. This method has been applied in the quantitative studies of grain boundaries [145]. The theory was established by considering a two-phase system, where a heterophane interface ξ exists at the boundary, as schematically illustrated in Figure 4-2 The Gibbsian interface excess Γ_i for solute i is defined as:

$$\Gamma_i = N_i^{excess} / A = (1/A)(N_i^{vol} - N_i^{\alpha} - N_i^{\beta}) \qquad 4\text{-}3$$
$$= (1/A)N^{vol}(C_i^{vol} - C_i^{\alpha} - C_i^{\beta})$$

where N_i^{excess} is the number of excess solute atoms *i* within the interface, and A is the interface area. The values of N_i^{α} and N_i^{β} are the number of atoms of element *i* in phases α and β, assuming that the two phases exist up to the Gibbs dividing surface ξ. The excess is, therefore, defined by comparing the total number of atoms of element i in the actual system containing the interface, to a reference system where the two phases making up the interface extend to the position of ξ. The quantities C_i^{α}, and C_i^{α} are the atomic concentrations of element *i* in the homogeneous regions of phase α and β [145].

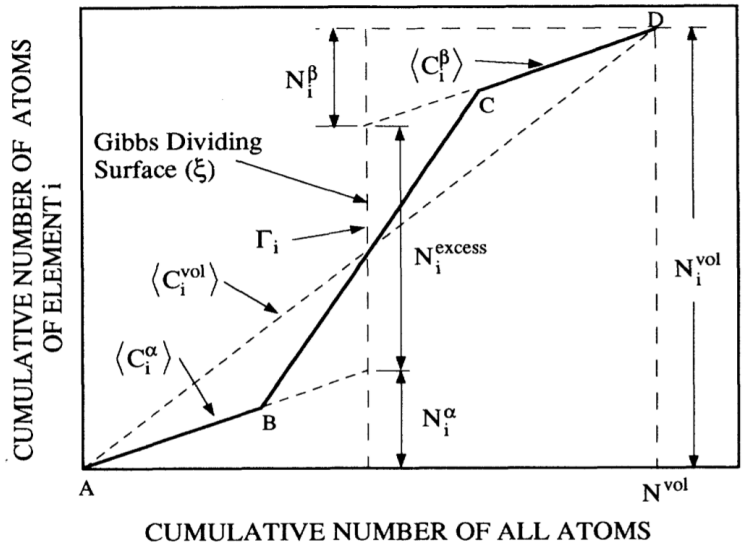

Figure 4-2 Hypothetical integral profile (line ABCD) showing how the excess number of solute atoms is determined in [145]

In this study the Gibbsian excess across a grain boundary is calculated using the same procedure as the following example. Figure 4-3 (a) shows a grain boundary highlighted by the segregation of Ni in an irradiated T91 steel. The 1 D concentration profile across the grain boundary is shown in (b). The analysis region-of-interest is a cylinder shape with 5 nm in radius and 15 nm in length. An increase of Ni, Si concentration on the grain

boundary can be directly seen from profile. In order to obtain the interface excess, ladder diagrams within the analysis cylinder are plotted for the main alloying elements, as shown in (c). One can clearly see that Si and Ni are segregated at the grain boundary. Obvious segregation of other elements (Cr, Mo and V) cannot be observed. Taking Si as an example, first two point A, B is selected as the boundaries of the interface. The interface position is assumed to be at the centre of A and B. The Gibbsian excess is then obtained using equation 4-3. At most cases when the concentration of *i* is similar at both sides of grain boundary, the choice of A and B point does not have a big influence on the resulting Γ_i. However when the concentration inside the adjacent grains are different, the choice of A and B point can bias the result. Thus the error of the Gibbsian excess is calculated by averaging four Γ_i values obtained from choosing different A, B points close to the edge region.

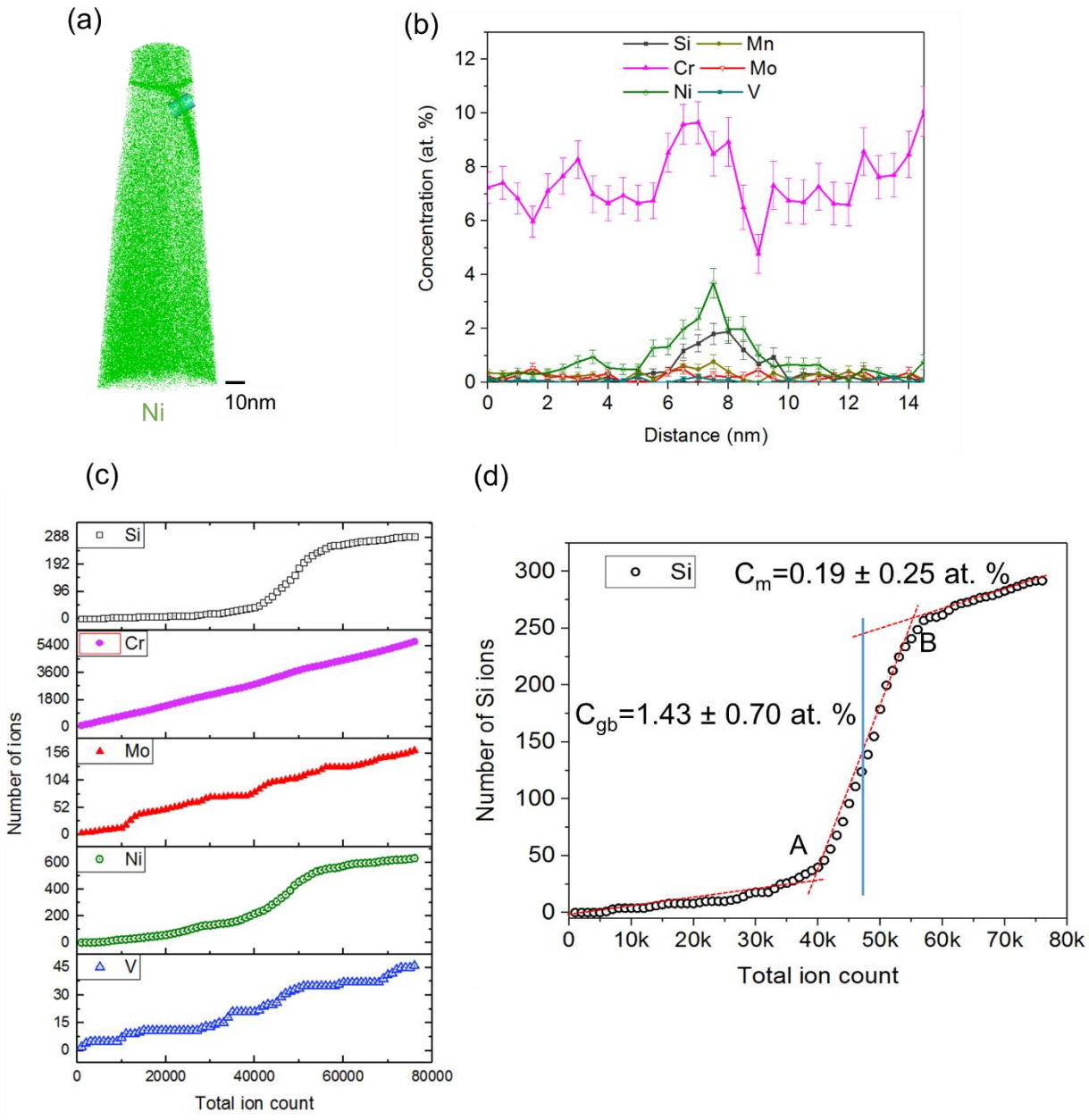

Figure 4-3 (a) Distribution of Ni atoms in T91 steel subjected to single ion beam (Fe++) irradiation to 10 dpa at 470 ^{o}C (b) 1 D concentration profile across the grain boundary (c) ladder diagrams across the grain boundary showing the accumulative solute count as a function of total ion count (d) ladder diagram of Si and schematic showing the calculation of average concentration of i on the grain boundary (C_{gb}) and in the matrix (C_m)

- Proximity histogram

The proximity histogram/proxigram is similar to the 1D concentration profile. But rather than a calculation along a fixed direction, a proxigram measures the composition with

respect to one or multiple interfaces [146]. In the case of a curved interface, the size of the cylinder to measure 1D concentration file should be small enough that it is not affected by the curvature of the interface. But too small an analysis size will lead to statistical variations. For proxigrams, the curvature is taken into account at the same time statistics have been maintained.

4.4 Techniques for characterising precipitates

A key strength of atom probe is the analysis of fine scale (i.e. 1 - 2 nm) precipitates in their early stages of development. A number of cluster analysis methods have been used to identify the precipitates at their different stages.

4.4.1 Nearest neighbour distribution

One of the most commonly used algorithms to characterise the interatomic distance in the immediate vicinity around each atom is the nearest neighbour (NN) distribution analysis [147]. The NN distribution is a histogram of neighbouring distances from every selected atom. This calculation can be conducted on all the atoms or only selected species, i.e. NN_{A-A}, NN_{A-B}.

NN analysis can also be extended to higher order NN distribution analysis [148]. Instead of the first nearest neighbour, kNN distribution is an examination of the interatomic distance between each atom and its k^{th} nearest neighbour. For solutes with higher concentration and clusters that are at the very early stages, kNN analysis is more effective than the 1NN analysis at identifying small clusters. An example of higher order NN distribution of Ni atoms from the same dataset presented in Figure 3-13 is shown in Figure 4-4. Clustering of Ni atoms can be directly observed from the Ni atom map presented in Figure 4-4 (a). From

the 1NN analysis plotted in (b), the experimental distribution broadens from the randomized distribution towards smaller distances, indicating the clustering of Ni atoms. In the 5NN distribution shown in (c), two separate peaks are obvious. The two peaks separate the contributions from the clustered Ni, and Ni ions randomly distributed in the matrix. When the concentration of a solute is relatively high, the average 1NN distance between two clustered atoms is close to that of two non-clustered neighbour atoms. However, higher order NN distribution can reveal the details of nano-scale segregation more effectively.

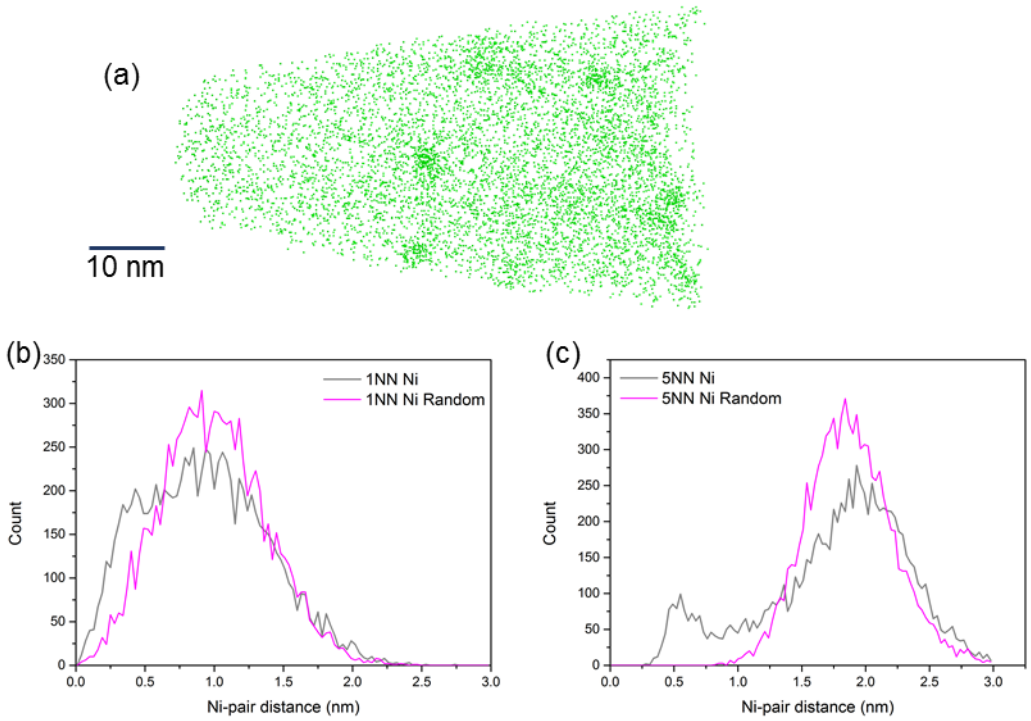

Figure 4-4 (a) Distribution of Ni atoms (green) in an irradiated T91 steel (a) 1NN distribution of Ni (b) 5th NN distribution of Ni

4.4.2 Cluster identification algorithms

In order to get information about the chemistry, morphology, number density and fraction of the precipitates (i.e. CRPs, and Cr-rich precipitates), an accurate and efficient cluster identification algorithm is required. A range of cluster identification algorithms have been

developed to characterise the formation and development of precipitates. The basics of two methods are introduced here.

- Maximum separation method

Maximum separation is one of the most commonly used algorithms to identify the clusters within APT data [149,150]. The approach is based on the principle that the distance between two nearest neighbour solute atoms is less if they are both within a cluster than in the matrix. The basic schematic of this algorithm is shown in Figure 4-5. Around each solute atom, a sphere of radius D_{max} is drawn, any solute atoms appearing within the sphere are determined to be clustered together. From every new added atom, another sphere of D_{max} is drawn. This step is repeated for all the solute atoms. The result is shown in Figure 4-5 (b). At this point, only solute atoms have been included in the cluster. The envelope method (implemented in IVAS software) is based on this maximum separation method and extends the functionality by defining a third parameter, the envelope parameter, L. A circle is placed on every solute atom determined to be in the cluster and all the matrix atoms within a set distance, L, are determined to be part of the same cluster. This will however also result in a shell of matrix atoms around the cluster, as shown in Figure 4-5 (c). In order to remove the shell, another parameter Erosion, E, is introduced. A circle of radius E is placed on all of the non-clustered atoms. Any atom co-located within the circle is removed. Finally, an additional parameter N_{min}, defining the minimum number of solute ions in a cluster, is used to filter small clusters statistically likely to randomly occur in the matrix.

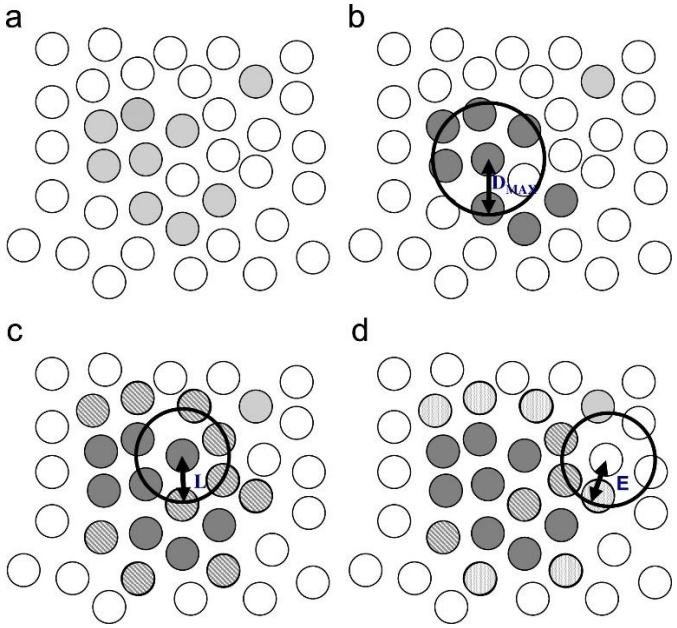

Figure 4-5 Schematic showing the maximum separation method: (a) solute atoms are shown shaded, (b) solute atoms within D_{max} of each other are shown shaded dark (the core atoms), (c) other atoms within a distance L of the core atoms are identified (hatched) and (d) atoms within a distance E of any other atom are removed by the erosion algorithm (dotted) [151]

The maximum separation method is based on interatomic spacing and is suitable for identification of clusters in their early stages or when the solute concentration is very low. In this study, CRPs and Nb-rich precipitates are separated using this method.

- Concentration threshold method

The concentration threshold method is based on the fact that the concentration of the solute atoms within a precipitate is greater than in the matrix [146]. The precipitates are defined using a concentration threshold, $c^{threshold}$. In this method, the dimension and number density of the clusters is very sensitive to the $c^{threshold}$. Thus, the value should be carefully chosen.

In 17-4PH steel, the concentration of Cr in the matrix is very high (>15 at. %). Iso-concentration surfaces have been generated to separate the Cr-rich precipitates and the matrix.

4.4.3 Selection of cluster analysis parameters for maximum separation method

The results from cluster analysis are very sensitive to the analysis parameters. The values of D_{max} and N_{min} are critical for properly defining precipitate composition and counts. Several methods to select appropriate values have been proposed in [148,150,152] and [153].

- D_{max}

It is common to estimate D_{max} by comparing the NN distribution of experimental and randomized data. Figure 4-6 shows the 1NN distribution of Cu in a 17-4PH steel after heat treatment. It is obvious that the distances in experimental data are much smaller than those in randomized data. The aim is to select a D_{max} large enough so as to identify all of the clustered Cu atoms, but not so large that it erroneously identifies Cu atoms in the matrix as clustered. In this case, D_{max} is firstly estimated as 0.37 nm. The result from cluster analysis within IVAS software is shown in Figure 4-7. Dots with the same colour represent an individual cluster. By comparing Figure 4-7 (a) and (b), one can see that some clusters have been incorrectly split into multiple clusters using this D_{max} value. Therefore, D_{max} number needs to be increased. Results from D_{max} of 0.8 nm and 1.2 nm are shown in (c) and (d) respectively. By comparing (c) and (d), it is apparent that 1.2 nm is too large that separate clusters are combined to a single one, as indicated by red dashed circles. 0.8 nm is therefore the most satisfactory choice between these three values. So it is the D_{max} value of 0.8 nm is chosen for this dataset.

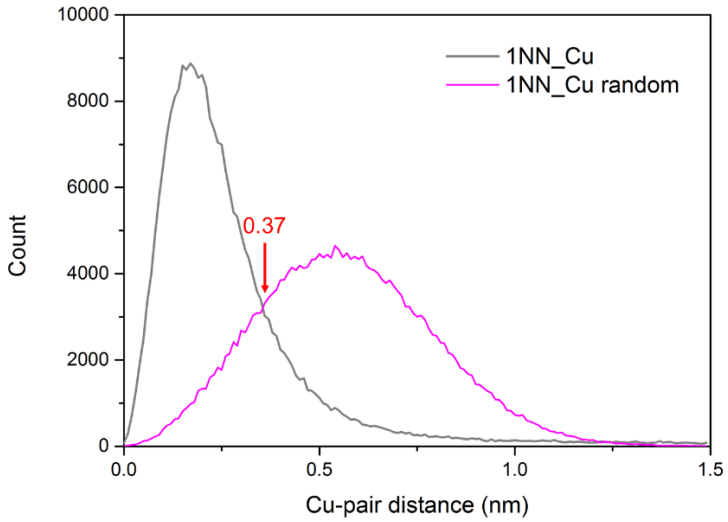

Figure 4-6 1NN distribution of Cu atoms in a 17-4PH steel after heat treatment

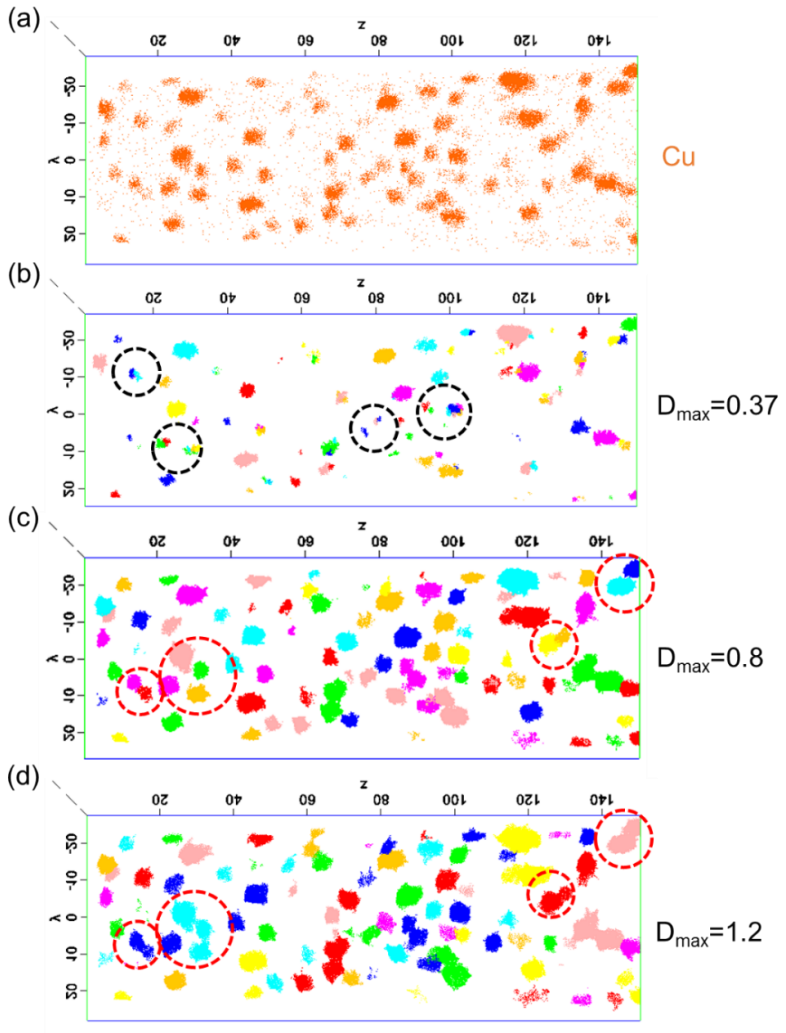

Figure 4-7 (a) Distribution of Cu atoms in heat treated 17-4PH steel. Cluster distribution when D_{max} is taken as (b) 0.37 nm, (c) 0.8 nm and (d) 1.2 nm. Different colours represent different clusters in (b), (c) and (d)

This is further refined by plotting cluster counts as a function of D_{max} with different N_{min} in Figure 4-8. There is no obvious "local minimum" observed for any N_{min}. However, if D_{max} is smaller than 0.6 nm, the cluster count will significantly increase. This indicates that clusters are misidentified and split into multiple clusters. Also, when D_{max} is larger than 1.2 um, the decreasing slope of the cluster count gets larger. The gradient of the slope is the smallest around 0.8 nm, which means slight variations of D_{max} will not largely affect the result. From Figure 4-5, it seems like D_{max} of 0.8 nm will include many random Cu atoms.

However, for 17-4PH steel, it is not a major concern as more than 90 % of Cu atoms are inside clusters. Generally, as long as combining individual clusters together can be avoided, the D_{max} number should be as large as possible.

Since the size of CRPs grows as the ageing time increases, this estimation is repeated for all the datasets. D_{max} increases with ageing time, and the range of values selected is taken between 0.8 nm to 1.2 nm for all the ageing conditions.

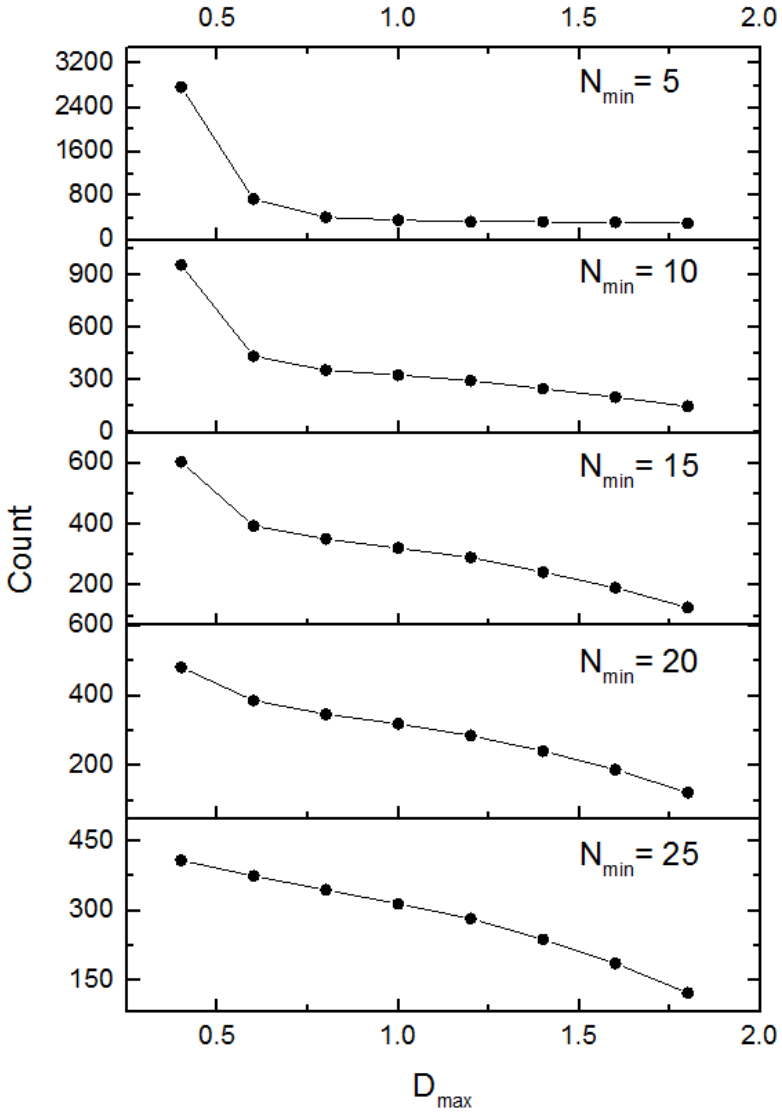

Figure 4-8 Cluster count as a function of D_{max}. N_{min} is taken from 5 to 25

- N_{min}

After defining D_{max}, the next step is to eliminate clusters containing less than a specified minimum number of solute atoms, N_{min}. A typical value of N_{min} is in the range 10–30, chosen aiming to exclude randomly occurring smaller clusters but including most real ones [150]. In the same 17-4PH specimen, when D_{max} is taken as 0.8 nm, if the N_{min} is set as 2, the resulting size distribution of clusters is shown in Figure 4-9. A local minimum is observed at clusters with around 20 atoms. If we assume that the CPRs have a random (Gaussian) size distribution, it can be inferred that the counts smaller than 20 atoms in Figure 4-9 are related to the random clusters and thus should be removed. It should be noted that D_{max} and N_{min} are co-relative and for a given D_{max}, the parameter N_{min} depends on the matrix solute concentration. In 17-4PH steel, N_{min} has been chosen between 20 - 25.

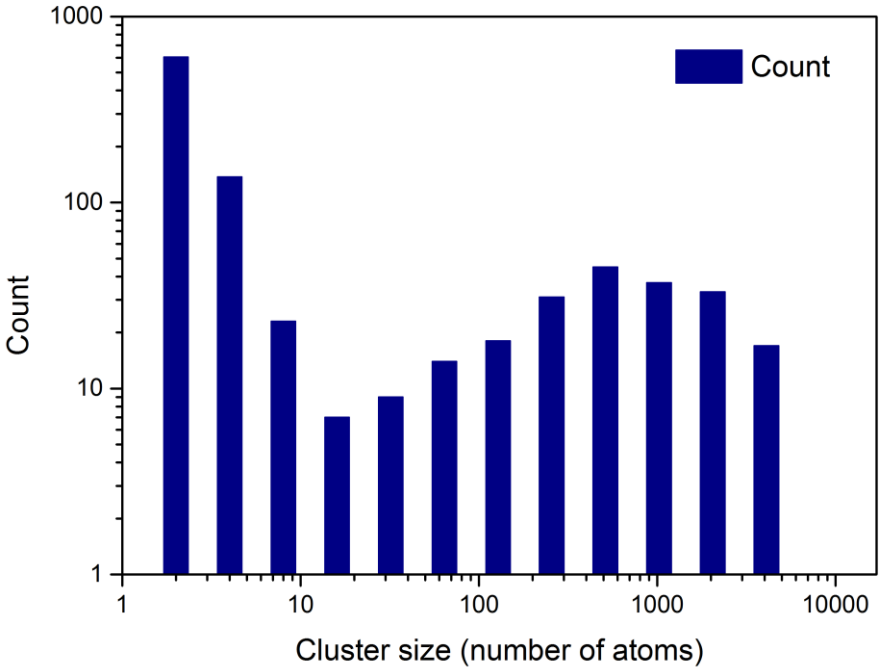

Figure 4-9 Size distribution of CRPs in 17-4PH after heat treatment. The D_{max} is taken as 0.8 nm and N_{min} is set as 2.

- L and E

The selection of envelope parameter, L, and erosion, E, will affect the composition of the clusters. In order to include all the potential matrix atoms in the clusters, the envelope parameter, L is taken as L= ½ D_{max} consistently throughout the analysis. E is chosen as 0.1 nm, smaller than the L value to remove the shell of matrix atoms from the clusters.

The Nb-rich clusters in 17-4PH are also analysed by the maximum separation method, and the D_{max} is taken as 1.4 nm and N_{min} as 10. These values are reasonable as Nb is mostly inside clusters and the distance between Nb-rich clusters are larger than that of CRPs. Therefore, a larger D_{max} value than CRPs is acceptable. Furthermore, Nb clusters are smaller than the CRPs. Thus the N_{min} number should be smaller than that selected to define CRPs.

4.4.4 Selection of Iso-concentration value for concentration threshold method

When using the concentration threshold method (introduced in § 4.4.2) to identify precipitates, a sphere of *d* is moved over each atom in the analysis volume and the concentration of the elements is measured. For an atom p, if the concentration of the solutes within the sphere is larger than the threshold value $c^{threshold}$, p is considered to be a clustered atom. In this method, the dimensions and number of precipitates identified within the analysed volume is dependent on the choice of $c^{threshold}$. The selection of $c^{threshold}$ is dependent on the composition of the precipitates. Cr-rich precipitates in 17-4PH are selected using iso-concentration surfaces. An example of a concentration proxigram (§ 4.3) for Cr-rich precipitates is shown in Figure 4-10. The iso-concentration surface is chosen at 40 at. %, where the concentration gradient is the largest. $c^{threshold}$ is taken as 40 at. % consistently throughout data sets.

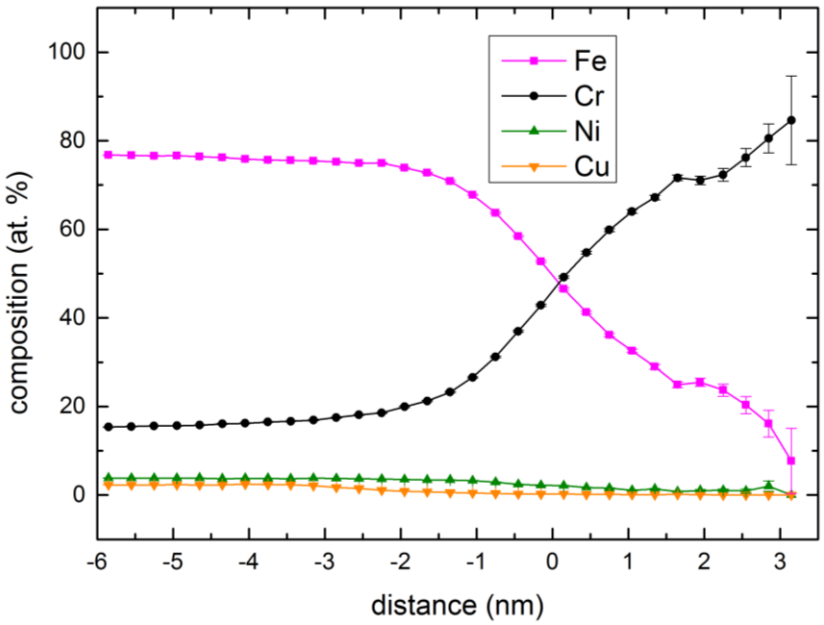

Figure 4-10 Concentration proxigram of Cr-rich precipitates in an aged 17-4PH. The error is standard error from averaging all the precipitates

4.4.5 Statistics of the precipitates

- Number density

Once the precipitates have been identified, it is useful to describe their density. The number density, *N*, of clusters identified within the reconstruction was calculated using the following formula:

$$N = \frac{n\eta}{N_{tot}\Omega}, \qquad 4\text{-}4$$

where n is the total number of clusters in the analysed volume, N_{tot} is total number of atoms in the reconstruction, Ω is the volume of one solute atom, taken as 1.178×10^{-2} nm^3, assuming the solutes have a similar volume as Fe, while η is the detection efficiency of the instrument. η is 0.37 for LEAP 3000X HR and 0.52 for the LEAP 5000 XR as specified by CAMECA.

- Volume fraction

The volume fraction of clusters is an important factor to estimate their influence on strength and hardness. The volume fraction, *f*, is estimated by:

$$f = \frac{\sum_{i=1}^{n} N_{sol}}{N_{tot}}, \qquad 4\text{-}5$$

Where N_{sol} is the total number of solute atoms (i.e. Cu) incorporated within a precipitate and N_{tot} is the total number of atoms in the sample.

- Precipitates size

The radius (*r*) of a precipitate was equated to that of the volume equivalent sphere:

$$r = \sqrt[3]{\frac{3N_{sol}\Omega}{4\pi\eta}}, \qquad 4\text{-}6$$

There is a possibility with this approach of under-estimating the size and volume fraction of solutes because the matrix atoms are excluded from the calculation. However, trajectory aberrations that affect the spatial resolution of reconstructed atoms in the region of the precipitates can cause an overestimation of matrix atoms to be associated to the precipitates. Furthermore, the APT measured composition of the dominant solute(s) in precipitates was very high: The Cr content in the Cr-rich α' phase exceeds 70 at. %; The Mn + Ni + Si content exceeds 80 at. % in the Mn, Ni, Si-rich (MNS) phase; and the Cu content in CRPs exceeds 50 at. %. Hence, the systematic method described above was deemed to be a reasonable approach for estimating the radius *r* and volume fraction *f*.

5 Effect of heat treatment on 17-4PH steel

5.1 Introduction

A major concern for 17-4PH steels operating at elevated temperatures is embrittlement due to Fe-rich (α) and Cr-enriched (α') phase separation, along with precipitation of other detrimental phases. In this study the sequence of microstructural changes at the atomic scale in a 17-4PH steel is characterized by atom probe tomography (APT) at two different ageing temperatures, 480 ^{o}C and 590 ^{o}C, for times up to 1000 h. The nucleation, growth and coarsening of precipitates at the various ageing stages has been characterized and correlated to results from Vickers hardness testing, linking microstructure to a key mechanical property.

5.2 Microstructure of 17-4PH steel after solution treatment

5.2.1 XRD

The XRD results from solution treated 17-4PH steel is shown in Figure 5-1. After solution treatment at 1040 ^{o}C and oil quenching the results showed a pure BCC lattice, indicating the formation of martensite.

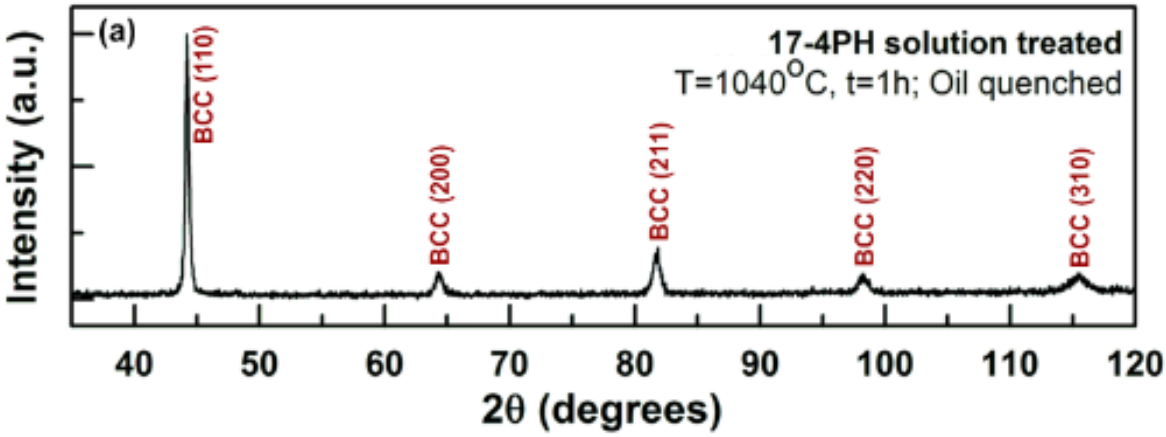

Figure 5-1 XRD patterns for 17-4PH solution treated at 1040 °C for 1 h followed by oil quenching

5.2.2 APT atom maps

As shown in Figure 5-2, no precipitation or segregation is observed in the APT reconstruction after solution treatment, with all the elements randomly distributed. Previous TEM studies have shown that at this solution treated stage, the microstructure is defined by a lath martensitic matrix having a high dislocation density and a low amount of carbide particles [46,48]. The absence of carbides observed throughout this study is most likely due to the relatively large distance between such features relative to the very small sampling volume of a typical APT analysis.

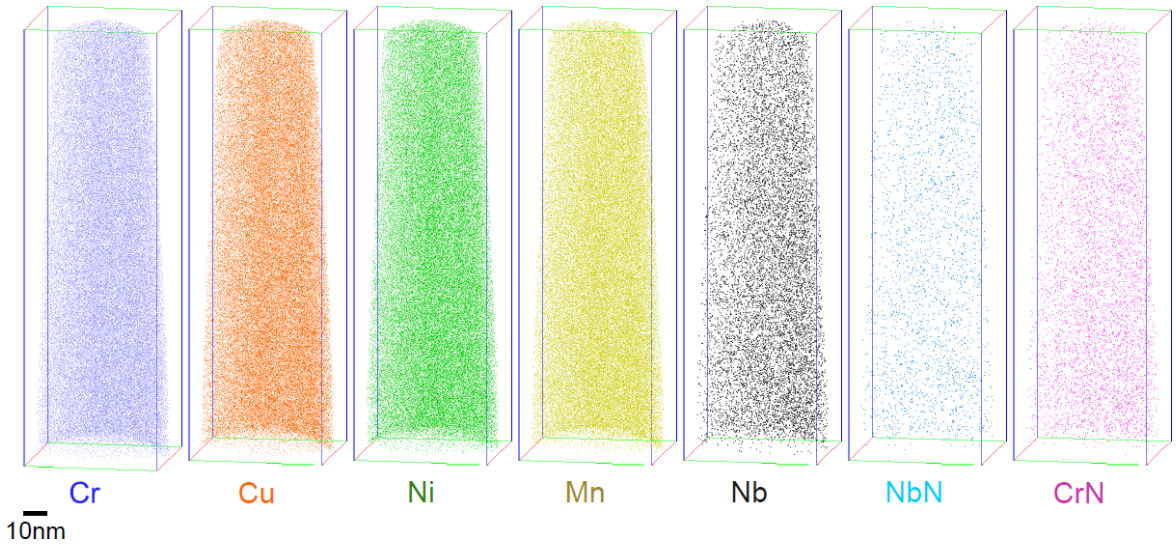

Figure 5-2 Atom maps of 17-4PH solution treated at 1040 ^{o}C for 1 h followed by oil quenching, showing random distribution of ionic species

5.3 Hardness variation of 17-4PH after heat treatment

The variation in Vickers hardness of the specimens at both heat treatment temperatures as a function of holding time is shown in Figure 5-3. The value at 0 h represents the hardness after solution treatment and oil quenching. The error is the standard deviation after averaging over 10 measurements. The hardness variation exhibits a dramatic difference between the two temperatures. At 480 ^{o}C, the hardness peaks around 1 h, and is higher than the initial value by ~ 145 (HV30). At later times, the hardness remains steady up to 360 h. A decreasing trend is only observed after the measurement at 1000 h. In contrast, at the higher temperature 590 ^{o}C, a sharp peak in hardness was observed after 10 min followed by a sharp drop. The peak hardness at 480 ^{o}C is higher than the peak hardness at 590 ^{o}C by ~ 40 (HV30).

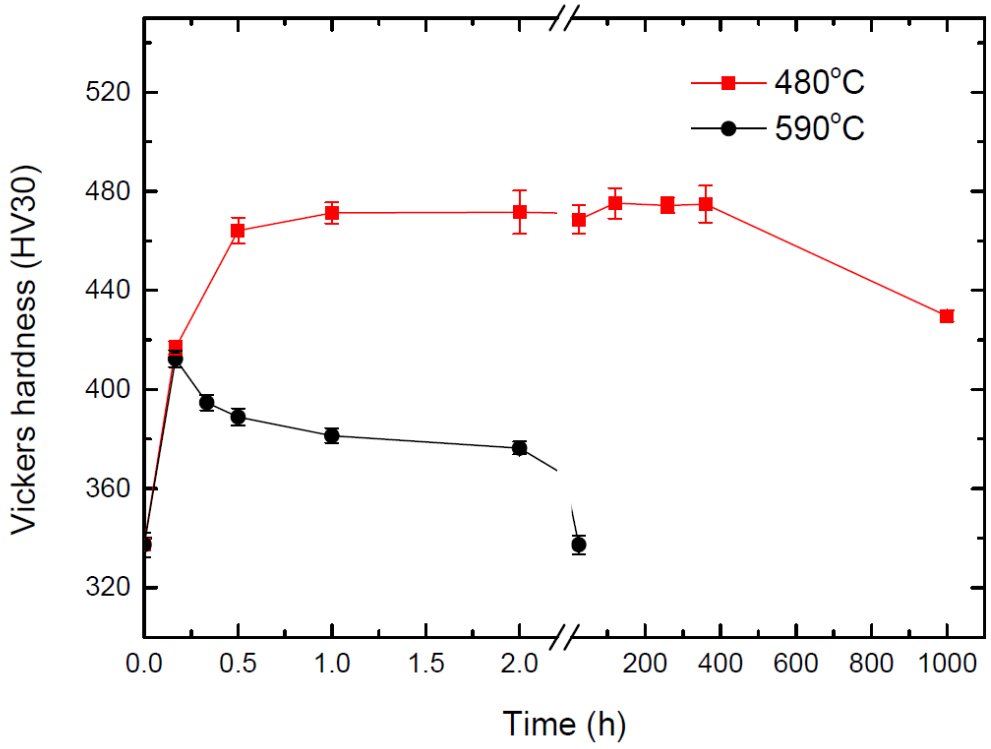

Figure 5-3 Variations in hardness of the 17-4PH steel with heat treatment time at 480 °C and 590 °C

5.4 Microstructural changes after heat treatment at 480 °C

5.4.1 XRD

The XRD patterns of 17-4PH steel heat treated at 480 °C for 10min and 1000h are shown in Figure 5-4. The results showed a pure BCC structure, indicating that martensite is stable at this temperature.

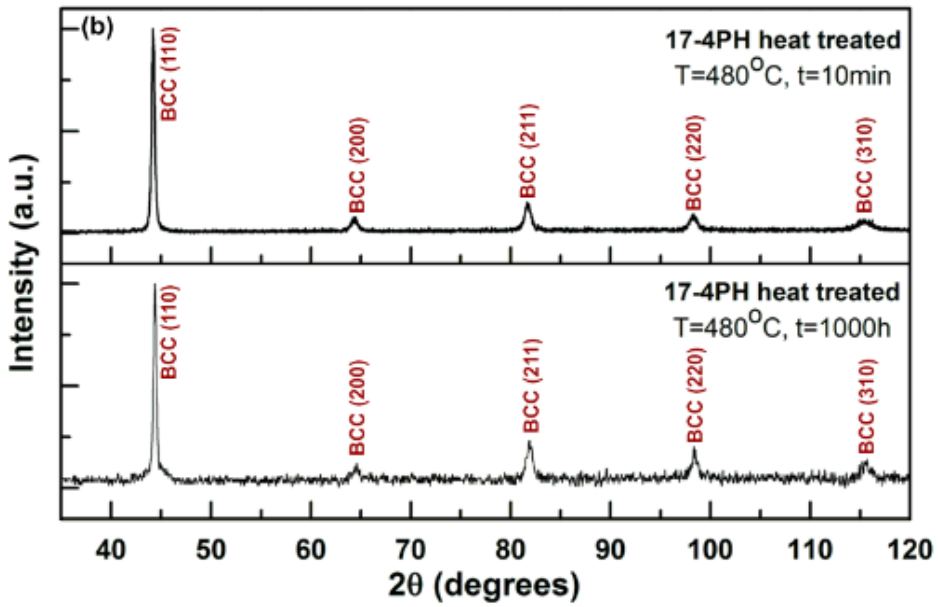

Figure 5-4 XRD patterns for 17-4PH heat treated 10 min and 1000h at 480 ^{o}C

5.4.2 Atom maps

The atom maps of 17-4PH steel after heat treatment at 480 ^{o}C for different times are shown in Figure 5-5(a)-(d). After ageing for only 10 minutes the first change in the atomic scale chemical distribution can already be observed by APT. The corresponding atom maps are shown in Figure 5-5 (a). In the APT experiment N is detected exclusively in the form of complex molecular ions, such as CrN^{+} and NbN^{+}. The interconnected structure displayed is possibly due to the migration of N to dislocations and matrix defects. All other elements appear homogeneously distributed at this stage. After heat treatment for 2 h at 480 °C, segregation of NbN and CrN ions is apparent, as shown in Figure 5-5 (b). Furthermore, a high number density of CRPs and Nb-rich precipitates are now observed to have formed. The Nb-rich precipitates are smaller in size than CRPs. After ageing for 120 h (Figure 5-5 (c)), the CRPs coarsened, and Cr-rich regions are observed. Large (~20 - 50 nm) Mn, Ni, Si-rich phase are present in the analysed volume after ageing for 360 h, as shown in Figure 5-5 (d). Each of the above phases is described in detail in the following sections.

Figure 5-5 Atom maps of 17-4PH heat treated at 480 ºC for (a) 10 min (b) 2 h (c) 120 h (d) 360 h

5.4.3 CRPs

From Figure 5-5, CRPs are consistently observed after 2 h. In order to understand the composition of the precipitates, an isoconcentration surface of Cu at 20 at. % is used to highlight the precipitates after ageing for 2 h and 120 h. The isoconcentration surfaces for each case are shown in Figure 5-6 (a) and (b) respectively. The corresponding concentration proxigrams are plotted in Figure 5-6 (c) and (d). Even after ageing for only 2h, the peak Cu concentration in the precipitates is ~ 60 at. %, twenty times higher than the overall Cu concentration. As the heat treatment time increases to 120 h, the Cu concentration at the "core" region of the precipitates increased to ~ 80 at. %. The decrease in number density and coarsening of CRPs can be directly observed from the atom maps in Figure 5-5.

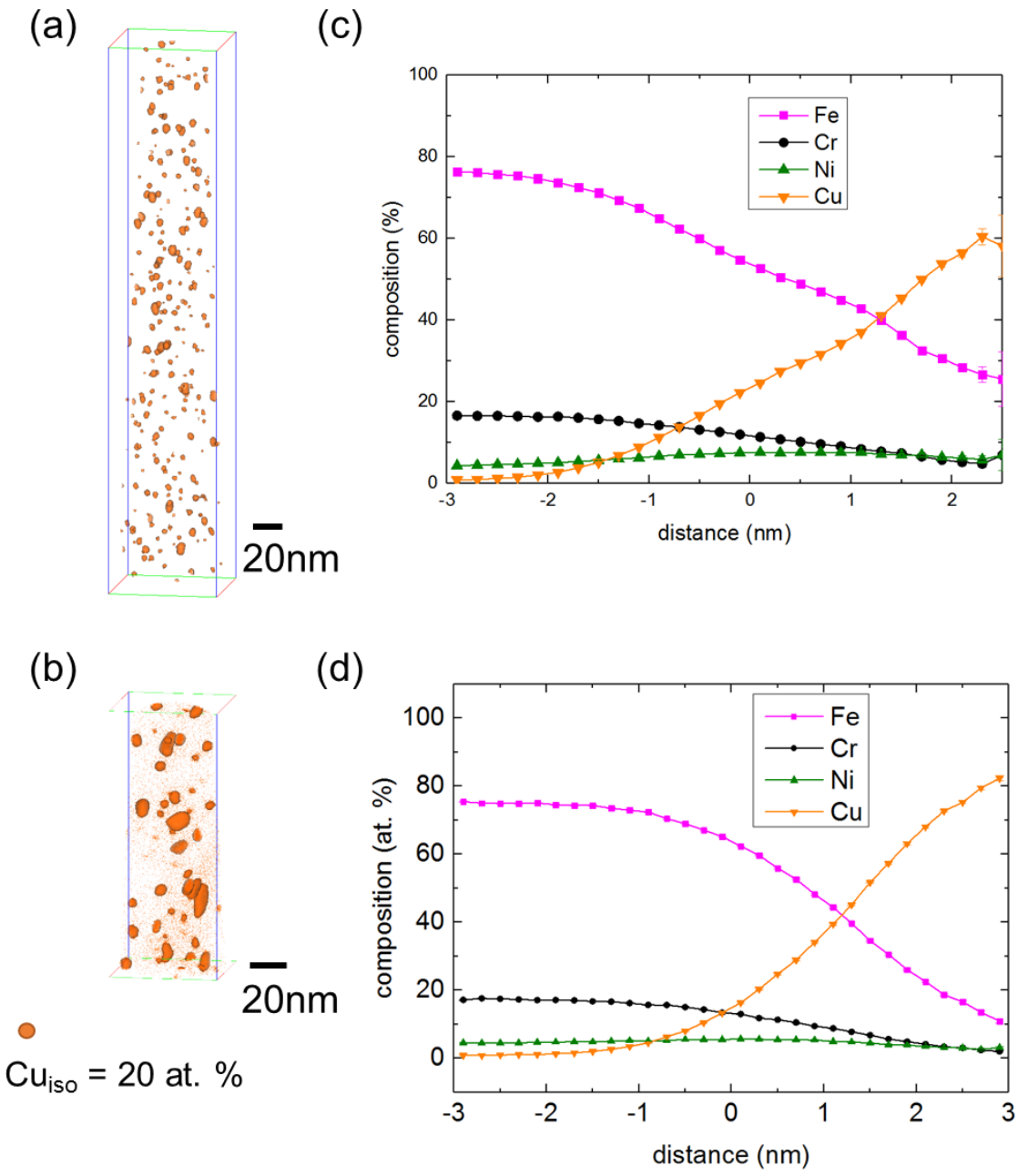

Figure 5-6 Isoconcentration surfaces of 20 at. % Cu concentration after heat treatment at 480 ^{o}C for (a) 2 h (b) 360 h. The corresponding concentration proxigrams plotted from the isoconcentration-surfaces in (a) and (b) are plotted in (c) and (d)

The Ni and Mn are found to co-segregate within the CRPs, as shown in Figure 5-7. Previous studies have shown that Ni and Mn can form a shell around Cu precipitates [154,155]. The atom maps and 2D concentration of Ni in the near vicinity of a CRP is shown in Figure 5-8. A 2 nm slice is taken across the CRP and the colour of each point on

the right side corresponds to the local concentration of Ni surrounding the point. From Figure 5-8, after ageing for 2 h a shell of Ni cannot be directly observed. After 260 h, a shell of Ni can be clearly seen. The segregation of Ni and Mn is attributed to these elements reducing the interfacial energy [156–158].

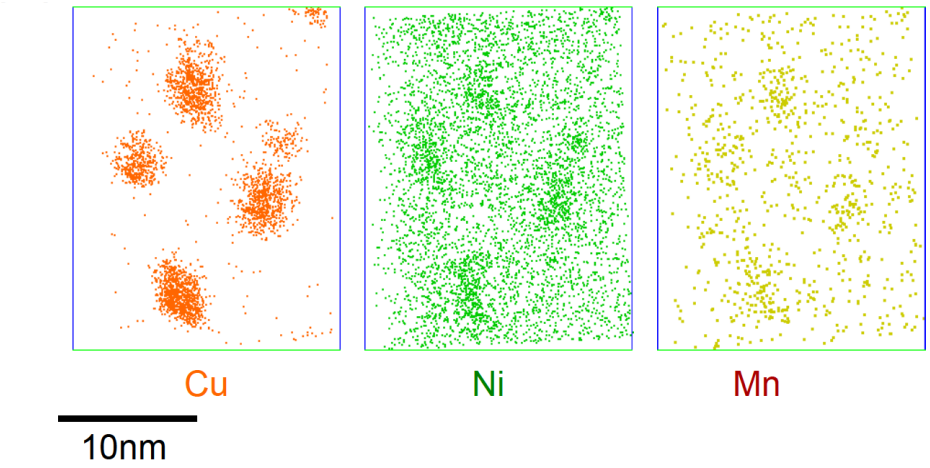

Figure 5-7 5 nm-thick slice taken from the analysis, highlighting the co-segregation of Ni and Mn with Cu. The sample is aged for 2 h at 480 ^{o}C

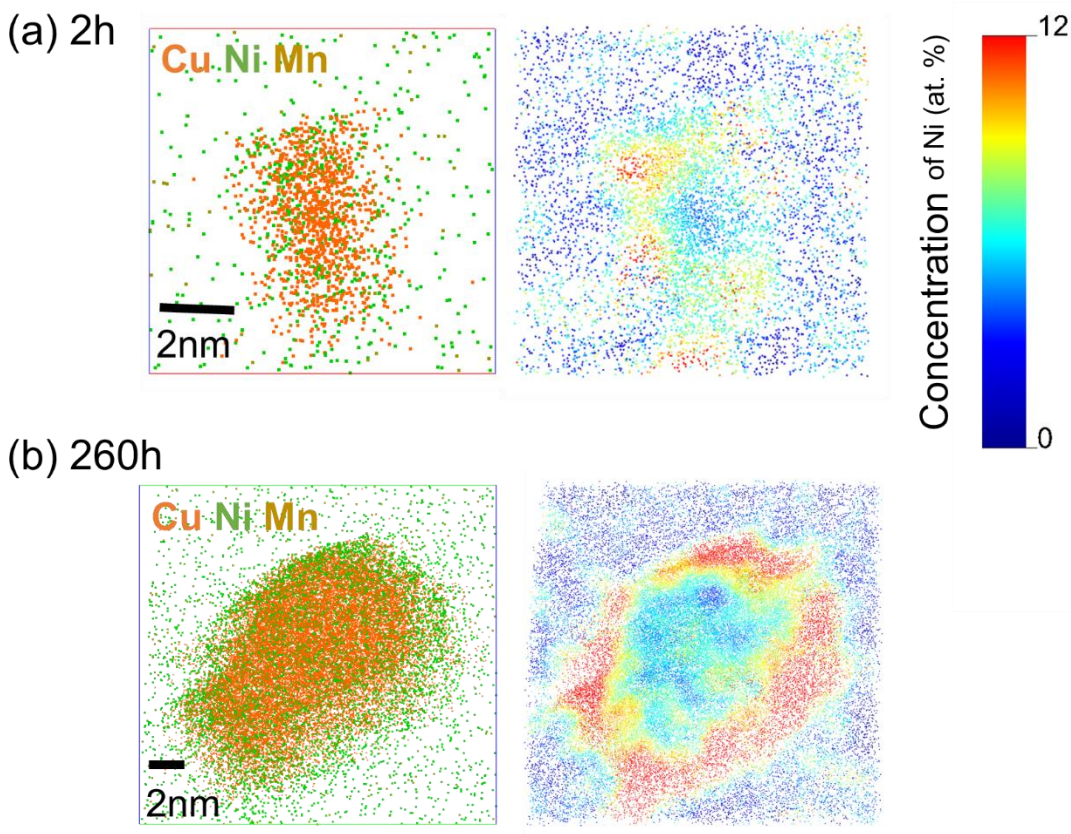

Figure 5-8 Atom maps on the cross section of a CRP and the 2D concentration map of Ni after ageing for (a) 2 h (b) 260 h. The thickness of the slice is 2 nm

5.4.4 Nb-rich precipitates

Nb-rich precipitates are present in all the APT analyses after ageing for 2 h. In order to characterise the composition of the Nb-rich precipitates, the isoconcentration surface of Nb content at 2 at. % is chosen to separate the precipitates from the matrix. As an example, an isoconcentration surface of 2 at. % Nb after ageing for 120 h is shown in Figure 5-9. The measured concentrations of major elements within the isoconcentration surface are listed as a function of ageing time in Table 5-1. In the beginning (2 - 120 h), the precipitates contain about 10 at. % Nb. The Ni content in the precipitates reaches higher levels as the ageing time increases. Cr is also enriched by 1 - 4 at. % in the precipitates. The enrichment factor

of Nb in the precipitates as compared to its concentration in the matrix was the largest for any element. After 260 h, the Nb concentration in the precipitates decreased, as did the levels of Fe and Cr. A significant enrichment of Si and Mn was found in the precipitates. After 360 h, Ni, Mn and Si become the dominant elements in the precipitates, which will be discussed in detail in the following section.

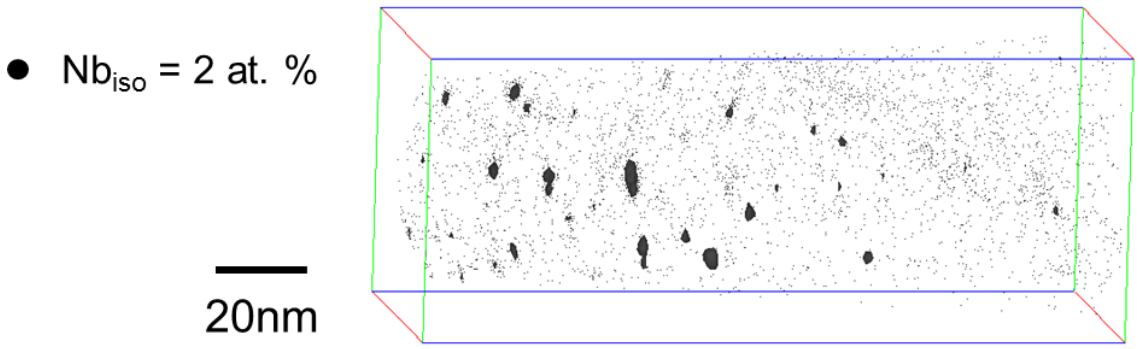

Figure 5-9 Isoconcentration surfaces of 2 at. % Nb concentration after heat treatment at 480 ^{o}C for 120 h

Table 5-1 Concentration of the Nb-rich precipitates after different ageing times at 480 ^{o}C

Ageing time (h)	Concentration (at. %)					
	Nb	Ni	Fe	Cr	Si	Mn
2	10.8±1.0	10.4±1.0	42.7±1.9	20.0±1.6	3.6±1.0	0.9±0.4
24	9.5±0.5	12.1±1.6	56.5±2.4	16.5±1.7	3.1±0.9	0.2±0.2
120	9.5±0.5	17.1±0.9	36.3±1.1	20.2±1.0	6.9±0.6	1.4±0.3
260	7.8±0.1	29.8±0.3	26.0±0.2	14.5±0.2	12.1±0.2	3.9±0.1
360	4.8±0.1	44.9±0.2	9.9±0.1	7.3±0.9	18.4±0.1	10.2±0.1

5.4.5 Spatial correlation between CRPs and Nb-rich precipitates

Figure 5-10 is a 6 nm thick vertical slice taken from the 3D reconstructed image in Figure 5-5 (b), to highlight the spatial correlation between the observed precipitates and the NbN/CrN segregation. CRPs were observed to nucleate both in the matrix and also heterogeneously at crystal defects. The latter, identified by the segregation of NbN/CrN

ions, has been highlighted by the red dashed lines in Figure 5-10. The Nb-rich precipitates were found to form adjacent to CRPs in the matrix, a trend highlighted within the black dashed circles of Figure 5-10. The same phenomenon was also observed in all the other samples aged for longer times. In order to confirm that the Nb-rich precipitates are adjacent to the CPRs, the distance between Nb-rich precipitates and CRPs are analysed as follows: First, the position of each Nb-rich precipitates and CRPs are noted as the centre of the precipitates. The position of the centre is taken as the centre position obtained from the cluster analysis in IVAS. Then the distance from each Nb-rich precipitates to its nearest CPRs have been calculated and denoted as dis_real. The same amount of randomly distributed Nb points were then generated within the analysed volume and the distance from each random Nb point to its nearest CRPs were calculated and denoted as dis_rnd. The schematic of this process is shown in Figure 5-11 (a). The distribution of dis_real and dis_rnd after ageing for 2 h and 24 h is presented in Figure 5-11 (b) and (c), respectively. It is clearly apparent that at both 2 h and 24 h the distribution of dis_real is smaller than that of dis_rnd, indicating that the distance between Nb-rich precipitates and CRPs are much closer than that of random distribution points representing Nb and CRPs.

The diffusion coefficient at 480 ^{o}C of Cu in α-iron is approximately (5 - 6) × 10^{-22} m^2/s according to the equation proposed in [159] and [160], while for Nb in α-iron this is approximately 5.4 × 10^{-23} m^2/s [161], substantially lower than Cu. Thus, it is probable that the CRPs start to nucleate in the matrix prior to the Nb-rich precipitates. The solubility of Nb in Cu is low, so it will be rejected into the matrix as the CRPs grow. Furthermore, the solubility of Nb in matrix Fe is also low, and so it will enrich at the interface between CRPs and the matrix.

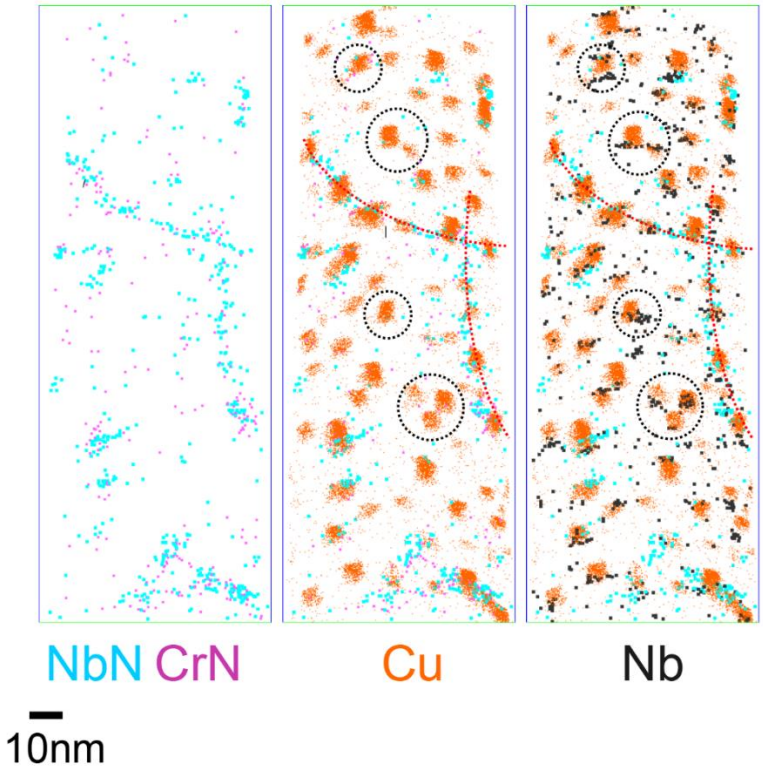

Figure 5-10 6nm-thick slice close-up view of segregation of CrN (pink), NbN (light blue), CRPs (orange) and Nb-rich precipitates (black) showing that CRPs are forming both at the defects (highlighted by red dashed line) and also in the matrix; Nb forms clusters adjacent to CRPs in the matrix (highlighted by black dashed line)

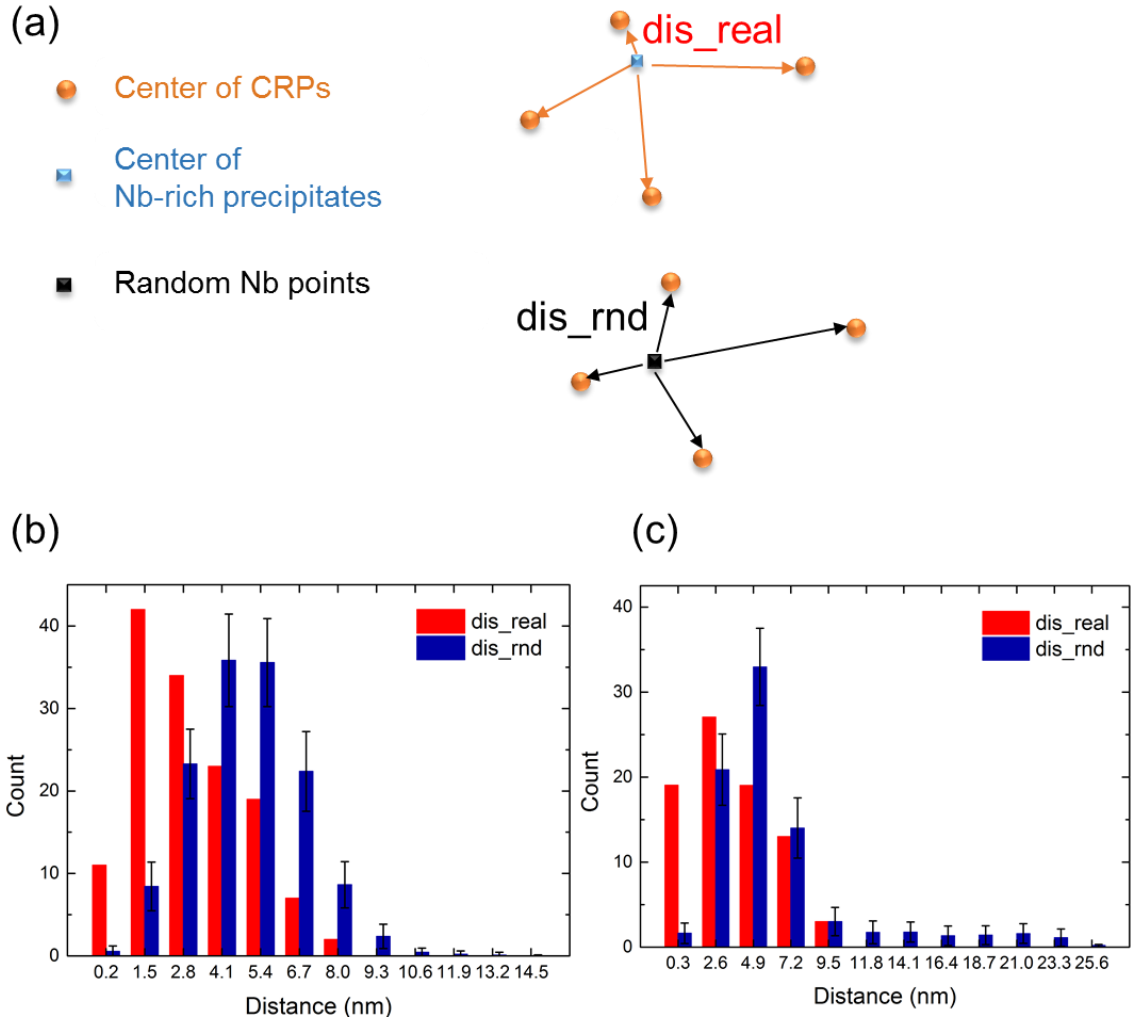

Figure 5-11 (a) Schematic of calculation of dis_real and dis_rnd (b) distribution of dis_real and dis_rnd for 17-4PH after heat treatment at 480 ^{o}C for 2 h (c) distribution of dis_real and dis_rnd for 17-4PH after heat treatment at 480 ^{o}C for 24 h

5.4.6 Cr-rich precipitates

In addition to the CRPs and Nb-rich precipitates, Cr-rich regions are also observed after 120 h. Distinct Cr-rich regions can be seen in the 5 nm thick Cr atom map slice in Figure 5-12. Isoconcentration surfaces for 40 at. % Cr are shown in Figure 5-13 (a) to highlight the Cr-rich regions, which are 1-3 nm in size. A compositional proximity histogram (proxigram) indicating the chemical composition as a function of distance from the Cr-rich region/matrix interface, as defined by these isoconcentration surfaces is shown in Figure

5-13 (b). The average Cr concentration at the core of Cr-rich particles is 70 - 80 at. %, somewhat lower than the estimated value from the phase diagram of 90 - 95 at. % [42]. The reason for this under estimation of Cr is most likely the well-known local magnification effect of APT [65,119,162]. Local magnification effects exist in many alloy systems. In Fe-Cr alloys, Cr has a lower evaporation field than Fe which results in a localised region of lower curvature at the surface of the specimen. The inability to account for this in the reconstruction algorithm causes an erroneous projection of matrix Fe into the precipitates, leading to a lower Cr-content to be measured inside the precipitates. In irradiated Fe-Cr alloys, a lower Cr content has also been found by various APT measurements [163,164]. The second possibility could be a modification of the solubility limit by other alloying elements.

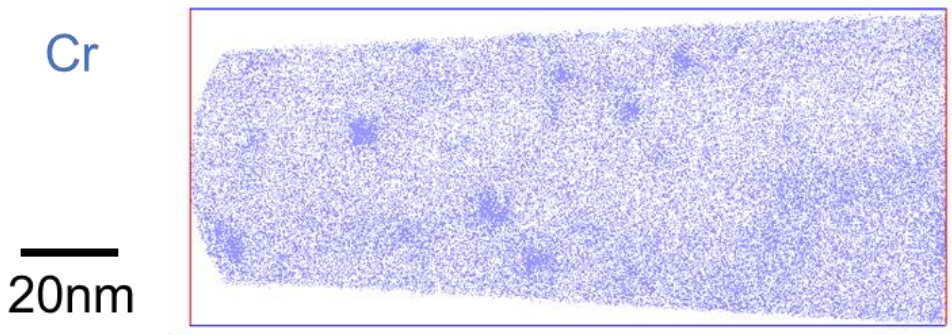

Figure 5-12 5 nm slice taken from the APT reconstruction shown in Figure 5-5 (c) highlighting the clustering of Cr

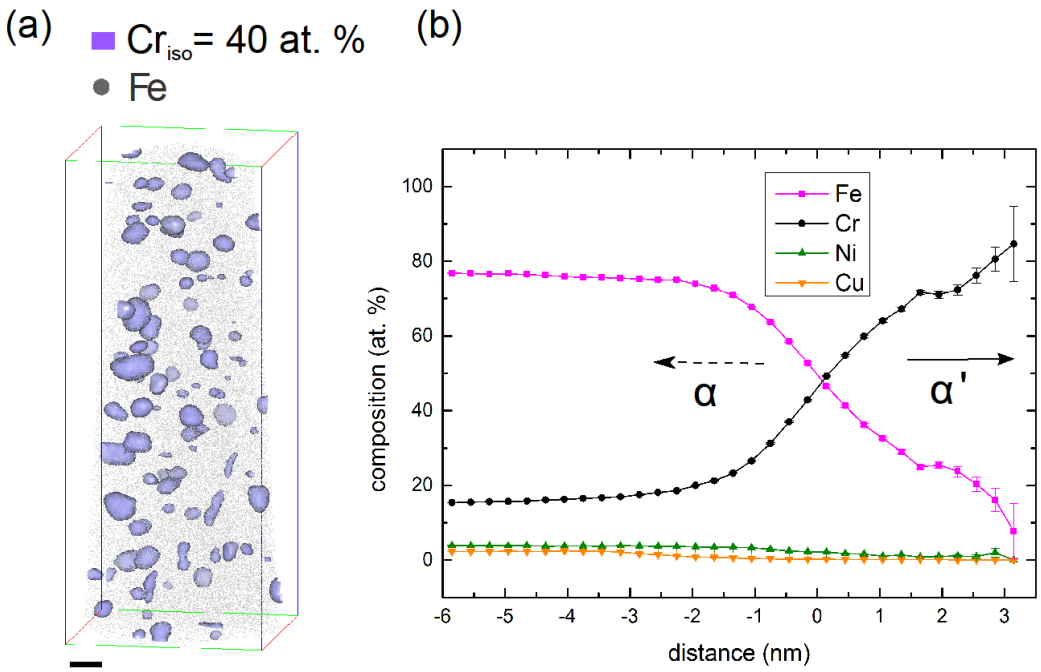

Figure 5-13 (a) Isoconcentration surfaces of 40 at. % Cr concentration. Grey dots represent 0.5% of total Fe atoms; (b) Concentration proxigram plotted from the isoconcentration-surfaces, indicating the average composition of the Cr-rich precipitates

Most of the α' precipitates are observed next to CRPs and Nb-rich precipitates, or else along the regions of NbN and CrN segregation. This is more obvious at longer ageing times, and when a larger number of α' precipitates have formed. Figure 5-14 shows two 5 nm thick slices taken from the APT analysis of a specimen aged for 260 h. Here, the Cr-rich region preferentially forms next to NbN-rich regions (highlighted in red circles) and Nb and Cu precipitates (highlighted in black circles). In 3D, most of the Cr-rich precipitates have nucleated heterogeneously adjacent to previously existing precipitates.

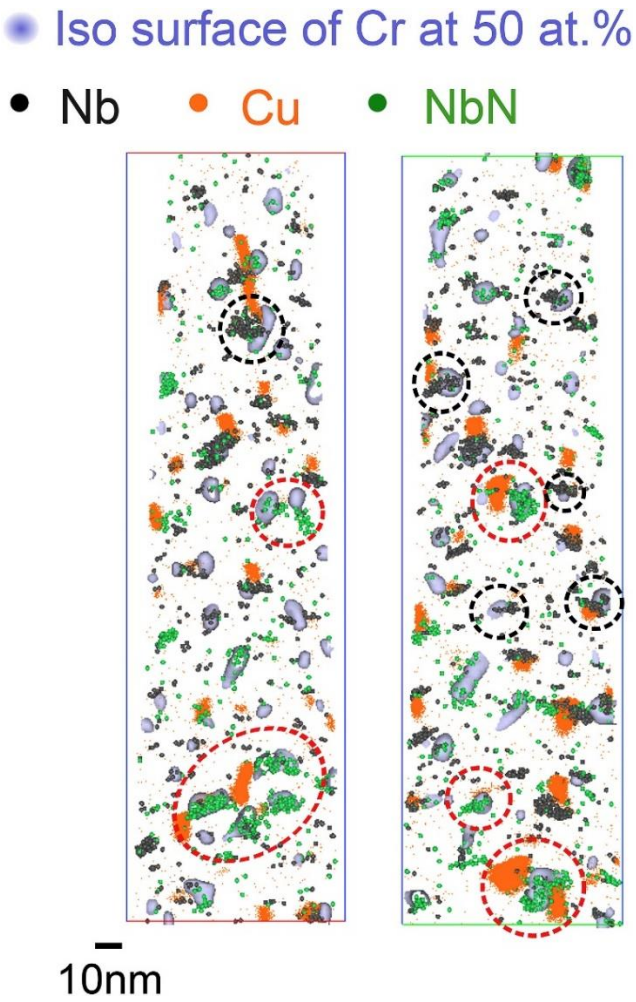

Figure 5-14 5nm slice taken from sample aged for 260 h at 480 ºC, showing the heterogeneous nucleation of Cr-rich α' phase (light blue surfaces)

5.4.7 MNS-rich phase

After 260 h, according to Table 5-1, the composition of the initial Nb-rich precipitates changes progressively with time, the Nb concentration falling and the Mn, Ni, and Si concentrations increasing to a level at which the particles are best described as MNS phase, rather than Nb-rich precipitates. The elemental distributions of Cu, Ni, Mn and Si within two slices of a sample aged for 260 h are shown in Figure 5-15. Here, the Ni and Mn atoms are not only co-segregating with Cu, but also forming discrete MNS precipitates (highlighted with black arrows). In irradiated reactor pressure vessel (RPV) steels, a MNS

phase first appeared as a shell around Cu precipitates to form a core-shell structure. With further ageing, discrete MNS dominant features grew as an appendage to the CRPs, thus the CRPs were considered to act as nucleants for the formation of MNS precipitates [165,166]. Most of the previous observation of such MNS phases were associated with CRPs [48]. Styman et al. [53] also reported the existence of MNS phases at grain boundaries in a long-term thermally aged RPV steel.

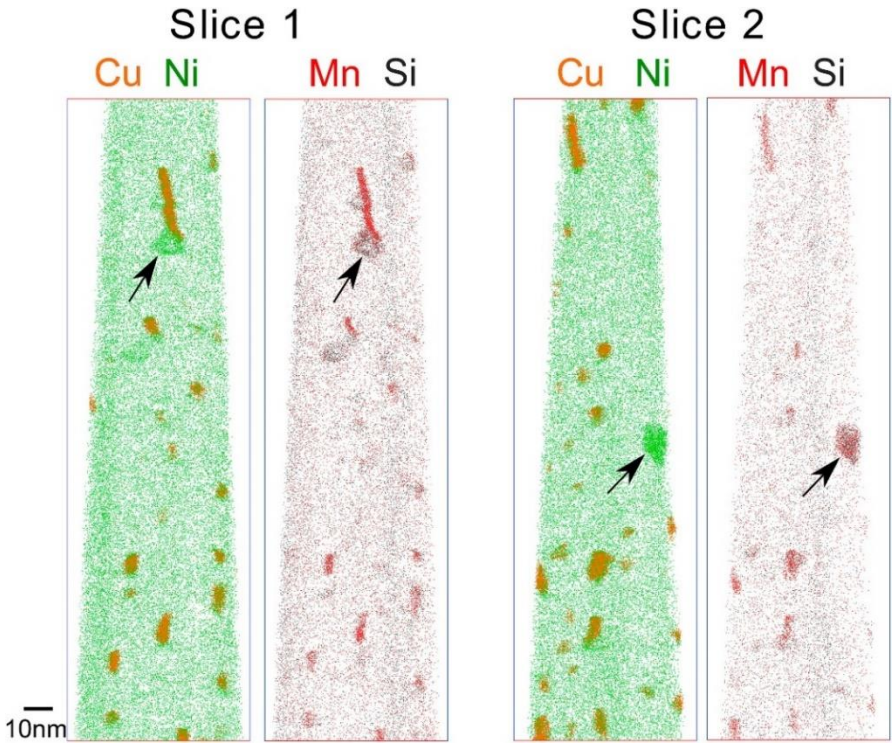

Figure 5-15 Atom maps of Mn, Ni, Si and Cu showing the formation of Mn, Ni, Si enriched phase (arrowed) in a sample aged for 260 h at 480 ^{o}C. The thickness of the slice is 10 nm

In the present study, the majority of the MNS phase was observed to precipitate attached to the CRPs, but not all. Furthermore, as discussed above, the CRPs, Nb-rich precipitates and Cr-rich precipitates all nucleate in close proximity to each other. Thus it is difficult to confirm which of these types of precipitates is primarily responsible for the heterogeneous precipitation of MNS phase or if there are synergistic effects. To investigate this further, examples of close-ups of isoconcentration surfaces where the concentration of Mn + Ni +

Si at 50 at. % (green surfaces), as well as the elemental distribution in the immediate area surrounding these phases are presented in Figure 5-16 (a). This highlights that every MNS enriched precipitate in the APT reconstruction is also enriched in Nb. Two compositional proximity histograms of the precipitates (Isosurface1 and Isosurface2) are shown in Figure 5-16 (b). From this concentration profile, the precipitates are seen to be enriched in Mn, Ni, Si and Nb. Hence in 17-4PH, it is proposed that Nb-rich precipitates have a dominant effect on formation of MNS phase. This can be further confirmed by the first nearest neighbour (1NN) distribution [167] of Ni and Nb as a function of time, as shown in Figure 5-17. Similar Nb-Mn and Nb-Si nearest neighbour distance distributions were also found. Figure 5-17 indicates clustering of Nb-Ni at 260 h and 360 h, when the MNS phase has been observed. At 2 h, there is some non-random distribution of Nb-Ni nearest neighbour distances. This is possibly related to the co-segregation of Ni to CRPs, adjacent to the Nb-rich precipitates, as shown in Figure 5-10. Thus, it is reasonable that some non-randomness should be observed in the Nb-Ni spatial distribution. A plausible formation process of the MNS phase can be proposed as follows: First, Nb-rich precipitates form next to CRPs. The Ni, Mn, Si content in the Nb-rich precipitates increases with ageing time and then the Nb-rich precipitates transform into MNS precipitates. Thus, these MNS precipitates also contain significant amount of Nb.

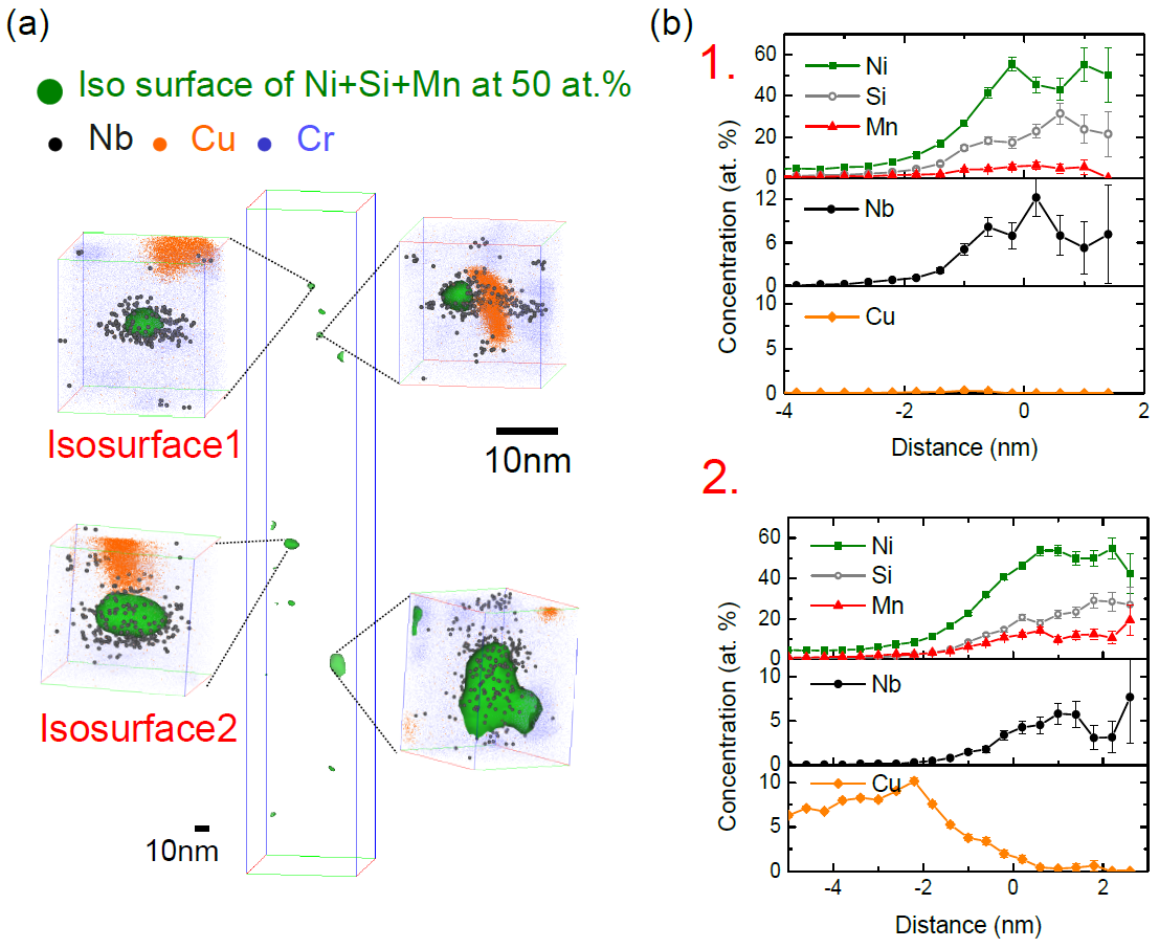

Figure 5-16 (a) Isoconcentration surfaces of Mn + Ni + Si at 50 at. % and atom maps of Nb, Cu and Cr close to these regions in a sample aged for 360h at 480 ºC; (b) Concentration proxigrams of two of the MNS rich precipitates (Isosurface1 and Isosurface2)

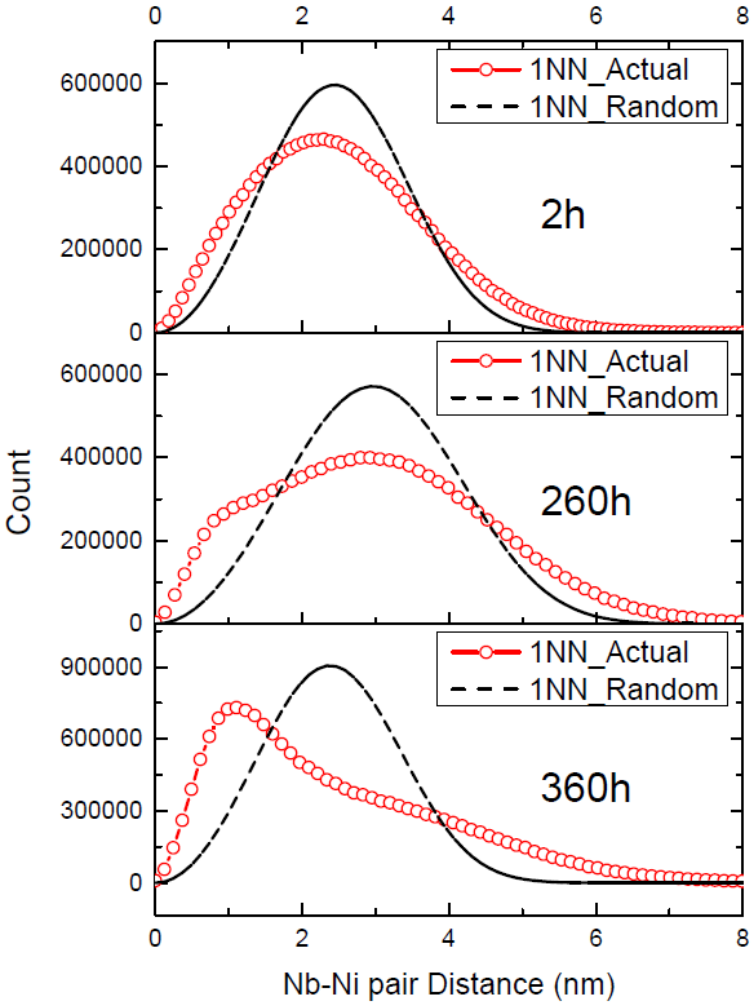

Figure 5-17 First Nb–Ni nearest-neighbour distance distributions in 17-4PH aged at 480 ºC for different heat treatment times

Between 260 h and 360 h of ageing, the MNS enriched phase developed very quickly, increasing to a much larger volume fraction, as shown in Figure 5-18 (a). An isoconcentration surface of Mn, Ni, Si at 50 at. % and the associated compositional proximity histogram at 360h is plotted in Figure 5-18 (b) and Figure 5-18 (c). From Figure 5-18 (c), a steady ratio between Mn:Ni:Si is apparent. The concentration of Mn, Ni, Si is consistent with the theoretical composition of G-phase ($Mn_6Ni_{16}Si_7$), as shown in Table 5-2. The Nb contents in the smaller MNS precipitates are much higher, consistent with the result from 260 h ageing. In the large precipitates, i.e. from Figure 5-18 (c), the Nb concentration

inside the MNS phase is about 1 at. %, which is lower than the value obtained from smaller precipitates, but still substantially higher than that in the matrix. A possible explanation for this is that after MNS phase formation from a small Nb-rich precipitate, the MNS phase grows larger and the limited amount of Nb available can spread throughout the precipitate, resulting in a lower average Nb concentration in the precipitates.

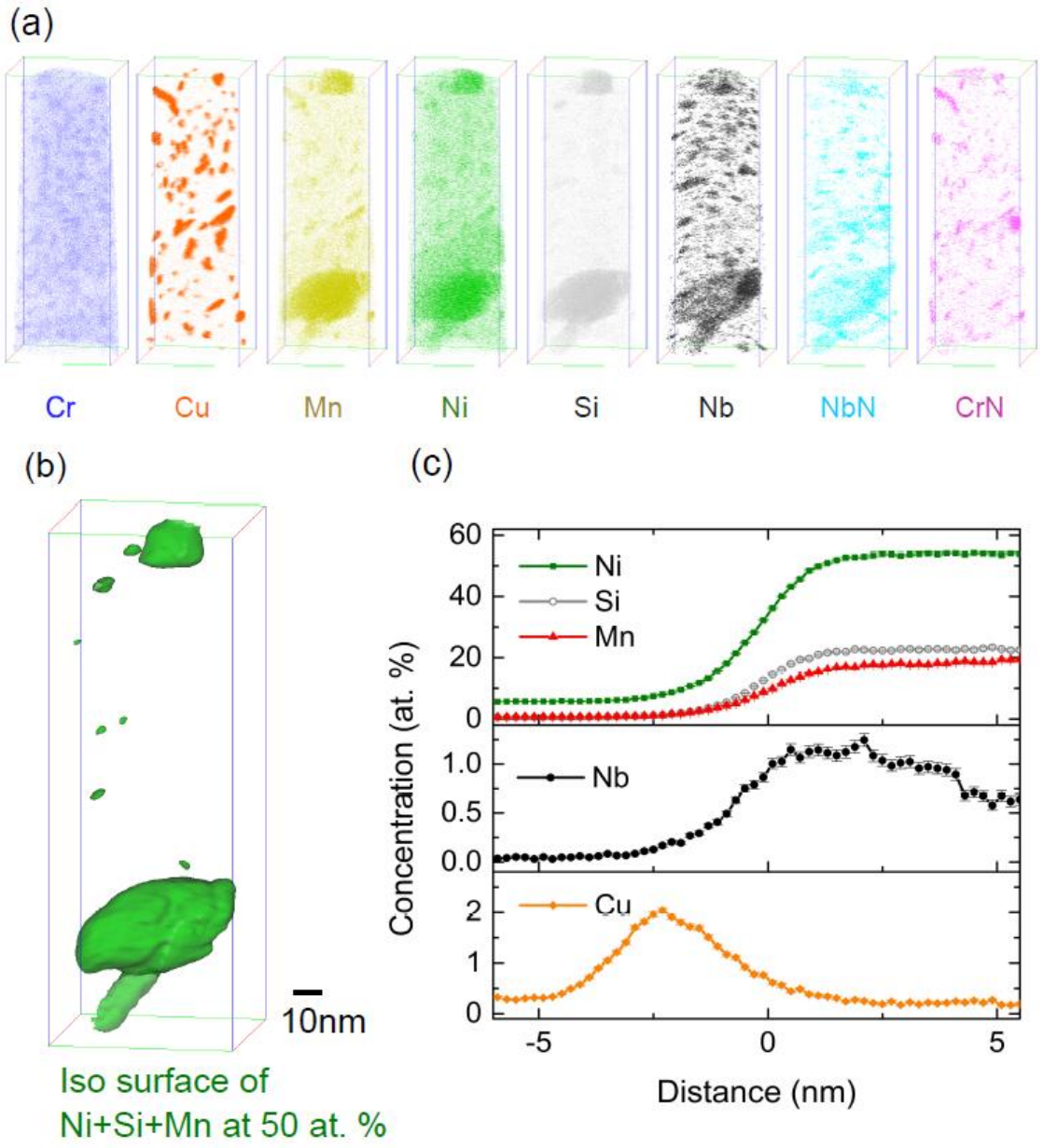

Figure 5-18 (a) Atom maps of 17-4PH heat treated for 360 h at 480 ºC; (b) Isoconcentration-surface at composition of Mn+Ni+Si at 50 at. % after 360 h; (c) Concentration proxigram of the larger precipitates at the bottom of analysis

Table 5-2 Compositions of MNS enriched phase from APT data and G-phase ($Mn_6Ni_{16}Si_7$)

Elements	G-phase (at. %)	Our study (at. %)
Mn	21	17-20
Ni	55	53-55
Si	24	22-24

The question of the thermodynamic stability of MNS precipitates in RPV steels has led to significant debate. Ngayam-Happy et al. [168], using density functional theory (DFT) and Monte Carlo simulations, found that the interaction energy between Ni and Mn is in fact repulsive, and hence rejected the existence of this phase thermodynamically. Bonny et al. [169] used similar methods and concluded that even though the DFT calculation did predict a repulsive interaction between Ni-Mn pairs or triples, larger clusters can be kept together by an attractive binding energy. The presence of Cu was found to extend the temperature range of thermodynamic stability of the precipitates further. A more recent study has predicted that the MNS precipitates can be thermodynamically stable themselves without the presence of Cu under thermal ageing based on CALPHAD modelling [170]. In the current 17-4 PH steel, the Ni and Cu content is much higher than that of RPV steels. Thus it is plausible that MNS precipitates are thermodynamically stable at 480 ^{o}C, even though this is a much higher temperature compared to the studies of RPV steels.

5.5 Microstructural changes after heat treatment at 590 ^{o}C

5.5.1 XRD

The measured XRD patterns from the heat treated 17-4PH steel are displayed in Figure 5-19. The results indicate the existence of a pure BCC structure at up to 2 hours of heat treatment at 590 ^{o}C. After 24 h, 25 % volume fraction of austenite is estimated to have formed.

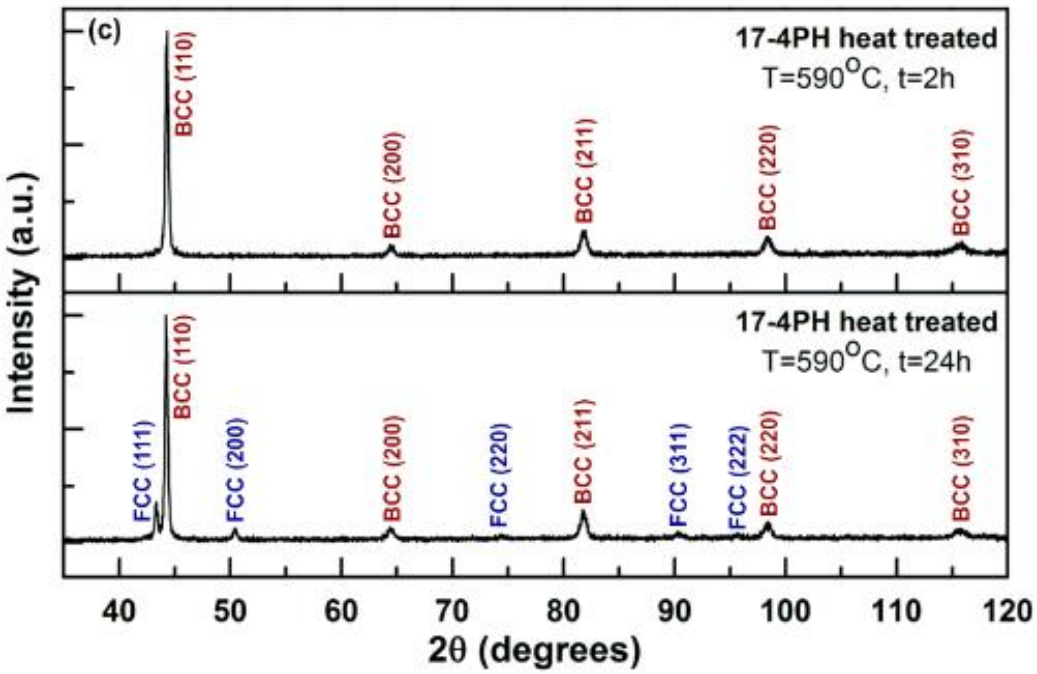

Figure 5-19 XRD patterns for 17-4PH heat treated for 2 h and 24 h at 590 °C

5.5.2 EBSD results

In order to further understand the austenite formation, EBSD measurement has been conducted using a JEOL JSM-6500F. The obtained EBSD maps are shown in Figure 5-20. The austenite fraction was measured to be ~ 26 %, which is consistent with the XRD result (25 % austenite). The austenite form predominantly on the martensite lath boundaries and prior austenite grain boundaries.

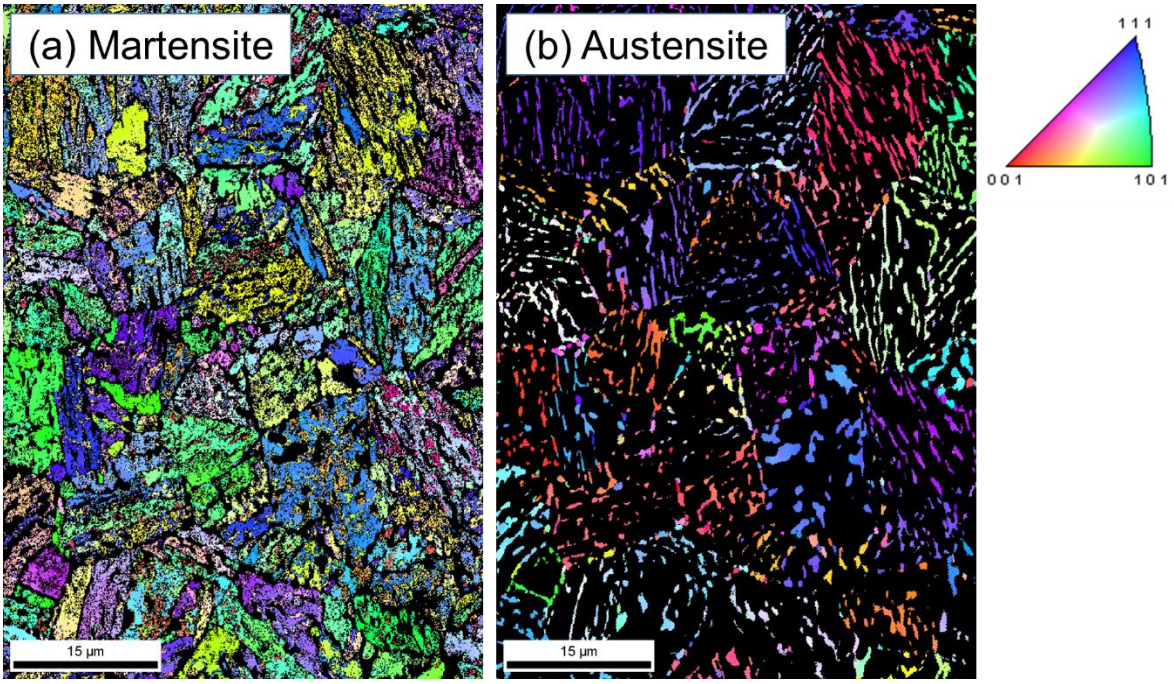

Figure 5-20 (a) IPF (inverse pole figure) of Martensite (b) IPF of Austenite

5.5.3 Atom maps

APT analysis revealed that, heat treatment at 590 ^{o}C for only 20 min is sufficient to produce CRPs, Nb-rich precipitates and NbN/CrN precipitates, as shown in Figure 5-21 (a). One can observe that at this temperature, the distribution of CRPs is less homogeneous than at 480 ^{o}C. Figure 5-21 (b) shows a 6nm slice taken from the same analysis. It can be seen that the majority of the CRPs and Nb-rich precipitates are found along regions of NbN segregation and precipitation. This suggests that in this case the main process is heterogeneous nucleation at dislocations and other matrix defects. At higher temperature, the migration of solutes is accelerated, meaning solutes can more easily diffuse to favorable nucleation sites. Also, from nucleation theory, the nucleation barrier for heterogeneous nucleation is smaller than that of homogeneous nucleation, making heterogeneous nucleation more favorable.

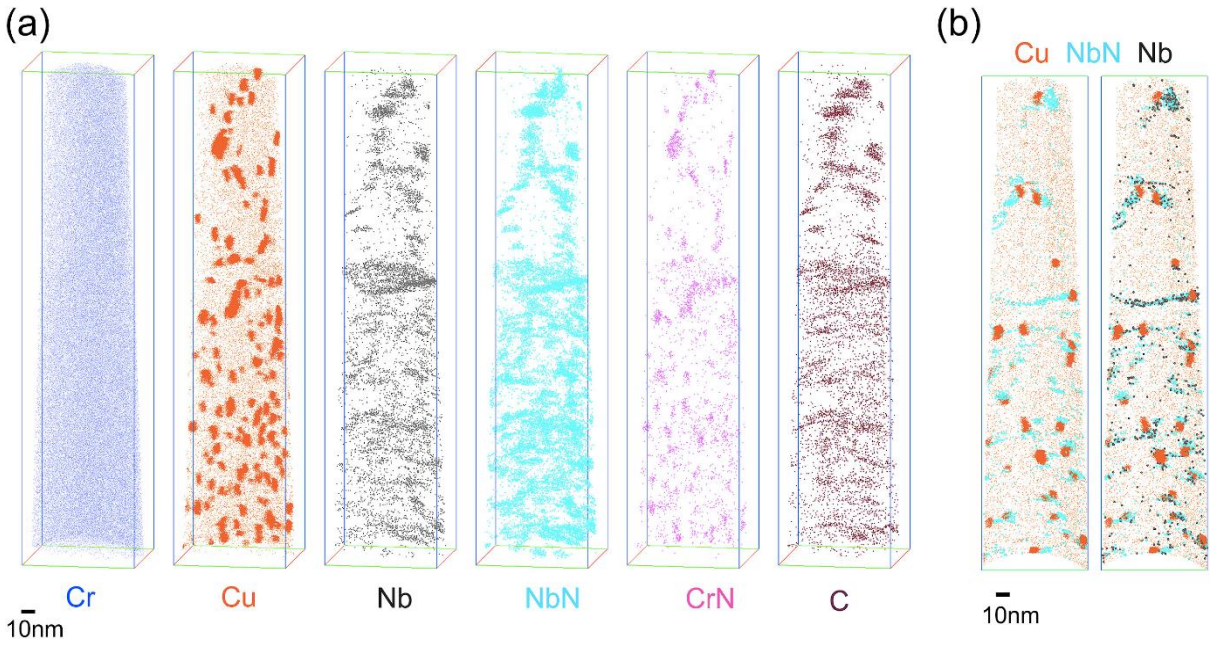

Figure 5-21 (a) Atom maps of 17-4PH heat treated for 20 min at 590 °C; (b) 6 nm-thick slice taken from the analysis, highlighting segregation of Cu and Nb at the NbN segregation (indicating dislocation and matrix defects).

Figure 5-22 shows the elemental distribution after 24 h at 590 ^{o}C. The CRPs have now coarsened to larger sizes, i.e. several tens of nm. However, no Cr-rich precipitates were present at this temperature. From the Fe-Cr phase diagram, the Cr content is within the solubility limit at 590 ^{o}C (863 K), which can explain the absence of Cr-rich precipitates.

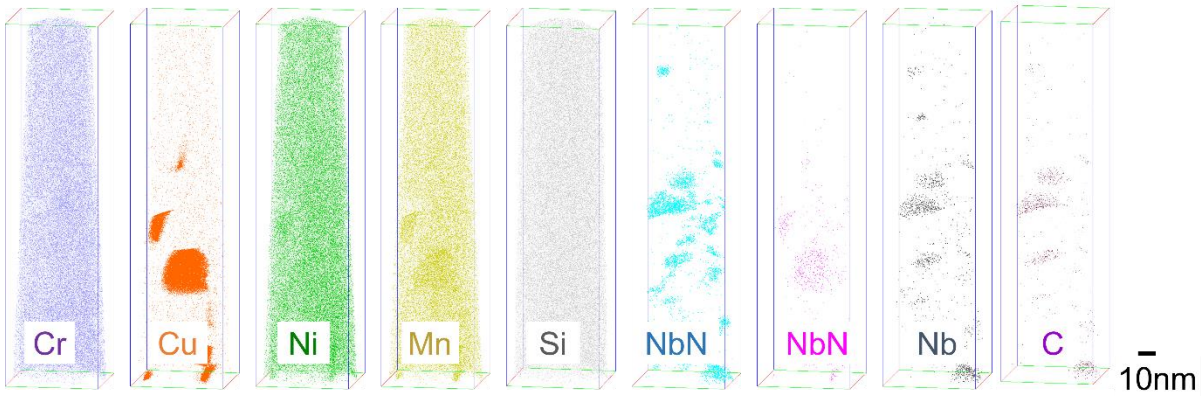

Figure 5-22 Atom maps of 17-4PH heat treated for 24 h at 590 °C.

5.6 Number density and volume fraction of CRPs and Cr-rich precipitates

The number density, volume fraction and mean radius of the CRPs and Cr-rich precipitates were quantified using the methods described in Chapter 4. Figure 5-23 shows the development of CRPs and Cr-rich precipitates in terms of number density (N) and average radius ($< r >$) as a function of time at both temperatures. From § 4.4.3, the number of clusters identified in the analysed volume is dependent on the selection of D_{max} value. The D_{max} value is selected manually based on the criteria of not combing precipitates together nor splitting them. The error of the number density is the standard error after averaging the number density obtained from the application of D_{max}, (D_{max} - 0.1 nm) and (D_{max} + 0.1 nm). The value 0.1 nm is chosen because in most cases the uncertainty in choosing D_{max} is within ± 0.1 nm. The error of the mean radius is the standard error after averaging the size of each precipitate population. Table 5-3 lists the volume fraction of the CRPs (f_{Cu}) and Cr-rich precipitates (f_{Cr}) across all ageing times and temperatures. The C_{Cu} and C_{Cr} values denote the overall concentration of Cu or Cr in the analysed volume.

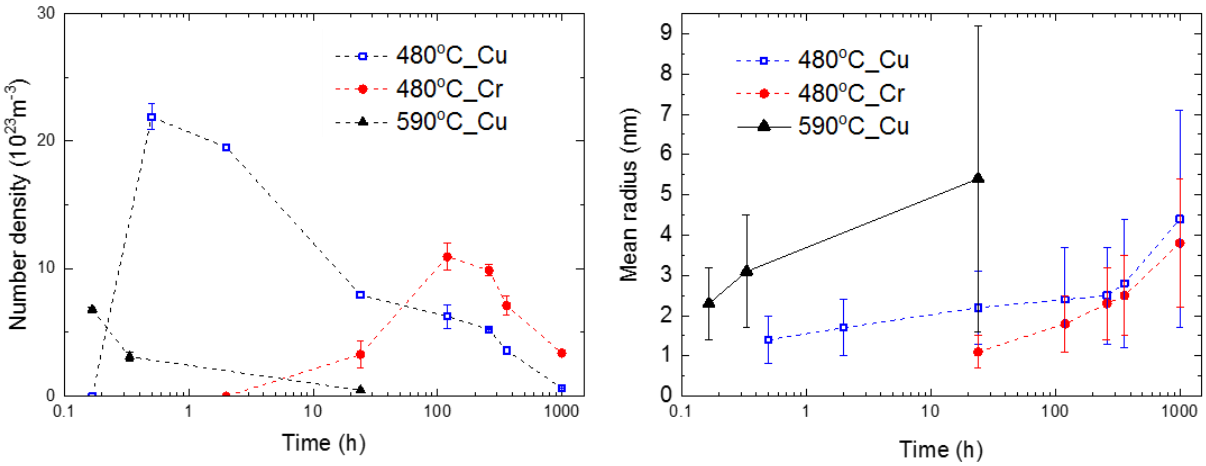

Figure 5-23 Number density and mean radius of CRPs and Cr-rich precipitates

Table 5-3 Volume fraction of CRPs and Cr-rich precipitates. The values of f_{Cu} and f_{Cr} represent the volume fraction of CRPs and Cr-rich precipitates, respectively, and C_{Cu} and C_{Cr} are the overall concentration of Cu and Cr in the sample

	480 °C							590 °C		
Time	30min	2h	24h	120h	260h	360h	1000h	10min	20min	24h
f_{Cu} (at.%)	2.48	2.34	2.07	2.39	2.34	2.39	1.83	1.89	2.06	2.72
	±0.03	±0.01	±0.01	±0.06	±0.00	±0.01	±0.00	±0.01	±0.01	±0.00
C_{Cu} (at.%)	2.53	2.35	2.08	2.39	2.35	2.40	1.84	1.93	2.19	2.93
f_{Cr} (at.%)	-	-	0.13	1.38	2.83	2.43	4.33	-	-	-
			±0.06	±0.22	±0.31	±0.24	±0.26			
C_{Cr} (at.%)	16.6	16.8	16.9	16.8	16.6	15.8	17.0	16.8	16.7	17.0

5.6.1 CRPs

According to Figure 5-23, at both temperatures the number density of CRPs increases at the early stage of heat treatment then decreases strongly with annealing time. This is offset by a continuous growth of the average precipitate radius throughout the annealing time. Table 5-3 indicates that the change in the volume fraction of CRPs (f_{Cu}) is quite small after the precipitates form. It can be noted that even the slight fluctuation of volume fraction is actually related to the difference in the overall Cu concentration (C_{Cu}) within different micro-volumes sampled by the APT experiment. Thus, it can be inferred that CRPs have reached a maximum number density and volume fraction within 30 min at 480 °C or 10min at 590 °C. Then, the existing smaller CRPs coarsen upon prolonged ageing, leading to a decrease in number density. Also the peak number density at 480 °C is much higher and the growth is much slower than that at 590 °C.

5.6.2 Cr-rich precipitates

According to Figure 5-23, at 480 °C the number density of Cr-rich precipitates starts to increase after 24 h, reaching a peak number density at about 120 h before dropping. Throughout this time the volume fraction and the mean radius of precipitates continuously

increase. The process can be described as: 24 – 120 h is the initial nucleation and growth stage, during which more precipitates form, but at the same time solutes also diffuse to existing precipitates, thus increasing their size. From 260 – 1000 h, the number density decreases while the volume fraction and mean radius of precipitates increase, indicating a growth and coarsening stage free of further nucleation but with more solute atom precipitating out from the matrix to existing precipitates.

5.7 Precipitation hardening effects

Upon thermal ageing of 17-4PH steels, CRPs, Nb-rich precipitates, Cr-rich precipitates and MNS precipitates have been observed. The contributions by these features are thought to increase the hardness. The number density of MNS precipitates are much lower and the size of MNS precipitates are much larger compared to other precipitates. Thus, for the following calculations their effect on hardness is considered to be negligible. The CRPs and Cr-rich precipitates are considered to be the main hardening precipitates. An estimation of the effect of CRPs and Cr-rich precipitates on yield strength is provided here and compared with the experimental yield strength increase measured from Vickers hardness tests.

- Contribution of CRPs to hardness

It is known that the CRPs are attractive particles for dislocations with a smaller modulus compared to the matrix, thus the Russell-Brown model is appropriate to estimate the strengthening contribution of CRPs. From the difference in the modulus between CRPs and matrix, the increase in shear strength can be calculated by [68,171,172]:

$$\Delta\tau(\mathrm{Cu}) = \frac{\alpha G b \sqrt{f_{\mathrm{Cu}}}}{1.77 < r >} \qquad 5\text{-}1$$

where α represents the strength of precipitates, *G* is the shear modulus of the matrix (83GPa from [171]), and *b* is Burgers vector (0.25nm for iron). For precipitates within a radius of 0.6nm-10nm, α varies between 0.2-0.4 [68,171]. Here, a common value 0.2 is used. Smaller precipitates represent weaker obstacles. Thus, there will be an over-estimation of the effects of smaller precipitates and under-estimation of larger precipitates. The volume fraction, *f*, and the mean radius, $< r >$, are those obtained experimentally from APT and presented in Table 5-3.

After solution treatment, Cu atoms are supersaturated in the matrix. Upon thermal ageing, nearly all of the Cu becomes incorporated into precipitates. Hence, the solute solution strengthening contribution from Cu after 30min should be negligible. The final expression of estimated increase in yield strength due to CRPs is then:

$$\Delta\sigma(\mathrm{Cu}) = \mathrm{T}\Delta\tau(\mathrm{Cu}) - \sigma^{\mathrm{o}}_{\mathrm{Cu}} = \mathrm{T}\frac{\alpha G b\sqrt{f_{\mathrm{Cu}}}}{1.77 < r >} - \sigma^{\mathrm{o}}_{\mathrm{Cu}} \qquad 5\text{-}2$$

where T is the Taylor factor, (2.5), σ^{o}_{Cu} refers to the Cu solute solution strengthening at solution treatment condition, estimated to be 30 MPa according to [173]. From equation 5-2, the yield strength increase is proportional to the square root of the volume fraction and varies inversely with the mean precipitates radius. From Table 5-3, the volume fraction of CRPs is steady after their formation, but the mean radius increases with ageing time. The effect of the coarsening of the CRPs on hardening should therefore be a monotonic decrease, which is not consistent with the observed steady hardness as a function of treatment time at 480 ^{o}C in Figure 5-3.

- Contribution of Cr-rich precipitates on hardness

Compared to the CRPs, the shear modulus of Cr-rich precipitates is higher than that of the Fe-rich matrix, thus the dislocation interaction is repulsive. The atomistic simulation developed by Terentyev et al [174] suggests that Cr-rich precipitates will be sheared and not bypassed. It is proposed that the increase in strength can be determined from the sum of modulus misfit strengthening (MMS) and chemical strengthening (CS). First consider the MMS model. Since the Cr-rich precipitates are of higher shear modulus, the Russell-Brown type model does not apply. Instead an expression previously utilised in [174] and [175] is employed, derived from a regular array of precipitates:

$$\Delta\tau_{MMS}(\mathrm{Cr}) = \frac{\Delta G}{4\pi^2}\left(\frac{3\Delta G}{Gb}\right)\left[0.8 - 0.143\ln(< r > /b)\right]^{3/2} r^{1/2} f^{1/2} \qquad 5\text{-}3$$

where ΔG is the difference of modulus between Fe and Cr which was taken to be 33 GPa [174]. Next, we consider the CS model. The yield stress increment due to the surface area increase when a dislocation passes through a coherent precipitate can be obtained from [175]:

$$\Delta\tau_{CS}(\mathrm{Cr}) = 2(3/\pi)^{1/2} G(\sigma_S / Gb)^{3/2} (b/< r >)^{1/2} f^{1/2} \qquad 5\text{-}4$$

where σ_s is the energy per surface area, which was taken as 0.4 according to Schwen et al. [176]. Considering the relation of yield strength and shear stress, the increase in yield strength from Cr is then:

$$\Delta\tau(\mathrm{Cr}) = T\left[\Delta\tau_{MMS}(\mathrm{Cr}) + \Delta\tau_{CS}(\mathrm{Cr})\right] \qquad 5\text{-}5$$

A comparison between the estimated theoretical strength increase and experimental measured strengthening from CRPs and Cr-rich precipitates is presented in Figure 5-24. The experimentally observed strength increase is obtained from the relationship between strength and hardness [45]. It should be noted that the interactions between different precipitates have not been considered here. Thus, the figure should be treated as an illustration of the counterbalancing effects from CRPs and Cr-rich precipitates. The number should be taken as an estimate. From Figure 5-24 at 480 ^{o}C, the calculated hardening effects of CRPs decrease with ageing time throughout the ageing time. This is related to the continuous coarsening of CRPs. The hardening from Cr-rich precipitates contributes significantly to the overall strength after 24 h and this continues to increase up to the longest characterised annealing time of 1000 h. Notably, the contribution from Cr-rich precipitates compensates for the decrease in strength arising from the coarsening of the CRPs. It is proposed that this counterbalancing effect explains the steady hardness curve observed for precipitation hardening at 480 ^{o}C up to 360 h. At 1000 h, the estimated contributions from CRPs and Cr-rich precipitates were effectively comparable.

At 590 ^{o}C, there is no strengthening from Cr-rich precipitates. Consistent with experimental results, the estimated strengthening from CRPs showed a monotonic decrease with ageing time. However, the estimated strength is higher than the experimental value. The most plausible reason for this is that at 590 ^{o}C, partial reversion to austenite occurs according to the XRD results. The hardness of austenite is substantially lower than that of martensite [177]. Also at higher temperature, matrix grain growth is faster than at lower temperature. Dislocations can be removed faster at higher annealing temperature. Thus, a softening of the matrix is expected, which is not considered in the current calculation of the precipitation hardening.

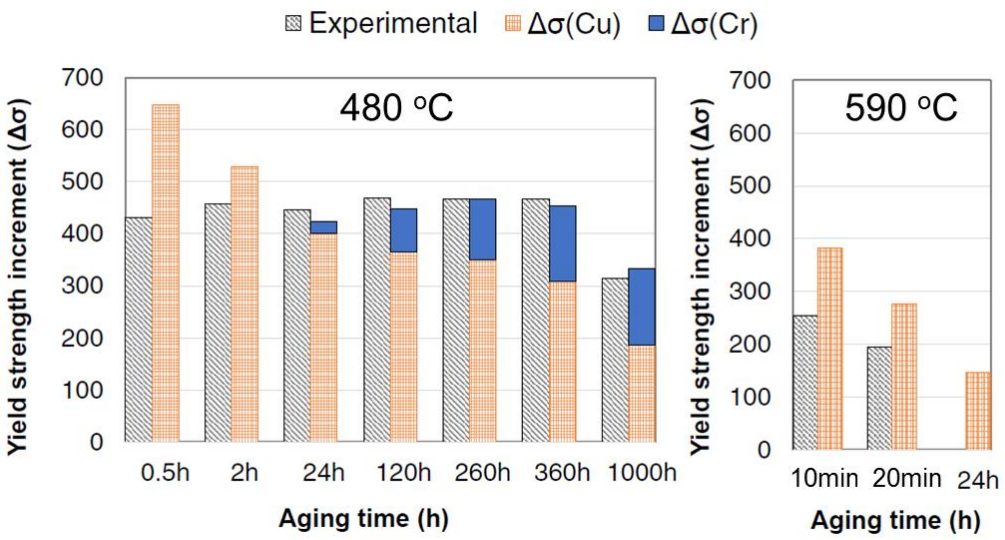

Figure 5-24 Comparison between yield strength increases derived from hardness (black diagonal) and theoretical increase due to CRPs (orange grid) and Cr-rich precipitates (blue solid)

5.8 Summary

In this study, a 17-4PH steel was heat treated at two precipitation hardening temperatures (480 °C and 590 °C). Atom probe tomography has offered insights into the precipitation sequence in this steel. The following conclusions can be drawn:

- At 480 °C, the precipitation sequence can be summarized as: segregation of CrN/NbN to dislocation and matrix defects → CRPs and Nb-rich precipitates → Cr-rich precipitates → MNS phase.
- The initially nucleated precipitates act as favoured sites for heterogeneous nucleation of subsequent phases. MNS phase precipitates were transformed from Nb-rich precipitates.
- At 590 °C, no Cr-rich precipitates or MNS phase were present, consistent with the prediction from the phase diagram.

- The development of CRPs and Cr-rich precipitates (at 480 ^{o}C) in terms of number density, volume fraction has been characterized. The CRPs were in a growth and coarsening stage for most of the conditions examined. However, an increase in number density and volume fraction of Cr-rich precipitates indicated that a nucleation stage was also observed from 24-120 h at 480 ^{o}C.
- The hardening from CRPs was estimated to decrease at both temperatures as a function of ageing time due to over-ageing. However, at 480 ^{o}C, the increasing contribution from Cr-rich precipitates largely compensate for the decreasing contribution from CRPs.

6 Effects of single ion beam irradiation on T91 steels

6.1 Introduction

Understanding the microstructural changes of T91 steel after ion irradiation is one of the key aims of the study. In this chapter T91 steel is subjected to single ion beam (SI) irradiation and the resulting microstructure is compared to those of non-irradiated materials. The details of the SI irradiation conditions are discussed in § 3.2.

6.2 SEM characterisation of T91 after heat treatment and irradiation

SEM images of T91 steel before and after irradiation, respectively, are shown in Figure 6-1. In this figure, (a) and (b) are taken from different unirradiated regions. The sample is subjected to the same heat treatment as the irradiated counterparts. The decoration of particles on the grain boundary is observed in both unirradiated and irradiated conditions. These particles are known to be pre-existing carbides/nitrides [84,178–180]. From direct observation, an increase in grain boundary coverage of particles is apparent after irradiation.

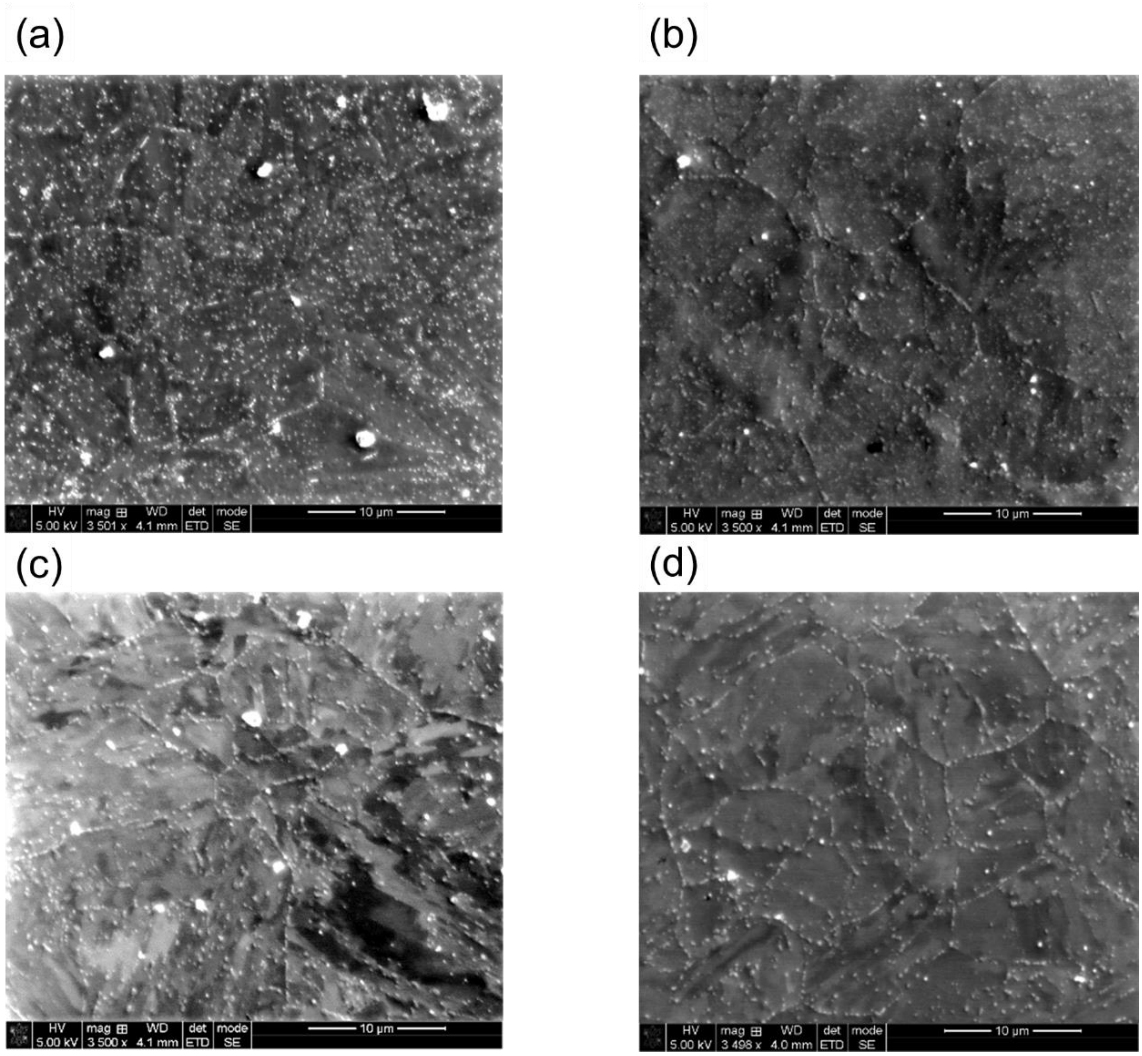

Figure 6-1 SEM images of T91 (a) and (b) heat treated at 470 ^{o}C (c) SI irradiated to 1 dpa at 470 ^{o}C (d) SI irradiated to 10 dpa at 470 ^{o}C

6.3 Microstructure of non-irradiated T91

6.3.1 As received T91

Three tip-shaped specimens of as-received T91 steel have been prepared and analyzed using the procedure described in §3.1 and § 3.5. The composition of the as-received T91 has been discussed in § 3.1.

Atom maps of individual elements from Tip 1 are shown in Figure 6-2. Precipitates enriched with V, VN, CrN, FeN and CrC ions are observed. N is mostly observed in the form of VN^{+}. An iso-surface defined by 2 at. % V is drawn in Figure 6-3 (a). Four compositional proxigrams extracted from each isosurface indicated by the black arrows are presented in Figure 6-3 (b) to (e). The composition of the precipitates are similar in (b), (c) and (e). An enrichment of Cr from 7.5 at. % (overall Cr in the analysed volume) to 20 at. %, V from 0.1 to 40 at. %, and N from approximately 0 to 30 at. % is observed. The composition of particle in (d) is slightly different. Still, the enrichment of V and Cr is observed. However it should be noted that in APT measurements the observed N contents could be reduced due to the fast surface migration of N atoms as well as the overlap of N^{+} and Si^{2+} peak in the mass spectrum. As shown in Figure 6-4, V, Cr and Fe enriched nitrides are also observed in Tip 2. Thus, the microstructure of the as-received T91 steel can be described by a matrix decorated with V, Cr enriched nitride particles. Other elements are homogenously distributed in the matrix.

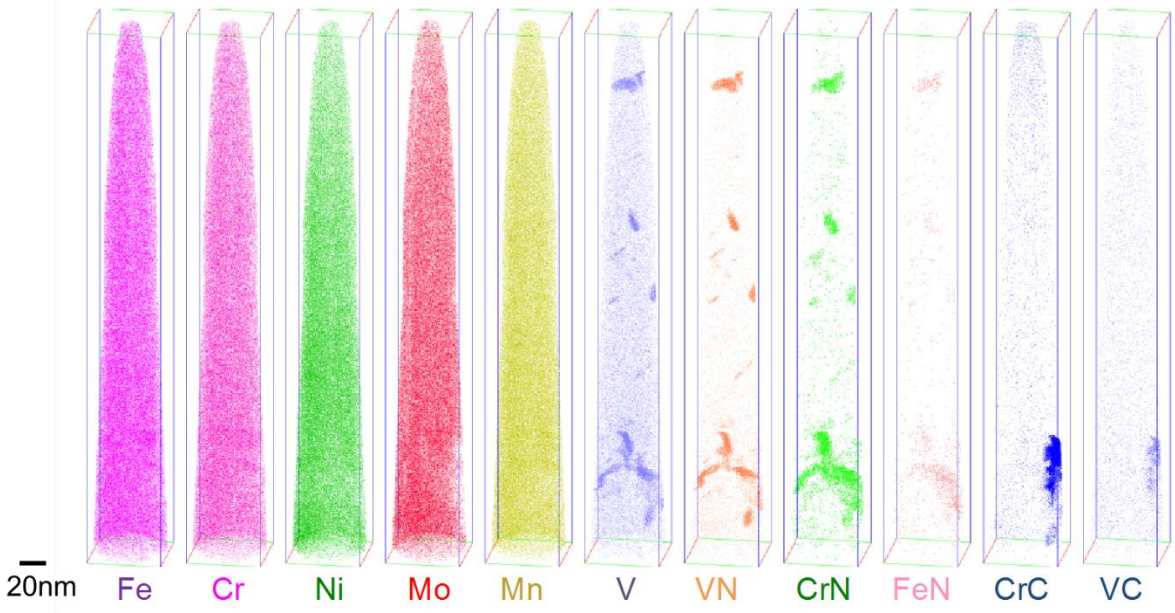

Figure 6-2 Atom maps of individual elements and nitrides, carbides ions in as-received T91 (Tip 1)

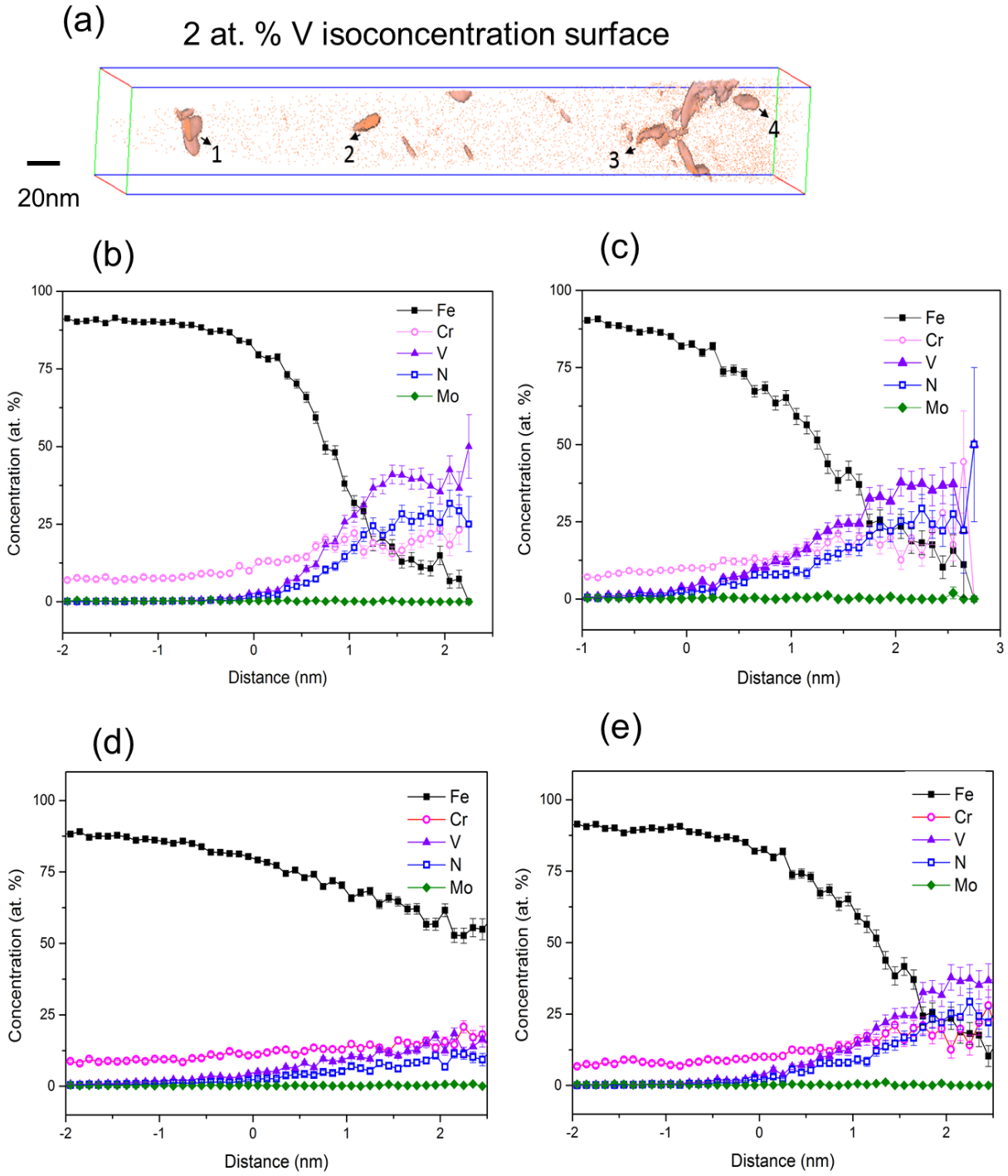

Figure 6-3 (a) 2 at % iso surface of V content in unirradiated T91 specimen (Tip 1). (b), (c), (d) and (e) are proxigrams plotted from interface 1, 2, 3 and 4, complex ions are decomposed into individual elements

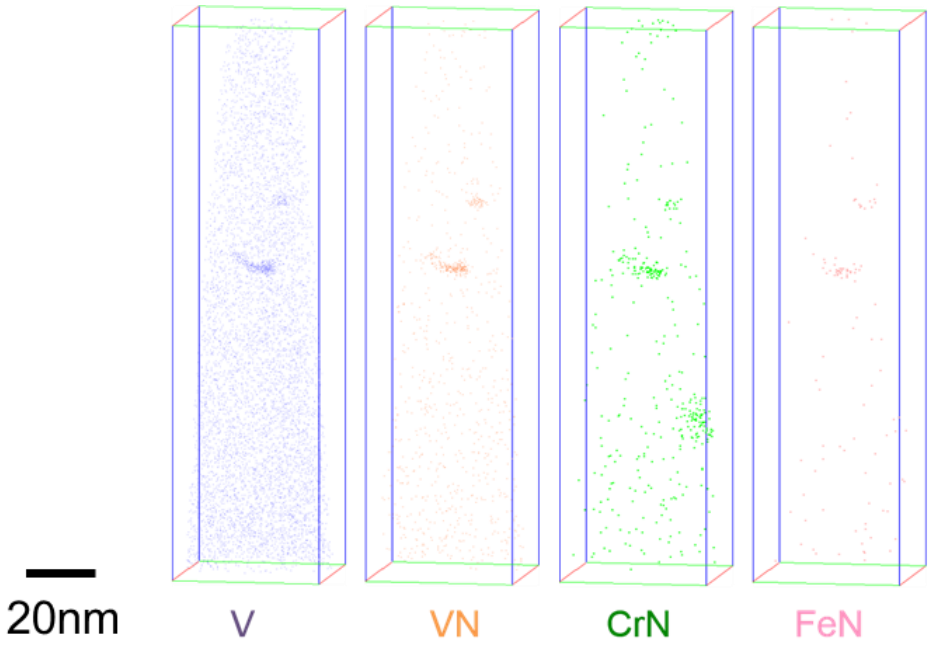

Figure 6-4 APT atom maps containing nitride precipitates in unirradiated T91 (Tip 2)

In Tip 3 of the unirradiated T91, two grain boundaries were observed. The V, VN and C segregation to grain boundaries is apparent in Figure 6-5 (a). 1D composition profiles across the grain boundaries are plotted in Figure 6-5 (b) and (c), respectively. From these 1D composition profiles, an enrichment of Cr at the grain boundaries is observed. Other elements (i.e. Ni, Mo, Mn, Si, V and C) are also found to be enriched at the grain boundaries. Unlike Tip1 and Tip 2, nitride precipitates were not observed in this Tip 3.

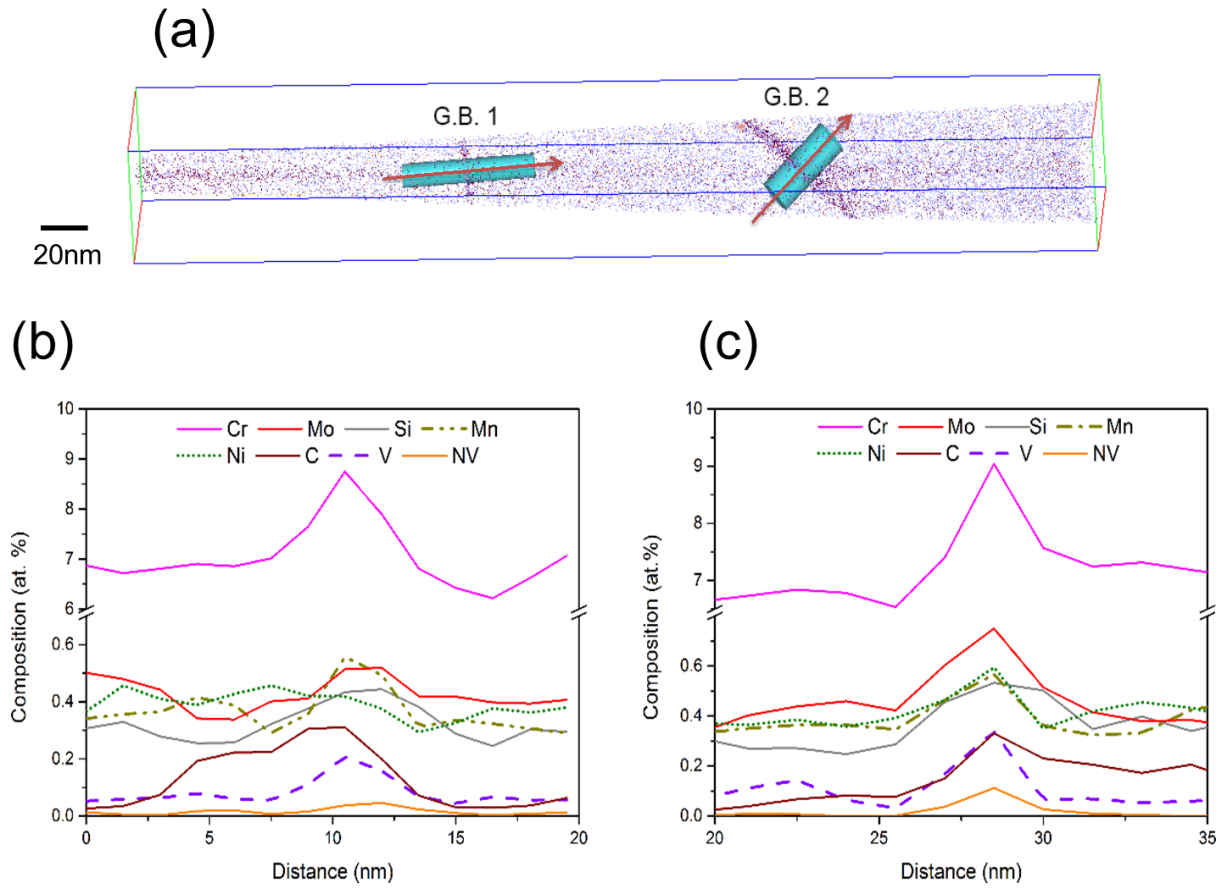

Figure 6-5 (a) Atom maps of V (blue), VN (orange) and C (brown) segregation on grain boundaries in as-received T91 (Tip 3). 1D concentration profiles (bin width is 1.5 nm) perpendicular to GB 1 (b) and GB 2 (c) in as-received T91

6.3.2 T91 steel heat treated at 470 ºC

Two tips from the non-irradiated region of T91, but subjected to the same heat treatment level at (470 ºC) as the irradiated region were analysed. A typical set of atom maps at this condition is shown in Figure 6-6. A large Cr and Mo enriched carbide particle and a number of smaller (i.e. 20 - 50 nm in diameter) V enriched nitride particles were captured in the analysis volume.

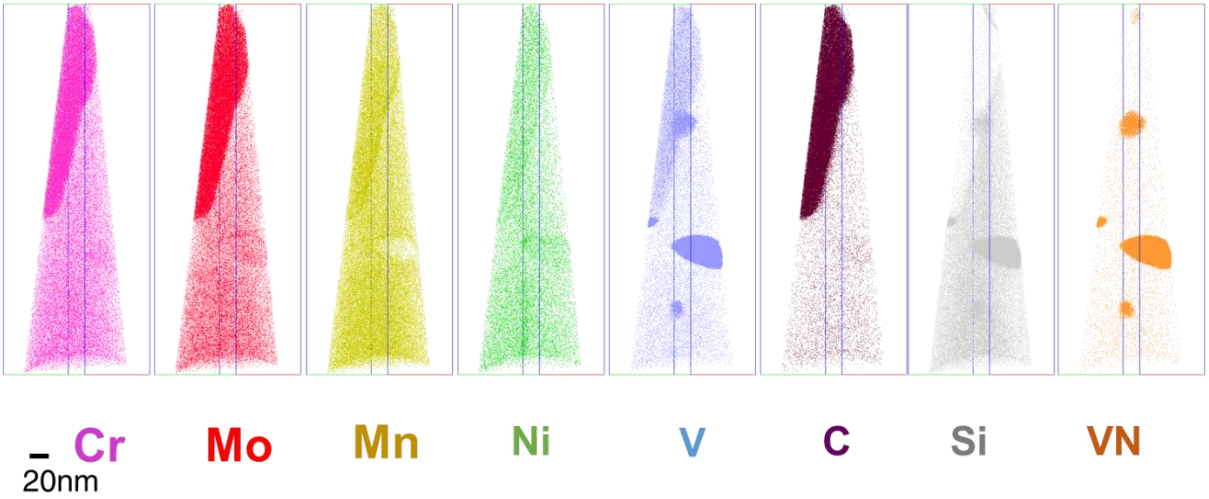

Figure 6-6 Atom maps of individual elements in non-irradiated T91 steel subjected to 470 ^{o}C

The proxigram from a 5 at. % C isosurface is plotted in Figure 6-7 (b). The carbide is enriched in Cr and Mo. Also, segregation of Ni/Si at the carbide matrix interface is not observed. A 10 × 10 × 10 nm^3 region-of-interest (ROI) is placed inside the carbide particle to obtain the composition at the core region and the result is listed in Table 6-1. The carbide contains approximately 51 at. % Cr, 29 at. % Fe, 4.3 at. % Mo, 1.13 at. % Ni (mostly in the form of NiN) and 14 at. % C. The ratio of the metal to carbon matches $M_{23}C_6$ type.

Table 6-1 Composition of the carbide particle in Figure 6-6

Elements	Concentration (at. %)	Error (±)
Cr	50.2	0.24
Fe	29.0	0.22
C	13.8	0.12
Mo	4.34	0.10
Mn	0.70	0.05
V	0.59	0.04
Ni	0.27	0.03
Si	0.04	0.01
N	0.02	0.00

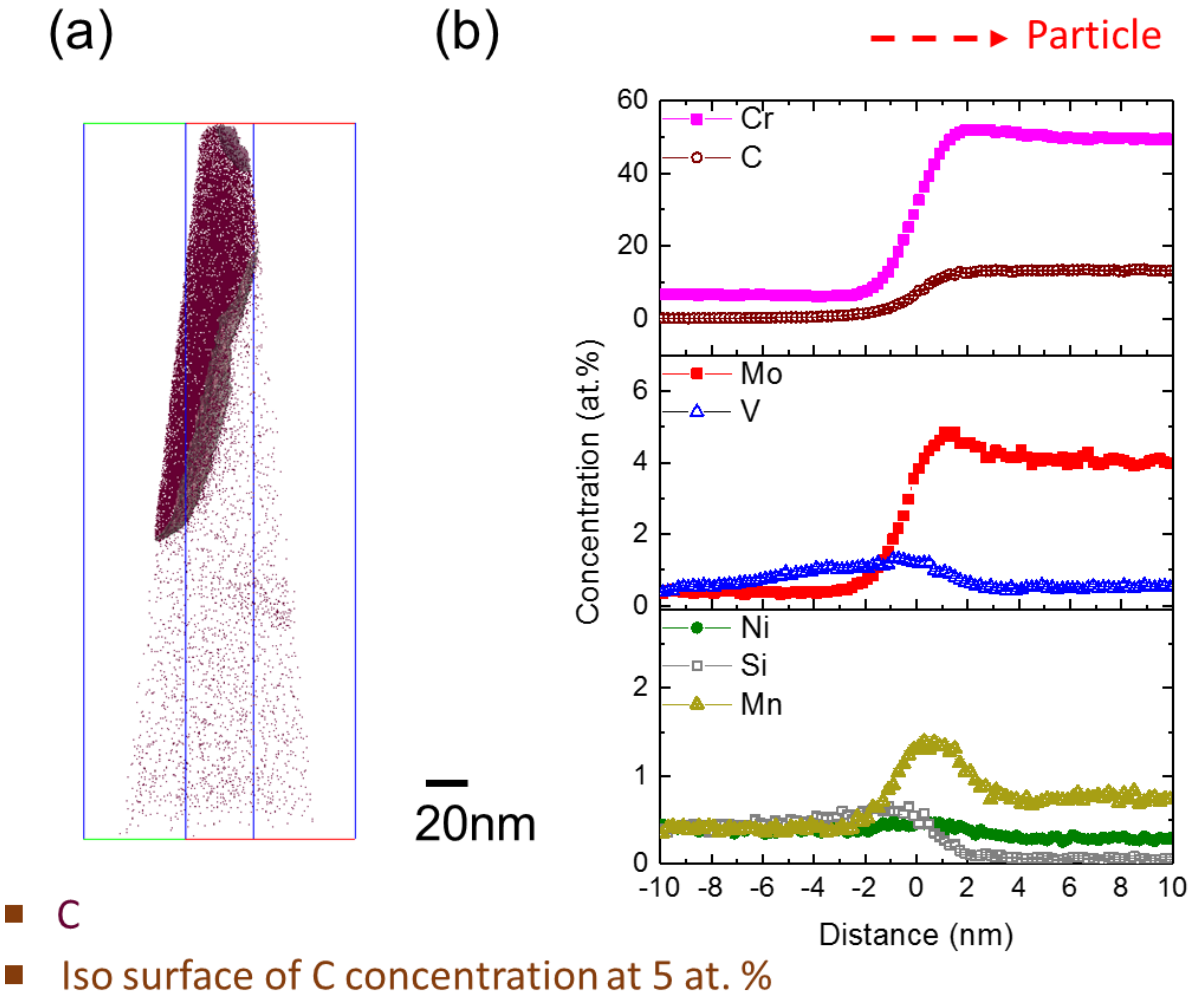

Figure 6-7 (a) 5 at. % C isoconcentration surface highlighting the carbide in the sample in Figure 6-6. (b) the concentrations of the major elements in the carbide

From Figure 6-6, Si is apparently enriched in the V-rich nitride. However, this is because the 14 Da and 15 Da peak in the mass spectrum is ranged as Si. One should note that there is an overlap between Si and Ni at these positions. In reconstructed volumes without nitride particles, there is much less N than Si, and thus the overlap is negligible. However, in the samples containing nitrides, the overlap cannot be assigned to either Si or N. A region-of-interest (ROI) excluding the nitride is taken from the reconstruction and the atom map of ions belonging to the 14 Da and 15 Da peaks in the mass spectrum is shown in Figure 6-8 (a). The mass spectrum corresponding to the atom maps within the ROI matches the natural

abundance of Si very well (Figure 6-8 (b)), indicating that 14 Da, 14.5 Da and 15 Da peaks are Si peaks outside of the nitride region. A 3 at. % N iso-concentration surface is used to isolate the nitride, and the corresponding mass spectra within the iso-concentration surface is shown in Figure 6-8 (b). The nature of the mass spectrum is very different from that derived from the matrix. The 14 Da and 15 Da peaks match the natural abundance of N, which means that within the nitride particle, the 14 Da and 15 Da are most likely due to N^+ ions. Considering the peak overlap, 14 Da and 15 Da peaks are assigned to N^+ when obtaining the nitride composition. In other cases, 14 Da and 15 Da peaks are assigned to Si. This approach is used in all the analysis of all nitrides in this work, whereby the 14 peak and 15 peak are treated separately inside the matrix or in the nitride, respectively.

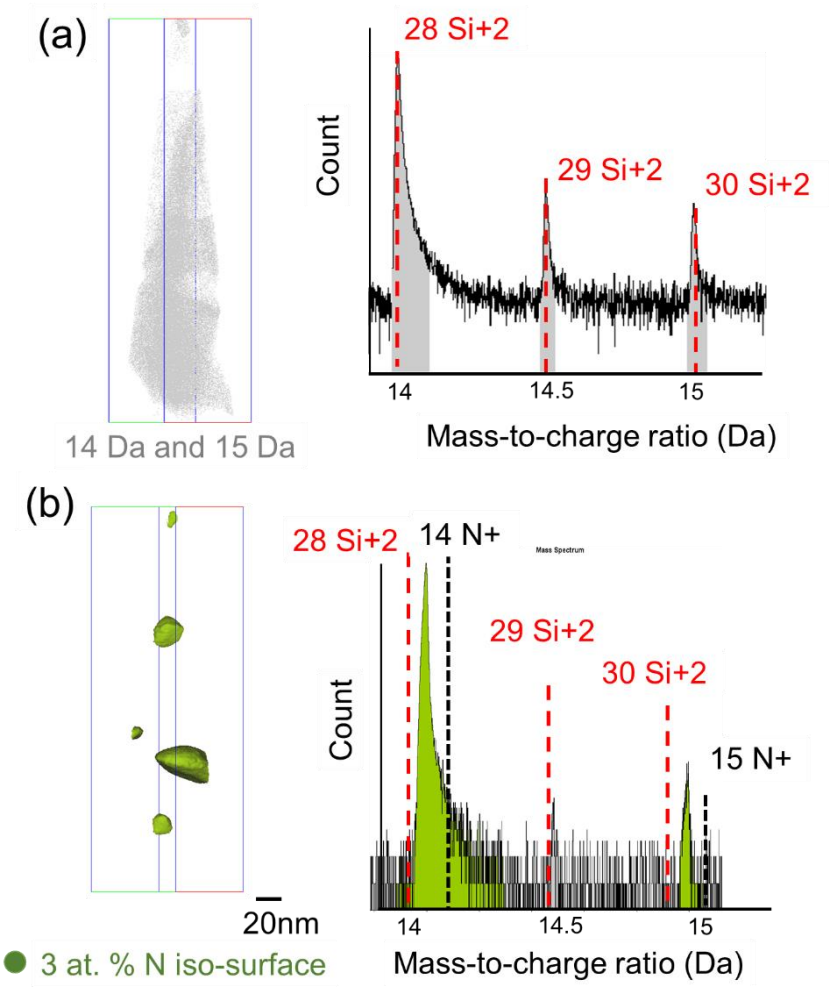

Figure 6-8 (a) Spatial distribution of ions from mass peak 14 Da and 15 Da in ROI excluding nitride and corresponding mass spectra within the ROI. The natural abundance of Si^{2+} is shown in red dashed line. The analysed volume is the same as in Figure 6-7 (b) 3 at. % N iso-concentration surface. The corresponding mass spectra within the iso-surface is displayed on the right-hand side. The natural abundance of Si^{2+} and N^{+} ion is shown by red and black dashed line respectively. In positions of the dashed lines are shifted to better show the mass peaks.

After assigning the 14 Da and 15 Da peaks to N^{+} ion, compositional proxigram from the N isosurface in Figure 6-8 (b) is plotted in Figure 6-9. The nitride particle contains approximately 40 at. % V and 36 at. % N and 2.5 at. % Nb and 10 at. % Cr. The rest is mainly matrix Fe. Ni segregation to the interface was not observed.

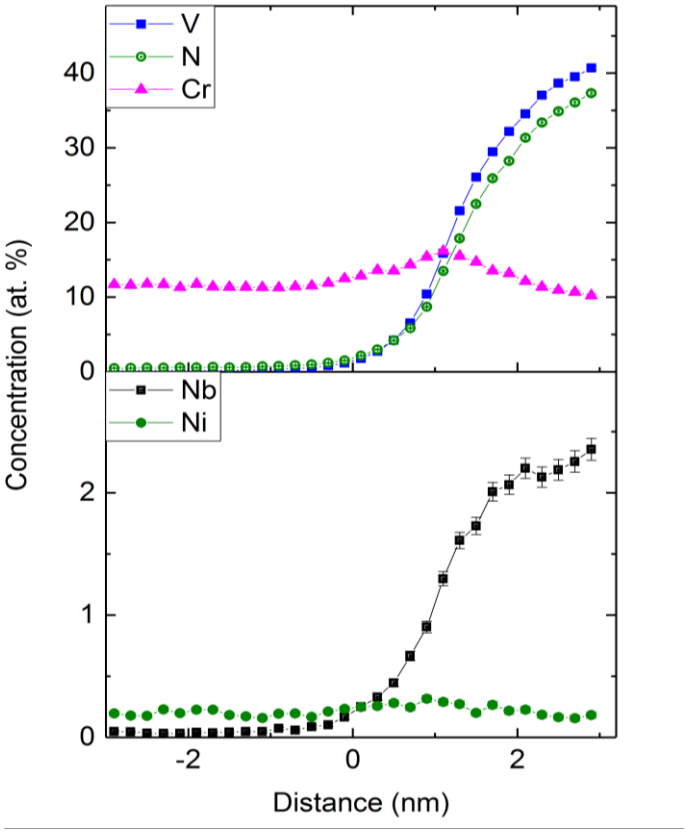

Figure 6-9 Compositional proxigram showing the averaged composition of the nitride particles in Figure 6-8 (b)

6.4 Microstructure of single ion irradiated T91

6.4.1 1 dpa at 470 °C

Four tips were analysed after SI irradiation to 1 dpa at 470 °C. All the tips are taken from 300 - 400 nm beneath the surface. The results show that at this condition all elements are homogenously distributed in the matrix. Atom maps showing the matrix microstructure are shown in Figure 6-10. No nitride/carbide particles or solute segregation was observed. Thus, at this condition the matrix is homogenous with elements randomly distributed.

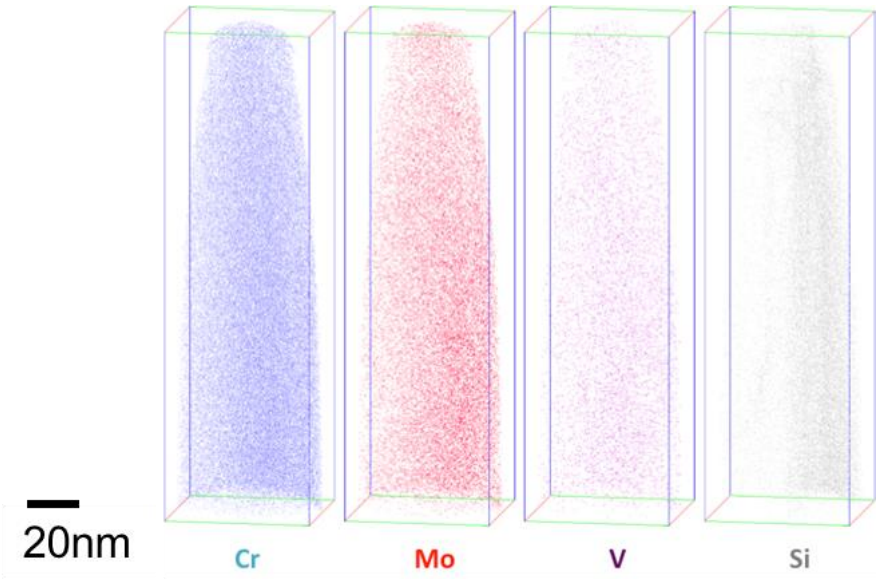

Figure 6-10 Distribution of different species in 1 dpa irradiated T91. The sample is taken from ~300 nm beneath the surface

One of the analyzed volumes enclosed a nitride particle and a grain boundary. Atom maps from this sample are shown in Figure 6-11. Mo, Ni, Mn and Si segregate to the grain boundary (GB). The nitride particle was also on the GB.

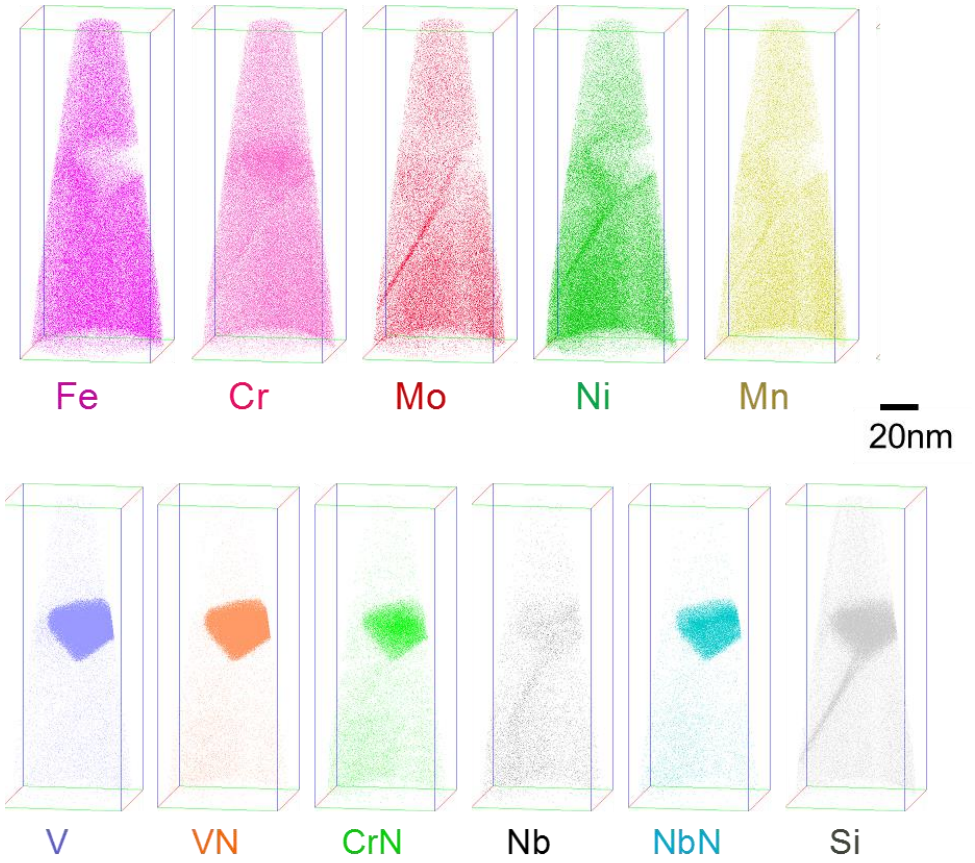

Figure 6-11 Distribution of different species in 1dpa irradiated T91. The sample is taken from ~ 400 nm beneath the surface

A proxigram from 5 at. % V isosurface is shown in Figure 6-12. The nitride is enriched in V and Nb. There is also a slight increase in Cr concentration. In order to obtain the core composition of the nitride, a $10 \times 10 \times 10$ nm^3 cubic ROI is placed inside the nitride and the composition inside the ROI is listed in Table 6-2. The precipitate contains about 41 at. % V and 39 at. % N, also contains around 14 at. % Cr and 3 at. % Nb. The ratio of the metal to nitrogen is approximately 3:2. In T91 steel, the presence of MX type nitride is consistently reported [181,182]. The loss in N concentration in this study may arise from APT artefacts. The lateral surface diffusion of substitutional and interstitial atoms on the APT tip may lead to inaccuracy in the determination of the composition of second phase regions by APT [144,183]. Since the diffusion of light elements is faster than that of heavier elements, the

determination of their original location in the APT is more severely influenced. Thus, the N content can be seriously affected. However, as proposed in [183], experiments provide no evidence of significant surface migration of N. The local magnification effect (LME) in APT can also result in a change in nitride composition. The nitride particles have a higher evaporation field than the surrounding matrix resulting in a preferential evaporation of the matrix.

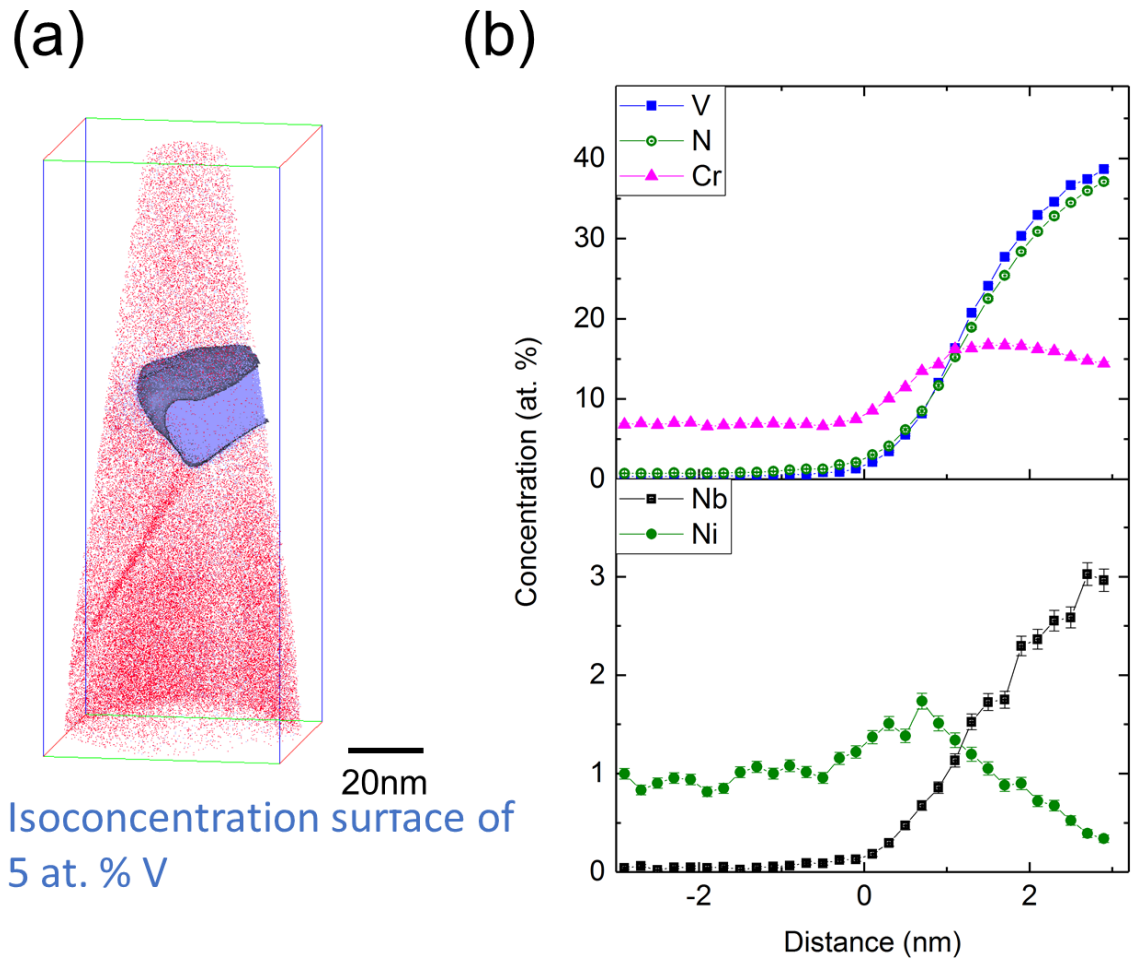

Figure 6-12 Concentration proxigram of the nitride particle in Figure 6-11

Table 6-2 Composition of the nitride particle in Figure 6-12

Elements	Concentration (at. %)	Error (±)
V	41.42	0.21
N	39.29	0.14
Cr	13.97	0.23
Nb	3.01	0.01
Fe	2.17	0.10
C	0.14	0.03

Two 1D concentration profiles across different positions of the grain boundary are plotted in Figure 6-13. An increase in solute concentration on the grain boundary is observable. The position of the grain boundary is ~ 500 nm - 580 nm beneath the surface and the received dose is ~ 1 dpa.

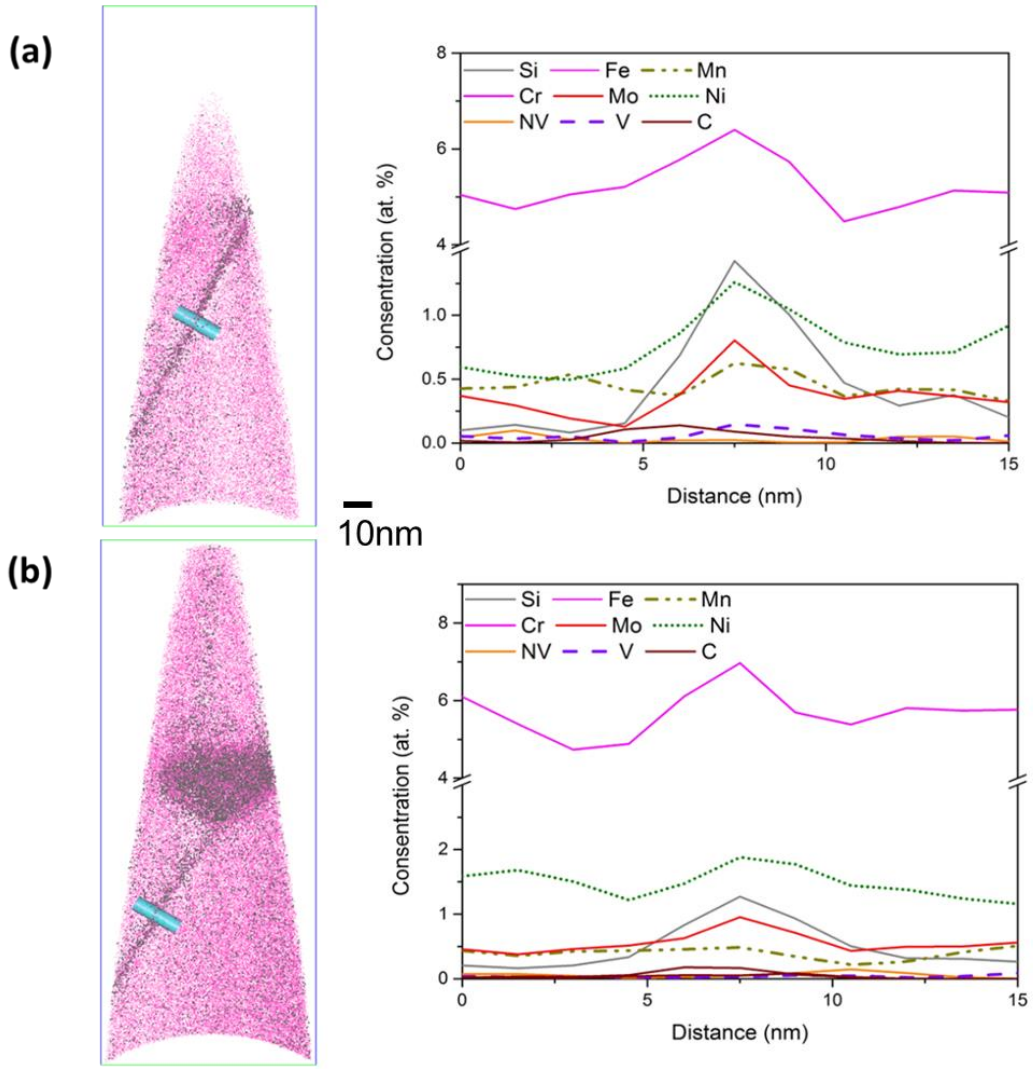

Figure 6-13 1D composition files across the grain boundary

6.4.2 10 dpa at 470 ºC

Four tips were analysed from a sample subjected to 10 dpa SI irradiation were analysed. All the samples are taken from 300 nm - 450 nm beneath the irradiation surface. Two of these specimens contain a Cr-rich carbide precipitate and one of them has a VN precipitate. The final specimen is typical of the matrix.

- **Tip1 (~ 300 nm beneath the surface):**

The atom maps of Tip 1 are displayed in Figure 6-14. One can see that the carbide is enriched in Cr, Mo and C. Ni and Si segregate to the interface of the carbide precipitate and the matrix. The precipitate is on a grain boundary, which itself is highlighted by segregation of Ni and Si.

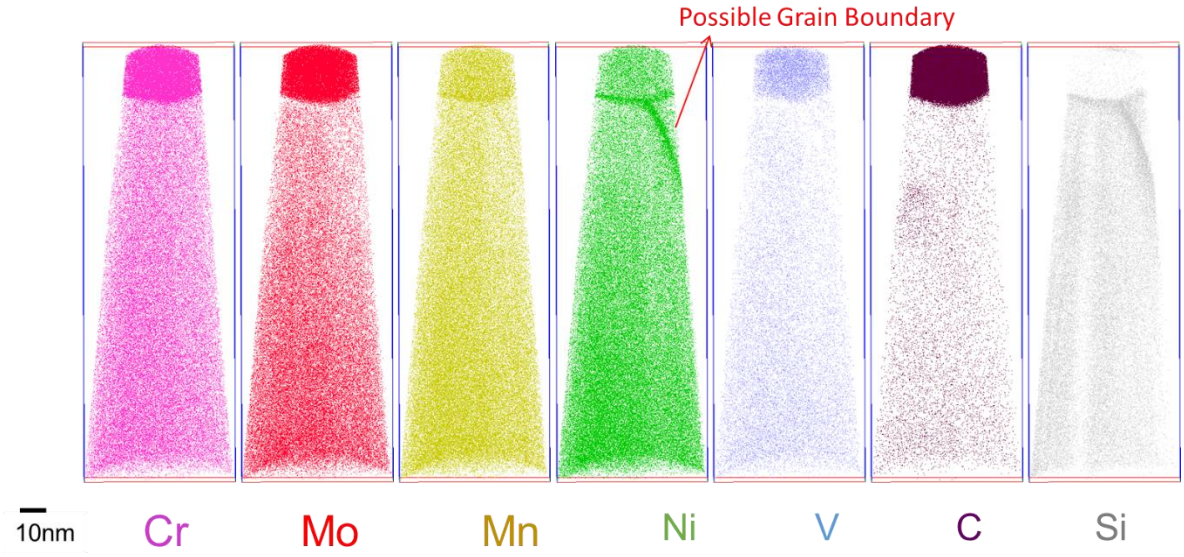

Figure 6-14 Ionic distribution of different species in 10 dpa irradiated T91 (Tip 1)

An isoconcentration surface of 5 at. % C and the corresponding proxigram is shown in Figure 6-15. The Ni is enriched from ~ 0.5 at. % to ~ 2 at. % at the carbide/matrix interface. Si has been eliminated from the precipitate. An increase in the Si composition at the precipitate surface is also can be observed. A 10 × 10 × 10 nm^3 cubic ROI is placed inside the carbide and the composition extracted from the ROI is listed in Table 6-3. The carbide contains about 52 at. % Cr, 29 at. % Fe, 3.5 at. % Mo and 14 at. % C. The ratio of metal to carbon matches the $M_{23}C_6$ type carbide.

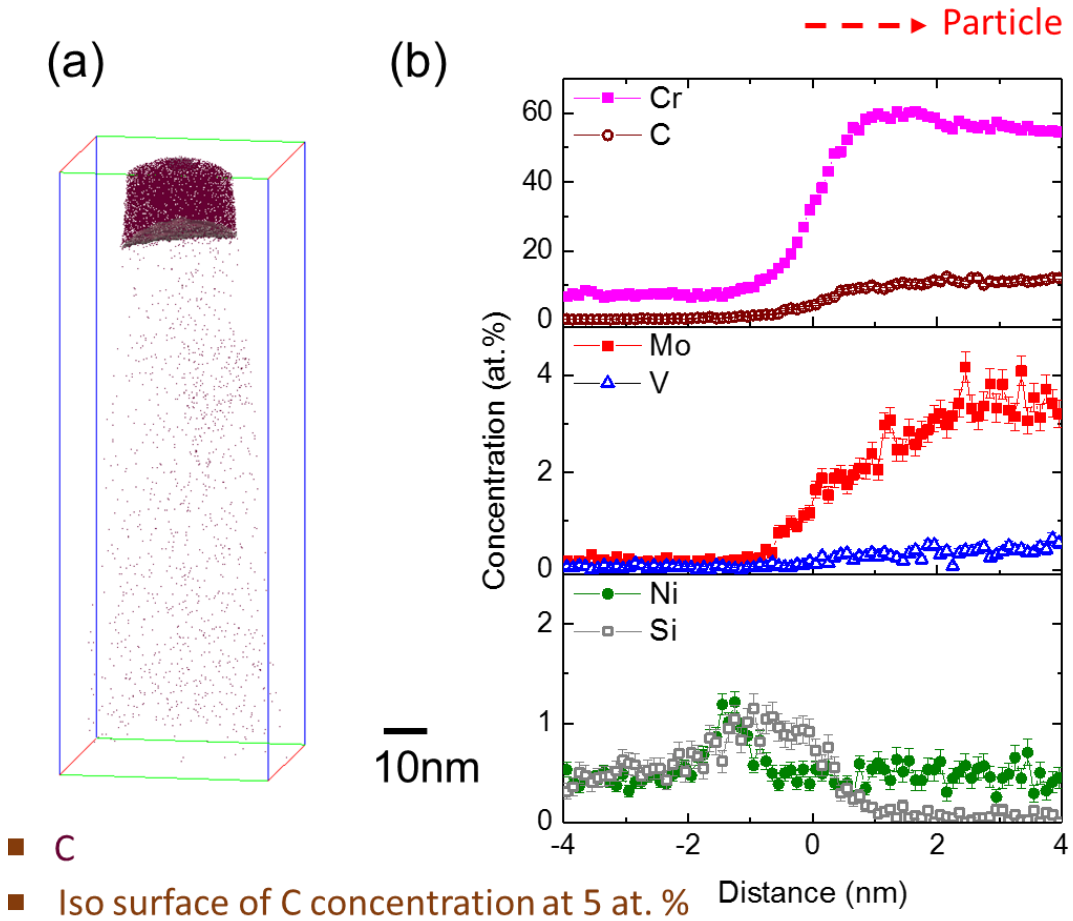

Figure 6-15 (a) Isosurface defined by 5 at. % C and (b) compositional proxigram from the isosurface

Table 6-3 Composition of the nitride particle in Figure 6-15

Elements	Concentration (at. %)	Error (±)
Cr	51.88	0.24
Fe	29.27	0.27
C	13.98	0.12
Mo	3.53	0.09
Mn	0.68	0.05
V	0.63	0.04
Ni	0.33	0.04
N	0.02	0.01
Si	0.02	0.00

A grain boundary highlighted by Ni segregation is also present in Figure 6-14. From the 1D composition profile across the grain boundary shown in Figure 6-16, Ni is enriched from 0.5 at. % to about 2 at. % and Si is enriched to about 1.2 at. % at the grain boundary.

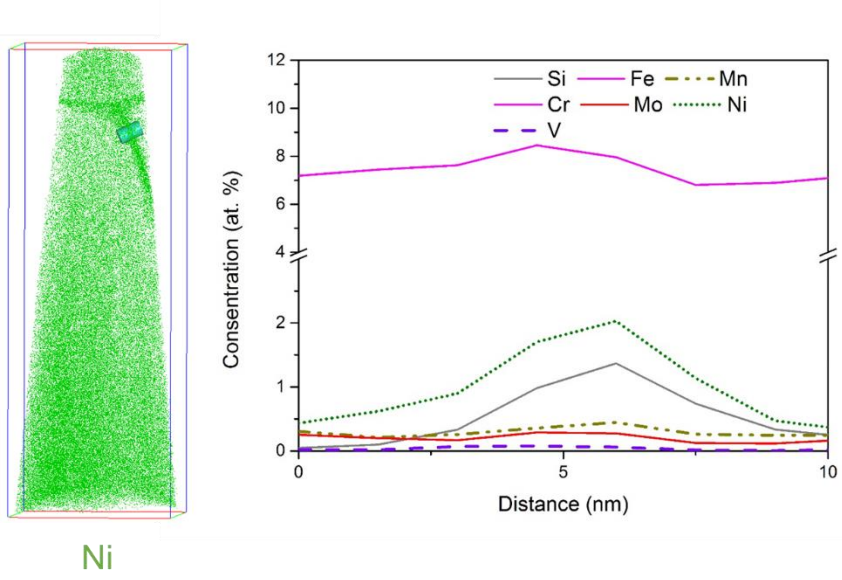

Figure 6-16 (a) Distribution of Ni and (b) 1D composition profile across the grain boundary. The position of the grain boundary is ~ 350 nm beneath the surface and the corresponding dose level is ~ 7.5 dpa according to Figure 3-2

- **Tip 2 (~ 400 nm beneath the surface):**

Atom maps of Tip 2, another carbide containing specimen are displayed in Figure 6-17. Similar to Tip 1, the carbide is enriched in Cr and Mo. The segregation of Ni and Si to the carbide/matrix interface is directly observable from the atom maps.

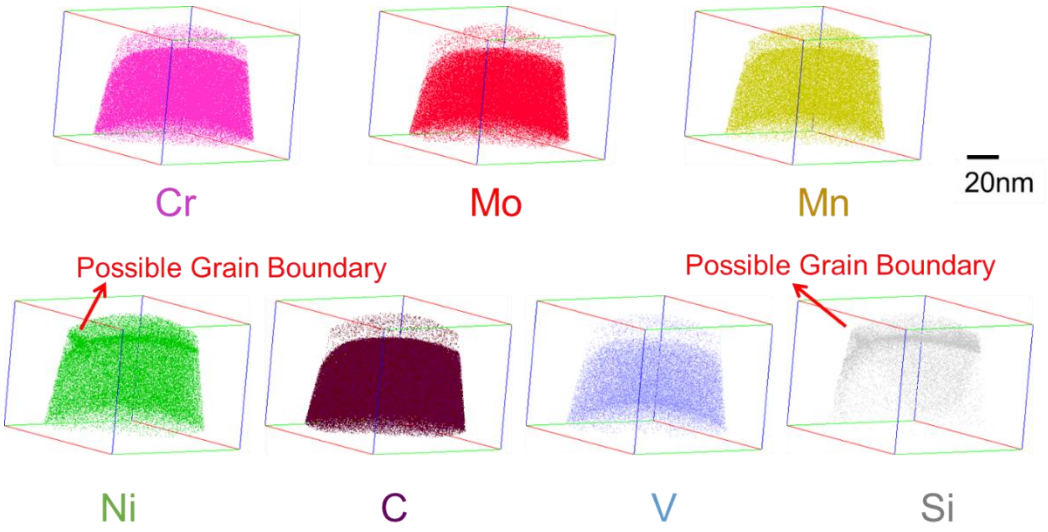

Figure 6-17 Atom maps of different species in 10 dpa irradiated T91 (Tip 2)

The 5 at. % C isosurface and compositional proxigram is shown in Figure 6-18 (a). Both Ni and Si are enriched from ~ 0.5 at. % in the matrix to greater than 2 at. % at the carbide/matrix interface. The composition obtained from a 10 ×10 ×10 nm^3 is listed in Table 6-4. The carbide particle contains about 52 at. % Cr, 28 at. % Fe, 3.8 at. % Mo and 15 at. % C. The precipitate composition is found to be similar to that of Tip 1.

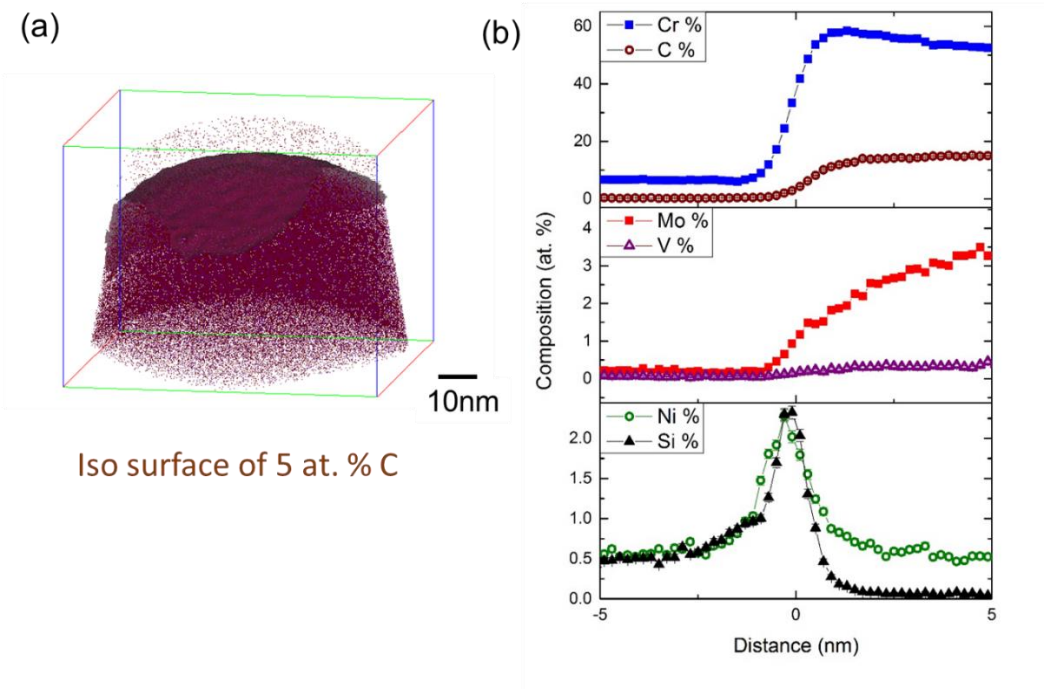

Figure 6-18 (a) 5 at. % C isoconcentration surface and (b) compositional proxigram defined by this isoconcentration surface

Table 6-4 Composition of the nitride particle in Figure 6-17

Elements	Concentration (at. %)	Error (±)
Cr	51.80	0.29
Fe	27.93	0.24
C	15.19	0.13
Mo	3.84	0.11
Mn	0.63	0.05
V	0.55	0.05
Ni	0.42	0.04
Si	0.04	0.00
N	0.01	0.01
P	0.01	0.01

- **Tip 3 (~ 450 nm beneath the surface):**

A V enriched nitride particle is observed at the edge of an APT analysis (Tip 3) of the 10 dpa T91 sample. The atom maps are shown in Figure 6-19. The composition of the precipitates is shown in Figure 6-20 (b). The precipitates contain 40 at. % V and 30 at. % N.

The composition is very similar to the nitride particle observed in unirradiated T91 (Figure 6-7) and T91 irradiated to 1 dpa (Figure 6-12). Unlike the Cr enriched carbide particles discussed above, enrichment of Ni or Si was not observed at the nitride/matrix interface.

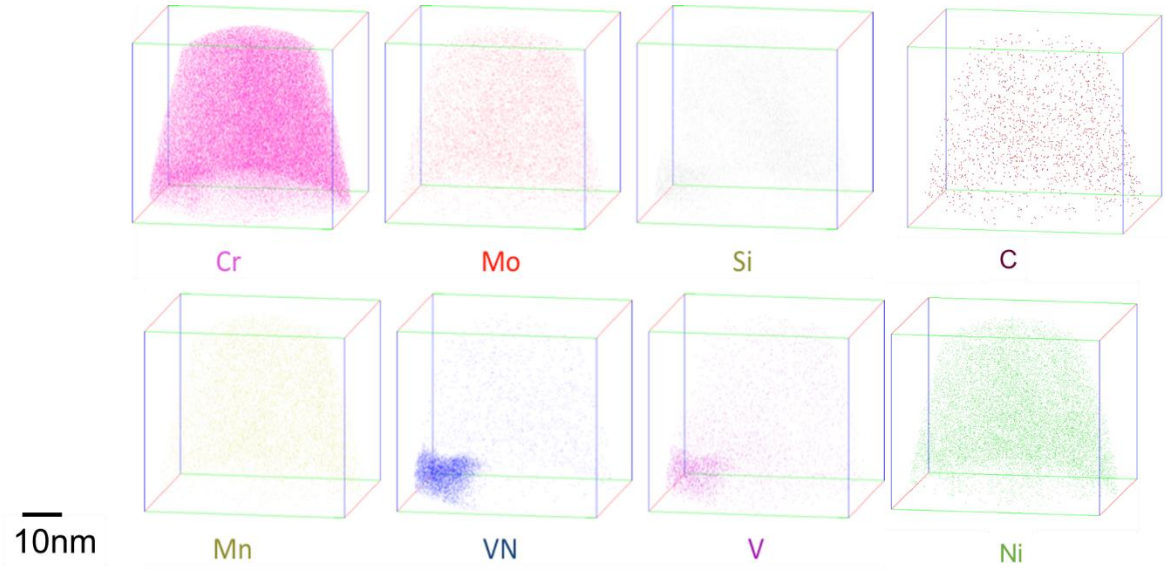

Figure 6-19 Ionic distribution of different species in 10 dpa irradiated T91

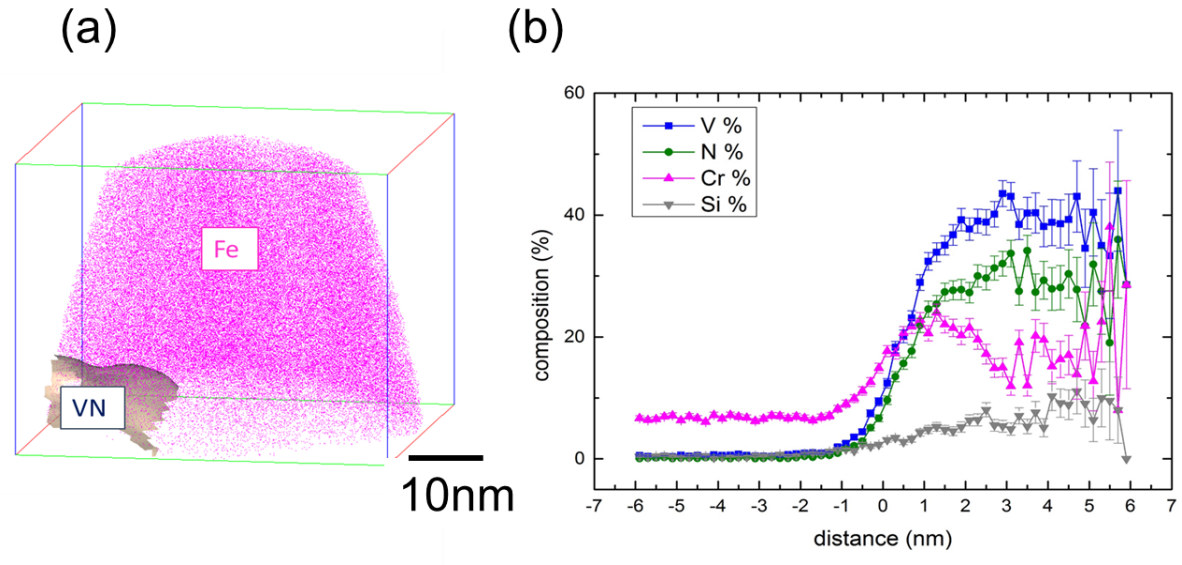

Figure 6-20 (a) 10 at. % V isoconcentration surface highlighting the V enriched nitride particle (b) Compositional proxigram of edge precipitates

- **Tip 4 (~ 300 nm beneath the surface):**

In the APT characterisation of Tip 4 (shown in Figure 6-21), no nitride or carbide precipitates were present within the analysis volume. Furthermore, in this analysis no solute segregation was observed.

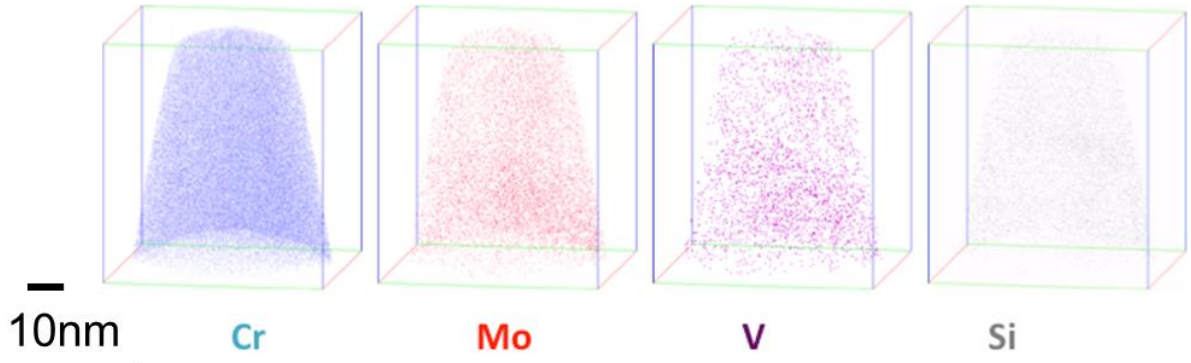

Figure 6-21 Ionic distribution of different species in 10 dpa irradiated T91

6.4.3 20 dpa irradiation at 420 ºC

Two tips of T91 irradiated to 20 dpa at 420 ºC were analysed by APT. Both tips were prepared from a region 200 - 600 nm beneath the surface of the sample. Atom maps from the analysis of Tip 1 are shown in Figure 6-22. Ni segregation to dislocation/matrix defects was observed. Some of the segregated features are dislocation loop-like. In the other analysed volume, clusters enriched in Ni, Mn and Si are observed, which were not seen in the 1 dpa or 10 dpa irradiated materials. The atom maps are displayed in Figure 6-23. The maximum separation method is used to define the clusters. The clustered solutes are chosen as Ni, Mn and Si. If the 5th nearest neighbour of the solute is less than 0.6 nm, the atom is considered as belonging to the precipitates. Any clusters containing less than 20 atoms, were deemed statistically likely to be found in a random distribution, and are therefore

removed. Four precipitates are present in the analysis. The main composition is listed in Table 6-5.

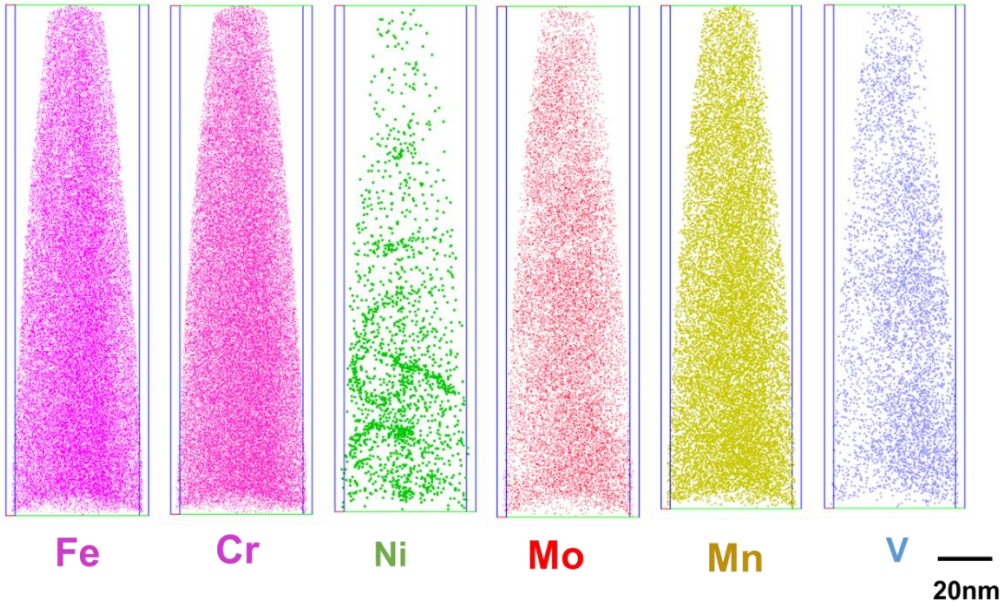

Figure 6-22 Ionic distribution of different species in 20 dpa irradiated T91 (Tip 1). The sample is taken from ~ 200nm beneath the surface. The corresponding dose level is 13 - 14 dpa

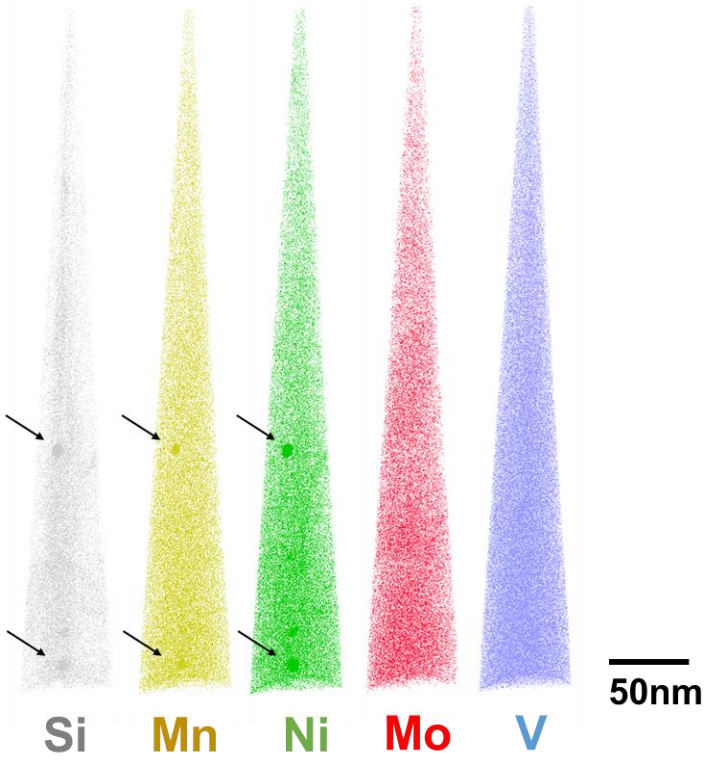

Figure 6-23 Ionic distribution of different species in 20 dpa irradiated T91 (Tip 2) The sample is taken from ~ 300nm beneath the surface. The corresponding dose level is 14 - 16 dpa

Table 6-5 Composition of precipitates in 20 dpa irradiated sample

Precipitate	Size of precipitates (number of solute ions)	Concentration (at .%)			
		Fe	Si	Mn	Ni
Precipitate 1	201	56.5	11.2	7.78	21.2
Precipitate 2	479	49.4	13.1	9.36	20.2
Precipitate 3	1709	48.2	17.0	6.88	20.5
Precipitate 4	1710	55.9	14.0	7.63	17.4

6.5 Discussion: microstructural changes after irradiation

6.5.1 Irradiation induced precipitation

Ni, Si and Mn (MNS) enriched clusters were observed in T91 steel irradiated to 20 dpa at 420 ^{o}C. The MNS-rich clusters were not present in any of the other conditions. MNS-rich G

phase is known to form in irradiated F/M steels [104,178,180,184–190]. Swenson and Wharry [178] have previously summarized the average sizes of G-phase for different irradiation temperatures and doses. In most cases G phase forms below 450 ^{o}C. G-phase was reported to be present in HCM12A steel at 500 ^{o}C [189]. However, the solute concentration in HCM12A is higher than in T91 steel. There are not many works focused on the G-phase formation in T91 steel. A summary from a survey of the literature of observed G-phase in irradiated T91 is presented in Table 6-6. In this table "Y" represents the presence of G-phase and "N" means that no G-phase was observed. From the table, G-phase was observed after 7 dpa proton irradiation but not after 1 dpa irradiation. For most Fe++ ion irradiation conditions, G-phase was not observed. However, it should be noted the range of Fe++ irradiation dose in Table 6-6 is much higher than in the current study. Due to the lack of experimental data, it is difficult to derive any conclusions about the temperature and dose conditions required for the formation of G-phase. In this study, after 1 dpa and 10 dpa irradiation at 470 ^{o}C, G-phase was not observed. This may be because 470 ^{o}C is too high for the formation of G-phase.

Table 6-6 Observed G phase in irradiated T91 steel

Reference	T (°C)	Dose (dpa)	Ion type	Technique used	G phase	Size (nm)
[180]	400	7	2.0 MeV protons	APT	Y	2.2
[180]	500	7	2.0 MeV protons	APT	Y	4
[180]	400	1	2.0 MeV protons	APT	N	-
[184]	460	130	5 MeV Fe++	TEM	N	-
[184]	460	250	5 MeV Fe++	TEM	N	-
[184]	460	350	5 MeV Fe++	TEM	Y	24.8
[184]	460	450	5 MeV Fe++	TEM	N	-
[184]	460	550	5 MeV Fe++	TEM	N	-
[184]	460	650	5 MeV Fe++	TEM	N	-
[191]	475	410	3.5 MeV Fe	APT	Y	-

6.5.2 Stability of pre-existing precipitates

The Cr-rich carbide and V-rich nitride particles are pre-existing precipitates in the as-received material.

– Cr-rich carbide

Cr-rich carbide particles were captured in the APT analysis of both the un-irradiated T91 and 10 dpa irradiated T91. By comparing the compositions listed in Table 6-1, Table 6-2 and Table 6-3, one can see that the carbide particles contain around 52 at. % Cr, 28-29 at. % Fe, 3 - 4 at. % Mo and 14 - 15 at. % C. The composition matches $M_{23}C_6$ type and remains stable after irradiation. However, prior to irradiation, the segregation of Ni and Si to the carbide/matrix interface is not observed. After irradiation to 10 dpa, the segregation of Ni and Si to carbide/matrix interface is clearly observed in both Figure 6-15 and Figure 6-18.

– V-rich nitride

V-rich nitride particle was observed in the non-irradiated heat treated T91 and both 1 dpa and 10 dpa irradiated T91. The composition remains stable after irradiation. Compared to the carbide particles, the segregation of Ni and Si to the particle/matrix interface after irradiation is not observed in nitride particles.

6.5.3 Grain boundary segregation

A GB has been observed in the APT reconstruction in T91 samples in the as received, 1 dpa and 10 dpa irradiation conditions, respectively. The concentration profiles of individual elements across the GB are plotted in Figure 6-24. Segregation of Cr is observed in all the conditions. The segregation of Ni and Si is not obvious before irradiation. After irradiated to 1 dpa and 10 dpa, clear segregation of Ni and Si to GB is observed. The grain boundary Gibbsian excess is estimated by the method outlined in § 4.3 and listed in Table 6-7. There is a large increase in the excess of Ni and Si after the irradiation. However, the excess of Cr decreased. One should also note that even at the same unirradiated condition, the grain boundary excess of Cr is different across different GBs,

The complex behaviour of Cr in FM steels is discussed in § 2.4.2. In the current study, the Cr is found to be enriched at the GB both before and after irradiation. After irradiation to 1 dpa and 10 dpa, as shown in Figure 6-24 (b) and (c), the magnitude of Ni and Si segregation to GB increased compared to the as-received T91. The segregation of Ni to the GB has been consistently reported in irradiated austenitic steel and FM steels. The segregation can be attributed to the Inverse-Kirkendall mechanism [192,193]. As discussed in § 2.4.2, Si is an undersized solute and binds strongly to interstitials, leading to enrichment at the sink.

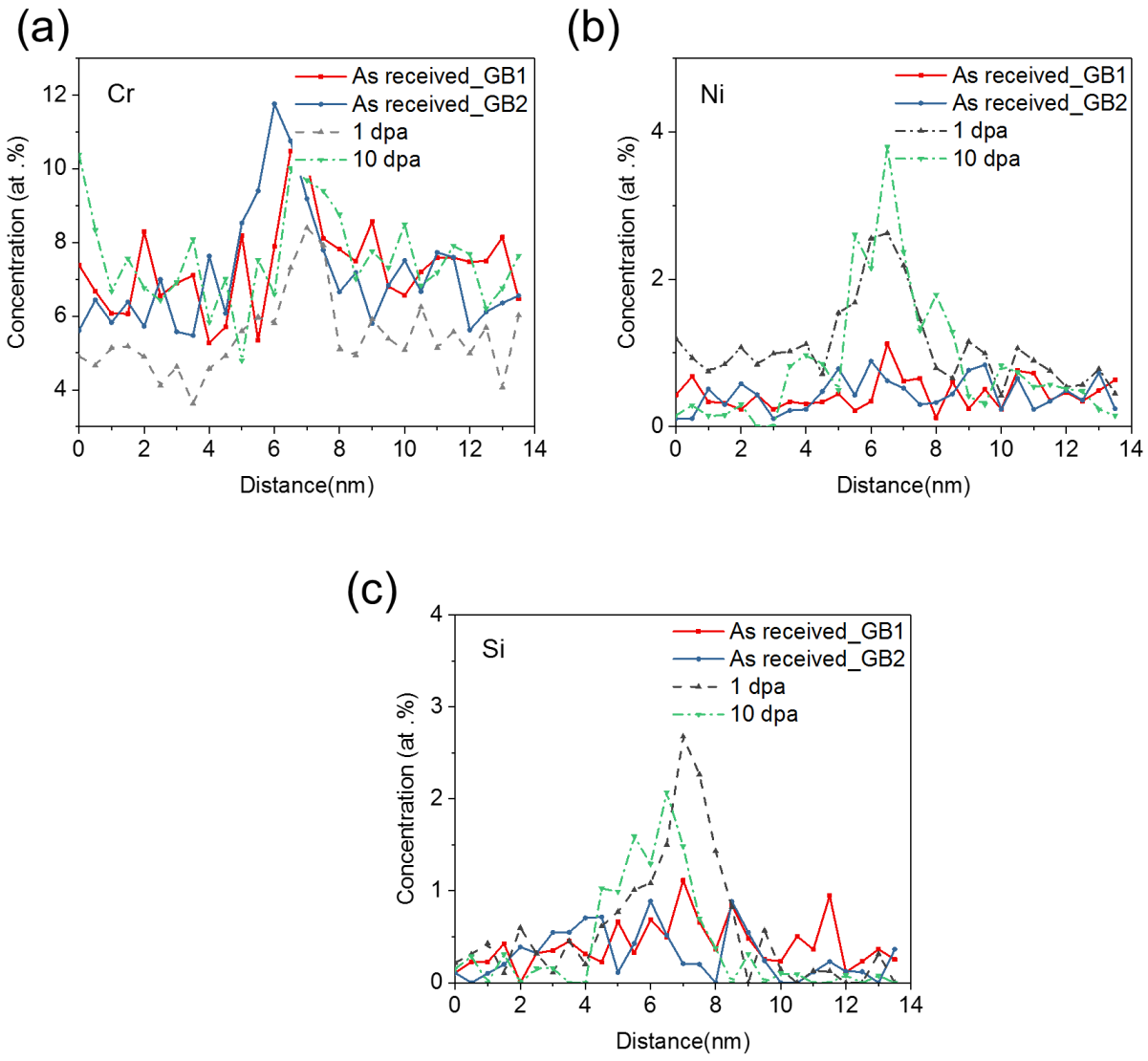

Figure 6-24 Solute segregation profiles across the GB in as-received, 1 dpa and 10 dpa (10 dpa at 600 nm, the actual dpa received at the GB is ~ 7.5 dpa) irradiated T91 steel: (a) Cr (b) Ni (c) Si

Table 6-7 Gibssian excess of gran boundary segregation of Cr, Ni and Si (10^{17} ions/m^2)

	Unirradiated GB1	Unirradiated GB2	1 dpa	10 dpa
Cr	80.4±4.8	37.2±2.6	26.2±3.2	22.0±3.2
Ni	1.5±0.3	2.6±0.3	22.2±0.2	52.3±2.1
Si	5.0±0.3	4.6±0.3	41.0±0.9	35.4±0.8

6.6 Summary:

- In the irradiated samples, both after 10 dpa and 1 dpa at 470 ^{o}C, no precipitates or segregation were found in the matrix.
- Ni, Mn and Si enriched precipitates form by 14 - 16 dpa (the dose was 20 dpa at 600 nm) irradiation at 420 ^{o}C.
- VN precipitates were observed both in 10 dpa and 1 dpa irradiated sample.
- Cr-rich carbide precipitates were observed in the 10 dpa irradiated sample. Ni and Si were found to enrich at the interface of carbide and matrix.
- The magnitude of Ni and Si segregation on the grain boundary was observed to be greater than for the unirradiated sample. This needs to be confirmed by more analyses.

7 BOR60 and Dual ion beam irradiation of T91

7.1 Introduction

Understanding the correlation of irradiation types in terms of resulting microstructural changes is one of the main aims of this study. In this chapter, APT analyses were carried out to study the microstructure of T91 steel subject to BOR60 reactor and dual ion (DI) beam irradiation. The BOR60 and DI irradiation conditions are outlined in § 3.1.4. The dose of DI irradiation at 600 nm is 16.6 dpa, which is equal to the dose of the corresponding BOR60 irradiation. The injected He level also matches the expected amount of transmutation He from the BOR60 reactor. Two irradiation temperatures, 386 ^{o}C and 412 ^{o}C were studied in BOR60 and the dual ion beam irradiation temperatures were 406 ^{o}C and 432 ^{o}C. A temperature shift of 20 ^{o}C for dual ion beam irradiation was made to account for the dose rate effect using the rate theory [194]. Detailed irradiation conditions are listed in § 3.1.4.

In the case of heavy ion irradiation, the resulting damage is dependent on the depth from the irradiation surface. Thus, the samples from DI irradiated T91 were prepared from different depths to understand the evolution of microstructure as a function of dose. Due to the nature of neutron irradiation, the neutron damage profile is relatively flat [195]. All the BOR60 irradiated samples were taken from a depth between 200 - 600 nm from the surface.

Ion irradiation was conducted in Michigan Ion Beam Laboratory and the samples were then shipped to Oxford. Zeiss Auriga dual beam microscope at University of Oxford was used for sample preparation for ion irradiated T91. Due to the radioactive nature of neutron

irradiated samples, lift-out process for BOR60 irradiated T91 was conducted at Oak Ridge and then shipped to Oxford.

The formation of MNS-rich clusters, solute segregation to defects, carbide/nitride compositions and grain boundary chemistry have been examined by APT analysis. The temperature dependence of clusters and the effect of irradiation types are discussed. The results are also compared with the complementary STEM results conducted at Oak Ridge on the same samples.

7.2 Microstructure of T91 after BOR60 irradiation

7.2.1 Elemental distribution of T91 after BOR60 irradiation at 412 ºC

Figure 7-1 presents the atom maps obtained from the different location in T91 steel samples irradiated in BOR60 at 412 ºC. In all the samples, distinct solute clusters containing Ni, Mn, and Si are observed. This clustering was not seen in the as received T91 (Figure 5-4). In Figure 7-1 (b), the half-torus shaped feature decorated by Ni and Si, indicates segregation to likely irradiation-induced dislocation loops. A Cr-rich carbide particle was present in the analysis of the sample in Figure 7-1 (d). These microstructures will be further discussed in the following sections.

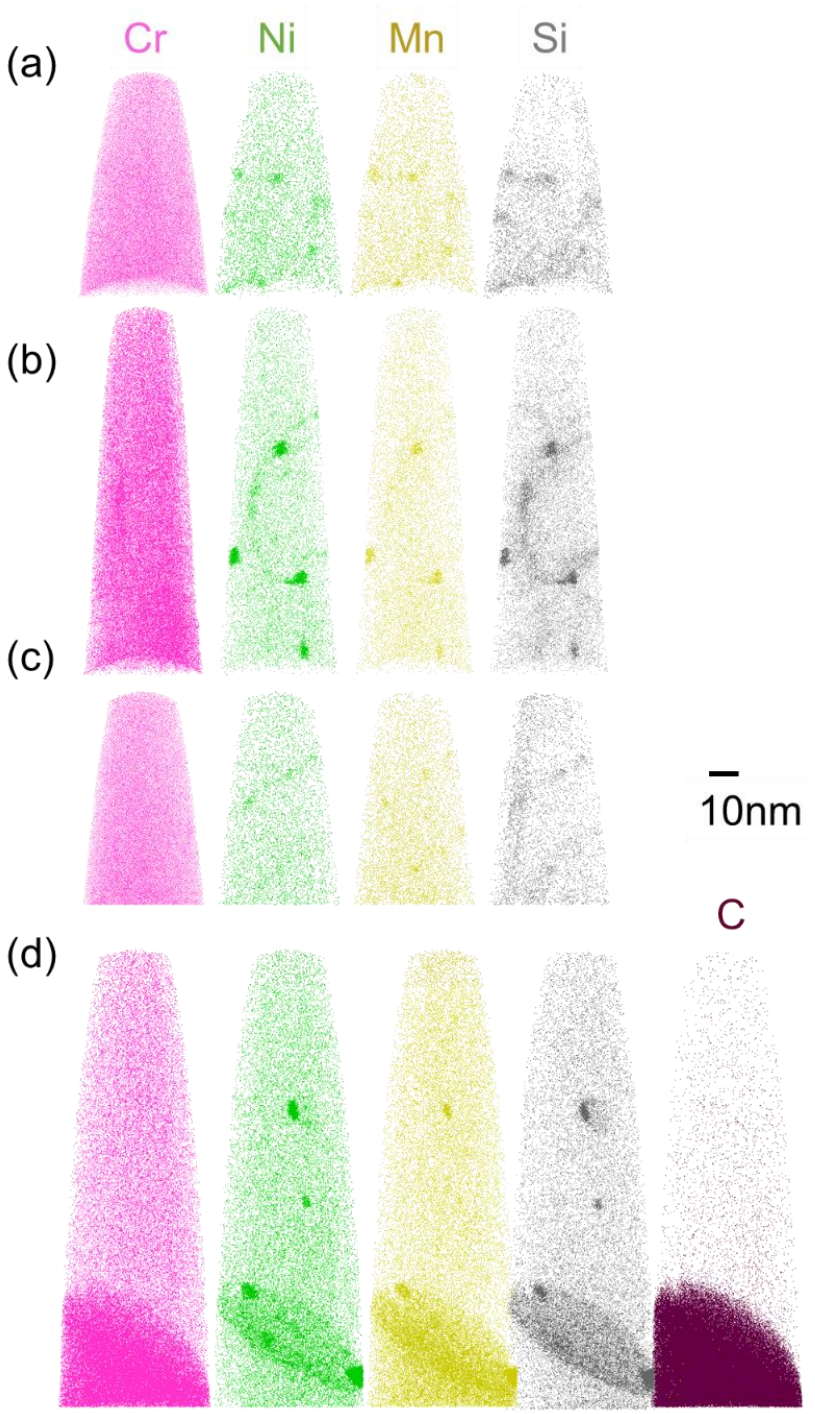

Figure 7-1 Atom maps of T91 steel irradiated in BOR60 to 16.6 dpa at 412 ºC

7.2.2 MNS-rich cluster composition after BOR60 irradiation at 412 ºC

In Figure 7-1 the distribution of MNS-rich clusters is not homogeneous. Sample-to-sample variation can be observed. An iso-concentration value of 5 at. % Ni + Mn + Si was used to separate the MNS-rich clusters. Typical composition proximity histograms of different types of clusters from the samples in Figure 7-1 (b) and Figure 7-1 (c) are plotted in Figure 7-2 (a) and (b), respectively. From Figure 7-2 (a) the core region of Cluster 1 contains around 40 at. % Ni, 20 at. % Si and 10 at. % Mn. Both Fe and Cr are depleted in the MNS cluster compared to the matrix. The highest Ni, Mn, Si content at the core of Cluster 2 in Figure 7-2 (b) is 3 - 4 at. %, much lower than that of Cluster 1.

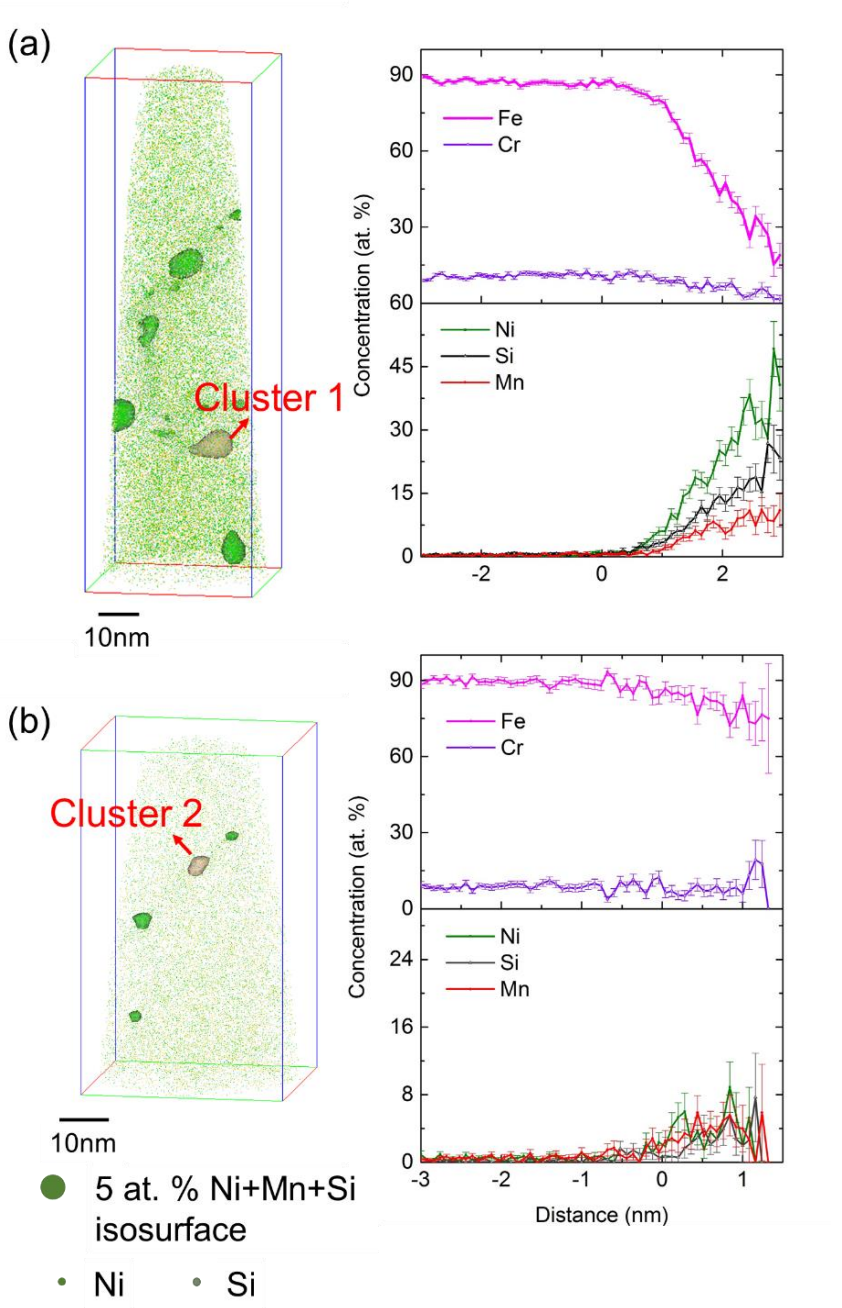

Figure 7-2 The iso-concentration surfaces of Mn + Ni + Si at 5 at. % and proximity histogram showing the concentrations of major elements in the clusters. The analysis volumes are the same as those shown in Figure 7-1 (b) and (c), respectively

7.2.3 Segregation to dislocation loops

The curved features in Figure 7-1 (b) are assumed to be segments of a dislocation loop. The solutes segregation is highlighted by iso-concentration surfaces of Ni + Si at 3 at. % in

Figure 7-3 (a). One can see that the MNS-rich clusters form adjacent to the dislocation loop. In order to study the solute segregation to dislocation loops, the dislocation segments that are not attached to precipitates are highlighted in pink. The concentration profile, by averaging proximity histograms is plotted in Figure 7-3 (b). From the profile, Cr, Ni and Si is enriched at the dislocation loops. The radius of segregation centred around the dislocation loop is around 1.5 nm.

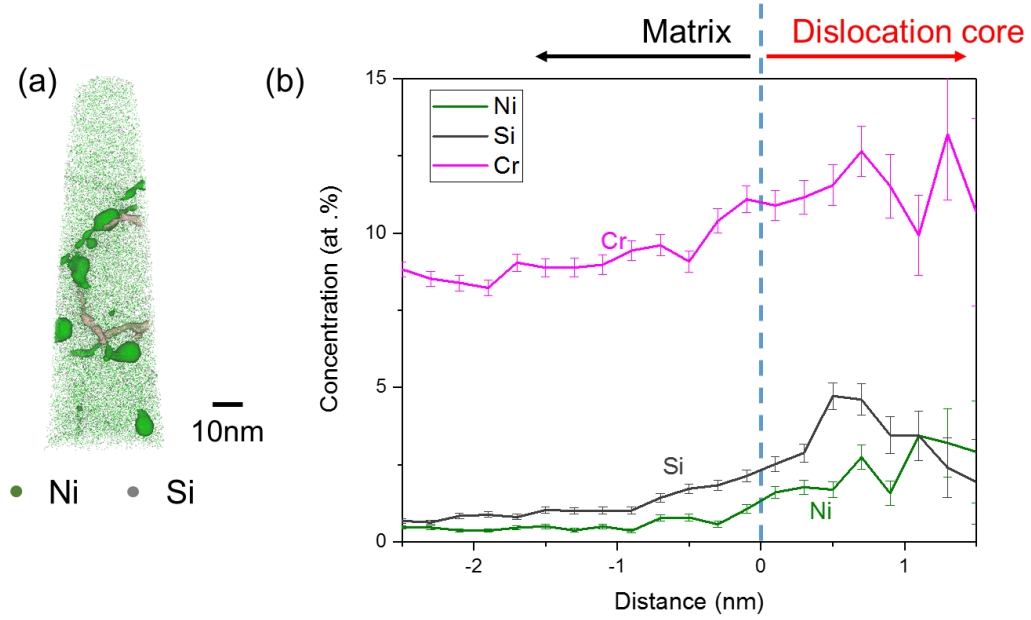

Figure 7-3 (a) 3 at. % Ni + Si iso-concentration surfaces of T91 steel irradiated in BOR60 to 16.6 dpa at 412 ºC (b) Ni and Si segregation profile obtained from the averaging the proxigrams of the iso-concentration surfaces highlighted in pink

- Number density and average size of MNS clusters

The number density and cluster size were calculated as outlined in § 3.1.4. The number density and mean radius of the MNS clusters are shown in Figure 7-4. The number density is obtained from averaging all the samples irradiated at the same condition. At 412 ºC and 386 ºC the average number density is $2.0 \times 10^{23}/m^3$ and $1.8 \times 10^{23}/m^3$, respectively, and the average radius is approximately 2.5 nm and 2.4 nm respectively. There is therefore no

significant difference in number density and cluster size at the two irradiation temperatures. Due to the sample-to-sample variation, the error bars are quite large. Thus, the numbers should be taken as an estimate.

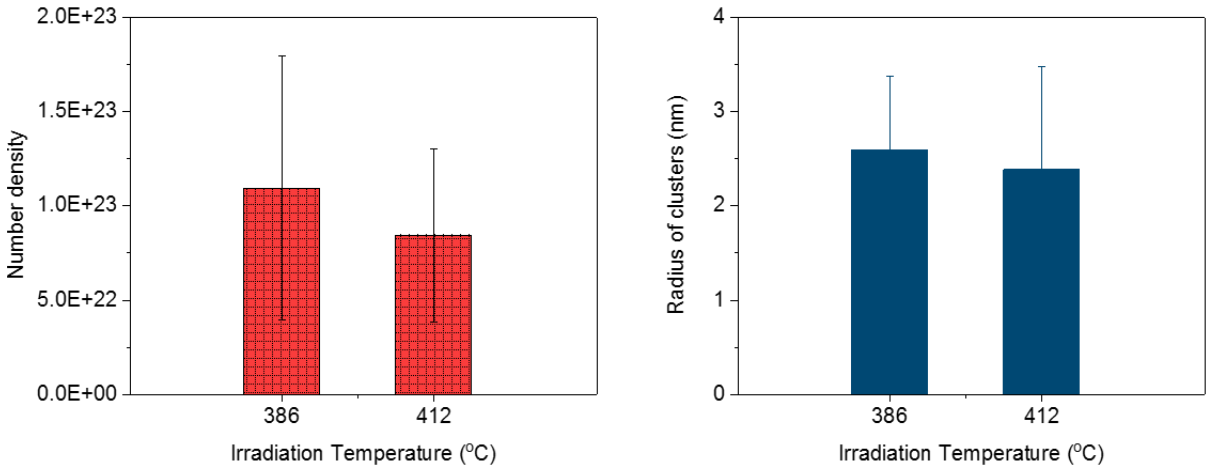

Figure 7-4 The number density (left) and mean radius (right) of MNS-rich clusters after BOR60 irradiation

7.2.4 Elemental distribution of T91 after BOR60 irradiation at 386 °C

Figure 7-5 shows the atom maps of T91 irradiated in BOR60 at 386 °C. The solute distributions are similar to the results from irradiation at 412 °C. MNS-rich clusters are present in all the analysed volumes. Two carbide particles were also observed, as seen in Figure 7-5 (b).

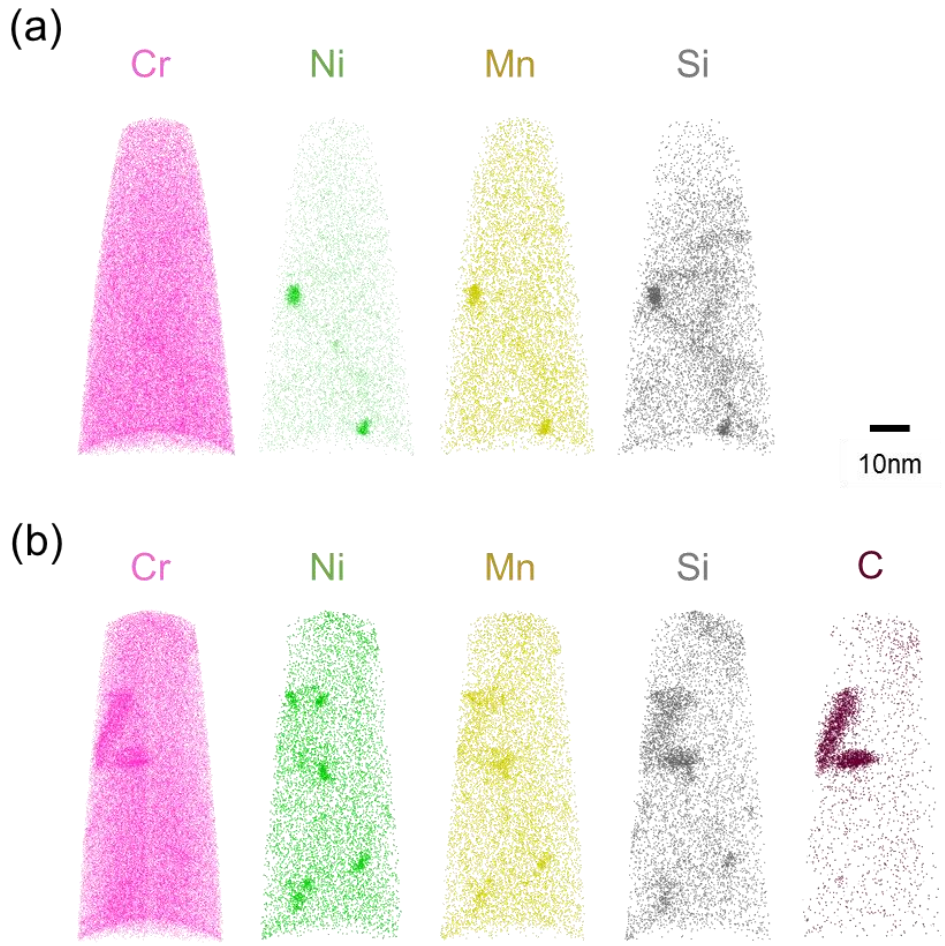

Figure 7-5 Atom maps of T91 steel irradiated in BOR60 to 16.6 dpa at 386 ºC

7.2.5 MNS-rich cluster composition after BOR60 irradiation at 386 ºC

An iso-concentration value of 5 at. % Ni + Si was used to delineate the MNS-rich precipitates. Typical composition proximity histograms of clusters from sample in Figure 7-5 (a) and Figure 7-5 (b) are plotted in Figure 7-6 (a) and (b), respectively. Similar to the results from 412 ºC irradiation, the composition of MNS clusters varies significantly from sample to sample. The peak Ni, Si and Mn content in cluster 1 exceeds 30 at. %, 20 at. % and 10 at. %, respectively. In cluster 2 in Figure 7-6 (b) however, the concentration is 14 at. %, 6 at. % and 8 at. % for Ni, Si and Mn, respectively.

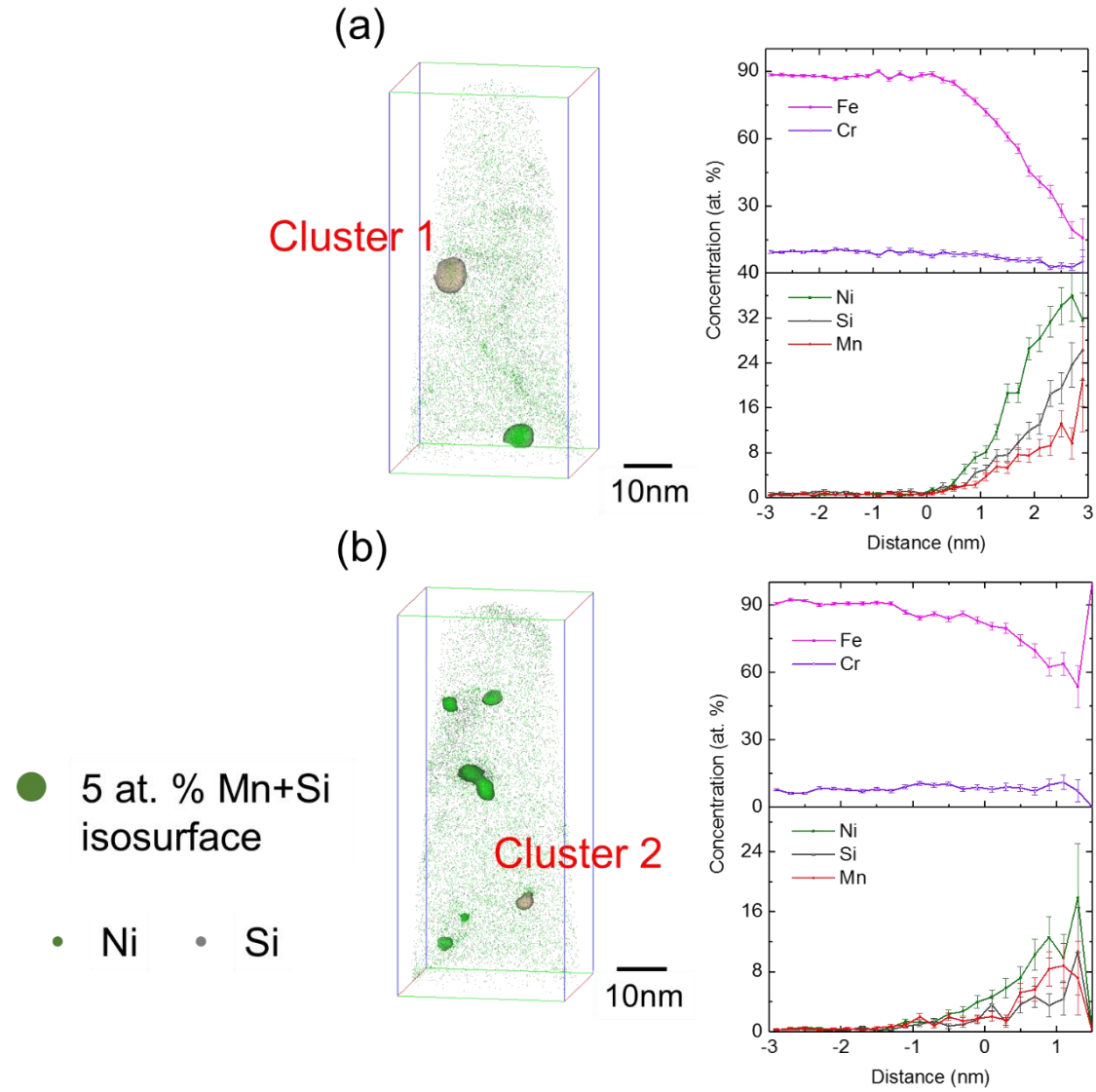

Figure 7-6 The iso-concentration surfaces of Mn + Ni + Si at 5 at. % and proximity histogram showing the concentrations of major elements in the clusters.

7.2.6 Size effect of MNS-rich cluster composition

In order to investigate the size dependence of the cluster composition, the average solute concentration within all the 5 at. % Mn + Ni + Si iso-concentration surfaces in BOR60 irradiated samples are listed as a function of size in Figure 7-7. The averaged concentrations of the major elements are listed in Table 5-1. The clusters are rich in Ni, Si, and Mn. The Fe contents in the clusters are around 80 at. %. There is no significant

variation between the cluster compositions at two irradiation temperatures, and there is also no clear trend in terms of cluster size. It should be noted that this approach will result in a low total solute concentration as the overall concentration is dominated by the surface, which is determined by the chosen iso value.

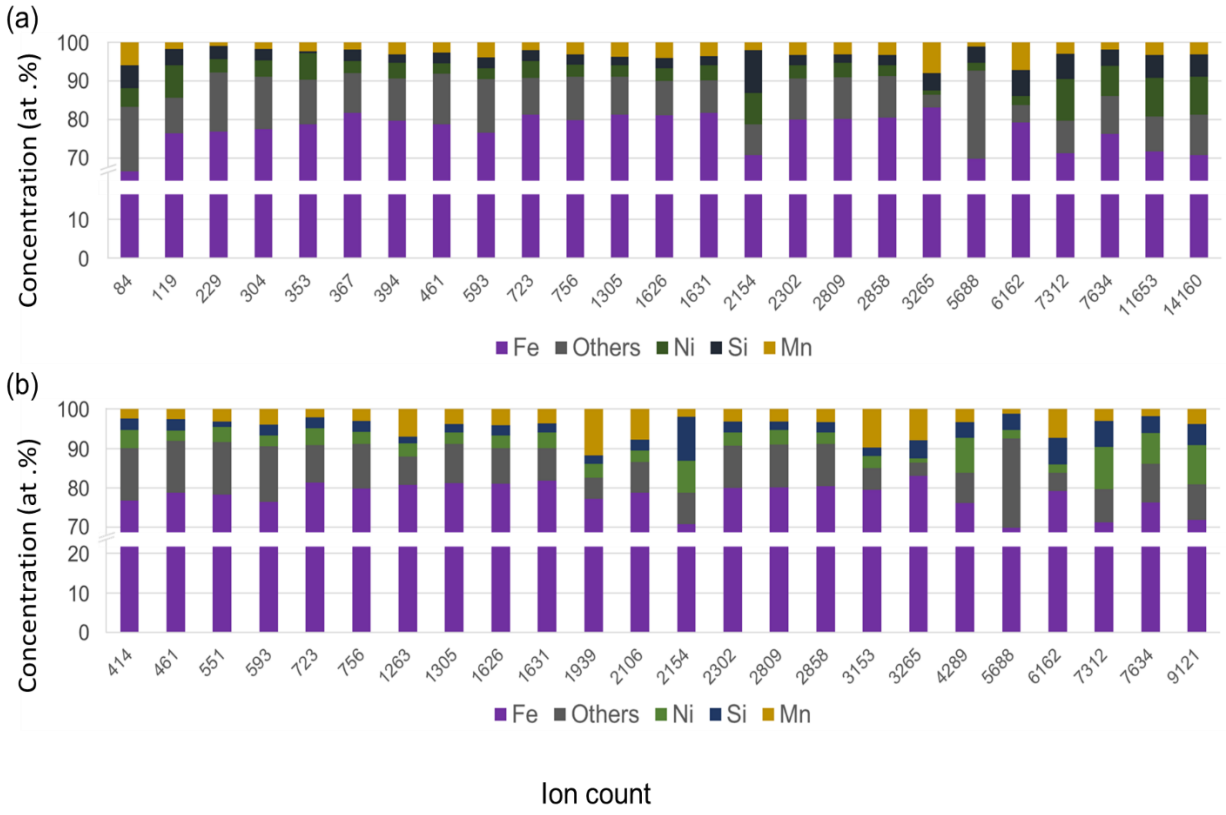

Figure 7-7 Composition of MNS-rich clusters as a function of cluster size after BOR60 irradiation at 412 ºC (b) at 386 ºC

Table 7-1 Concentrations of the major elements in MNS-rich clusters in BOR60 irradiated T91. The error is obtained from averaging different clusters.

	Fe	Others	Ni	Si	Mn
Concentration_386°C (at .%)	77.31	8.63	4.98	2.82	6.08
Error (±)	2.54	2.89	2.60	1.23	3.23
Concentration_412°C (at .%)	77.31	10.84	4.77	3.89	3.18
Error(±)	4.40	3.73	2.71	2.14	1.68

7.2.7 Carbide composition after BOR60 irradiation

In Figure 7-1 (d), part of a carbide particle was enclosed in the analysed volume. The formation of MNS-rich clusters at the carbide/matrix interface was observed. The composition profile across the carbide/matrix is plotted in Figure 7-8. The carbide is Cr, Mo enriched and the composition is consistent with a $M_{23}C_6$ type carbide. The interface is enriched with Ni, Si and Mn, with the maximum concentration of Ni, Si and Mn exceeding 2 at. %.

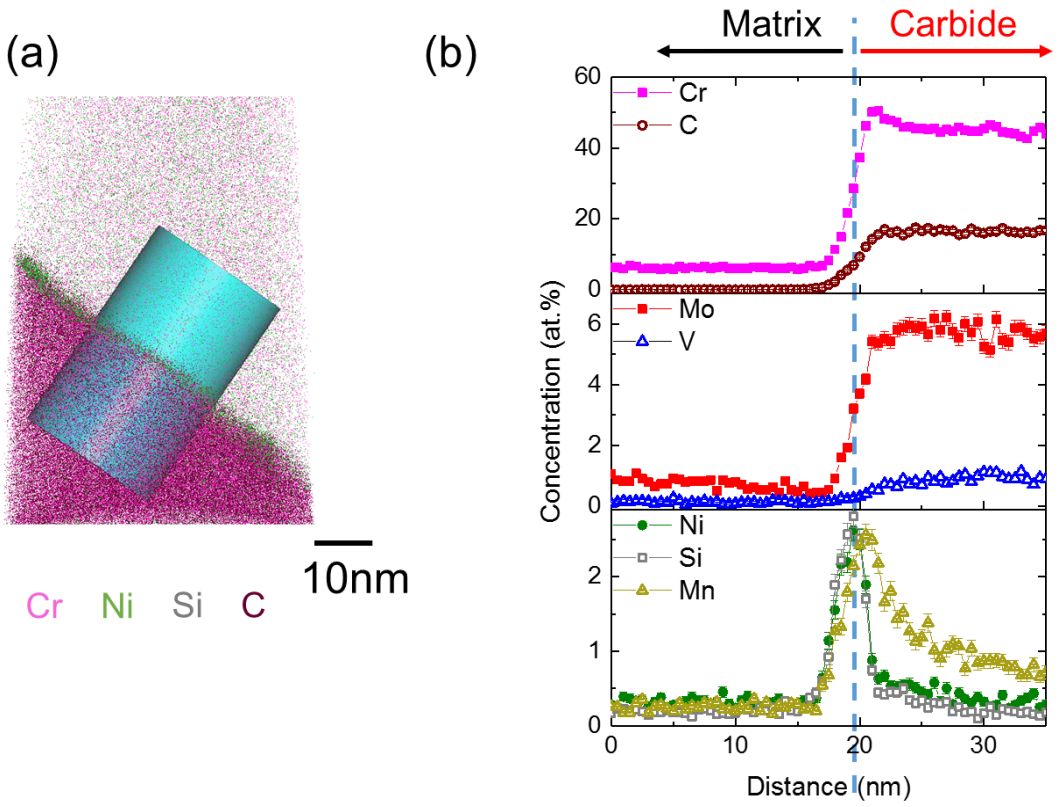

Figure 7-8 (a) Close-up of atom maps at the carbide/matrix interface (b) 1 D concentration profile across the interface

Smaller Cr-rich carbide particles were also observed in the 412 ^{o}C irradiated samples, as shown in Figure 7-5 (b). An iso-concentration surface of 5 at. % C was used to highlight the two carbide particles, Figure 7-9 (a) and the averaged concentration profile is shown in Figure 7-9 (b). Compared to the large pre-existing carbide, the smaller carbide particles do not have a sharp interface with the matrix. Towards the core region of the particles, the composition is similar to the large $M_{23}C_6$ carbide. A slight increase in the Si and Ni concentration in the carbide region can be noted. However, unlike the case of the large carbide particle, Ni/Si segregation to the carbide/matrix interface is not observed in small carbide particles.

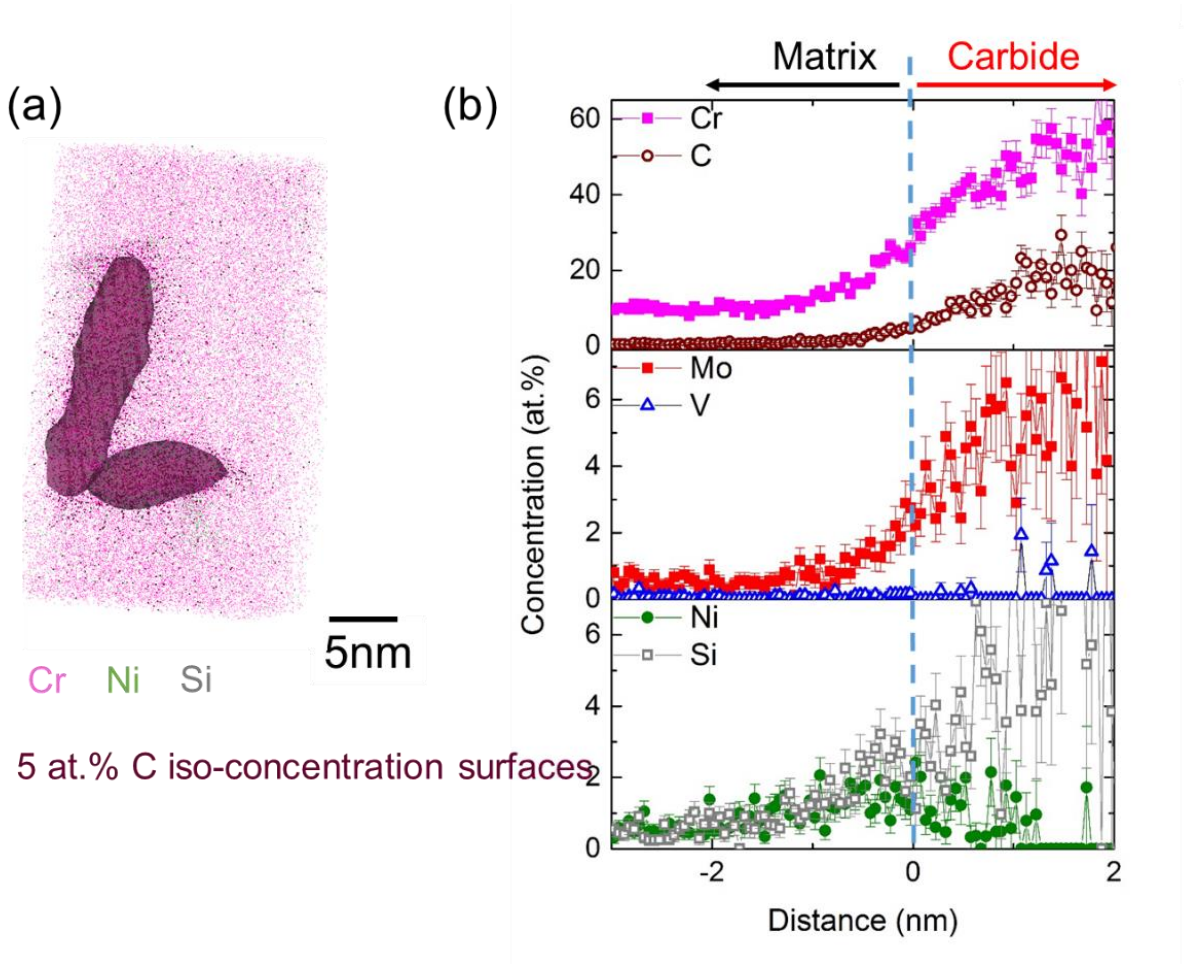

Figure 7-9 (a) Iso-concentration surface of 5 at. % C (b) Concentration proximity histogram across the carbide/matrix interface

7.2.8 Comparison to TEM results

Jiao et al. [196] conducted ChemiSTEM on the same material to examine the precipiates after BOR60 irradiation at Oak Ridge National Laboratory. Figure 7-10 shows the elemental maps of BOR60 irradiated T91 at 386 °. The microstructure is comparable to that obtained from APT. Pre-existing Cr-rich carbides, V/Nb-rich nitrides on the grain boundary and Ni/Si rich precipitates were all observed. Ni segregates to the grain boundary, which also matches the results from APT.

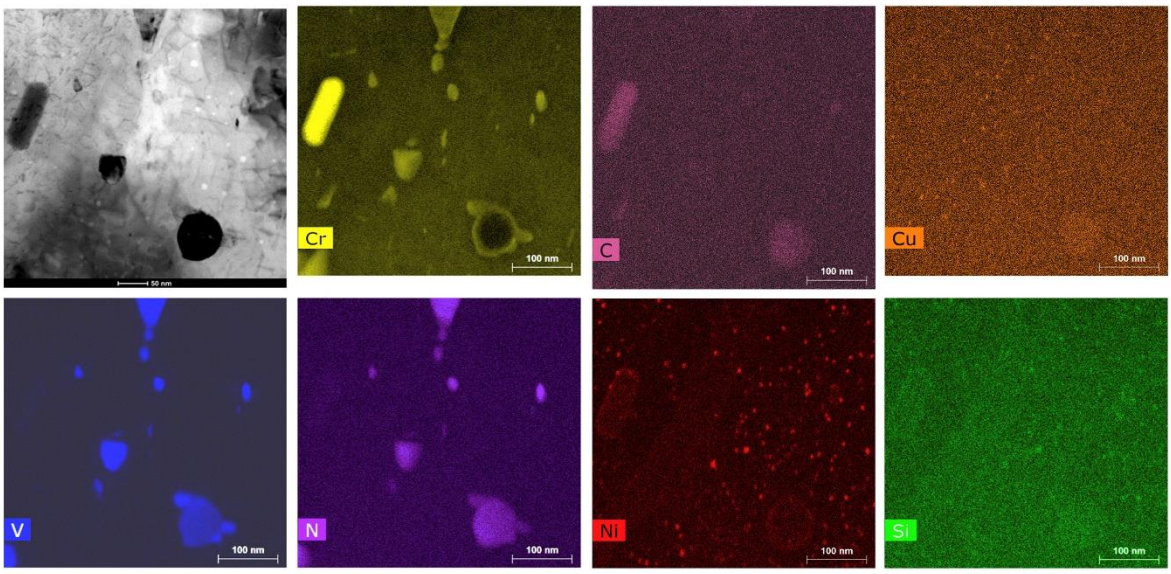

Figure 7-10 Elemental maps showing Cr-rich carbides, V-rich nitrides, Ni/Si-rich and Cu-rich precipitates in BOR60 irradiated T91 at 386 ^{o}C

7.3 Microstructure of T91 after dual ion beam irradiation

7.3.1 SEM images

The SEM images of DI-irradiated T91 at 432 ^{o}C and 406 ^{o}C are shown in Figure 7-11 (a) and (b) respectively. There is no significant difference observed between the two temperatures. The grain boundaries are decorated by large pre-existing carbide/nitride particles, which are similar to the single ion beam irradiated T91, as discussed in the previous chapter.

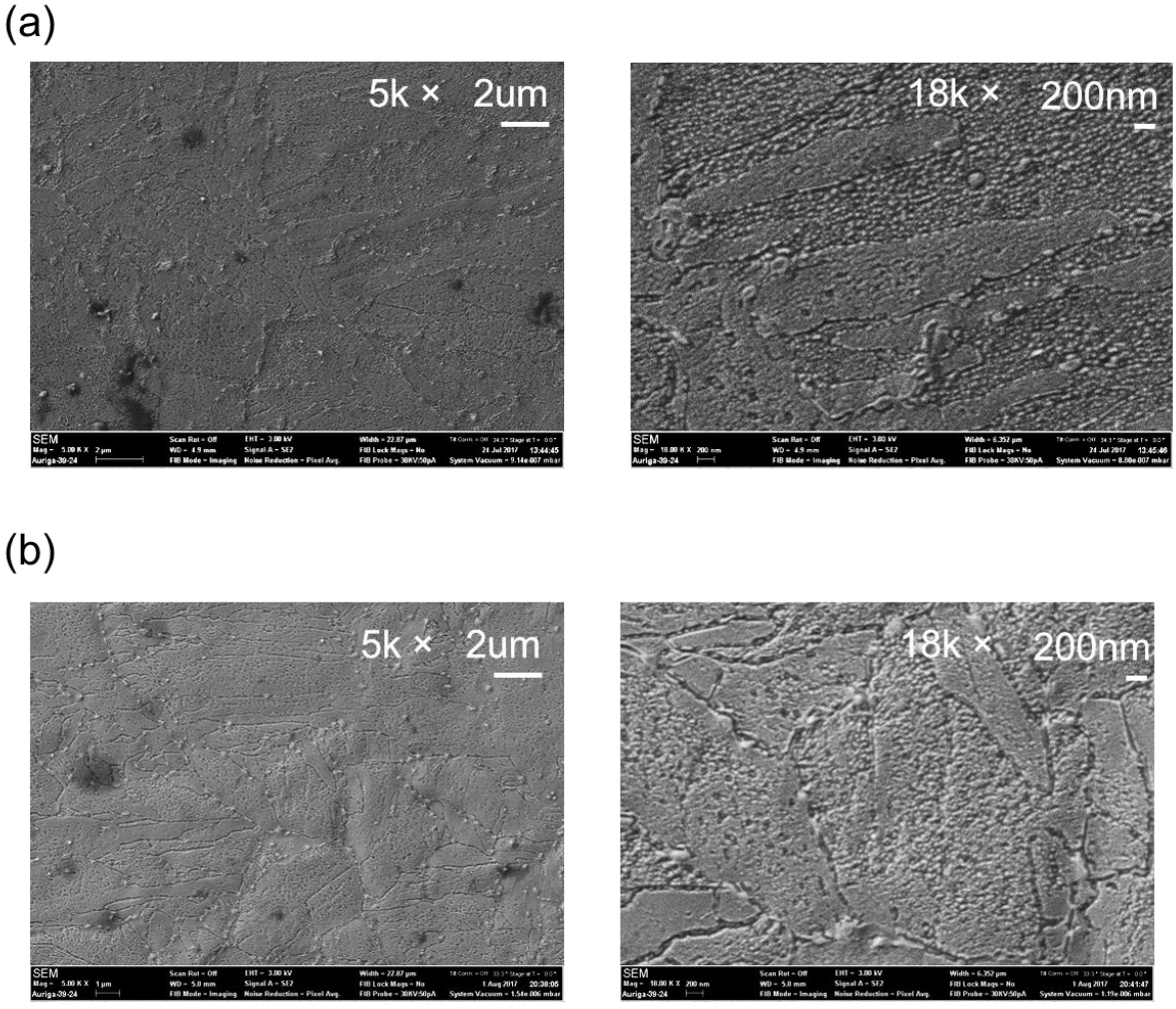

Figure 7-11 SEM images of T91 after dual ion beam irradiation at (a) 432 ^{o}C and (b) 406 ^{o}C

7.3.2 Atom maps after DI beam irradiation at 432 ^{o}C

Mn, Ni and Si are the main clustering elements in BOR60 irradiated T91. In the dual ion beam irradiated samples, Mn segregation is not obvious. The main clustering/segregation elements are Ni and Si.

The distributions of Ni and Si in dual ion irradiation at 432 ^{o}C are displayed in Figure 7-12. In Tip 1 and Tips 3-5, where the sample depth is 300 nm - 600 nm from the surface, the distribution of Ni and Si is clearly heterogeneous, with segregation to defects observed. Some of the regions of solute segregation are linear, while others are curved like segments

of dislocation loops. Also, small clusters of Ni and Si are observed along the segregation features. Only in the tips sampling 600 nm below the surface (Tip 6 and Tip 7), were clear MNS clusters observed.

Tip 2 also captured a pre-existing carbide on a grain boundary. Ni and Si enriches at the carbide/matrix interface and at the grain boundary. A grain boundary is also visible in Tip 8, where Ni and Si segregation can again be seen. Notably, in both Tip 2 and Tip 8, no clustering of Ni and Si is observed in the vicinity of grain boundaries. A V-rich nitride particle was present in Tip 7, Ni is found to be enriched at the nitride/matrix interface. Considering the overlap between Si and Ni, the peaks at 14 Da and 15 Da are treated separately inside the matrix and in the nitride, as described in § 6.3.2.

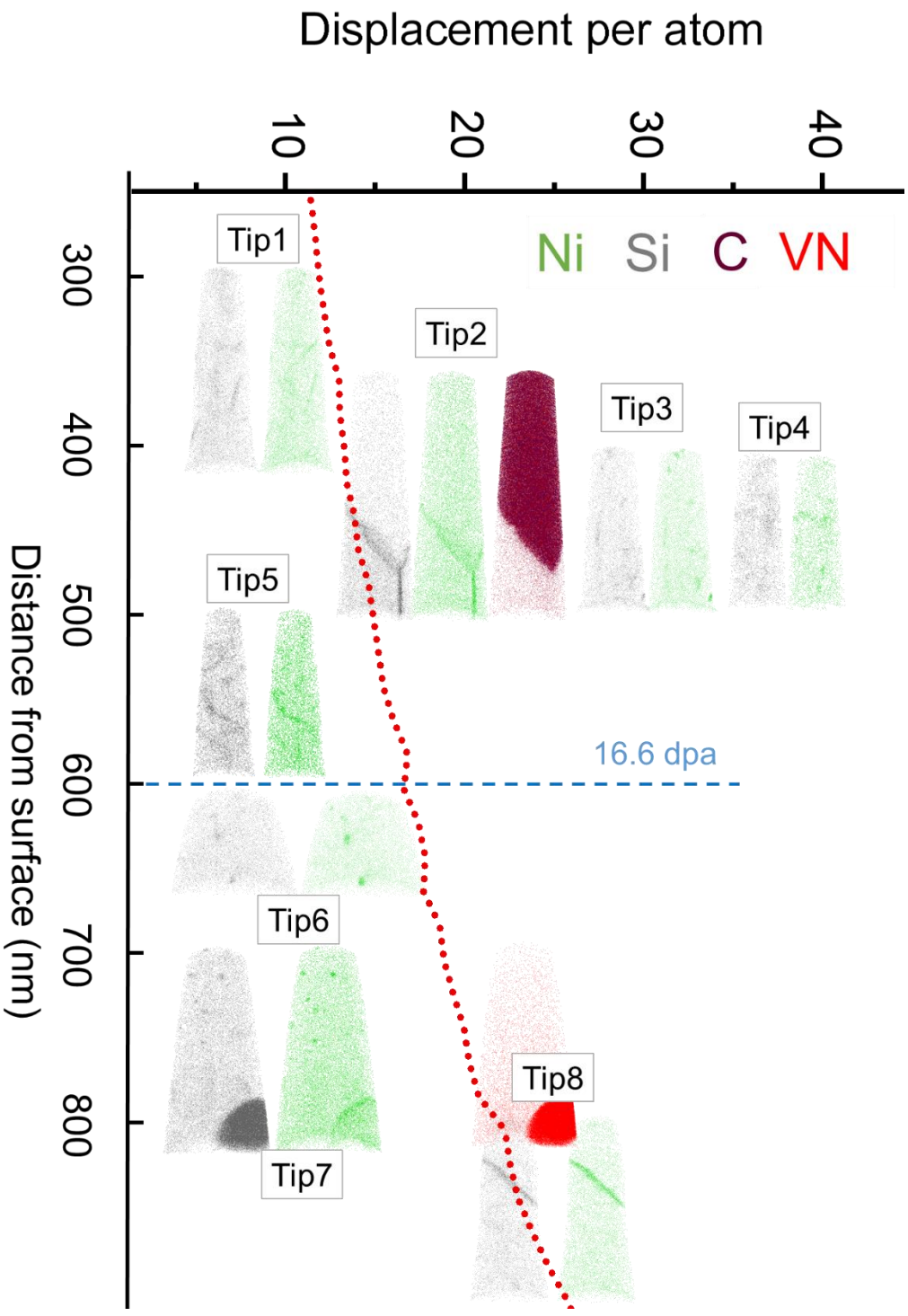

Figure 7-12 Atom maps of Ni and Si in dual ion irradiated T91 at 432 ^{o}C as a function of damage profile. The axis on the left indicates the depth of the samples form the surface and the scale of the analysed volume. The axis on the top represent the estimates obtained from 5MeV Fe++ irradiation. The He is doped between 500 nm - 1000 nm and the dose at 600 nm is 3.66 appm.

7.3.3 MNS-rich cluster composition after Dual ion beam irradiation at 432 ºC

In Tip 6 shown in Figure 7-12, distinct Ni and Si enriched clusters are observed. An iso-concentration surface where Ni + Si at 5 at. % was used to separate the clusters, and the corresponding proxigrams are shown in Figure 7-13 (b) and (c) respectively. Both of the clusters are enriched in Ni and Si. However, the magnitude of this enrichment differs significantly. In cluster 1, the peak Ni and Si content is about 7 at. % and 6 at. %. In cluster 2, this value increases to 30 at. % Ni, 15 at. % Si, while Mn is also enriched to 5 at. %. Another notable difference in the composition profile is the Cr content. Cluster 1 is Cr enriched, to nearly 30 at. % at the core. This is not seen in the clusters in the BOR60 irradiated samples. In Cluster 2, no obvious difference in clusters Cr content is seen compared to the matrix.

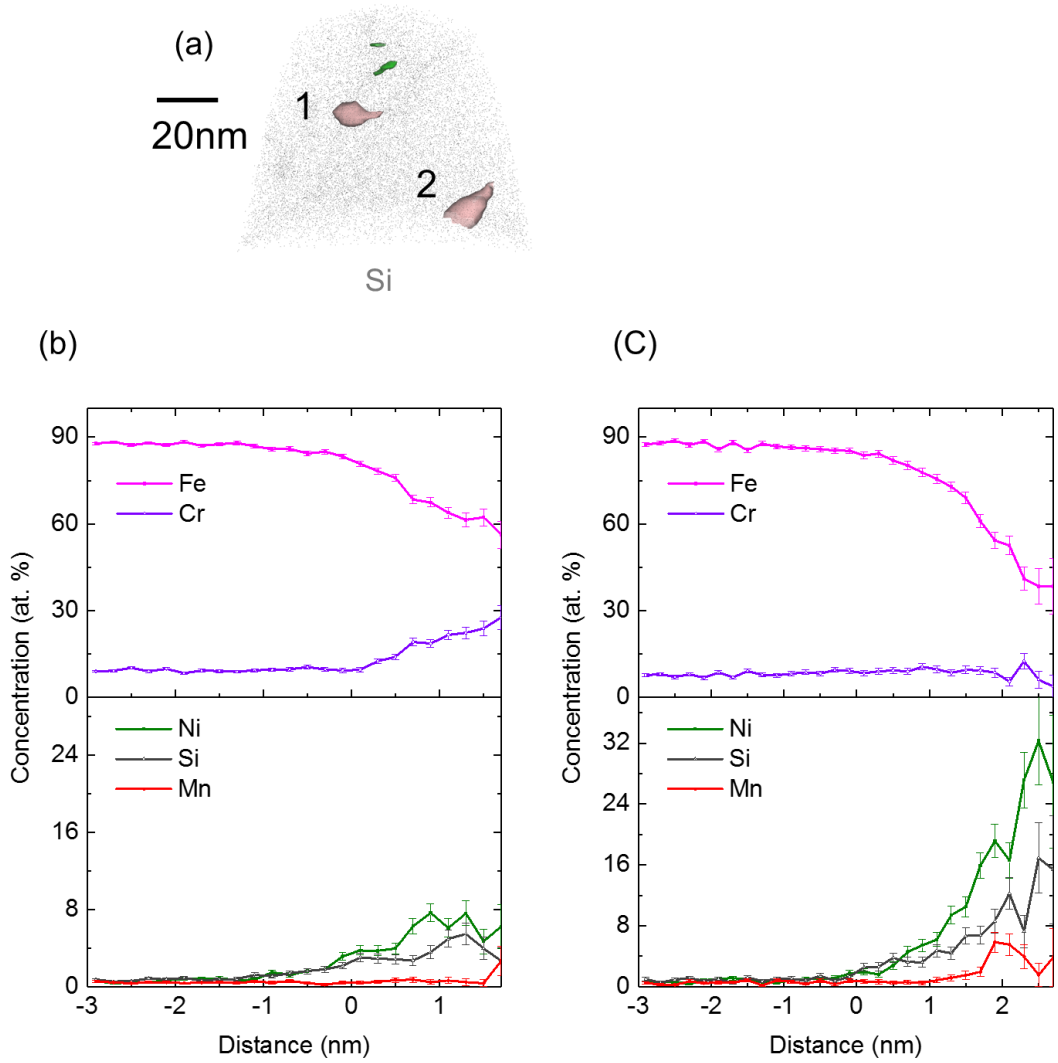

Figure 7-13 (a) Iso-concentration surfaces of Ni + Si at 5 at. % (b) proxigram of isosurface 1 (c) proxigram of isosurface 2

7.3.4 Solute segregation to dislocations after dual ion irradiation at 432 °C

After dual ion beam irradiation, at beneath the surface (300 nm – 600 nm), segregation of Ni and Si to defects is clearly visible from the atom maps. Some of the solute concentrated features are curved and shaped like parts of dislocation loops. An example is given in Figure 7-14, in which 2 at. % Ni + Si iso-concentration surfaces are displayed. Certain dislocation loop-like features are highlighted in pink, and the corresponding proxigrams are plotted in (b)-(e). Ni and Si are consistently observed to be enriched at these dislocations.

The highest concentration of both Ni and Si is 2 - 4 at. %. The behaviour of Cr is not consistent even in the same sample. Cr is enriched at the dislocations in Figure 7-14 (a) and (c), slightly depleted in (d) and does not show a significant difference in (e).

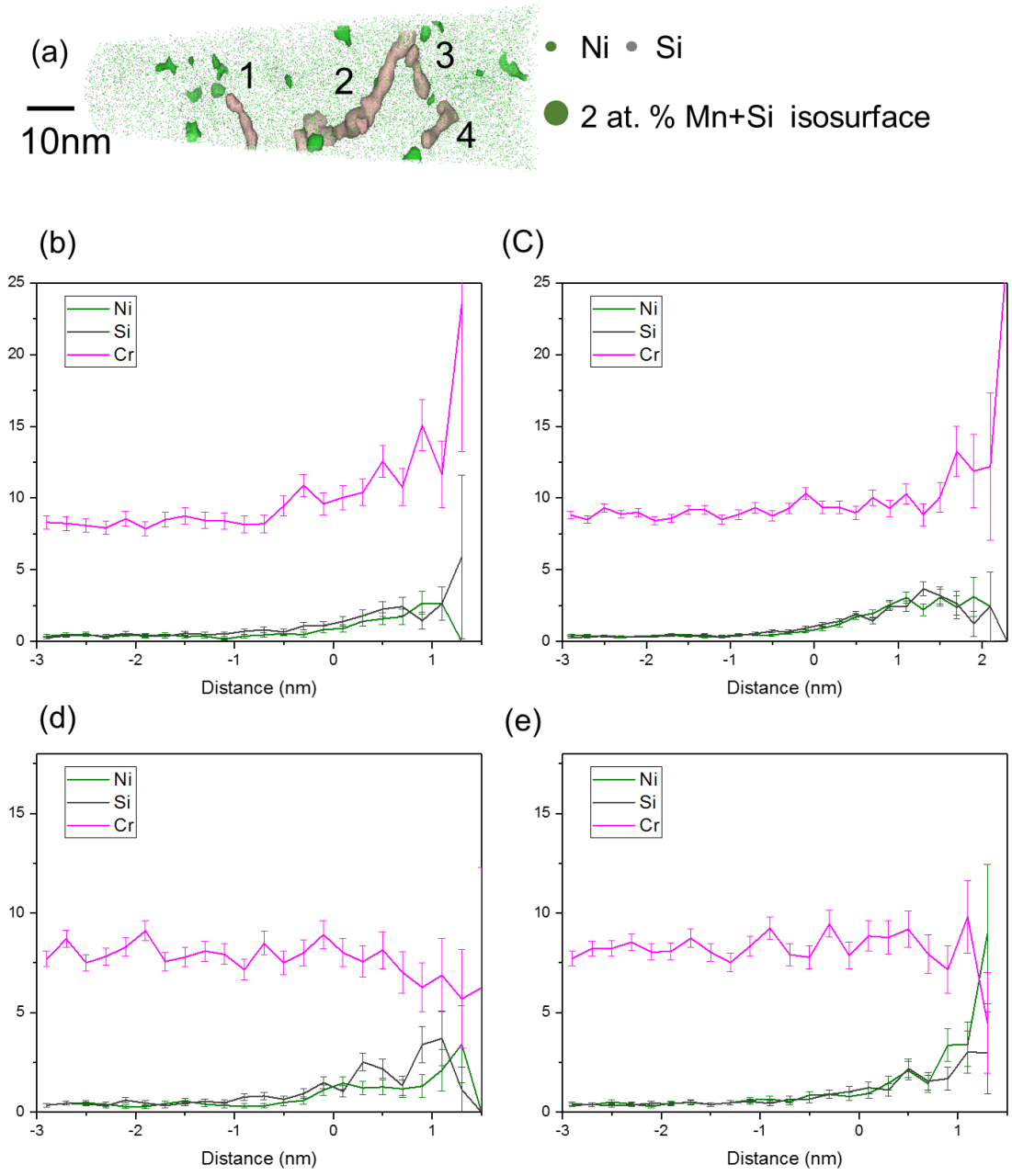

Figure 7-14 (a) Iso-concentration surfaces of Ni+Si at 2 at .% highlighting the segregation of the solutes to matrix defects. The dislocation loop-like features are highlighted in pink. The corresponding proxigrams of the four interfaces are plotted in (b)-(e)

7.3.5 Carbide/matrix interface after dual ion beam irradiation at 432 °C

Part of a pre-existing carbide on a grain boundary was captured in the APT analysis of DI irradiation at 432 °C. The depth of the carbide/matrix interface in this sample is ~ 500 nm. A 1D concentration file is plotted in Figure 7-15. The carbide is $M_{23}C_6$ type, and mostly enriched in Cr and some Mo. Segregation of Ni and Si to the carbide/matrix interface is observed. Compared to Figure 7-8 (b) the enrichment amplitude in DI irradiated sample is smaller than that in BOR60 irradiated sample. Unlike the BOR60 irradiation sample, Mn enrichment at the interface is not observed.

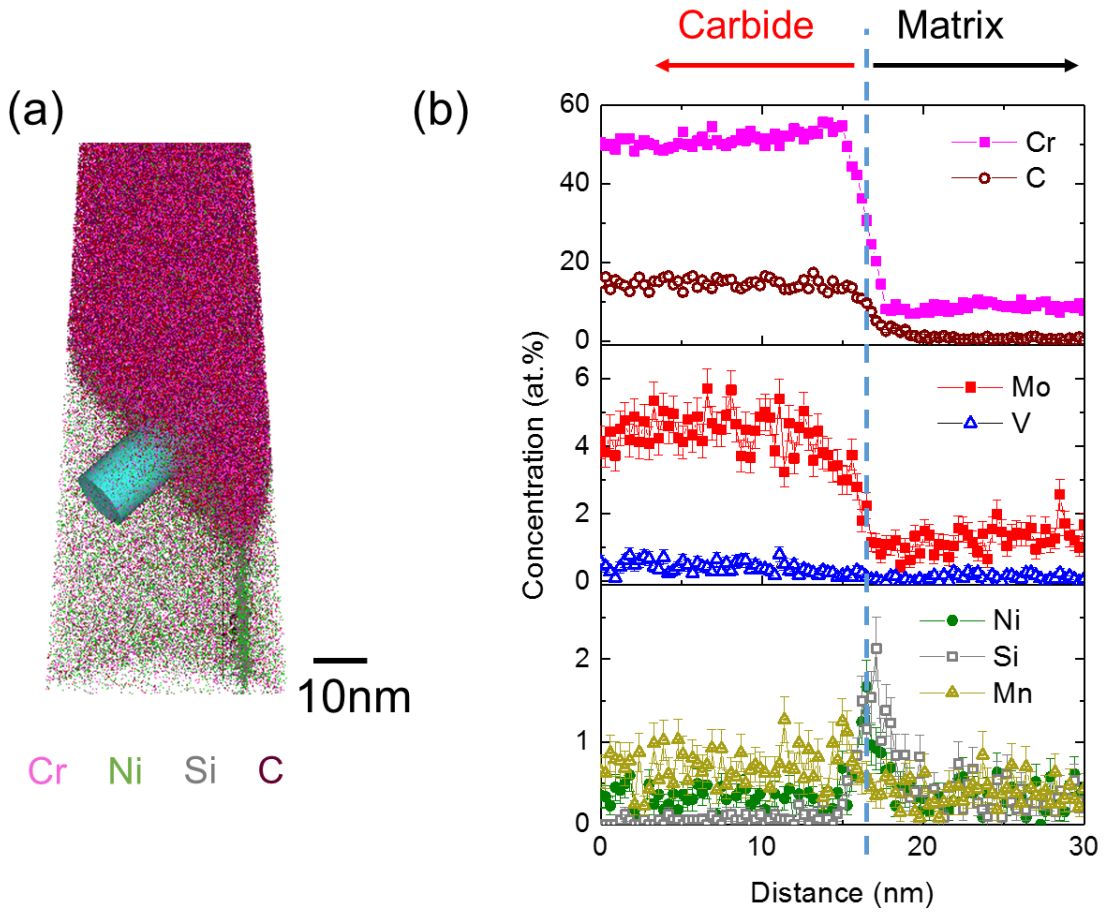

Figure 7-15 (a) Solute distribution at a carbide/matrix interface in T91 after DI irradiation at 432 °C (b) 1D concentration profile showing the composition of carbide/matrix interface

7.3.6 Grain boundary segregation after Dual ion beam irradiation

A grain boundary (GB) was visible (due to the solute segregation) in the same sample shown in Figure 7-15. The GB is 400 nm - 500 nm beneath the surface. A 1D concentration profile across the GB is plotted in Figure 7-16 (b). The grain boundary is enriched in Ni and Si. The peak concentration of Ni and Si is 1.5 at. % and 2.5 at. % respectively. There is no obvious change in Cr or Mn levels.

Another GB was observed in a different sample at the same irradiation condition (Tip 8 in Figure 7-12). The depth of the GB in this sample is 800 nm - 900 nm beneath the original sample surface. Figure 7-17 shows the atomic distribution of Ni, Si and corresponding 1D concentration profile across the GB. The peak concentration of Ni and Si exceeds 5 at. %. The concentration of Cr fluctuates significantly in the vicinity of the GB, and a slight depletion at the GB is observed. The GB excess of Ni and Si on the two grain boundaries are listed in Table 7-2.

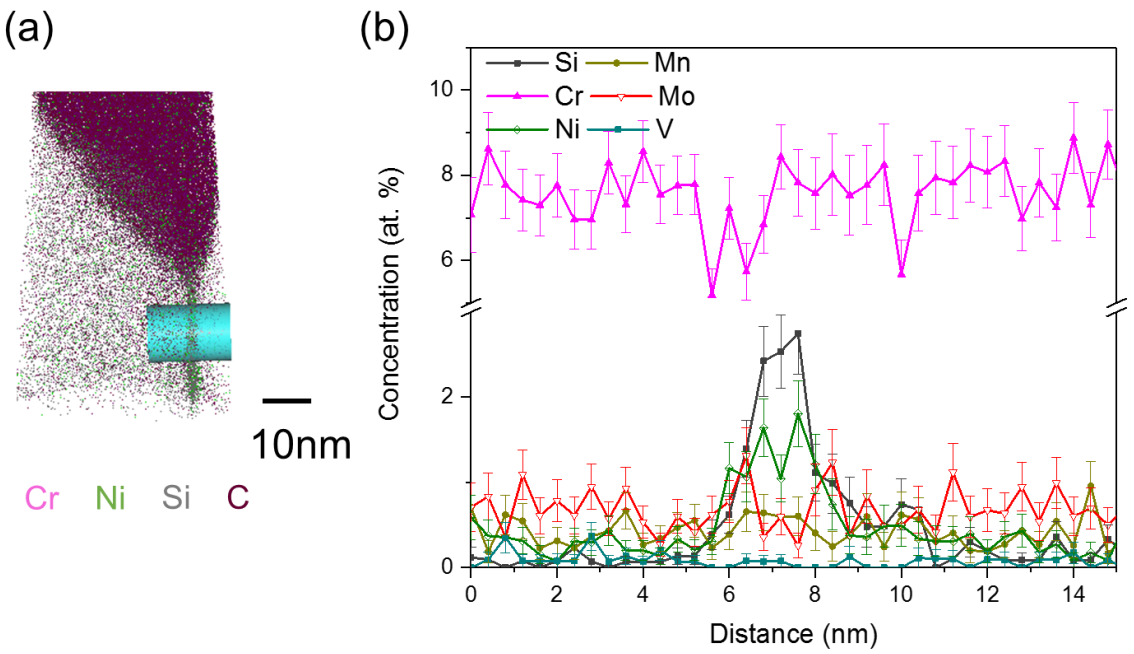

Figure 7-16 (a) atom maps of Cr, Ni, Si and C in the vicinity of a GB after DI irradiation at 432ºC to 16.6 dpa. The analysis volume is approximately 500 - 600 nm beneath the sample surface. (b) 1D concentration file across the GB

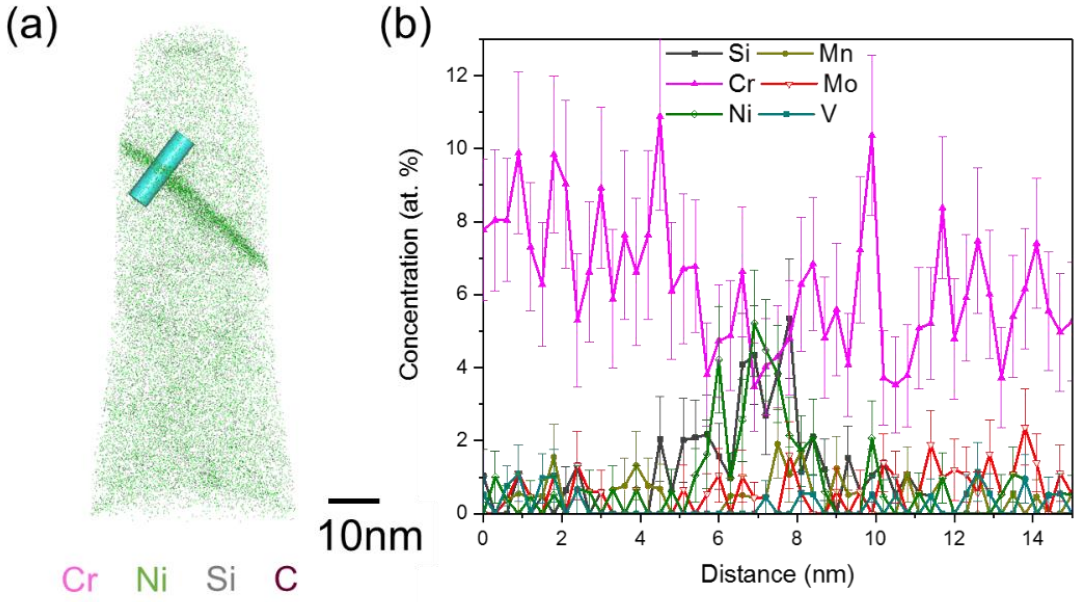

Figure 7-17 (a) atom maps of Ni and Si in the vicinity of a GB after DI irradiation at 432 ºC to 16.6 dpa. The analysis volume is approximately 800 - 900 nm beneath the sample surface (b) 1D concentration file across the GB

Table 7-2 Gibssian excess of gran boundary segregation of Cr, Ni and Si (10^{17} ions/m^2)

	GB at 500 nm	GB at 800 nm
Ni	24.6±0.6	68.3±0.8
Si	64.2±1.6	80.5±2.0

7.3.7 V-rich nitride composition after DI irradiation at 432ºC

A V-rich nitride was present in Tip 7. The nitride particle is 800 nm from the surface. A 5 at. % V iso-concentration surface is shown in Figure 7-18 (a) and the corresponding proxigram in (b). The V and N content is approximately 29 at. % and 32 at. % respectively. The Cr content increases from 5 at. % to 20 at. % in the nitride, while Nb is also enriched from 0 at. % in the matrix to 3 at. % in the nitride. Ni is also slightly enriched at the nitride/matrix interface. However, unlike the Ni enrichment seen at the Cr-rich carbide/matrix interface (in Figure 7-15), a sharp Ni peak is not observed.

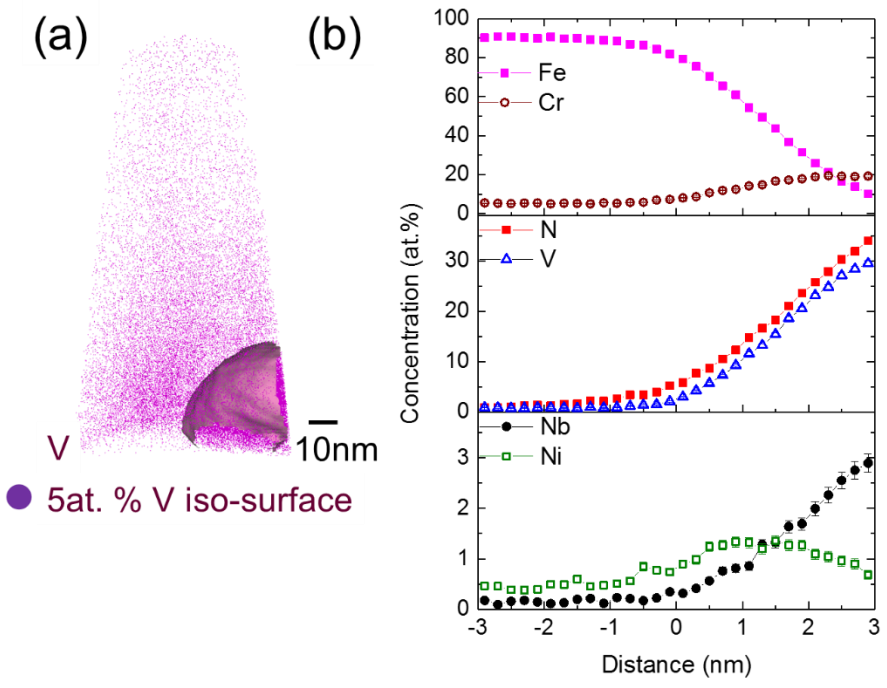

Figure 7-18 (a) 5 at. % V iso-concentraion surface (b) proximaty histogram of the V iso-surface

7.3.8 Atom maps after DI irradiation at 406 ºC

The Ni and Si atom maps of T91 steel after DI irradiation at 406 ºC as a function of irradiation depth are presented in Figure 7-19. With the exception of those from Tip 2, in all the samples, even below 600 nm, no distinct clustering was observed, which differs from both the resulting microstructure following BOR60 irradiation at 386 ºC, and the DI irradiation at the higher temperature of 432 ºC. Ni and Si were instead found to segregate to defects in the matrix.

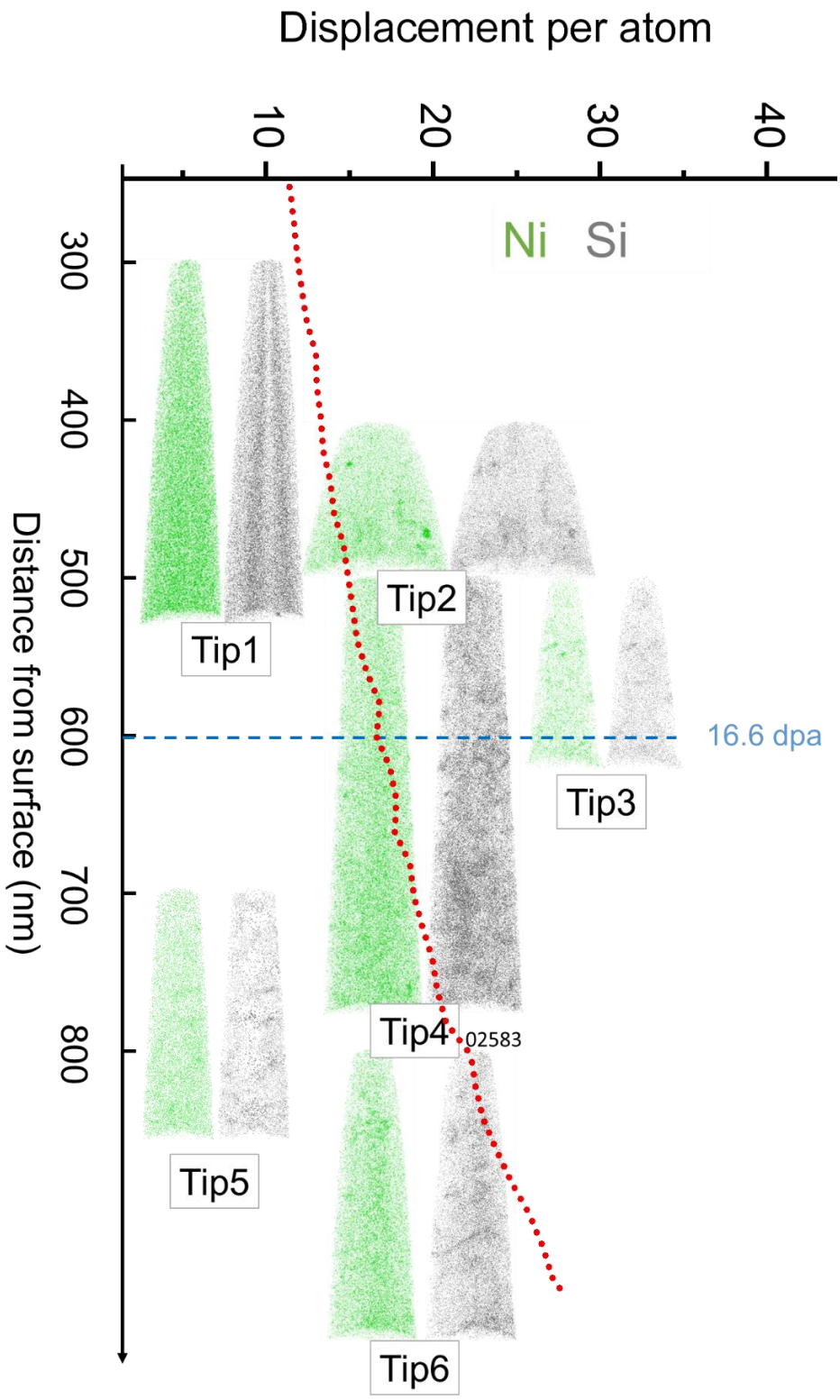

Figure 7-19 Atom maps of Ni and Si in dual ion irradiated T91 at 406 ºC as a function of damage profile. The axis on the left indicates the depth of the samples form the surface and the scale of the analysed volume. The axis on the top represent the dose estimates obtained from Fe++. The He is doped between 500 nm - 1000 nm and the dose at 600 nm is 3.66 appm.

7.3.9 Solutes segregation at defects in DI irradiated T91 at 406 ºC

In order to investigate the behaviour of solute segregation in further detail, 6 nm thick slice from Tip 4 and Tip 6, respectively, was generated, and the distribution of the main solutes are shown in Figure 7-20 (a). A small torus shaped dislocation loop is indicated in red arrow in Tip 4. Cr enriched clusters were also found at the defects. In some segregation sites, traces of C enrichment were also observed. This phenomenon is systematically observed in all the samples extracted 500 nm below the surface. Another similar example is shown in Figure 7-20 (b).

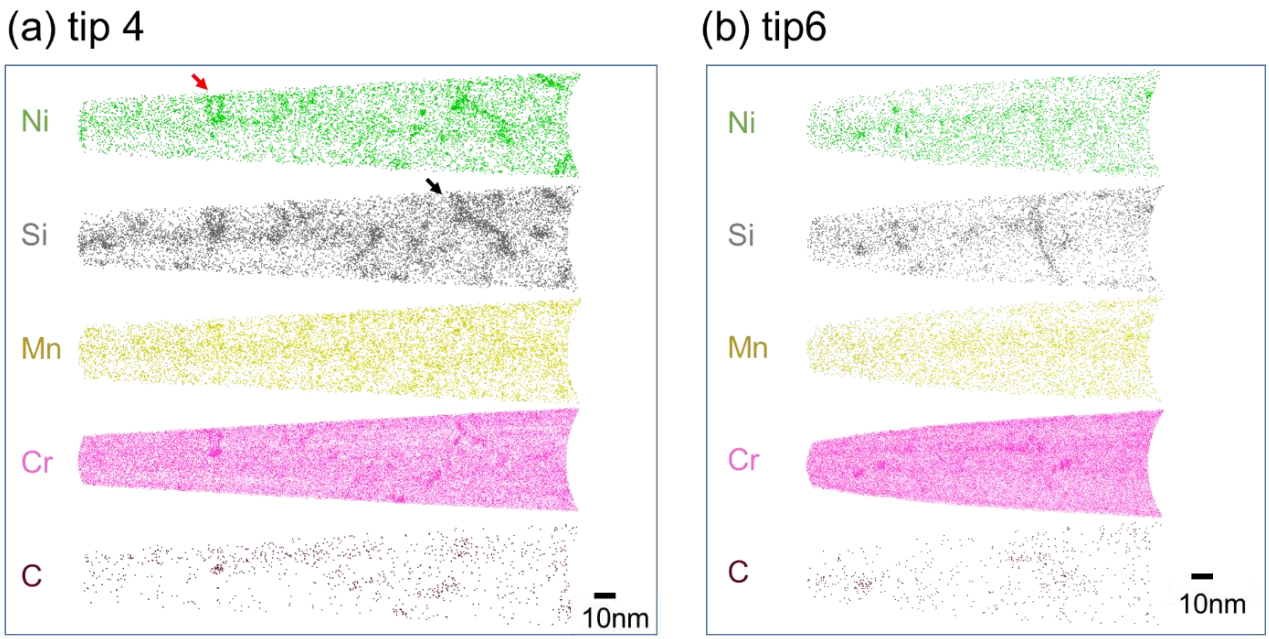

Figure 7-20 Atom maps within a 6 nm thick slice in (a) Tip 4 and (b) Tip 6. A small torus shaped dislocation loop is indicated in red arrow and a line shaped defect is indicated in black arrow

- Segregation profile

2 at. % Ni + Si iso-concentration surfaces were used to highlight the segregation to matrix defects in Tip 4, as shown in Figure 7-21 (a). Two proxigrams are plotted to show the

concentration of the main solutes at the defects. Ni and Si were found to enrich consistently in every iso-surface. In some cases, i.e. the dislocation loop indicated with the red arrow, Cr enrichment was observed. The Cr content in the centre exceeds 20 at. %. In other cases, i.e. the dislocation indicated with the black arrow, little change in Cr concentration can be seen. Similar results were observed consistently between different datasets.

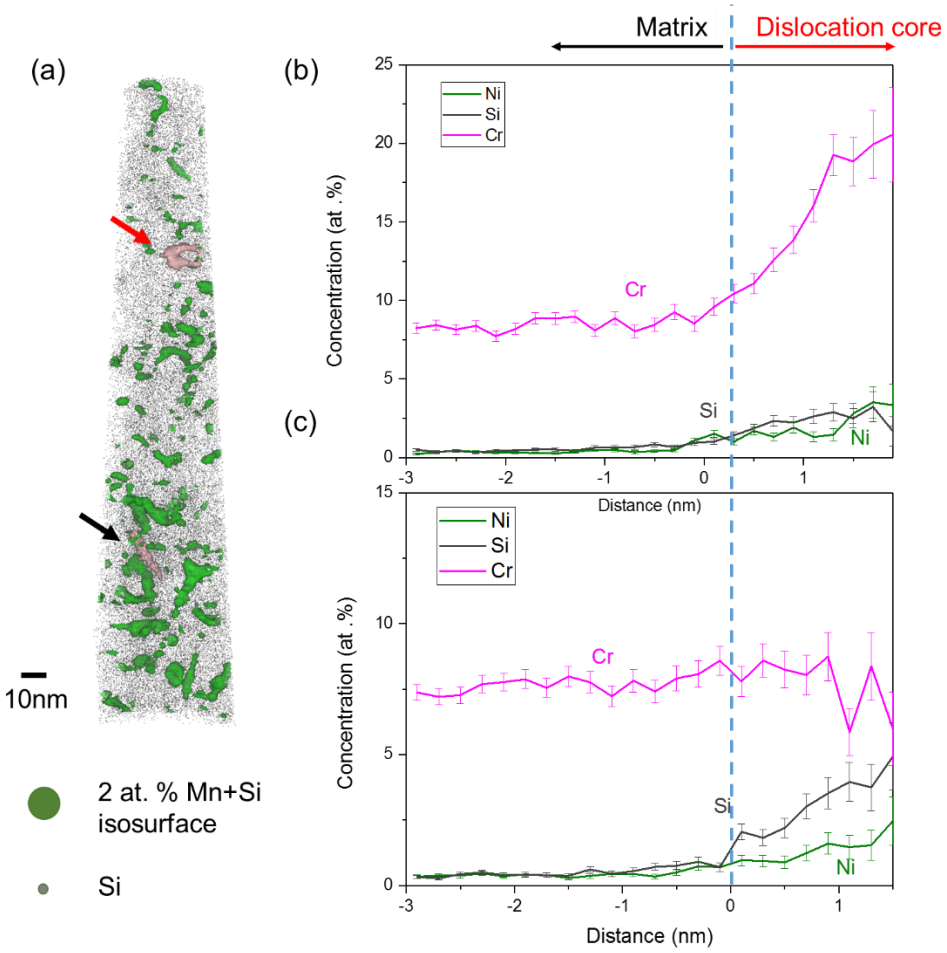

Figure 7-21 (a) Iso concentration surfaces of 2 at. % Mn+Si (b) proximity histogram of interface indicated by red arrow (c) proximity histogram of interface indicated by black arrow

7.4 Discussion: BOR60 vs DI irradiation

7.4.1 Nearest neighbour distribution of Ni-Ni

As shown in § 7.2, BOR60 irradiation produces significant levels of MNS clusters. In dual ion beam irradiated samples, however clustering is only observed at 432 ^{o}C and 600 nm below the surface. At 406 ^{o}C there is no distinct clustering of Ni, Si or Mn identified in the atom maps. Instead, diffuse MNS segregation to defects is observed. Thus, it is difficult to compare the cluster statistics between irradiation conditions, i.e. number density, fraction etc. An alternative approach was therefore used to directly compare the "degree of clustering" in dual ion beam and BOR60 irradiated T91. Figure 7-22 shows the 5th NN distribution of Ni-Ni pairs in a typical BOR60 irradiated T91 at 386 ^{o}C in (a) and DI irradiation at 406 ^{o}C in (b). There is a clear difference in the two distributions. In the BOR60 irradiated sample, there are two separate peaks in the Ni-Ni distributions, indicating two clear Ni distribution populations. The left peak at small Ni-Ni separations represents atoms of distinct clusters and the right peak with larger Ni-Ni distance represents contributions of Ni in the matrix. In contrast, there is no separate peak present in most of the DI irradiated samples, instead only a broadening in comparison to the random distribution is observed. The broadening is likely to be related to the solute segregation to the matrix defects (in Figure 7-19). In order to compare between samples, a V-value called "variation" is determined to be the normalized area between the actual distribution and the random distribution. The area in grey normalized by the total area in the figure is the V-value. If a sample is less homogeneous than another, the V-value is larger. Since the length of the APT analyses can extend longer than 200 nm, for the DI irradiated samples, each reconstruction can actually be representative of a range of sampling depth beneath the surface. In such cases, the samples are sectioned into 100 nm in length. If there are multiple

samples from a certain depth, i.e. from 400 nm - 500 nm, the V-value used is the average of all the samples in this region, and the V-value is plotted at 450 nm. The damage profile of neutron irradiation as a function of depth is flat [74]. The V-values of the BOR60 irradiated samples are therefore obtained by averaging the all the samples at the same irradiation conditions.

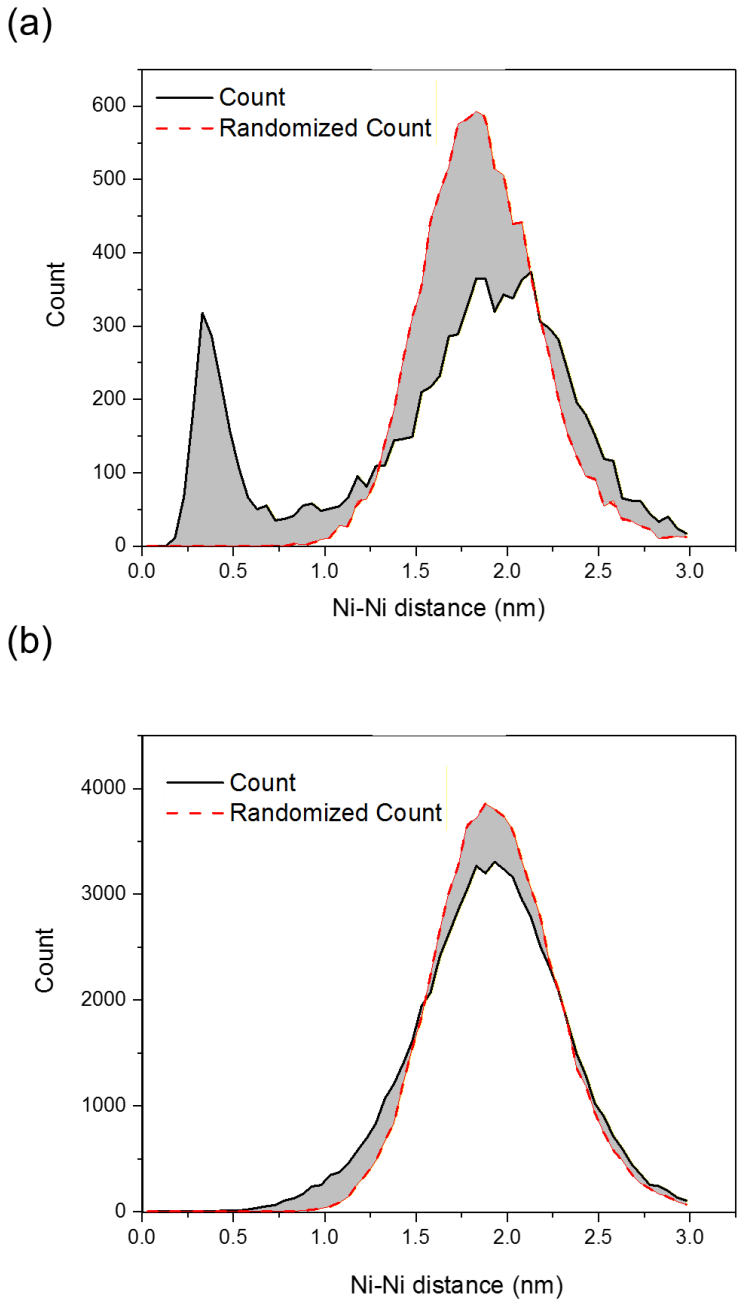

Figure 7-22 V-value of 5th NN distribution of Ni-Ni pair in (a) BOR60 irradiation at 386ºC. The sample is the same one as Figure 7-1 (b). (b) DI irradiation at 406 ºC. The sample is the same one as Tip 4 in Figure 7-19

- The effect of dose

The V-values of the dual ion beam irradiated samples as a function of depth and those of BOR60 irradiated samples are plotted in Figure 7-23. In both dual ion beam irradiations,

there is an overall trend of increasing V-value with increasing depth. One should also note that the peak damage of the ion beam irradiation is at 1.2 μm and the dose at 600 nm is supposed to be equal to that of BOR60 irradiation dose. Thus, an increase in damage level is expected as the dose increases. However, even at the same dose level, the V-value of the dual ion beam irradiation is smaller than the BOR60 irradiation, indicating a more homogeneous distribution of Ni in dual ion beam irradiation. The results are consistent with the visual observation from Ni atom maps in the APT analyses.

- The effect of irradiation temperature

From Figure 7-23, V-value of BOR60 irradiations at 412 ºC is higher than that of 386 ºC. For two DI irradiation temperatures, there is a significant difference in the V-values. This is also directly visible from the atom maps. The Ni and Si distribution in samples at the higher temperature (432 ºC) irradiation are less homogeneous than those of the lower temperature irradiation (406 ºC). This is consistent with the previous studies in the literature. Jin et al. [197] studied the Ni and Si enriched clusters in a 17Cr-11Ni steel austenitic steel irradiated at 400 ºC, 300 ºC and 200 ºC. Clustering of Ni and Si was reported in the higher temperature irradiation (400 ºC) and not at lower temperatures (300 ºC and 200 ºC).

In this study, a temperature shift of 20 ºC is applied to the ion irradiation. In the current case of MNS-rich clusters, the "degree of clustering" in both dual ion beam irradiation condition is lower than that of BOR60 irradiation. The higher temperature DI irradiation (432 ºC) produces level of clustering closer to the BOR60 irradiation compared to lower temperature DI irradiation (406 ºC). Thus, in order to replicate the BOR60 irradiation, a larger temperature shift than 20 ºC appears to be necessary in terms of MNS clustering behaviour.

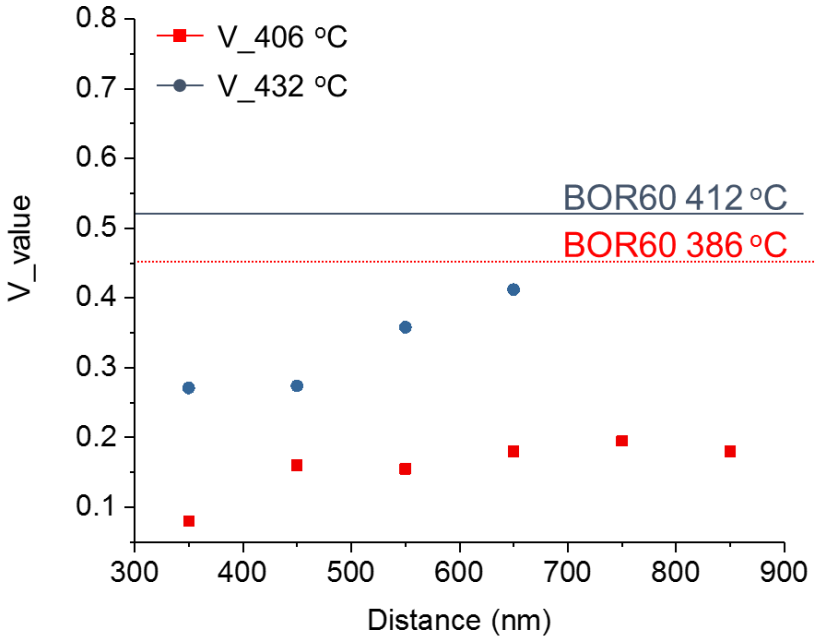

Figure 7-23 The variation of 5th NN distribution of Ni T91 steel as a function of depth for DI irradiation at 406 °C and 432 °C, respectively. Blue and red lines are V-value obtained from samples irradiated in BOR60 at 386 °C and 412 °C

7.4.2 Cr segregation to dislocation loops

Dislocations can act as sinks for defects, and segregation of solutes is expected at dislocation lines/loops. The enrichment of Ni and Si at dislocations have been consistently observed in different irradiated steel systems [83,198–200]. However, similar to the Cr behaviour at grain boundaries, large variations in segregation/depletion behaviour have been observed for Cr. In austenitic steels, Cr is found to deplete on dislocation loops [1-2]. In F/M steels, different studies have reported different observations. Yoshida et al. [200] investigated segregation to dislocation loops in electron-irradiated Fe–10% Cr and Fe–10% Cr–1% Ni alloys, and found the enrichment of Cr at the dislocation loop. Neklyudov and Voyevodin [83] also reported the enrichment of Cr on dislocations in an ion irradiated 13Cr–2Mo–Nb ferritic steel. Note that both of these results were obtained using energy

dispersive X-ray spectroscopy (EDS). Ono et al. [201] reported the enrichment of Cr on dislocation loops in He+ irradiated Fe-9Cr steel by STEM-EELS. Jiao and Was [96] directly observed segregation of Cr in proton irradiated T91 steel. However, the same work also reported depletion of Cr on dislocations in heavy-ion irradiated HCM12A steel. The inconsistency may be explained by the non-homogeneous distribution of Cr-rich carbide precipitates, resulting in large fluctuations in the local Cr content.

In the BOR60 samples, a trace of Cr segregation to dislocation loops is only observed in one sample (Figure 7-3). After dual ion beam irradiation, segregation of Cr is however clearly observed in all the samples below 500 nm from the surface. This can be attributed to the fact that the dose rate in the ion beam irradiation is much higher than that of neutron irradiation. The high dose rate is known to result in a higher loop density [202]. Thus, the segregation of Cr is more obvious in the dual ion beam irradiated samples than in the BOR60 irradiated ones.

7.4.3 Carbide/matrix interface

From both BOR60 and dual ion beam irradiation results, a small variation is found in carbide compositions compared to the single ion irradiation results. Ni and Si are found to consistently segregate to carbide matrix interface. Due to the lack of enough repeated data, conclusions cannot however be drawn to the segregation magnitude. Mn is only found to segregate to the pre-existing carbide/matrix interface in BOR60 irradiated sample. In DI irradiation, the segregation of Mn is not observed. Also, as seen in the previous chapter, in single ion beam irradiation results, Mn segregation is again not observed.

8 Conclusions

One of the key issues determining the lifetime of the nuclear reactor is the stability of the structural materials operating at high temperature under high neutron flux. Despite the fact that Fe-Cr based steels are widely used as structural materials, the atomic-scale mechanisms of microstructural changes under heat treatment/irradiation are not fully understood. The aim of this work has been to improve this understanding of microstructural evolution using atom probe tomography. This work has contributed new insights to this research field through the following findings:

8.1 Characterizing Fe-Cr based steels using APT

The nano-sized features formed after heat treatment or irradiation require ultra-high-resolution techniques to fully characterize their composition and structure. APT is considered to be one of the best techniques for this purpose, but care needs to be taken when interpreting the data.

- The importance of correctly calibrating the APT reconstruction has been demonstrated.
- A suitable method to determine appropriate cluster selection parameters has been established, minimizing the sensitivity of these on the measured number density and volume fraction of the precipitates.

8.2 Microstructural changes of 17-4PH after heat treatment

17-4PH steel was heat treated at two precipitation hardening temperatures (480 and 590 ^{o}C). Atom probe tomography has offered new insights into the precipitation sequences within this steel.

- At 480 ^{o}C, the precipitation sequence can be summarized as: segregation of CrN/NbN to dislocation and matrix defects → CRPs and Nb-rich precipitates → Cr-rich precipitates → MNS phase. At 590 ^{o}C, no Cr-rich precipitates or MNS phase were present, consistent with the prediction from the phase diagram.
- The initially nucleating precipitates act as favoured sites for heterogeneous nucleation of subsequent phases.
- Precipitation hardening models have been successfully applied to the CRPs and Cr-rich precipitates and the estimated hardening contributions from the precipitates show a good agreement with the Vickers hardness testing results. The models confirm the unchanging hardness value at 480 ^{o}C, despite the significantly changing microstructure, is due to the emergence of the Cr-rich phase counteracting the effects of the coarsening CRPs. At 590 ^{o}C however, there is no such counteracting effects due to the absence of Cr-rich precipitates, which can therefore explain the monotonic hardness decrease noted at this temperature.

8.3 Effects of ion/reactor irradiation on T91 steel

SI, DI irradiation and reactor irradiation has been performed on T91 steel samples. The following conclusions can be drawn:

- The formation of irradiation induced MNS-rich clusters is dependent on irradiation type, dose and temperature. MNS-rich clusters were observed in all the T91 steel specimens irradiated in BOR60, both at 386 ^{o}C and 412 ^{o}C. After dual ion beam irradiation, clustering was only observed in specimens irradiated at higher temperature (432 ^{o}C) and in the higher dose region (i.e 600 - 800 nm beneath the surface). When the irradiation temperature was lowered to 406 ^{o}C, segregation of Ni and Si to defects

was observed, however, distinct clusters were not present. After single ion irradiation at higher temperature (470 ^{o}C), no clustering/segregation was observed in the matrix.

- Cr-rich carbide and V-rich nitride particles were observed after SI, DI and BOR60 irradiation. The composition of the carbide and nitride particles remained stable after irradiation, while the ratio matches $M_{23}C_6$ and MN type respectively. Segregation of Ni and Si to the carbide/matrix interface was consistently observed after irradiation, which was not seen in regions subjected only to the same temperature but not the radiation dose.
- Segregation of both Ni and Si to the grain boundary was consistently observed in T91 after irradiation. The magnitude of the segregation increased after irradiation.
- In terms of irradiation-induced precipitates, dual ion beam irradiation at higher temperature (432 ^{o}C) produces microstructures comparable to BOR60 reactor irradiation, indicating a greater temperature shift is preferable to better match the reactor irradiation in this case.

8.4 Implications of the findings

The study on the heat treatment of 17-4PH steel shows that the microstructure is dependent on the heat treatment time and temperature. It is clearly possible to tune desired properties by controlling the heat treatment conditions. The key findings in terms of industrial application of 17-4PH are: (i) The hardness of 17-4PH following heat treatment at 480 ^{o}C is 15 % higher than that of 590 ^{o}C. Thus, when higher strength/hardness is required, a lower precipitation hardening temperature is preferable. (ii) Cr-rich precipitates form between 2 - 24 h at 480 ^{o}C. It is known that chromium contributes to the corrosion resistance of stainless steels by forming protective Cr-oxide/hydroxide passive film [203]. Thus, an ageing time between 0.5 - 2 h is recommended at 480 ^{o}C to eliminate Cr-rich precipitate

formation so as to maintain the corrosion resistance of this material. (iii) At 590 ^{o}C, reverse austenite was observed after ageing for 24 h. This can cause a decrease in strength and alteration of the matrix chemistry. Thus, a short heat treatment time is recommended to prevent formation of reversed austenite, i.e. 10 min - 2h at this temperature.

The study on irradiation of T91 directly compared irradiation induced clustering of DI and BOR60 irradiated T91. The extent of solute cluster formation in BOR60 is shown to be more significant than that after ion irradiation at the same dose in this study. The ion irradiation induced microstructure is strongly dependent on the dose and irradiation temperature. In general, the "degree of clustering" increases with increasing dose and temperature. Therefore, by adjusting the irradiation parameters (i.e. temperature), it is possible to yield comparable irradiation induced features (i.e. precipitates) to those from reactor irradiation. It should be point out that if we change the temperature, the thermodynamics will be affected and therefore it is a complicated matter. Despite of the challenges, if we can successfully predict the conditions for ion irradiation to match reactor irradiated microstructure, then this has implications for lots of future experiments where handling neutron irradiated materials can be a problem, or to be able to more easily simulate materials effects in a wide range of potential reactor conditions. An especially important implication is that we could simulate much longer in-service exposure times - this would be critical for predicting safe operational lifetimes of current reactors and design of advanced reactors.

8.5 Future work

One important future research direction of heat treatment of 17-4PH lies in the investigation of the microstructural changes after the long-term ageing at in-service temperature (300 –

350 ºC). This could provide direct information about how this material behaves at in-service temperatures and can be directly related to the industrial application of this material. As discussed in Chapter 2, under 400 ºC spinodal decomposition of Cr can occur after long time ageing. Another important aspect is to study the effect of precipitation hardening conditions on the in-service behaviour. This study shows that precipitation hardening at 480 ºC and 590 ºC result in very different microstructures. How the pre-existing precipitates evolve at in-service temperatures and the resulting effects on the mechanical properties are both interesting and complex, requiring significant future work. From this study one can see that APT is very suitable to study this material due to the extensive atomic scale changes in microstructure and microchemistry. Complementary TEM would further improve the understanding since it can provide clear information on the structure of precipitates, along with better statistics on number densities and volume fractions at a larger length scale.

As for the field of using dual ion beams as a surrogate of reactor irradiation, the most obvious future research direction is the investigation into microstructure changes at different ion irradiation conditions. For example, there is a clear link between the ion irradiation temperature and the resulting microstructure, and this needs further investigation to better match reactor irradiation. A temperature shift larger than 20 ºC is suggested at the same dose to match the reactor irradiation.

In order to predict the surrogate ion irradiation parameters, a fuller understanding of the microstructure is required. This study has shown that APT and chemiSTEM are highly complementary. TEM is essential to characterise voids and dislocation loops. In the future, Transmission Kikuchi Diffraction (TKD) can be added in to better characterise the nature of grain boundaries. One should note that different irradiation induced features may require

different ion irradiation conditions to emulate the reactor irradiated results, i.e. the irradiation parameters to produce equivalent GB segregation are not necessarily the same as those to produce similar sizes and number densities of dislocation loops or voids. This is another reason why characterisation of the full range of microstructural features is required. Although it is beyond the scope of the current study, the mechanical properties of irradiated specimens are also critical to fully understand the material behaviour, and likewise require significant future work. At the same time, a comprehensive theoretical framework needs to be established. If we can simulate different irradiation effects using ion irradiation with more confidence, the development of materials to withstand the extended lifetime of current reactors or enable development of advanced reactor concepts can be greatly accelerated.

9 References

[1] International Agency for Atomic Energy, International status and prospects for nuclear power 2017, 2017.

[2] Nuclear Energy Agency, Nuclear Energy Data, 2016.

[3] IEA, World Energy Outlook 2016, Int. Energy Agency. (2016) 1–684. doi:http://www.iea.org/publications/freepublications/publication/WEB_WorldEnergyOutlook2015ExecutiveSummaryEnglishFinal.pdf.

[4] J.T.A. Roberts, Structural Materials in Nuclear Power Systems, Springer US, Boston, MA, 1981. doi:10.1007/978-1-4684-7194-6.

[5] K.L. Murty, I. Charit, Structural materials for Gen-IV nuclear reactors: Challenges and opportunities, J. Nucl. Mater. 383 (2008) 189–195. doi:10.1016/j.jnucmat.2008.08.044.

[6] F. Danoix, P. Auger, Atom Probe Studies of the Fe–Cr System and Stainless Steels Aged at Intermediate Temperature, Mater. Charact. 44 (2000) 177–201. doi:10.1016/S1044-5803(99)00048-0.

[7] S.J. Zinkle, J.T. Busby, Structural materials for fission & fusion energy, Mater. Today. 12 (2009) 12–19. doi:10.1016/S1369-7021(09)70294-9.

[8] Y.Q. Wang, B. Yang, J. Han, F. Dong, Y.L. Wang, Localized Corrosion of Thermally Aged Cast Duplex Stainless Steel for Primary Coolant Pipes of Nuclear Power Plant, Procedia Eng. 36 (2012) 88–95. doi:10.1016/j.proeng.2012.03.015.

[9] A.A.F. Tavassoli, E. Diegele, R. Lindau, N. Luzginova, H. Tanigawa, Current status and recent research achievements in ferritic/martensitic steels, J. Nucl. Mater. 455 (2014) 269–276. doi:10.1016/j.jnucmat.2014.06.017.

[10] R.L. Klueh, A.T. Nelson, Ferritic/martensitic steels for next-generation reactors, J. Nucl. Mater. 371 (2007) 37–52. doi:10.1016/j.jnucmat.2007.05.005.

[11] S.J. Zinkle, G.S. Was, Materials challenges in nuclear energy, Acta Mater. 61 (2013) 735–758. doi:10.1016/j.actamat.2012.11.004.

[12] P. Yvon, F. Carré, Structural materials challenges for advanced reactor systems, J. Nucl. Mater. 385 (2009) 217–222. doi:10.1016/j.jnucmat.2008.11.026.

[13] A. Kohyama, A. Hishinuma, D.S. Gelles, R.L. Klueh, W. Dietz, K. Ehrlich, Low-activation ferritic and martensitic steels for fusion application, J. Nucl. Mater. 233–237 (1996) 138–147. doi:10.1016/S0022-3115(96)00327-3.

[14] S. Chu, A. Majumdar, Opportunities and challenges for a sustainable energy future.,

Nature. 488 (2012) 294–303. doi:10.1038/nature11475.

[15] International Atomic Energy Agency, Nuclear Technology Review, 2014.

[16] IEA, Energy Technology Perspectives 2016, Iea. (2016) 14. doi:10.1787/energy_tech-2014-en.

[17] B. Frost, Materials Science and Technology, Volume 10B, Nuclear Materials, Masters Thesis. (1996).

[18] T. Allen, J. Busby, M. Meyer, D. Petti, Materials challenges for nuclear systems, Mater. Today. 13 (2010) 14–23. doi:10.1016/S1369-7021(10)70220-0.

[19] C. Fazio, A. Alamo, A. Almazouzi, S. De Grandis, D. Gomez-Briceno, J. Henry, et al., European cross-cutting research on structural materials for Generation IV and transmutation systems, J. Nucl. Mater. 392 (2009) 316–323. doi:10.1016/j.jnucmat.2009.03.020.

[20] L.K. Mansur, A.F. Rowcliffe, R.K. Nanstad, S.J. Zinkle, W.R. Corwin, R.E. Stoller, Materials needs for fusion, Generation IV fission reactors and spallation neutron sources – similarities and differences, J. Nucl. Mater. 329–333 (2004) 166–172. doi:10.1016/j.jnucmat.2004.04.016.

[21] H.K.D.H. Bhadeshia, S.R. Honeycombe, Steels, Elsevier, 2006. doi:10.1016/B978-075068084-4/50011-X.

[22] O.K. Chopra, A.S. Rao, A review of irradiation effects on LWR core internal materials - IASCC susceptibility and crack growth rates of austenitic stainless steels, J. Nucl. Mater. 409 (2011) 235–256. doi:10.1016/j.jnucmat.2010.12.001.

[23] K.H.H. Lo, C.H.H. Shek, J.K.L.K.L. Lai, Recent developments in stainless steels, Mater. Sci. Eng. R Reports. 65 (2009) 39–104. doi:10.1016/j.mser.2009.03.001.

[24] C. Cawthorne, E.J. Fulton, Voids in Irradiated Stainless Steel, Nature. 216 (1967) 575–576.

[25] F.A. Garner, M.B. Toloczko, High dose effects in neutron irradiated face-centered cubic metals, J. Nucl. Mater. 206 (1993) 230–248.

[26] V.S. Neustroev, F.A. Garner, Severe embrittlement of neutron irradiated austenitic steels arising from high void swelling, J. Nucl. Mater. 386–388 (2009) 157–160. doi:10.1016/j.jnucmat.2008.12.077.

[27] G. Krauss, Steels: heat treatment and processing principles, ASM Int. 1990,. (1990) 497.

[28] A. Kelly, R.B. Nicholson, Precipitation hardening, Prog. Mater. Sci. 10 (1963) 151–391.

[29] J. Davis, J. Bourrat, C. Goux, Stainless steels, Les editions de physique, 1993.

[30] N.F. Mott, F.R.N. Nabarro, An attempt to estimate the degree of precipitation hardening, with a simple model, Proc. Phys. Soc. 52 (1940) 86–89. doi:10.1088/0959-5309/52/1/312.

[31] J.W. Martin, Precipitation Hardening, Butterworth-Heinemann, 1968.

[32] L. Brown, R. Ham, Dislocation-particle interactions, Strength. Methods Cryst. (1971).

[33] K.C. Russell, L.M.M. Brown, A dispersion strengthening model based on differing elastic moduli applied to the iron-copper system, Acta Metall. 20 (1972) 969–974. doi:10.1016/0001-6160(72)90091-0.

[34] Z. Guo, W. Sha, Quantification of Precipitation Hardening and Evolution of Precipitates, Mater. Trans. 43 (2002) 1273–1282. doi:10.2320/matertrans.43.1273.

[35] K.C. Antony, Aging reactions in precipitation hardenable stainless steel, J. Met. 15 (1963).

[36] H.J. Ryu, Y.S. Kim, A.M. Yacout, Thermal creep modeling of HT9 steel for fast reactor applications, J. Nucl. Mater. 409 (2011) 207–213. doi:10.1016/j.jnucmat.2010.12.232.

[37] M.B. Toloczko, F.A. Garner, C.R. Eiholzer, Irradiation creep and swelling of the US fusion heats of HT9 and 9Cr-1Mo to 208 dpa at ~ 400°C, J. Nucl. Mater. 212–215 (1994) 604–607. doi:10.1016/0022-3115(94)90131-7.

[38] A. Heinzel, M. Kondo, M. Takahashi, Corrosion of steels with surface treatment and Al-alloying by GESA exposed in lead–bismuth, J. Nucl. Mater. 350 (2006) 264–270. doi:10.1016/j.jnucmat.2006.01.014.

[39] A. Zeman, L. Debarberis, J. Kočík, V. Slugeň, E. Keilová, Microstructural analysis of candidate steels pre-selected for new advanced reactor systems, J. Nucl. Mater. 362 (2007) 259–267. doi:10.1016/j.jnucmat.2007.01.068.

[40] G. Bonny, D. Terentyev, L. Malerba, On the α–α′ miscibility gap of Fe–Cr alloys, Scr. Mater. 59 (2008) 1193–1196. doi:10.1016/j.scriptamat.2008.08.008.

[41] W. Xiong, M. Selleby, Q. Chen, J. Odqvist, Y. Du, Phase Equilibria and Thermodynamic Properties in the Fe-Cr System, Crit. Rev. Solid State Mater. Sci. 35 (2010) 125–152. doi:10.1080/10408431003788472.

[42] L. Malerba, A. Caro, J. Wallenius, Multiscale modelling of radiation damage and phase transformations: The challenge of FeCr alloys, J. Nucl. Mater. 382 (2008) 112–125. doi:10.1016/j.jnucmat.2008.08.014.

[43] M. Bachhav, G. Robert Odette, E.A. Marquis, α′ precipitation in neutron-irradiated Fe–Cr alloys, Scr. Mater. 74 (2014) 48–51. doi:10.1016/j.scriptamat.2013.10.001.

[44] H.J. Rack, D. Kalish, The strength, fracture toughness, and low cycle fatigue behavior of 17-4 PH stainless steel, Metall. Trans. 5 (1974) 1595–1605. doi:10.1007/BF02646331.

[45] B. Yrieix, M. Guttmann, Aging between 300 and 450°C of wrought martensitic 13–17 wt-%Cr stainless steels, Mater. Sci. Technol. 9 (1993) 125–137.

[46] U.K. Viswanathan, S. Banerjee, R. Krishnan, Effects of aging on the microstructure of 17-4 PH stainless steel, Mater. Sci. Eng. A. 104 (1988) 181–189.

[47] C.N. Hsiao, C.S. Chiou, J.R. Yang, Aging reactions in a 17-4 PH stainless steel, Mater. Chem. Phys. 74 (2002) 134–142. doi:10.1016/S0254-0584(01)00460-6.

[48] M. Murayama, K. Hono, Y. Katayama, Microstructural evolution in a 17-4 PH stainless steel after aging at 400 °C, Metall. Mater. Trans. A. 30 (1999) 345–353. doi:10.1007/s11661-999-0323-2.

[49] J. Wang, H. Zou, C. Li, S. Qiu, B. Shen, The effect of microstructural evolution on hardening behavior of type 17-4PH stainless steel in long-term aging at 350 °C, Mater. Charact. 57 (2006) 274–280. doi:10.1016/j.matchar.2006.02.004.

[50] P.J. Othen, M.L. Jenkins, G.D.W. Smith, High-resolution electron microscopy studies of the structure of Cu precipitates in α-Fe, Philos. Mag. A. 70 (1994) 1–24. doi:10.1080/01418619408242533.

[51] G.M. Worrall, J.T. Buswell, C.A. English, M.G. Hetherington, G.D.W. Smith, A study of the precipitation of copper particles in a ferrite matrix, J. Nucl. Mater. 148 (1987) 107–114. doi:10.1016/0022-3115(87)90525-3.

[52] R.G. Carter, N. Soneda, K. Dohi, J.M. Hyde, C.A. English, W.L. Server, Microstructural characterization of irradiation-induced Cu-enriched clusters in reactor pressure vessel steels, J. Nucl. Mater. 298 (2001) 211–224. doi:10.1016/S0022-3115(01)00659-6.

[53] P.D. Styman, J.M. Hyde, K. Wilford, A. Morley, G.D.W. Smith, Precipitation in long term thermally aged high copper, high nickel model RPV steel welds, Prog. Nucl. Energy. 57 (2012) 86–92. doi:10.1016/j.pnucene.2011.10.010.

[54] M.K.M.K. Miller, K.F.K.F. Russell, K. Thompson, R. Alvis, D.J.D.J. Larson, Review of atom probe FIB-based specimen preparation methods., Microsc. Microanal. 13 (2007) 428–36. doi:10.1017/S1431927607070845.

[55] M.K. Miller, M.G. Burke, Characterization of copper precipitation in a 17/4 PH steel: A combined APFIM/TEM study, in: Proc. 5th Inter. Conf. Environ. Degrad. Mater. Nucl. Power Syst. React., LaGrange Park, IL, 1991: pp. 689–695.

[56] H.R. Habibi Bajguirani, The effect of ageing upon the microstructure and mechanical properties of type 15-5 PH stainless steel, Mater. Sci. Eng. A. 338 (2002) 142–159. doi:10.1016/S0921-5093(02)00062-X.

[57] J. Wang, H. Zou, C. Li, Y. Peng, S. Qiu, B. Shen, The microstructure evolution of type 17-4PH stainless steel during long-term aging at 350°C, 2006.

[58] R.M. Fisher, E.J. Dulis, K.G. Carroll, Identification of the Precipitate Accompanying 885°F Embrittlement in Chromium Steels, Trans. Metall. Soc. AIME. 197 (1953) 690–695.

[59] S. Kobayashi, T. Takasugi, Mapping of 475 °c embrittlement in ferritic Fe-Cr-Al alloys, Scr. Mater. 63 (2010) 1104–1107. doi:10.1016/j.scriptamat.2010.08.015.

[60] J. Langer, M. Bar-on, H. Miller, New computational method in the theory of spinodal decomposition, Phys. Rev. A. 11 (1975) 1417–1429. doi:10.1103/PhysRevA.11.1417.

[61] V.M. Lopez-Hirata, O. Soriano-Vargas, H.J. Rosales-Dorantes, M.L.S. Muñoz, Phase decomposition in an Fe-40at.% Cr alloy after isothermal aging and its effect on hardening, Mater. Charact. 62 (2011) 789–792. doi:10.1016/j.matchar.2011.05.012.

[62] S.S. Brenner, M.K. Miller, W.A. Soffa, Spinodal decomposition of iron-32 at.% chromium at 470°C, Scr. Metall. 16 (1982) 831–836. doi:10.1016/0036-9748(82)90239-3.

[63] J.M. Hyde, M.K. Miller, M.G. Hetherington, A. Cerezo, G.D.W. Smith, C.M. Elliott, Spinodal decomposition in Fe-Cr alloys: Experimental study at the atomic level and comparison with computer models—II. Development of domain size and composition amplitude, Acta Metall. Mater. 43 (1995) 3403–3413. doi:10.1016/0956-7151(95)00041-S.

[64] M.K. Miller, J.M. Hyde, M.G. Hetherington, A. Cerezo, G.D.W. Smith, C.M. Elliott, Spinodal decomposition in Fe-Cr alloys: Experimental study at the atomic level and comparison with computer models—I. Introduction and methodology, Acta Metall. Mater. 43 (1995) 3385–3401. doi:10.1016/0956-7151(95)00040-3.

[65] M.K. Miller, M.G. Hetherington, Local magnification effects in the atom probe, Surf. Sci. 246 (1991) 442–449. doi:10.1016/0039-6028(91)90449-3.

[66] J. Wang, H. Zou, C. Li, S. Qiu, B. Shen, The spinodal decomposition in 17-4PH stainless steel subjected to long-term aging at 350 °C, Mater. Charact. 59 (2008) 587–591. doi:10.1016/j.matchar.2007.04.018.

[67] A.V. Barashev, S.I. Golubov, D.J. Bacon, P.E.J. Flewitt, T.A. Lewis, Copper precipitation in Fe–Cu alloys under electron and neutron irradiation, Acta Mater. 52 (2004) 877–886. doi:10.1016/j.actamat.2003.10.023.

[68] K. Nogiwa, N. Nita, H. Matsui, Quantitative analysis of the dependence of hardening on copper precipitate diameter and density in Fe–Cu alloys, J. Nucl. Mater. 367–370 (2007) 392–398. doi:10.1016/j.jnucmat.2007.03.123.

[69] B. Radiguet, A. Barbu, P. Pareige, Understanding of copper precipitation under electron or ion irradiations in FeCu0.1wt% ferritic alloy by combination of experiments and modelling, J. Nucl. Mater. 360 (2007) 104–117. doi:10.1016/j.jnucmat.2006.09.007.

[70] Y.F. Yin, R.G. Faulkner, Z. Lu, Irradiation-induced precipitation modelling of ferritic steels, J. Nucl. Mater. 389 (2009) 225–232. doi:10.1016/j.jnucmat.2009.02.006.

[71] G.S. Was, J.P. Wharry, B. Frisbie, B.D. Wirth, D. Morgan, J.D. Tucker, et al., Assessment of radiation-induced segregation mechanisms in austenitic and ferritic–martensitic alloys, J. Nucl. Mater. 411 (2011) 41–50. doi:10.1016/j.jnucmat.2011.01.031.

[72] C. Abromeit, Aspects of simulation of neutron damage by ion irradiation, J. Nucl. Mater. 216 (1994) 78–96. doi:10.1016/0022-3115(94)90008-6.

[73] C.D. Hardie, C. a. Williams, S. Xu, S.G. Roberts, Effects of irradiation temperature and dose rate on the mechanical properties of self-ion implanted Fe and Fe–Cr alloys, J. Nucl. Mater. 439 (2013) 33–40. doi:10.1016/j.jnucmat.2013.03.052.

[74] G.S. Was, Fundamentals of radiation materials science: Metals and alloys, second edition, 2016. doi:10.1007/978-1-4939-3438-6.

[75] G.S. Was, Fundamentals of Radiation Materials Science, 2nd ed., Springer, MI, 2007. doi:10.1007/978-3-540-49472-0.

[76] K.C.C. Russell, Phase stability under irradiation, Prog. Mater. Sci. 28 (1984) 229–434. doi:10.1016/0079-6425(84)90001-X.

[77] R.G. Faulkner, Radiation-induced grain boundary segregation in nuclear reactor steels, J. Nucl. Mater. 251 (1997) 269–275. doi:10.1016/S0022-3115(97)00248-1.

[78] R.G. Faulkner, N.C. Waite, E.A. Little, T.S. Morgan, Radiation-induced grain boundary segregation in dilute alloys, Mater. Sci. Eng. A. 171 (1993) 241–248. doi:10.1016/0921-5093(93)90411-7.

[79] T.R. Allen, G.S. Was, Modeling radiation-induced segregation in austenitic Fe–Cr–Ni alloys, Acta Mater. 46 (1998) 3679–3691. doi:10.1016/S1359-6454(98)00019-6.

[80] L. Kornblit, A. Ignatiev, The size effect in radiation-induced segregation of solutes in binary metallic alloys, J. Nucl. Mater. 126 (1984) 77–78. doi:10.1016/0022-3115(84)90535-X.

[81] Z. Lu, R.G. Faulkner, N. Sakaguchi, H. Kinoshita, H. Takahashi, P.E.J. Flewitt, Irradiation-induced grain boundary chromium microchemistry in high alloy ferritic steels, J. Nucl. Mater. 351 (2006) 155–161. doi:10.1016/j.jnucmat.2006.02.026.

[82] Z. Lu, R.G. Faulkner, G. Was, B.D. Wirth, Irradiation-induced grain boundary chromium microchemistry in high alloy ferritic steels, Scr. Mater. 58 (2008) 878–881. doi:10.1016/j.scriptamat.2008.01.004.

[83] I.M. Neklyudov, V.N. Voyevodin, Features of structure-phase transformations and segregation processes under irradiation of austenitic and ferritic-martensitic steels, J. Nucl. Mater. 212–215 (1994) 39–44. doi:10.1016/0022-3115(94)90031-0.

[84] J.P. Wharry, Z. Jiao, V. Shankar, J.T. Busby, G.S. Was, Radiation-induced segregation and phase stability in ferritic-martensitic alloy T 91, in: J. Nucl. Mater., North-Holland, 2011: pp. 140–144. doi:10.1016/j.jnucmat.2010.12.052.

[85] S. Ohnuki, H. Takahashi, T. Takeyama, Void swelling and segregation of solute in ion-irradiated ferritic steels, J. Nucl. Mater. 104 (1981) 1121–1125. doi:10.1016/0022-3115(82)90751-6.

[86] T. Kato, H. Takahashi, S. Ohnuki, K. Nakata, J. Kuniya, The effect of solute content on grain boundary segregation in electron-irradiated Fe-Cr-Mn alloys, J. Nucl. Mater. 179–181 (1991) 623–625. doi:10.1016/0022-3115(91)90165-4.

[87] R.E. Clausing, L. Heatherly, A.F. Rowcliffe, K. Farrell, R.G. Faulkner, Radiation-induced segregation in HT-9 martensitic steel, (1986).

[88] T. Allen, L. Tan, J. Tucker, J. Gan, Radiation resistance of advanced ferritic-martensitic steel HCM12A, J. ASTM. (2005).

[89] P. Dubuisson, D. Gilbon, J.L. Séran, Microstructural evolution of ferritic-martensitic steels irradiated in the fast breeder reactor Phénix, J. Nucl. Mater. 205 (1993) 178–189. doi:10.1016/0022-3115(93)90080-I.

[90] H. Takahashi, S. Ohnuki, T. Takeyama, Radiation-induced segregation at internal sinks in electron irradiated binary alloys, J. Nucl. Mater. 104 (1981) 1415–1419. doi:10.1016/0022-3115(82)90798-X.

[91] G. Gupta, Z. Jiao, A.N. Ham, J.T. Busby, G.S. Was, Microstructural evolution of proton irradiated T91, J. Nucl. Mater. 351 (2006) 162–173. doi:10.1016/j.jnucmat.2006.02.028.

[92] K.G. Field, B.D. Miller, H.J.M. Chichester, K. Sridharan, T.R. Allen, Relationship between lath boundary structure and radiation induced segregation in a neutron irradiated 9wt.% Cr model ferritic/martensitic steel, J. Nucl. Mater. 445 (2014) 143–148. doi:10.1016/j.jnucmat.2013.10.056.

[93] E.A. Marquis, S. Lozano-Perez, V. de Castro, Effects of heavy-ion irradiation on the

grain boundary chemistry of an oxide-dispersion strengthened Fe–12wt.% Cr alloy, J. Nucl. Mater. 417 (2011) 257–261. doi:10.1016/j.jnucmat.2010.12.251.

[94] J.P. Wharry, G.S. Was, A systematic study of radiation-induced segregation in ferritic–martensitic alloys, J. Nucl. Mater. 442 (2013) 7–16. doi:10.1016/j.jnucmat.2013.07.071.

[95] J.P. Wharry, G.S. Was, The mechanism of radiation-induced segregation in ferritic–martensitic alloys, Acta Mater. 65 (2014) 42–55. doi:10.1016/j.actamat.2013.09.049.

[96] Z. Jiao, G.S. Was, Segregation behavior in proton- and heavy-ion-irradiated ferritic–martensitic alloys, Acta Mater. 59 (2011) 4467–4481. doi:10.1016/j.actamat.2011.03.070.

[97] X. Jia, Y. Dai, Microstructure in martensitic steels T91 and F82H after irradiation in SINQ Target-3, J. Nucl. Mater. 318 (2003) 207–214. doi:10.1016/S0022-3115(03)00101-6.

[98] R.L. Klueh, K. Shiba, M.A. Sokolov, Embrittlement of irradiated F82H in the absence of irradiation hardening, J. Nucl. Mater. 386–388 (2009) 191–194. doi:10.1016/j.jnucmat.2008.12.090.

[99] P.J. Maziasz, R.L. Klueh, J.M. Vitek, Helium effects on void formation in 9Cr-1MoVNb and 12Cr-1MoVW irradiated in HFIR, J. Nucl. Mater. 141–143 (1986) 929–937. doi:10.1016/0022-3115(86)90120-0.

[100] D.S. Gelles, L.E. Thomas, Effects of neutron irradiation on microstructure in experimental and commercial ferritic alloys, (1984).

[101] B.H. Sencer, J.R. Kennedy, J.I. Cole, S.A. Maloy, F.A. Garner, Microstructural analysis of an HT9 fuel assembly duct irradiated in FFTF to 155dpa at 443°C, J. Nucl. Mater. 393 (2009) 235–241. doi:10.1016/j.jnucmat.2009.06.010.

[102] Z. Jiao, V. Shankar, G.S. Was, Phase stability in proton and heavy ion irradiated ferritic–martensitic alloys, J. Nucl. Mater. 419 (2011) 52–62. doi:10.1016/j.jnucmat.2011.08.020.

[103] J.J. Kai, R.L. Klueh, Microstructural analysis of neutron-irradiated martensitic steels, J. Nucl. Mater. 230 (1996) 116–123. doi:10.1016/0022-3115(96)00165-1.

[104] J. Van den Bosch, O. Anderoglu, R. Dickerson, M. Hartl, P. Dickerson, J.A. Aguiar, et al., SANS and TEM of ferritic–martensitic steel T91 irradiated in FFTF up to 184dpa at 413°C, J. Nucl. Mater. 440 (2013) 91–97. doi:10.1016/j.jnucmat.2013.04.025.

[105] M.H. Mathon, Y. de Carlan, G. Geoffroy, X. Averty, A. Alamo, C.. de Novion, A SANS investigation of the irradiation-enhanced α–α′ phases separation in 7–12 Cr martensitic steels, J. Nucl. Mater. 312 (2003) 236–248. doi:10.1016/S0022-

3115(02)01630-6.

[106] M.L. Jenkins, C.A. English, B.L. Eyre, Heavy-ion irradiation of α-iron, Philos. Mag. A Phys. Condens. Matter, Struct. Defects Mech. Prop. 38 (1978) 97–114. doi:10.1080/01418617808239220.

[107] M.R. Halstead, S. Lee, J. Petrosky, A. Bickley, P. Sokol, Neutron energy spectrum characterization on TMR-1 at the Indiana University neutron source, Phys. Procedia. 26 (2012) 188–195. doi:10.1016/j.phpro.2012.03.024.

[108] D.L. Hill, The neutron energy spectrum from U235 thermal fission, Phys. Rev. 87 (1952) 1034–1037. doi:10.1103/PhysRev.87.1034.

[109] L.K. Mansur, Correlation of neutron and heavy-ion damage, J. Nucl. Mater. 78 (1978) 156–160. doi:10.1016/0022-3115(78)90514-7.

[110] S.J. Zinkle, L.L. Snead, Opportunities and limitations for ion beams in radiation effects studies: Bridging critical gaps between charged particle and neutron irradiations, Scr. Mater. (2016). doi:10.1016/j.scriptamat.2017.06.041.

[111] Z. Jiao, J. Michalicka, G.S. Was, Self-ion emulation of high dose neutron irradiated microstructure in stainless steels, J. Nucl. Mater. 501 (2018) 312–318. doi:10.1016/J.JNUCMAT.2018.01.054.

[112] G.S.S. Was, Z. Jiao, E. Getto, K. Sun, A.M.M. Monterrosa, S.A.A. Maloy, et al., Emulation of reactor irradiation damage using ion beams, Scr. Mater. 88 (2014) 33–36. doi:10.1016/j.scriptamat.2014.06.003.

[113] Y.E. Kupriiyanova, V. V. Bryk, O. V. Borodin, A.S. Kalchenko, V.N. Voyevodin, G.D. Tolstolutskaya, et al., Use of double and triple-ion irradiation to study the influence of high levels of helium and hydrogen on void swelling of 8-12% Cr ferritic-martensitic steels, J. Nucl. Mater. 468 (2016) 264–273. doi:10.1016/j.jnucmat.2015.07.012.

[114] W.B. Liu, Y.Z. Ji, P.K. Tan, C. Zhang, C.H. He, Z.G. Yang, Microstructure evolution during helium irradiation and post-irradiation annealing in a nanostructured reduced activation steel, J. Nucl. Mater. 479 (2016) 323–330. doi:10.1016/j.jnucmat.2016.07.030.

[115] C. Heintze, F. Bergner, M. Hern??ndez-Mayoral, R. K??gler, G. M??ller, A. Ulbricht, Irradiation hardening of Fe-9Cr-based alloys and ODS Eurofer: Effect of helium implantation and iron-ion irradiation at 300 ??c including sequence effects, J. Nucl. Mater. 470 (2016) 258–267. doi:10.1016/j.jnucmat.2015.12.041.

[116] J.P. Biersack, J.F. Ziegler, The Stopping and Range of Ions in Solids, in: Ion Implant. Tech., Springer Berlin Heidelberg, Berlin, Heidelberg, 1982: pp. 122–156. doi:10.1007/978-3-642-68779-2_5.

[117] N. Juslin, K. Nordlund, J. Wallenius, L. Malerba, Simulation of threshold displacement energies in FeCr, Nucl. Instruments Methods Phys. Res. Sect. B Beam Interact. with Mater. Atoms. 255 (2007) 75–77. doi:10.1016/j.nimb.2006.11.046.

[118] C. Zheng, M.A. Auger, M.P. Moody, D. Kaoumi, Radiation induced segregation and precipitation behavior in self-ion irradiated Ferritic/Martensitic HT9 steel, J. Nucl. Mater. 491 (2017) 162–176. doi:10.1016/j.jnucmat.2017.04.040.

[119] B. Gault, M.P. Moody, J.M. Cairney, S.P. Ringer, Atom Probe Microscopy, Springer Science & Business Media, New York, 2012.

[120] A. Cerezo, P.H. Clifton, M.J. Galtrey, C.J. Humphreys, T.F. Kelly, D.J. Larson, et al., Atom probe tomography today, Mater. Today. 10 (2007) 36–42. doi:10.1016/S1369-7021(07)70306-1.

[121] B. Gault, D. Haley, F. de Geuser, M.P.P. Moody, E.A.A. Marquis, D.J.J. Larson, et al., Advances in the reconstruction of atom probe tomography data, Ultramicroscopy. 111 (2011) 448–457. doi:10.1016/j.ultramic.2010.11.016.

[122] K. Hono, T. Ohkubo, Y.M. Chen, M. Kodzuka, K. Oh-ishi, H. Sepehri-Amin, et al., Broadening the applications of the atom probe technique by ultraviolet femtosecond laser, Ultramicroscopy. 111 (2011) 576–583. doi:10.1016/j.ultramic.2010.11.020.

[123] A. Vella, On the interaction of an ultra-fast laser with a nanometric tip by laser assisted atom probe tomography: A review, Ultramicroscopy. 132 (2013) 5–18. doi:10.1016/j.ultramic.2013.05.016.

[124] F. Vurpillot, C. Oberdorfer, Modeling Atom Probe Tomography: A review, Ultramicroscopy. 159 (2015) 202–216. doi:10.1016/j.ultramic.2014.12.013.

[125] D.J. Larson, T.J. Prosa, R.M. Ulfig, B.P. Geiser, T.F. Kelly, Local Electrode Atom Probe Tomography, Springer Science & Business Media, New York, 2013. doi:10.1007/978-1-4614-8721-0.

[126] K. Thompson, D. Lawrence, D.J. Larson, J.D. Olson, T.F. Kelly, B. Gorman, In situ site-specific specimen preparation for atom probe tomography., Ultramicroscopy. 107 (2007) 131–9. doi:10.1016/j.ultramic.2006.06.008.

[127] P. Bas, A. Bostel, B. Deconihout, D. Blavette, A general protocol for the reconstruction of 3D atom probe data, Appl. Surf. Sci. 87–88 (1995) 298–304. doi:10.1016/0169-4332(94)00561-3.

[128] B. Geiser, D. Larson, E. Oltman, S. Gerstl, D. Reinhard, T. Kelly, et al., Wide-Field-of-View Atom Probe Reconstruction, Microsc. Microanal. 15 (2009) 292. doi:10.1017/S1431927609098249.

[129] B. Gault, F. de Geuser, L.T. Stephenson, M.P. Moody, B.C. Muddle, S.P. Ringer, Estimation of the Reconstruction Parameters for Atom Probe Tomography, Microsc.

Microanal. 14 (2008) 296–305. doi:10.1017/S1431927608080690.

[130] B. Gault, M.P. Moody, F. De Geuser, G. Tsafnat, A. La Fontaine, L.T. Stephenson, et al., Advances in the calibration of atom probe tomographic reconstruction, J. Appl. Phys. 105 (2009) 34913. doi:10.1063/1.3068197.

[131] L. Yao, A filtering method to reveal crystalline patterns from atom probe microscopy desorption maps, MethodsX. 3 (2016) 268–273. doi:10.1016/j.mex.2016.03.012.

[132] L. Yao, T. Withrow, O.D. Restrepo, W. Windl, E.A. Marquis, Effects of the local structure dependence of evaporation fields on field evaporation behavior, Appl. Phys. Lett. 107 (2015) 241602. doi:10.1063/1.4937454.

[133] P.J. Warren, A. Cerezo, G.D.W. Smith, Observation of atomic planes in 3DAP analysis, in: Ultramicroscopy, 1998: pp. 261–266. doi:10.1016/S0304-3991(97)00165-4.

[134] B. Gault, M.P. Moody, F. De Geuser, A. La Fontaine, L.T. Stephenson, D. Haley, et al., Spatial Resolution in Atom Probe Tomography, Microsc. Microanal. 16 (2010) 99–110. doi:10.1017/S1431927609991267.

[135] B.P. Geiser, T.F. Kelly, D.J. Larson, J. Schneir, J.P. Roberts, Spatial Distribution Maps for Atom Probe Tomography, Microsc. Microanal. 13 (2007) 437–447. doi:10.1017/S1431927607070948.

[136] J. Takahashi, K. Kawakami, D. Raabe, Comparison of the quantitative analysis performance between pulsed voltage atom probe and pulsed laser atom probe, Ultramicroscopy. 175 (2017) 105–110. doi:10.1016/j.ultramic.2017.01.015.

[137] B. Deconihout, R. Saint-Martin, C. Jarnot, A. Bostel, Improvement of the mass resolution of the atom probe using a dual counter-electrode, Ultramicroscopy. 95 (2003) 239–249. doi:10.1016/S0304-3991(02)00322-4.

[138] D.R. Kingham, The post-ionization of field evaporated ions: A theoretical explanation of multiple charge states, Surf. Sci. 116 (1982) 273–301. doi:10.1016/0039-6028(82)90434-4.

[139] O. Dmitrieva, P. Choi, S.S.A. Gerstl, D. Ponge, D. Raabe, Pulsed-laser atom probe studies of a precipitation hardened maraging TRIP steel, Ultramicroscopy. 111 (2011) 623–627. doi:10.1016/j.ultramic.2010.12.007.

[140] R.K. Zheng, M.P. Moody, B. Gault, Z.W. Liu, H. Liu, S.P. Ringer, On the understanding of the microscopic origin of the properties of diluted magnetic semiconductors by atom probe tomography, J. Magn. Magn. Mater. 321 (2009) 935–943. doi:10.1016/j.jmmm.2008.03.014.

[141] J. Takahashi, K. Kawakami, A quantitative model of preferential evaporation and retention for atom probe tomography, Surf. Interface Anal. 46 (2014) 535–543.

doi:10.1002/sia.5555.

[142] F. Danoix, M.K. Miller, A. Bigot, Analysis conditions of an industrial Al-Mg-Si alloy by conventional and 3D atom probes, Ultramicroscopy. 89 (2001) 177–188. doi:10.1016/S0304-3991(01)00098-5.

[143] F. De Geuser, B. Gault, A. Bostel, F. Vurpillot, Correlated field evaporation as seen by atom probe tomography, Surf. Sci. 601 (2007) 536–543. doi:10.1016/j.susc.2006.10.019.

[144] B. Gault, F. Danoix, K. Hoummada, D. Mangelinck, H. Leitner, Impact of directional walk on atom probe microanalysis, Ultramicroscopy. 113 (2012) 182–191. doi:10.1016/j.ultramic.2011.06.005.

[145] B.W. Krakauer, D.N. Seidman, Absolute atomic-scale measurements of the Gibbsian interfacial excess of solute at internal interfaces, Phys. Rev. B. 48 (1993) 6724–6727. doi:10.1103/PhysRevB.48.6724.

[146] O.C. Hellman, J.A. Vandenbroucke, J. Rüsing, D. Isheim, D.N. Seidman, Analysis of Three-dimensional Atom-probe Data by the Proximity Histogram, Microsc. Microanal. 6 (2000) 437–444. doi:10.1007/s100050010051.

[147] A. Shariq, T. Al-Kassab, R. Kirchheim, R.B. Schwarz, Exploring the next neighbourhood relationship in amorphous alloys utilizing atom probe tomography, Ultramicroscopy. 107 (2007) 773–780. doi:10.1016/j.ultramic.2007.02.030.

[148] L.T. Stephenson, M.P. Moody, P.V. Liddicoat, S.P. Ringer, New techniques for the analysis of fine-scaled clustering phenomena within atom probe tomography (APT) data., Microsc. Microanal. 13 (2007) 448–463. doi:10.1017/S1431927607070900.

[149] J. Hyde, C. English, An analysis of the structure of irradiation induced Cu-enriched clusters in low and high nickel welds, in: MRS Proc., 2000.

[150] D. Vaumousse, A. Cerezo, P.J. Warren, A procedure for quantification of precipitate microstructures from three-dimensional atom probe data, Ultramicroscopy. 95 (2003) 215–221. doi:10.1016/S0304-3991(02)00319-4.

[151] J.M. Hyde, E.A. Marquis, K.B. Wilford, T.J. Williams, A sensitivity analysis of the maximum separation method for the characterisation of solute clusters, Ultramicroscopy. 111 (2011) 440–447. doi:10.1016/j.ultramic.2010.12.015.

[152] A. Cerezo, L. Davin, Aspects of the observation of clusters in the 3-dimensional atom probe, in: Surf. Interface Anal., John Wiley & Sons, Ltd., 2007: pp. 184–188. doi:10.1002/sia.2486.

[153] R.P. Kolli, D.N. Seidman, Comparison of compositional and morphological atom-probe tomography analyses for a multicomponent Fe-Cu steel., Microsc. Microanal. 13 (2007) 272–84. doi:10.1017/S1431927607070675.

[154] D. Isheim, M.S. Gagliano, M.E. Fine, D.N. Seidman, Interfacial segregation at Cu-rich precipitates in a high-strength low-carbon steel studied on a sub-nanometer scale, Acta Mater. 54 (2006) 841–849. doi:10.1016/j.actamat.2005.10.023.

[155] L. Couturier, F. De Geuser, M. Descoins, A. Deschamps, Evolution of the microstructure of a 15-5PH martensitic stainless steel during precipitation hardening heat treatment, Mater. Des. 107 (2016) 416–425. doi:10.1016/j.matdes.2016.06.068.

[156] A. Seko, S.R. Nishitani, I. Tanaka, H. Adachi, E.F. Fujita, First-principles calculation on free energy of precipitate nucleation, Calphad. 28 (2004) 173–176. doi:10.1016/j.calphad.2004.07.003.

[157] A. Seko, N. Odagaki, S.R. Nishitani, I. Tanaka, H. Adachi, Free-Energy Calculation of Precipitate Nucleation in an Fe-Cu-Ni Alloy, Mater. Trans. 45 (2004) 1978–1981. doi:10.2320/matertrans.45.1978.

[158] O.I. Gorbatov, Y.N. Gornostyrev, P.A. Korzhavyi, A.V. Ruban, Effect of Ni and Mn on the formation of Cu precipitates in α-Fe, Scr. Mater. 102 (2015) 11–14. doi:10.1016/j.scriptamat.2015.01.016.

[159] M.S. Anand, R.P. Agarwala, Diffusion of copper in iron, J. Appl. Phys. 37 (1966) 4248–4251. doi:10.1063/1.1708006.

[160] G. Salje, M. Feller-Kniepmeier, The diffusion and solubility of copper in iron, J. Appl. Phys. 48 (1977) 1833–1839. doi:10.1063/1.323934.

[161] N. Oono, H. Nitta, Y. Iijima, Diffusion of niobium in .ALPHA.-iron, Mater. Trans. 44 (2003) 2078–2083.

[162] F. Vurpillot, A. Bostel, D. Blavette, Trajectory overlaps and local magnification in three-dimensional atom probe, Appl. Phys. Lett. 76 (2000) 3127. doi:10.1063/1.126545.

[163] V. Kuksenko, C. Pareige, C. Genevois, P. Pareige, Characterisation of Cr, Si and P distribution at dislocations and grain-boundaries in neutron irradiated Fe–Cr model alloys of low purity, J. Nucl. Mater. 434 (2013) 49–55. doi:10.1016/j.jnucmat.2012.11.027.

[164] V. Kuksenko, C. Pareige, P. Pareige, Cr precipitation in neutron irradiated industrial purity Fe–Cr model alloys, J. Nucl. Mater. 432 (2013) 160–165. doi:10.1016/j.jnucmat.2012.07.021.

[165] C.L. Liu, G.R. Odette, B.D. Wirth, G.E. Lucas, A lattice Monte Carlo simulation of nanophase compositions and structures in irradiated pressure vessel Fe-Cu-Ni-Mn-Si steels, Mater. Sci. Eng. A. 238 (1997) 202–209. doi:10.1016/S0921-5093(97)00450-4.

[166] P.B. Wells, T. Yamamoto, B. Miller, T. Milot, J. Cole, Y. Wu, et al., Evolution of

manganese–nickel–silicon-dominated phases in highly irradiated reactor pressure vessel steels, Acta Mater. 80 (2014) 205–219. doi:10.1016/j.actamat.2014.07.040.

[167] J.M. Cairney, K. Rajan, D. Haley, B. Gault, P.A.J. Bagot, P.-P. Choi, et al., Mining information from atom probe data, Ultramicroscopy. 159 (2015) 324–337. doi:10.1016/j.ultramic.2015.05.006.

[168] R. Ngayam-Happy, C.S. Becquart, C. Domain, L. Malerba, Formation and evolution of MnNi clusters in neutron irradiated dilute Fe alloys modelled by a first principle-based AKMC method, J. Nucl. Mater. 426 (2012) 198–207. doi:10.1016/j.jnucmat.2012.03.033.

[169] G. Bonny, D. Terentyev, A. Bakaev, E.E. Zhurkin, M. Hou, D. Van Neck, et al., On the thermal stability of late blooming phases in reactor pressure vessel steels: An atomistic study, J. Nucl. Mater. 442 (2013) 282–291. doi:10.1016/j.jnucmat.2013.08.018.

[170] W. Xiong, H. Ke, R. Krishnamurthy, P. Wells, L. Barnard, G.R. Odette, et al., Thermodynamic models of low-temperature Mn–Ni–Si precipitation in reactor pressure vessel steels, MRS Commun. (2014) 1–5. doi:10.1557/mrc.2014.21.

[171] K.C. Russell, L.M. Brown, A dispersion strengthening model based on differing elastic moduli applied to the iron-copper system, Acta Metall. 20 (1972) 969–974. doi:10.1016/0001-6160(72)90091-0.

[172] K. Fujii, K. Fukuya, R. Kasada, A. Kimura, T. Ohkubo, Effects of tensile stress on Cu clustering in irradiated Fe-Cu alloy, J. Nucl. Mater. 458 (2015) 281–287. doi:10.1016/j.jnucmat.2014.12.108.

[173] J. Syarif, K. Nakashima, T. Tsuchiyama, S. Takaki, Effect of Solute Copper on Yield Strength in Dislocation-strengthened Steels, ISIJ Int. 47 (2007) 340–345. doi:10.2355/isijinternational.47.340.

[174] D.A. Terentyev, G. Bonny, L. Malerba, Strengthening due to coherent Cr precipitates in Fe–Cr alloys: Atomistic simulations and theoretical models, Acta Mater. 56 (2008) 3229–3235. doi:10.1016/j.actamat.2008.03.004.

[175] J.W. Martin, Micromechanisms in Particle-Hardened Alloys, Cambridge University Press, Cambridge, UK, 1980.

[176] D. Schwen, E. Martinez, A. Caro, On the analytic calculation of critical size for alpha prime precipitation in FeCr, J. Nucl. Mater. 439 (2013) 180–184. doi:10.1016/j.jnucmat.2013.03.057.

[177] G. Krauss, Martensite in steel: strength and structure, Mater. Sci. Eng. A. 273–275 (1999) 40–57. doi:10.1016/S0921-5093(99)00288-9.

[178] M.J. Swenson, J.P. Wharry, Nanocluster irradiation evolution in Fe-9%Cr ODS and

ferritic-martensitic alloys, J. Nucl. Mater. 496 (2017) 24–40. doi:10.1016/j.jnucmat.2017.08.045.

[179] M.J. Swenson, J.P. Wharry, The comparison of microstructure and nanocluster evolution in proton and neutron irradiated Fe-9%Cr ODS steel to 3 dpa at 500 °c, J. Nucl. Mater. 467 (2015) 97–112. doi:10.1016/j.jnucmat.2015.09.022.

[180] Z. Jiao, V. Shankar, G.S. Was, Phase stability in proton and heavy ion irradiated ferritic-martensitic alloys, J. Nucl. Mater. 419 (2011) 52–62. doi:10.1016/j.jnucmat.2011.08.020.

[181] L. Tan, B.K. Kim, Y. Yang, K.G. Field, S. Gray, M. Li, Microstructural evolution of neutron-irradiated T91 and NF616 to ~4.3 dpa at 469 °C, J. Nucl. Mater. 493 (2017) 12–20. doi:10.1016/j.jnucmat.2017.05.041.

[182] L. Cipolla, H.K. Danielsen, D. Venditti, P.E. Di Nunzio, J. Hald, M.A.J. Somers, Conversion of MX nitrides to Z-phase in a martensitic 12% Cr steel, Acta Mater. 58 (2010) 669–679. doi:10.1016/j.actamat.2009.09.045.

[183] G. Miyamoto, S. Suetsugu, K. Shinbo, T. Furuhara, Surface Hardening and Nitride Precipitation in the Nitriding of Fe-M1-M2 Ternary Alloys Containing Al, V, or Cr, Metall. Mater. Trans. A Phys. Metall. Mater. Sci. 46 (2015) 5011–5020. doi:10.1007/s11661-015-3133-8.

[184] E. Getto, K. Sun, A.M. Monterrosa, Z. Jiao, M.J. Hackett, G.S. Was, Void swelling and microstructure evolution at very high damage level in self-ion irradiated ferritic-martensitic steels, J. Nucl. Mater. 480 (2016) 159–176. doi:10.1016/j.jnucmat.2016.08.015.

[185] B.H. Sencer, J.R. Kennedy, J.I. Cole, S.A. Maloy, F.A. Garner, Microstructural analysis of an HT9 fuel assembly duct irradiated in FFTF to 155 dpa at 443 ??C, J. Nucl. Mater. 393 (2009) 235–241. doi:10.1016/j.jnucmat.2009.06.010.

[186] V. Kuksenko, C. Pareige, P. Pareige, Intra granular precipitation and grain boundary segregation under neutron irradiation in a low purity Fe–Cr based alloy, J. Nucl. Mater. 425 (2012) 125–129. doi:10.1016/j.jnucmat.2011.10.031.

[187] V. Kuksenko, C. Pareige, C. Genevois, F. Cuvilly, M. Roussel, P. Pareige, Effect of neutron-irradiation on the microstructure of a Fe-12at.%Cr alloy, J. Nucl. Mater. 415 (2011) 61–66. doi:10.1016/j.jnucmat.2011.05.042.

[188] V. Kuksenko, C. Pareige, C. Genevois, P. Pareige, Characterisation of Cr, Si and P distribution at dislocations and grain-boundaries in neutron irradiated Fe-Cr model alloys of low purity, J. Nucl. Mater. 434 (2013) 49–55. doi:10.1016/j.jnucmat.2012.11.027.

[189] Z. Jiao, G.S. Was, Precipitate evolution in ion-irradiated HCM12A, in: J. Nucl. Mater., North-Holland, 2012: pp. 105–111. doi:10.1016/j.jnucmat.2011.12.017.

[190] O. Anderoglu, J. Van Den Bosch, P. Hosemann, E. Stergar, B.H. Sencer, D. Bhattacharyya, et al., Phase stability of an HT-9 duct irradiated in FFTF, J. Nucl. Mater. 430 (2012) 194–204. doi:10.1016/j.jnucmat.2012.06.038.

[191] J.G. Gigax, T. Chen, H. Kim, J. Wang, L.M. Price, E. Aydogan, et al., Radiation response of alloy T91 at damage levels up to 1000 peak dpa, J. Nucl. Mater. 482 (2016) 257–265. doi:10.1016/j.jnucmat.2016.10.003.

[192] S. Zhang, X. He, T. Ko, Non-equilibrium segregation of solutes to grain boundary - Part III Mechanism of non-equilibrium segregation, J. Mater. Sci. 29 (1994) 2663–2670. doi:10.1007/BF00356815.

[193] E.P. Simonen, L.A. Charlot, S.M. Bruemmer, Quantification of defect-solute coupling from inverse-Kirkendall segregation, J. Nucl. Mater. 225 (1995) 117–122. doi:10.1016/0022-3115(95)00063-1.

[194] L.K. Mansur, Correlation of neutron and heavy-ion damage. II. The predicted temperature shift if swelling with changes in radiation dose rate, J. Nucl. Mater. 78 (1978) 156–160. doi:10.1016/0022-3115(78)90514-7.

[195] G.S. Was, T.R. Allen, Radiation damage from different particle types, in: Radiat. Eff. Solids, Springer Netherlands, Dordrecht, 2007: pp. 65–98. doi:10.1007/978-1-4020-5295-8_4.

[196] Z. Jiao, S. Taller, K. Field, G. Yeli, M.P. Moody, G.S. Was, Microstructure evolution of T91 irradiated in the BOR60 fast reactor, J. Nucl. Mater. 504 (2018) 122–134. doi:10.1016/j.jnucmat.2018.03.024.

[197] H.H. Jin, E. Ko, S. Lim, J. Kwon, C. Shin, Effect of irradiation temperature on microstructural changes in self-ion irradiated austenitic stainless steel, J. Nucl. Mater. 493 (2017) 239–245. doi:10.1016/j.jnucmat.2017.06.019.

[198] A. Etienne, B. Radiguet, N.J. Cunningham, G.R. Odette, P. Pareige, Atomic scale investigation of radiation-induced segregation in austenitic stainless steels, J. Nucl. Mater. 406 (2010) 244–250. doi:10.1016/j.jnucmat.2010.08.043.

[199] M. Hatakeyama, S. Tamura, I. Yamagata, Direct observation of solute–dislocation interaction on screw dislocation in a neutron irradiated modified 316 stainless steel, Mater. Lett. 122 (2014) 301–305. doi:10.1016/j.matlet.2014.01.109.

[200] N. Yoshida, A. Yamaguchi, T. Muroga, Y. Miyamoto, K. Kitajima, Characteristics of point defects and their clustering in pure ferritic steels, J. Nucl. Mater. 155–157 (1988) 1232–1236. doi:10.1016/0022-3115(88)90502-8.

[201] K. Ono, K. Arakawa, H. Shibasaki, H. Kurata, I. Nakamichi, N. Yoshida, Release of helium from irradiation damage in Fe-9Cr ferritic alloy, J. Nucl. Mater. 329–333 (2004) 933–937. doi:10.1016/j.jnucmat.2004.04.061.

[202] T. Muroga, H. Watanabe, N. Yoshida, Correlation of fast neutron, fusion neutron and electron irradiations based on the dislocation loop density, J. Nucl. Mater. 174 (1990) 282–288. doi:10.1016/0022-3115(90)90241-E.

[203] S.C. Tjong, R.W. Hoffman, E.B. Yeager, Electron and Ion Spectroscopic Studies of the Passive Film on Iron- Chromium Alloys, J. Electrochem. Soc. 129 (1982) 1662. doi:10.1149/1.2124232.